UNIVERSITÀ
DEGLI STUDI
FIRENZE

DIPARTIMENTO
DI FISICA E
ASTRONOMIA

Lens
European Laboratory for
Non-Linear Spectroscopy

Università degli Studi di Firenze & European Laboratory for Non-linear Spectroscopy

INTERNATIONAL DOCTORATE IN
ATOMIC AND MOLECULAR PHOTONICS

CYCLE XXXVI

Coordinator Prof. Diederik Wiersma

Generating quantum coherence with incoherent radiation

Academic Discipline (SSD) FIS/03 - Fisica della Materia

Doctoral Candidate:
Ludovica Donati

Ludovica Donati

Supervisor:
Prof. Francesco Saverio Cataliotti

PhD Coordinator:
Prof. Diederik Wiersma

Co-Supervisor:
Dr. Stefano Gherardini

Stefano Gherardini

Years 2020/2024

Abstract

In multi-level quantum systems, coherent superposition states can unexpectedly arise from interactions with the continuum of modes associated with incoherent processes, such as spontaneous emission and incoherent pumping. This type of coherence, known as noise-induced Fano coherence, represents a novel observation that has not yet been documented.

In this thesis, I investigate a V-type three-level quantum system driven by incoherent radiation, examining both isotropic and unpolarized as well as anisotropic and polarized fields. The study identifies conditions for achieving quasi-stationary and stationary Fano coherence between the excited levels of the system within an overdamped dynamical regime. An optimization analysis of the main parameters, as the frequency splitting Δ between the excited levels, the intensity $\bar{n}$ of the incoherent radiation and the alignment parameter p between transition dipole moments, provides a suitable scenario for the detection of Fano coherence.

The V-type system is then implemented in the hyperfine structure of hot ^{87}Rb atoms inside a vapor cell and a proof-of-principle experiment is designed and conducted. The experimental setup employs angle-resolved fluorescence measurements to detect Fano coherence through spatial anisotropy in the emitted fluorescence around the vapor cell. Preliminary results are promising and are consistent with theoretical predictions.

Additionally, the thesis explores the quantum thermodynamics of noise-induced Fano coherence to certify the presence of genuinely quantum traits underlying its generation. This includes analyzing the conditions under which the Kirkwood-Dirac quasiprobability distribution of the stochastic energy changes exhibits negativity, indicating non-classical traits. The study also demonstrates the existence of nonequilibrium regimes where, the generation of coherence leads to a significant excess of energy compared to the initial state, provided that the system begins in a superposition of energy eigenstates.

Understanding how Fano coherence arises in multi-level systems through incoherent optical processes is crucial for its potential applications in enhancing the efficiency of quantum heat engines, photosynthetic light-harvesting complexes, and photovoltaics. The associated excess energy could be exploited as extractable work by external loads or storage systems, thereby offering significant technological advancements.

Contents

Abstract i

Abstract i

Contents iii

Introduction 1

1 Multi-level system driven by an incoherent source **5**

1.1 Quantum mechanical theory of radiation and atomic systems 6

1.1.1 Quantization of the electromagnetic field 6

1.1.2 Atoms as quantum systems 9

1.2 Open quantum system theory 11

1.2.1 Isolated quantum systems and unitary evolution 12

1.2.2 Interaction picture 13

1.2.3 Open quantum systems and their time evolution 15

1.3 Derivation of the quantum master equation 19

1.3.1 Interaction Hamiltonian for a V-type three level system driven by incoherent radiation 20

1.3.2 Interaction with an isotropic, unpolarized non-coherent source 28

1.3.3 Interaction with a polarized non-coherent source 31

1.4 Theoretical prediction for V-type three-level systems 34

1.4.1 Dynamical regimes with isotropic unpolarized radiation 34

1.4.2 Dynamical regimes with anisotropic polarized radiation 41

2 Energetics and quantumness of noise -induced Fano coherences **47**

2.1 Non-equilibrium quantum thermodynamics in a finite - dimensional system 48

2.1.1 Energy and heat exchange in closed and open quantum systems . . . 49

2.1.2 Two-Point Measurement scheme and no-go theorem 52

2.1.3 Kirkwood-Dirac quasiprobabilities approach 55

2.2 Energy fluctuations of a three-level system generating Fano-coherence . . . 58

2.2.1 KDQ distribution for the V-type three-level system 58

2.2.2 Quantumness certification 60

2.2.3 Optimization of excess energy 64

- 2.2.4 Efficiency of the process 67
- 2.2.5 Discussion 68

3 Implementation on ^{87}Rb atoms: theoretical and experimental results 70

- 3.1 ^{87}Rb atoms as V-type three level sysyems 71
  - 3.1.1 V-type three level systems in the hyperfine structure of ^{87}Rb atoms . 72
  - 3.1.2 Theoretical prediction with ^{87}Rb atoms 78
  - 3.1.3 Angle-resolved fluorescence detection 80
- 3.2 Proof-of-principle experiment for Fano-coherence detection 86
  - 3.2.1 Rb vapor cell and magnetic cage 86
  - 3.2.2 Detection scheme 90
  - 3.2.3 Laser system and control 93
  - 3.2.4 Optical setup 94
- 3.3 Experimental results 96
  - 3.3.1 Towards Fano coherence detection: preliminary measurements . . . 97
  - 3.3.2 Discussion 100

Conclusion 102

List of Pubblications 105

Bibliography 106

Introduction

The phenomenon of quantum coherence within multi-level atomic systems has garnered significant attention over an extensive period of time and continues to do so. It forms the foundation for numerous quantum phenomena, enabling the manipulation of atomic degrees of freedom through optical methods, and thus facilitating a comprehensive inquiry into their intricate internal structure. In 1950, A. Kastler published a landmark paper introducing one of the first techniques for manipulating atoms with light, namely *optical pumping* [1–3]. This technique is distinguished by the resonant exchange of angular momentum between atoms and circularly polarized light. The result is the polarization of atomic spins, yielding not just a well-defined distribution of steady-state populations, but also coherences between levels.

Laser techniques have been then employed towards the detection of a variety of quantum coherence phenomena in atomic systems, as the *Hanle effect* [4], the *level-crossing effect* [5] or the *quantum beating effect* [6], theoretically derived few years earlier in the context of atomic fluorescence emission. These phenomena involve exciting a multi-level atomic system into a coherent superposition of states using laser fields. Quantum coherence can emerge, as in the quantum beating effect, when two atomic excited levels, closely spaced in frequency, decay to a common ground level. The indistinguishability of the two decay paths leads to an interference effect reflected in the time-evolution of fluorescence, which exhibits an exponential decay modulated by a periodic oscillation, known as quantum beat. When the emitted fluorescence can be distinctly attributed to one of the excited levels, the quantum beats vanish, highlighting the interference nature of this phenomenon, similar to the Young's double-slit experiment [7, 8].

Quantum coherence also plays a crucial role in atomic absorption processes. For instance, when two laser fields interact with two optical atomic transitions from different ground levels to a common excited level, quantum interference in absorption can occur. The interference leads to a phenomenon known as *coherent population trapping* (CPT) [9–11]. In CPT, the coherent superposition of atomic states prevents the system from interacting with one of the coherent fields, effectively trapping the population in a dark state, that does not absorb light. Consequently, the atomic medium becomes *electromagnetically-induced transparent* [12, 13]. In these scenarios the state of the system changes coherently being driven by a coherent field.

Since the 1990s, there has been a growing interest in generating quantum coherence in multi-level atomic systems using alternative mechanism, remarkably by means of *incoherent* sources, such as a broadband laser or a thermal radiation, as well as interactions with the surrounding environment [14, 15]. In this case, this sources are distinguished by a continuum of modes, as opposed to a single coherent mode of a laser beam. For instance, during the process of spontaneous emission, a multi-level system can interact with the vacuum's continuum modes. In a V-type three level system with closely spaced emission pathways, this interaction can result in quantum interference and population inversion [16]. A Λ-type three-level system can exhibit similar phenomena [17]. The coherence arising from the interference of spontaneous emission can also lead to the formation of dark lines and narrower linewidths in the emission spectrum [18–20] or even result in emission quenching [21].

Gaining control over the fluorescence spectrum can be challenging when relying solely on the interference of two decay channels. However, introducing an additional incoherent mechanism can significantly enhance the flexibility of control parameters without compromising the coherence of the quantum system, contrary to what one might expect [22, 23]. A good example is external pumping with a broadband radiation source, that excites two nearly degenerate states in a three-level system. The bandwidth of the radiation must be sufficiently broad to drive both transitions, meaning the frequency splitting between the excited levels must be narrower than the bandwidth. In this way, interference occurs between the two excitation pathways, making it impossible to distinguish which excited level has been populated.

Interestingly, the presence of such incoherent mechanisms in a V-type three-level system, with nearly degenerate excited levels, results in the formation of *quantum (Fano) coherence* between excited states via *Fano interference*. Fano interference emerges when discrete atomic energy levels are coupled to a continuum of states [24, 25], which in this case is represented by the continuum of modes associated with the broadband radiation or the interaction with a thermal reservoir. The interference between transition amplitudes leads to an in-phase superposition of the excited states, referred to as Fano coherence, which can be either stationary or quasi-stationary [26–30]. This phenomenon has also been demonstrated in other configurations, as in Λ-type systems [27, 31, 32]. Fano coherence differs from that generated by coherent sources, where the coherence of the radiation is directly "transferred" to the system via dipole interaction. Mathematically, Fano coherence originates from the incoherent or dissipation terms in the master equation governing the system's dynamics, whereas coherence from coherent sources arises from the Hamiltonian's coherent terms.

The resilience of Fano coherence under the aforementioned "noisy" conditions, essential for its generation, has particular significance for systems in contact with thermal reservoirs, such as quantum heat engines [33], or exposed to thermal radiation, as customary in photo-conversion devices [34]. In particular, in the latter case, Svidzinsky *et al.* [34] theoretically demonstrate that Fano interferences might enable the mitigation of spontaneous emission, thereby reducing radiative recombination phenomena. The photo-conversion device (a photocell) is modeled with a V-type three-level system driven by incoherent light source, wherein the excited states represent conduction band states decaying into a common valence band state. Quantum coherence between the excited states of the system would theoretically lead to an increase in the extractable current from the device. Consequently, this enhancement would boost the output power and conversion efficiency. On the other hand, implementing a Λ-type system can enhance photon absorption, as demonstrated by Scully *et al.* in [33]. In this quantum heat engine model, a rapid transfer of atoms from the ground levels to the excited level enables an increase in extractable work. The boost in performance for both applications—whether in photocells or quantum heat engines—can be realized if the input light source is broad enough to excite both transitions, thereby producing interference between them.

Despite extensive research conducted on the topic and evident technological applications, an experiment proving the existence of Fano coherences produced by incoherent pumping and spontaneous emission is still missing, according to my knowledge. Currently, the atomic platform stands as the most suitable candidate for such measurements, given its capability to finely adjust the parameters that define a V-type three-level system. In [29] and later in [30], a proposal was outlined for an experiment using beams of Calcium atoms excited by a broadband polarized laser within a uniform magnetic field. Moreover, in a magneto-optical trap of Rubidium atoms, enhanced beat amplitudes due to the collective emission of light, akin to Fano coherences originated by the interaction with the vacuum modes, have been recently observed [35].

This thesis investigates the generation of quantum coherence in a V-type three-level system with optical transitions driven by an incoherent radiation source. Specifically, the study focuses on a system with nearly degenerate upper levels, aligning with previous research [28–30], yet deviating from [23, 34]. This framework indeed aims to replicate a more realistic system, akin to those achievable in atomic platforms. However, I maintain the same formalism for modelling the dynamics, namely a quantum Markovian master equation in the Schrödinger picture. The findings are then applied to a V-type system implemented in the hyperfine structure of ^{87}Rb atoms, for which a proof-of-principle experiment is designed and realized. The optical setup enables the first detection of noise-induced Fano coherence in a V-type three-level system under incoherent driving.

Furthermore, special attention is given to the energetic aspects underlying the generation of Fano coherence in the system. A quantum thermodynamic analysis is conducted using Kirkwood-Dirac quasiprobability distribution of the stochastic energy changes within the discrete system. The analysis aims to certify that the generation of Fano coherences has genuinely quantum traits, despite its "noisy" nature. To adress this, the loss of positivity (i.e., negative real parts or even non-null imaginary parts) of the Kirkwood-Dirac quasiprobabilities is observed. The latter are evaluated at both the initial and final stages of the transformation that results in Fano coherence. An optimization analysis is performed to enhance the non-positivity of certain quasiprobabilities by adjusting both the initial quantum state and the parameters governing the system's dynamics. This dual focus is crucial: it helps identify the conditions under which Fano coherence emerges with pronounced quantum traits, and it explores potential thermodynamic advantages. In fact, in quantum systems subjected to a work protocol, the presence of negativity is a necessary condition for enhanced work extraction [36–38]. Thus, this study also examines the extent to which the process generating Fano coherence can be utilized for energy conversion purposes. The potential for exploiting the resulting excess energy as extractable work is considered, provided an appropriate load or storage system is designed. The thermodynamic efficiency of this process is also evaluated.

The thesis is structured as follows:

Chapter 1

This chapter introduces the fundamental mathematical tools used in deriving the Markovian quantum master equation, that describes the dynamics of the V-type three-level system exposed to a broadband radiation. Two distinct types of incoherent radiation are considered: isotropic unpolarized radiation and anisotropic polarized radiation. For each case, the differential equations governing the time evolution of the elements of the system's density operator are derived. The chapter concludes with simulations for both scenarios, illustrating the solutions across various dynamical regimes, defined by the governing parameters.

Chapter 2

This chapter describes the key quantum thermodynamic quantities and the Kirkwood-Dirac quasiprobabilities used to verify the quantum nature of the Fano coherence generated in the V-type three-level system excited by isotropic unpolarized radiation. It includes an optimization analysis aimed at maximizing the excess energy produced during the processes that lead to the generation of Fano coherence. Additionally, the thermodynamic efficiency of the process is evaluated. This analysis is crucial for understanding not only the quantum characteristics of the coherence, but also the potential for extracting useful work from the system.

Chapter 3

This final chapter details the implementation of the V-type three-level system within the hyperfine structure of ^{87}Rb atoms, excited by a broadband polarized laser. Theoretical results are presented, identifying the optimal dynamical regime where Fano coherence is maximized. The results guide the design of key experimental components to achieve the desired dynamical parameters. The chapter includes a comprehensive description of the experimental setup, alongside preliminary measurements and observations. The discussion highlights how the experimental findings align with theoretical predictions and outlines potential implications for future work.

Conclusion

The discussion of the key results are reported along with future developments of the research.

1 | Multi-level system driven by an incoherent source

In the context of multi-level systems with optical transitions, coherent superpositions of states can arise through interactions with a radiation field. In a V-type three-level system with nearly degenerate excited levels, quantum coherence can non-trivially arise through interactions with non-coherent radiation sources. These interactions can induce Fano-like interference effects, either during absorption and spontaneous emission processes, as the continuum of modes of the incoherent source drives the discrete quantum system [24, 25]. Hence the name “Fano coherence”. To accurately describe this quantum phenomenon, it is essential to thoroughly investigate the interaction between light and matter, which can be explored from various perspectives, each offering different levels of detail and insight.

The first approach is represented by *classical theory*, which describes atoms as continuum systems, with the model of classical harmonic oscillators, and the radiation as a wave, with Maxwell’s equation of electromagnetic fields [39–41]. This approach, though simpler, yields valuable insights into optical properties of materials. A more in-depth exploration involves the use of the *semi-classical theory*, wherein atoms are treated as quantum systems with distinct, discrete energy levels, while the electromagnetic field retains a classical representation. This theory, for example, accurately elucidates absorption and emission processes, allowing for precise calculation of Einstein A and B coefficients as well as their interrelation [39–41]. Unlike the classical model, the semi-classical approach provides a more comprehensive description of atomic behavior [41]. Finally, quantum mechanics extends its application beyond the atomic system to include the electromagnetic field in the fully *quantum-mechanical theory* of light-matter interaction. This theory serves as a turning point for a rigorous treatment of phenomena that can not be explained semi-classically, such as the spontaneous emission in an atomic system [39, 40]. Nevertheless, the fully quantum-mechanical treatment of the interaction confirms the transition rates for absorption and stimulated emission determined with the semi-classical theory. The latter theory is therefore only appropriate and reliable when the results obtained with it are in agreement with the results determined with quantum theory [39].

In this chapter I describe the fundamental tools for a quantum-mechanical description of the interaction between a V-type three-level system and an incoherent radiation, examining the role of the latter in the generation of Fano coherence within the multi-level system. Through rigorous analysis, the quantum master equation describing the dynamic of the system is derived and the time evolution of system’s populations and coherences are shown. Section 1.1 lays the foundation for the study by introducing the key quantum operators essential for modeling both the radiation field and the atomic system. The main concepts of open quantum systems are then elucidated in Section 1.2. In Section 1.3, the quantum master equation is derived for both isotropic unpolarized and anisotropic polarized radiation cases, with detailed descriptions of all approximations used. Finally, Section 1.4 identifies different dynamical regimes for each type of radiation, illustrating how the system's populations and coherences evolve in time.

1.1 Quantum mechanical theory of radiation and atomic systems

1.1.1 Quantization of the electromagnetic field

In a fully quantum mechanical approach to light-matter interaction, the classical electromagnetic field vectors **E** and **B** transform into the quantum operators $\hat{E}$ and $\hat{B}$, respectively. This conversion typically begins by starting with the *Maxwell's equations* for free-space electromagnetic fields, *i.e.* [39, 40, 42]:

$$\begin{aligned} \nabla \cdot \mathbf{E}(\mathbf{r}, t) &= 0 & (1.1) \\ \nabla \cdot \mathbf{B}(\mathbf{r}, t) &= 0 & (1.2) \\ \nabla \times \mathbf{E}(\mathbf{r}, t) &= -\frac{\partial \mathbf{B}(\mathbf{r}, t)}{\partial t} & (1.3) \\ \nabla \times \mathbf{B}(\mathbf{r}, t) &= \frac{1}{c^2}\frac{\partial \mathbf{E}(\mathbf{r}, t)}{\partial t}, & (1.4) \end{aligned}$$

where $c = \mu_0 \varepsilon_0$ is the vacuum light speed with μ_0 and ε_0 denoting the magnetic permeability and electric permittivity of vacuum, respectively. For free-space electromagnetic fields Maxwell's equations are gauge invariant, facilitating their reformulation in terms of a vector potential $\mathbf{A}(\mathbf{r}, t)$ in the *Coulomb gauge* [39, 42]:

$$\begin{aligned} \mathbf{B}(\mathbf{r}, t) &= \nabla \times \mathbf{A}(\mathbf{r}, t) & (1.5) \\ \mathbf{E}(\mathbf{r}, t) &= -\frac{\partial \mathbf{A}(\mathbf{r}, t)}{\partial t}, & (1.6) \end{aligned}$$

where the gauge condition is satisfied if:

$$\nabla \cdot \mathbf{A}(\mathbf{r}, t) = 0. \tag{1.7}$$

The wave equation

$$\frac{1}{c^2}\frac{\partial^2 \mathbf{A}(\mathbf{r}, t)}{\partial t^2} - \nabla^2 \mathbf{A}(\mathbf{r}, t) = 0 \tag{1.8}$$

is obtained by substituting equations (1.5) and (1.6) in equation (1.4). By imposing periodic boundary conditions in a cubic region of side L and volume $V = L^3$, identified as the *quantization cavity*, the travelling wave solution $\mathbf{A}(\mathbf{r}, t)$ can be expressed in a Fourier expansion of the field's modes:

$$\mathbf{A}(\mathbf{r},t) = \sum_{\lambda=1,2} \sum_{\mathbf{k}} \left[\mathbf{A}_{\mathbf{k},\lambda}(t) \mathbf{A}_{\mathbf{k},\lambda}(\mathbf{r}) + \mathbf{A}^*_{\mathbf{k},\lambda}(t) \mathbf{A}^*_{\mathbf{k},\lambda}(\mathbf{r}) \right]. \tag{1.9}$$

The free-space solution is obtained by considering the space filled with a fictitious array of quantization cavities. The summations cover all the possible discrete modes of the field, each identified by the wavevector $\mathbf{k}$ and the polarization index λ. The polarization index is associated with the unit polarization vector $\boldsymbol{\epsilon}_{\mathbf{k},\lambda}$, which must satisfy the transversality condition imposed by the Coulomb gauge:

$$\boldsymbol{\epsilon}_{\mathbf{k},\lambda} \cdot \mathbf{k} = 0 \qquad \forall\, \mathbf{k}, \lambda. \tag{1.10}$$

The above condition implies that the fields are purely transverse, requiring two independent, *i.e.* orthonormal, polarization vectors $\boldsymbol{\epsilon}_{\mathbf{k},1}$ and $\boldsymbol{\epsilon}_{\mathbf{k},2}$ to express an arbitrary polarization direction for each wavevector $\mathbf{k}$. The orthogonality of the vectors $\boldsymbol{\epsilon}_{\mathbf{k},1}$ and $\boldsymbol{\epsilon}_{\mathbf{k},2}$ can be expressed using the Kronecker delta:

$$\boldsymbol{\epsilon}_{\mathbf{k},\lambda} \cdot \boldsymbol{\epsilon}_{\mathbf{k}',\lambda'} = \delta_{\lambda,\lambda'} \qquad \forall\, \mathbf{k}. \tag{1.11}$$

The terms $\mathbf{A}_{\mathbf{k},\lambda}(\mathbf{r})$ in equation (1.9) are the *mode functions*, that carry the spatial dependence of the field; the time dependence is instead contained in the terms $\mathbf{A}_{\mathbf{k},\lambda}(t)$ which are explicitly separated from the spatial dependencies. Both terms independently satisfy the wave equation (1.8). The mode function associated to a given mode of wavevector $\mathbf{k}$ and polarization $\boldsymbol{\epsilon}_{\mathbf{k},\lambda}$, appropriate to free-space, can be expressed as:

$$\mathbf{A}_{\mathbf{k},\lambda}(\mathbf{r}) = \frac{1}{\sqrt{V}} \boldsymbol{\epsilon}_{\mathbf{k},\lambda}\, e^{i\mathbf{k}\cdot\mathbf{r}}, \tag{1.12}$$

with the wavevector components subject to periodic boundary conditions:

$$k_{x,y,z} = \frac{2\pi n_{x,y,z}}{L}, \tag{1.13}$$

where $n_{x,y,z}$ are integers.

Substituting equation (1.12) in equation (1.9), the contributions to $\mathbf{A}(\mathbf{r},t)$ from all modes $\mathbf{k}, \lambda$ is rewritten as:

$$\mathbf{A}(\mathbf{r},t) = \frac{1}{\sqrt{V}} \sum_{\lambda=1,2} \sum_{\mathbf{k}} \boldsymbol{\epsilon}_{\mathbf{k},\lambda} \left[\mathbf{A}_{\mathbf{k},\lambda}(t) e^{i\mathbf{k}\cdot\mathbf{r}} + \mathbf{A}^*_{\mathbf{k},\lambda}(t) e^{-i\mathbf{k}\cdot\mathbf{r}} \right]. \tag{1.14}$$

As regards the temporal component $\mathbf{A}_{\mathbf{k},\lambda}(t)$, it satisfies the wave equation independently of the spatial component, leading to:

$$\frac{d^2 \mathbf{A}_{\mathbf{k},\lambda}(t)}{dt^2} + \nu^2_{\mathbf{k},\lambda} \mathbf{A}_{\mathbf{k},\lambda}(t) = 0. \tag{1.15}$$

The above equation represents a single harmonic oscillator with angular frequency $\nu_{\mathbf{k},\lambda}$. The general solution of equation (1.15) is:

$$\mathbf{A}_{\mathbf{k},\lambda}(t) = \alpha_{\mathbf{k},\lambda}(0)e^{-i\nu_{\mathbf{k},\lambda}t} + \alpha^*_{\mathbf{k},\lambda}(0)e^{i\nu_{\mathbf{k},\lambda}t}, \tag{1.16}$$

where $\alpha_{\mathbf{k},\lambda}(0)$ are complex amplitudes related to the initial conditions of the mode $\mathbf{k}, \lambda$. The classical amplitudes $\alpha_{\mathbf{k},\lambda}(0)$ are replaced with $\hat{a}_{\mathbf{k},\lambda}$ and $\hat{a}^\dagger_{\mathbf{k},\lambda}$, which are a pair of dimensionless quantum operators, named the *annihilation* and *creation operators*, respectively. Equation (1.16) becomes:

$$\hat{A}_{\mathbf{k},\lambda}(t) = i\sqrt{\frac{\hbar}{2\nu_{\mathbf{k},\lambda}\varepsilon_0}}\left[\hat{a}_{\mathbf{k},\lambda}e^{-i\nu_{\mathbf{k},\lambda}t} + \hat{a}^\dagger_{\mathbf{k},\lambda}e^{i\nu_{\mathbf{k},\lambda}t}\right], \tag{1.17}$$

with a normalization pre-factor that incorporates the relevant physical quantities.

The physical interpretation of the annihilation and creation operators is elucidated by introducing the Hamiltonian operator associated with the field, which is expressed as:

$$\hat{H} = \sum_{\lambda=1,2}\sum_{\mathbf{k}} \hbar\nu_{\mathbf{k},\lambda}\left(\hat{a}^\dagger_{\mathbf{k},\lambda}\hat{a}_{\mathbf{k},\lambda} + \frac{1}{2}\right). \tag{1.18}$$

The Hamiltonian operator describes the electromagnetic energy in terms of the number of photons in each mode $\mathbf{k}, \lambda$, plus the term $\hbar\nu_{\mathbf{k},\lambda}/2$, that accounts for the energy of the vacuum fluctuations. In quantum optics, it is a common practice to write the Hamiltonian of the field by discarding the vacuum energy term. Indeed, this term does not affect the relative energy levels of the system, since it represents an absolute value of energy. In the dynamics of quantum systems, what matters are energy differences, and the vacuum energy cancels out.

The eigenvalues of the operator $\hat{H}$ for the mode $\mathbf{k}, \lambda$ are the energy levels $\mathrm{E}_{n,\mathbf{k},\lambda}$ with eigenstates $|n_{\mathbf{k},\lambda}\rangle$; the former represents the excitation energy of the electromagnetic field in the mode $\mathbf{k}, \lambda$ as due to $n_{\mathbf{k},\lambda}$ photons in the state $|n_{\mathbf{k},\lambda}\rangle$. The eigenstates $|n_{\mathbf{k},\lambda}\rangle$ are named *photon-number states* or *Fock states*, after the Soviet physicist Vladimir Fock, and they have no analog in the classical treatment of the field. The annihilation and creation operators modify the photon-number states as follows:

$$\hat{a}_{\mathbf{k},\lambda}|n_{\mathbf{k},\lambda}\rangle = \sqrt{n_{\mathbf{k},\lambda}}|n_{\mathbf{k},\lambda} - 1\rangle \tag{1.19}$$

$$\hat{a}^\dagger_{\mathbf{k},\lambda}|n_{\mathbf{k},\lambda}\rangle = \sqrt{n_{\mathbf{k},\lambda} + 1}|n_{\mathbf{k},\lambda} + 1\rangle. \tag{1.20}$$

Here, the operator $\hat{a}_{\mathbf{k},\lambda}$ decreases the number of photons in mode $\mathbf{k}, \lambda$ by one unit of energy $\hbar\nu_{\mathbf{k},\lambda}$. Conversely, the operator $\hat{a}^\dagger_{\mathbf{k},\lambda}$ increases the number of photons in mode $\mathbf{k}, \lambda$ by the same unit. These actions justify the names “annihilation” and “creation” for these operators. Thus, the annihilation operator removes one photon from the mode $\mathbf{k}, \lambda$, while the creation operator adds a photon to the mode $\mathbf{k}, \lambda$. The number of photons in the mode $\mathbf{k}, \lambda$ is given by the eigenvalues of the *photon-number operator* $\hat{n}_{\mathbf{k},\lambda}$ defined as:

$$\hat{n}_{\mathbf{k},\lambda} = \hat{a}^\dagger_{\mathbf{k},\lambda}\hat{a}_{\mathbf{k},\lambda}. \tag{1.21}$$

The quantum expression of the vector potential $\mathbf{A}(\mathbf{r}, t)$ is obtained by substituting equation (1.17) in equation (1.14), obtaining:

$$\hat{A}(\mathbf{r},t) = i\sum_{\lambda=1,2}\sum_{\mathbf{k}}\sqrt{\frac{\hbar}{2\nu_{\mathbf{k},\lambda}\varepsilon_0 V}}\boldsymbol{\epsilon}_{\mathbf{k},\lambda}\left[\hat{a}_{\mathbf{k},\lambda}e^{-i\nu_{\mathbf{k}}t+i\mathbf{k}\cdot\mathbf{r}} + \hat{a}^{\dagger}_{\mathbf{k},\lambda}e^{i\nu_{\mathbf{k}}t-i\mathbf{k}\cdot\mathbf{r}}\right]. \tag{1.22}$$

In this way, the vector potential is rewritten in terms of the annihilation operator $\hat{a}_{\mathbf{k},\lambda}$ and the creation operator $\hat{a}^{\dagger}_{\mathbf{k},\lambda}$, which are crucial in the quantum treatment of radiation, enabling the field to be described in terms of “discrete” photons. It is interesting to note that the quantum nature of the field is introduced through the time dependent terms $\hat{A}_{\mathbf{k},\lambda}(t)$.

The electric and magnetic field quantum operators have then the following expression:

$$\begin{aligned}\hat{E}(\mathbf{r},t) &= i\sum_{\lambda=1,2}\sum_{\mathbf{k}}\sqrt{\frac{\hbar\nu_{\mathbf{k},\lambda}}{2\varepsilon_0 V}}\boldsymbol{\epsilon}_{\mathbf{k},\lambda}\left[\hat{a}_{\mathbf{k},\lambda}e^{-i\nu_{\mathbf{k}}t+i\mathbf{k}\cdot\mathbf{r}} - \hat{a}^{\dagger}_{\mathbf{k},\lambda}e^{i\nu_{\mathbf{k}}t-i\mathbf{k}\cdot\mathbf{r}}\right] \qquad (1.23)\\ \hat{B}(\mathbf{r},t) &= i\sum_{\lambda=1,2}\sum_{\mathbf{k}}\sqrt{\frac{\hbar}{2\nu_{\mathbf{k},\lambda}\varepsilon_0 V}}\mathbf{k}\times\boldsymbol{\epsilon}_{\mathbf{k},\lambda}\left[\hat{a}_{\mathbf{k},\lambda}e^{-i\nu_{\mathbf{k}}t+i\mathbf{k}\cdot\mathbf{r}} - \hat{a}^{\dagger}_{\mathbf{k},\lambda}e^{i\nu_{\mathbf{k}}t-i\mathbf{k}\cdot\mathbf{r}}\right]. \qquad (1.24)\end{aligned}$$

To fully characterize the interaction of light and matter within a quantum-mechanical framework, it is essential to describe atoms quantum-mechanically as well. This is addressed in the following section.

1.1.2 Atoms as quantum systems

The first postulate of quantum mechanics introduces the key elements of the theory: the *state vector*, that describes the quantum system considered, and the *Hilbert space*, the mathematical framework in which the system exists [43]. Quoting from [43]:

Postulate 1. *Associated to any* isolated *physical system ψ is a complex vector space $\mathcal{H}$,* i.e. *Hilbert space, known as the* state space *of the system. The system is completely described by its* state vector $|\psi\rangle$*, which is a unit vector in the system's state space.*

The state vector $|\psi\rangle$ represents a *pure* state, containing all information about the system. A more general approach involves the use of the *density operator* ρ, which enables the description of both pure and *mixed states*, for system in which the state is not entirely known [41, 43]. In case of a pure state $|\psi\rangle$, the density operator is defined as:

$$\hat{\rho} \equiv |\psi\rangle\langle\psi|. \tag{1.25}$$

In this case, the density operator and the state vector contain the same information and can therefore be used interchangeably. However, in cases where there is lack of information – such as when the preparation of the system is not fully known or the system interacts with an external system whose evolution is unknown, as in the case of interactions with the surrounding environment – we are dealing with a mixed state. The system therefore can be described by an ensemble of states $\{|\psi_i\rangle\}$ and the formalism of pure state can not be applied. The density operator in this situation is defined as:

$$\hat{\rho} \equiv \sum_i p_i|\psi_i\rangle\langle\psi_i|. \tag{1.26}$$

The above definition indicates that, while it is not exactly known which of the ensemble state $|\psi_i\rangle$ the system is in, a probability p_i can be assigned to each state.

The density operator $\hat{\rho}$, whether it corresponds to a pure state $|\psi\rangle$ or a statistical mixture of states $|\psi_i\rangle$, must satisfy certain fundamental properties:

1. the density operator is an hermitian operator, *i.e.* $\hat{\rho} = \hat{\rho}^\dagger$;
2. the density operator has a unitary trace, ensuring proper normalization;
3. the density operator is positive semidefinite, meaning all its eigenvalues are real and non-negative;
4. the density operator describing a pure state satisfies $\mathrm{Tr}(\hat{\rho}^2) = 1$, while the density operator describing a mixed state satisfies $\mathrm{Tr}(\hat{\rho}^2) < 1$.

These properties guarantee that $\hat{\rho}$ is a valid representation of a quantum state. Furthermore, each element of the density operator conveys different types of information. For instance, in the case of a pure state, the diagonal elements ρ_{jj}, defined as $\langle j|\rho|j\rangle$, give the probability of measuring the system in the state $|j\rangle$. The diagonal elements are referred to as *populations*. On the other hand, the off-diagonal elements $\rho_{jl} = \langle j|\rho|l\rangle$, referred as *coherences*, arise when the system is in a coherent superposition of states $|j\rangle$ and $|l\rangle$. The above terminology also applies to mixed states.

In a fully quantum description of light-matter interaction, atoms are modeled as systems with a discrete set of energy levels. Each level corresponds to a distinct quantum state that the atom can occupy, known as the eigenstates of the atom's Hamiltonian $\hat{H}_{at}$. The eigenstates are represented by state vectors $|j\rangle$, which form an orthonormal basis $\{|j\rangle\}$, and the atom's state at any given time can be expressed as a superposition of these basis vectors, i.e.:

$$|\psi(t)\rangle = \sum_j c_j(t)|j\rangle. \tag{1.27}$$

Terms $c_j(t)$ are complex coefficients representing the probability amplitude for the atom to be in the state $|j\rangle$ at time t. Each state $|j\rangle$ is associated with a specific energy level E_j, which is determined by solving the relevant Schrödinger equation. Therefore, in the basis $\{|j\rangle\}$, the Hamiltonian of the atom can be expressed as:

$$\hat{H}_{at} = \sum_j \mathrm{E}_j |j\rangle\langle j|. \tag{1.28}$$

When an atom interacts with an external electromagnetic field, the physical quantity that describes the strength of the interaction is the *dipole moment operator* $\hat{\mu}$. Assuming that the wavelength of the field is significantly lager than the size of the atom, then the *dipole approximation* applies and the dipole moment operator is defined as:

$$\hat{\mu} \equiv -e\mathbf{r} = \sum_{\substack{lj \\ l\neq j}} \boldsymbol{\mu}_{lj} |l\rangle\langle j|, \tag{1.29}$$

where $\boldsymbol{\mu}_{lj} \equiv \langle l|e\mathbf{r}|j\rangle$ is the *transition dipole matrix element*, that characterizes strength and direction of the dipole transition only between different states $|l\rangle$ and $|j\rangle$. Here, e denotes the fundamental charge and $\mathbf{r}$ is the atomic electron position vector. In equation (1.29), the elements where $l = j$ are omitted. The dipole operator induces transitions states $|j\rangle \leftrightarrow |l\rangle$, where a change in the atom's space charge distribution is involved. Furthermore, it is possible to choose the phase of the dipole matrix element $\boldsymbol{\mu}_{lj} = \langle l|e\mathbf{r}|j\rangle$ to be real, in which case it is possible to write $\boldsymbol{\mu}_{lj} = \boldsymbol{\mu}^*_{jl}$ [41].

Further key operators are the *atom transition operators*, or the *atom lowering and raising operators* $\hat{\sigma}^+$ and $\hat{\sigma}^-$, respectively, defined as:

$$\hat{\sigma}^+_{lj} \equiv |l\rangle\langle j| \tag{1.30}$$

$$\hat{\sigma}^-_{lj} \equiv \left(\hat{\sigma}^+_{lj}\right)^\dagger = |j\rangle\langle l|. \tag{1.31}$$

If $|l\rangle$ is an excited state and $|j\rangle$ a ground state, then $\hat{\sigma}^+_{lj}$ represents a transition from the ground state to the excited state (raising), and $\hat{\sigma}^-_{lj}$ represents a transition from the excited state to the ground state (lowering).

For a multi-level atom, $\hat{\rho}$ captures both the probabilities of the atom occupying each energy state (populations) and the phase relationships between different states (coherences), which enables the modeling of processes like spontaneous emission, stimulated emission and absorption, occurring during the interaction between a resonant radiation and atomic transitions.

1.2 Open quantum system theory

When addressing systems that interact with their surrounding environment, it is necessary to introduce the concepts of *open quantum systems.* In thermodynamics, an *open system* is defined as a system that exchanges energy and/or matter with its environment. This definition extends into the quantum realm, where the open quantum system interacts with a *reservoir* or a *bath*, through to the exchange of energy and information. Unlike isolated quantum systems, which evolve unitarily according to the Schrödinger equation, open quantum systems experiences dissipation, resulting in the loss of information from the system to its environment. This interaction leads to non-unitary dynamics, necessitating a more comprehensive approach [44]. One of the central challenges in open quantum systems is understanding how environmental interactions affect coherence and populations of an atomic system. These interactions often lead to phenomena such as *decoherence* and *relaxation.* The former physically describes the loss of information related to the relative phase between the system state components; the latter occurs when the system reaches thermal equilibrium with the environment.

The density operator $\hat{\rho}$ is a key tool, enabling the description of mixed states and statistical mixtures. In this context, the density operator evolves in time under non-unitary dynamics, which are effectively treated using *quantum master equations* [44]. These equations describe the time evolution of open quantum systems by incorporating the effects of the environment in a perturbative manner. Given their inherently perturbative nature, solutions to these equations rely on approximations, which must be carefully assessed.

Understanding quantum systems in realistic settings, where perfect isolation is impossible, is crucial for a wide range of applications, from quantum computing and information processing to condensed matter physics and quantum optics. The insights gained from the behavior of open quantum systems are not only fundamental to advancing quantum mechanics but also pivotal for the practical realization of quantum technologies.

1.2.1 Isolated quantum systems and unitary evolution

Consider a non-interacting, or isolated, quantum system S, which is completely described by the state vector $|\psi_S(t)\rangle$ at every time t. Its time evolution is governed by the Schrödinger equation:

$$i\hbar \frac{d|\psi_S(t)\rangle}{dt} = \hat{H}_S(t)|\psi_S(t)\rangle, \tag{1.32}$$

where $\hat{H}_S(t)$ is the Hamiltonian of the system.

The solution to equation (1.32) can be written in terms of a unitary operator $\hat{U}(t, t_0)$, which relates the state of the system at time t to the initial state $|\psi_S(t_0)\rangle$ as follows:

$$|\psi_S(t)\rangle = \hat{U}(t, t_0)|\psi_S(t_0)\rangle. \tag{1.33}$$

The operator $\hat{U}(t, t_0)$ is specified as unitary to preserve the norm of the state vector. In other words, since the system is not interacting with any environment, the state remains pure after the evolution. The unitarity is expressed as:

$$\hat{U}(t, t_0)\hat{U}^\dagger(t, t_0) = \hat{U}^\dagger(t, t_0)\hat{U}(t, t_0) = \hat{\mathbb{I}}, \tag{1.34}$$

where $\hat{\mathbb{I}}$ is the identity operator.

By substituting equation (1.33) into the Schrödinger equation, the differential equation for the unitary time-evolution operator $\hat{U}(t, t_0)$ is obtained:

$$i\hbar \frac{\partial \hat{U}(t, t_0)}{\partial t} = \hat{H}_S(t)\hat{U}(t, t_0). \tag{1.35}$$

As outlined in [44], an isolated system is described by a time independent Hamiltonian $\hat{H}(t) = \hat{H}$. However, if the Hamiltonian is time-dependent, the system is considered closed. This implies that the system can be influenced by external time-dependent fields, such as electromagnetic fields, while its time evolution remains unitary despite the Hamiltonian's dependence on time.

For an isolated system the solution to equation (1.35) is:

$$\hat{U}(t, t_0) = \exp\left[-\frac{i}{\hbar}\hat{H}_S(t - t_0)\right]. \tag{1.36}$$

In contrast, for a closed system the solution to the time-evolution operator is given by:

$$\hat{U}(t,t_0) = \hat{\mathrm{T}}_{\leftarrow} \exp\left[-\frac{i}{\hbar}\int_{t_0}^{t} \hat{H}_S(t')dt'\right]. \tag{1.37}$$

Here, $\hat{\mathrm{T}}_{\leftarrow}$ represents the *chronological time-ordering operator*, which specifies that the exponential is a time-ordered product of time-dependent operators, so that their time-arguments increase from right to left, as indicated by the arrow [41, 44].

By using the density operator formalism, where the state of the isolated or closed system is described by the pure state operator $\hat{\rho}_S = |\psi_S\rangle\langle\psi_S|$, the Schrödinger equation can be rewritten as:

$$\frac{d\hat{\rho}_S(t)}{dt} = -\frac{i}{\hbar}\left[\hat{H}_S(t), \hat{\rho}_S(t)\right]. \tag{1.38}$$

This equation is referred to as the *Schrödinger-Von Neumann equation.* It is common to express the Schrödinger-Von Neumann equation using a *Liouville super-operator*, so as to express the time evolution of $\hat{\rho}_S(t)$ similarly to the time evolution for the state vector $|\psi_S(t)\rangle$, requiring a higher-dimensional representation:

$$\frac{d\hat{\rho}_S(t)}{dt} = \hat{\mathcal{L}}(t)\hat{\rho}_S(t). \tag{1.39}$$

This implies that $\hat{\mathcal{L}}(t)\hat{\rho}_S(t) = -i/\hbar\left[\hat{H}_S(t), \hat{\rho}_S(t)\right]$. For an isolated system, the solution is:

$$\hat{\rho}_S(t) = \exp\left[\hat{\mathcal{L}}(t-t_0)\right]\hat{\rho}_S(t_0), \tag{1.40}$$

while for a closed system the solution is:

$$\hat{\rho}_S(t) = \hat{\mathrm{T}}_{\leftarrow} \exp\left[\int_{t_0}^{t} \hat{\mathcal{L}}(t')dt'\right]\hat{\rho}_S(t_0). \tag{1.41}$$

1.2.2 Interaction picture

Up to now, the description of time evolution of quantum systems was set in the framework of the so called *Schrödinger picture.* The Schrödinger picture is perhaps the most familiar and intuitive representation: the state of a quantum system evolves with time according to the Schrödinger equation, which describes how the system's state vector changes over time in response to its Hamiltonian. In contrast to the Schrödinger picture, the *Heisenberg picture* places the emphasis on the time evolution of operators rather than states. This approach is especially valuable when studying the time dependence of observables and how they interact with the system's dynamics. These two different pictures can be merged, giving rise to a more general framework, known with the name of *interaction picture.* The interaction picture offers a unique perspective by separating the time evolution of a quantum system into two distinct components: the natural evolution, governed by the free Hamiltonian $\hat{H}_0$, and the so called *interaction Hamiltonian*, $\hat{V}$, describing the influence of external fields or environments onto the system. In this picture, both states and operators evolve in time, with the interaction Hamiltonian playing a central role.

Consider a quantum system S and its Hamiltonian $\hat{H}_S(t)$. The latter can be decomposed as:

$$\hat{H}_S(t) = \hat{H}_0 + \hat{V}(t), \tag{1.42}$$

where the Hamiltonian operator $\hat{H}_0$ is time-independent and it represents the energies of the system S. The interaction Hamiltonian $\hat{V}(t)$ instead carries the time dependency of the system Hamiltonian $\hat{H}_S(t)$. In this context, the subscript I is used to denote the interaction picture formalism, while operators in the Schrödinger picture remains unsubscripted. The Heisenberg picture is not considered in this thesis.

The canonical transformations from the Schrödinger picture to the interaction picture are given by:

$$\begin{aligned} \hat{\rho}_I(t) &\equiv \hat{U}_0^\dagger(t,t_0)\hat{\rho}(t)\hat{U}_0(t,t_0) & (1.43)\\ \hat{V}_I(t) &\equiv \hat{U}_0^\dagger(t,t_0)\hat{V}(t)\hat{U}_0(t,t_0) & (1.44)\\ \hat{U}_I(t,t_0) &\equiv \hat{U}_0^\dagger(t,t_0)\hat{U}(t,t_0), & (1.45)\end{aligned}$$

where $\hat{U}_0(t,t_0)$ is the unitary operator defined as:

$$\hat{U}_0(t,t_0) \equiv \exp\left[-\frac{i}{\hbar}\hat{H}_0(t-t_0)\right]. \tag{1.46}$$

As an example, the electric field operator and the atomic transition operators in the interaction and Schrödinger pictures are derived. This procedure is useful in subsequent sections of the thesis. The electric field operator from equation (1.23) is expressed with time-dependent creation and annihilation operators, thus being in the interaction picture. In the Schrödinger picture, operators are time-independent, thus for the electric field operator one has:

$$\hat{E}(\mathbf{r}) = i\sum_{\lambda=1,2}\sum_{\mathbf{k}}\sqrt{\frac{\hbar\nu_{\mathbf{k},\lambda}}{2\varepsilon_0 V}}\boldsymbol{\epsilon}_{\mathbf{k},\lambda}\left[\hat{a}_{\mathbf{k},\lambda}e^{i\mathbf{k}\cdot\mathbf{r}} - \hat{a}^\dagger_{\mathbf{k},\lambda}e^{-i\mathbf{k}\cdot\mathbf{r}}\right]. \tag{1.47}$$

Indeed, inserting the above expression in definition (1.44) for the transformation of operators from the Schrödinger to the interaction picture, results in:

$$\hat{E}_I(\mathbf{r},t) = \hat{U}_0^\dagger(t,t_0)\hat{E}(\mathbf{r})\hat{U}_0(t,t_0), \tag{1.48}$$

where

$$\hat{U}_0(t,t_0) = \exp\left[-i\sum_{\lambda=1,2}\sum_{\mathbf{k}}\nu_{\mathbf{k},\lambda}\hat{a}^\dagger_{\mathbf{k},\lambda}\hat{a}_{\mathbf{k},\lambda}(t-t_0)\right]. \tag{1.49}$$

In the above expression, the free Hamiltonian of the electric field (equation (1.18)) is used. In equation (1.48) there are terms satisfying the following relation:

$$e^{i\nu_{\mathbf{k},\lambda}\hat{a}^\dagger_{\mathbf{k},\lambda}\hat{a}_{\mathbf{k},\lambda}t}\hat{a}_{\mathbf{k},\lambda}e^{-i\nu_{\mathbf{k},\lambda}\hat{a}^\dagger_{\mathbf{k},\lambda}\hat{a}_{\mathbf{k},\lambda}t} = \hat{a}_{\mathbf{k},\lambda}e^{-i\nu_{\mathbf{k},\lambda}t}, \tag{1.50}$$

where $t_0 = 0$ and the power series for the operator exponential:

$$e^{\hat{A}} = \sum_{j=0}^{\infty}\frac{\hat{A}^j}{j!} \qquad \text{with} \quad \hat{A}^0 = \hat{\mathbb{I}} \tag{1.51}$$

is used. The electric field operator in the interaction picture thus has the form:

$$\hat{E}_I(\mathbf{r},t) = i \sum_{\lambda=1,2} \sum_{\mathbf{k}} \sqrt{\frac{\hbar\nu_{\mathbf{k},\lambda}}{2\varepsilon_0 V}} \boldsymbol{\epsilon}_{\mathbf{k},\lambda} \left[\hat{a}_{\mathbf{k},\lambda} e^{-i\nu_{\mathbf{k}}t+i\mathbf{k}\cdot\mathbf{r}} - \hat{a}^{\dagger}_{\mathbf{k},\lambda} e^{i\nu_{\mathbf{k}}t-i\mathbf{k}\cdot\mathbf{r}}\right]. \tag{1.52}$$

The above expression is that of equation (1.23) described in Subsection 1.1.1.

Regarding atom transition operators $\hat{\sigma}^{\pm}_{lj}$, a similar procedure is applied. The time-independent atomic Hamiltonian $\hat{H}_{at}$, as previously expressed in equation (1.28), is rewritten in terms of the transition operators as follows:

$$\hat{H}_{at} = \sum_j \left(\mathrm{E}_j - \mathrm{E}_g\right) \hat{\sigma}^{+}_{jg}\hat{\sigma}^{-}_{jg} = \sum_j \hbar\omega_{jg}\hat{\sigma}^{+}_{jg}\hat{\sigma}^{-}_{jg}, \tag{1.53}$$

where E_g denotes the lowest energy level of the system (ground level), and $\omega_{jg} = \omega_j - \omega_g$ represents the angular frequency difference between the other levels and the ground level. In the above expression, the ground level is chosen as the reference point with zero energy. Hence, the associated unitary operator $\hat{U}_0$ has the form:

$$\hat{U}_0(t,t_0) = \exp\left[-i\sum_j \omega_{jg}\hat{\sigma}^{+}_{jg}\hat{\sigma}^{-}_{jg}(t-t_0)\right]. \tag{1.54}$$

It follows:

$$\hat{\sigma}^{\pm}_{jg,I} = \hat{U}^{\dagger}_0(t,t_0)\hat{\sigma}^{\pm}_{jg}\hat{U}_0(t,t_0) = \hat{\sigma}^{\pm}_{jg}e^{\pm i\omega_{jg}t}, \tag{1.55}$$

where, again, the power series of operator exponential is used. These two examples show that the field and atomic operators in the interaction picture effectively evolve according to their respective free Hamiltonians.

As for the time evolution of the density operator in the interaction picture, $\hat{\rho}_I(t)$, the corresponding differential equation is derived by differentiating equation (1.43) with respect to time, using the Schrödinger-von Neumann equation (1.38) and the transformation given by equation (1.44):

$$\frac{d\hat{\rho}_I(t)}{dt} = -\frac{i}{\hbar}\left[\hat{V}_I(t), \hat{\rho}_I\right]. \tag{1.56}$$

The above equation is known as the *Liouville-von Neumann equation.*

The interaction picture proves invaluable for analyzing those systems subjected to external stimuli or engaged in the exchange of energy and information with their environment, that are open quantum systems.

1.2.3 Open quantum systems and their time evolution

An *open quantum system* S is a system that is coupled to another quantum system represented by the external environment. The environment encompasses all degrees of freedom that are not explicitly considered in the primary system's description, but still influence its dynamics through interaction. The external system is referred as R, which stands for *reservoir.* In the literature, the terms "environment" and "reservoir" are often used interchangeably. However, as explained in [44], they can refer to external systems with different characteristics. Specifically, the term "environment" is used in a general sense, while the term "reservoir" refers to an environment with an infinite number of degrees of freedom. An example of a reservoir is a non-coherent radiation, whose modes can be described as a continuum of frequencies, which is considered in this thesis work. This distinction is important for discussing the coherences formed in the system S due to interaction with the environment, known as *Fano coherences*. Finally, the term "bath" is used to describe a reservoir in a state of thermal equilibrium.

The system S is associated to the complex Hilbert space $\mathcal{H}_S$, while the reservoir state is associated to the complex Hilbert space $\mathcal{H}_R$. The combination of these two subsystems generates the composite system $S+R$, whose Hilbert space is given by the tensor product $\mathcal{H}=\mathcal{H}_S\otimes\mathcal{H}_R$. In most cases, the composite system is assumed to be closed. As previously stated, it is not possible to describe the dynamics of a system S interacting with another system R using unitary, Hamiltonian dynamics when decoherence and relaxation are present [44]. However, the dynamics of the combined system $S+R$ remains unitary.

The evolution of the subsystem S, resulting from the unitary evolution of the composite system, is referred to as *reduced system dynamics*, which can be described with the formalism of quantum master equations. The derivation of the master equation governing the dynamics of the examined multi-level system is conducted through a microscopic approach. The latter begins with the Hamiltonian of the combined system, which includes both the system and the reservoir Hamiltonians [44, 45], and it is given by:

$$\hat{H}(t)=\hat{H}_S\otimes\hat{\mathbb{I}}_R+\hat{\mathbb{I}}_S\otimes\hat{H}_R+\hat{V}(t), \tag{1.57}$$

where $\hat{H}_S$ and $\hat{H}_R$ are the time-indipendent Hamiltonians of the system and reservoir, respectively. Here, $\hat{\mathbb{I}}_S$ and $\hat{\mathbb{I}}_R$ represent the identity operators for the system and the reservoir and $\hat{V}(t)$ denotes the interaction Hamiltonian. Equation (1.57) highlights that any operator acting solely on one of the subsystems must be expressed in the Hilbert space $\mathcal{H}$ of the composite system $S+R$. Hence, the tensor product of the operator in question with the identity operator of the other subsystem is performed. The interaction Hamiltonian $\hat{V}(t)$, on the other hand, encompasses the dimensions of the composite system. The dynamic of the latter is described by the Schrödinger-Von Neumann equation (1.38) within the density operator formalism:

$$\frac{d\hat{\rho}(t)}{dt}=-\frac{i}{\hbar}\left[\hat{H}(t),\hat{\rho}(t)\right]. \tag{1.58}$$

The initial condition is assumed to be described by the uncorrelated state $\hat{\rho}(0)=\hat{\rho}_S(0)\otimes\hat{\rho}_R(0)$, where $\hat{\rho}_S$ and $\hat{\rho}_R$ are the *reduced density operators* describing the system and the reservoir state, respectively. In many practical scenarios, such as those addressed in this thesis, the focus is exclusively on the state of the primary system S, rather than on the environment. The concept of the reduced density operator allows to obtain the state of the system S alone, by tracing out the environment degrees of freedom from the composite system density operator $\hat{\rho}$. Mathematically, this process is called the *partial trace* over the environment R, denoted as:

$$\hat{\rho}_S(t)\equiv\mathrm{Tr}_R\left(\hat{\rho}(t)\right), \tag{1.59}$$

where Tr_R denotes the trace over the Hilbert space $\mathcal{H}_R$. The reduced density operator $\hat{\rho}_S$, thus, encapsulates all the information about the subsystem S that is available, without knowledge of the environment R [43, 44].

The derivation of the quantum master equation for the dynamics of the open quantum system S is conveniently performed in the interaction picture, rather than in the Schrödinger picture. Equation (1.58) is then substituted with the Liouville-von Neumann equation for the composite system:

$$\frac{d\hat{\rho}_I(t)}{dt} = -\frac{i}{\hbar}\left[\hat{V}_I(t), \hat{\rho}_I(t)\right]. \tag{1.60}$$

The exact formal solution is given by:

$$\hat{\rho}_I(t) = \hat{\rho}_I(0) - \frac{i}{\hbar}\int_0^t \left[\hat{V}_I(t'), \hat{\rho}_I(t')\right] dt'. \tag{1.61}$$

Substituting equation (1.61) in equation (1.60), the integro-differential form of the Liouville-von Nuemann equation is obtained:

$$\frac{d\hat{\rho}_I(t)}{dt} = -\frac{i}{\hbar}\left[\hat{V}_I(t), \hat{\rho}_I(0)\right] - \frac{1}{\hbar^2}\int_0^t \left[\hat{V}_I(t), \left[\hat{V}_I(t'), \hat{\rho}_I(t')\right]\right] dt'. \tag{1.62}$$

Applying the trace over the reservoir degrees of freedom, the differential equation for the dynamics of the open quantum system S in the interaction picture is obtained:

$$\begin{aligned}\frac{d\hat{\rho}_{S,I}(t)}{dt} &= -\frac{i}{\hbar}\mathrm{Tr}_R\left(\left[\hat{V}_I(t), \hat{\rho}_S(0)\otimes\hat{\rho}_R(0)\right]\right) + \\ &- \frac{1}{\hbar^2}\int_0^t \mathrm{Tr}_R\left(\left[\hat{V}_I(t), \left[\hat{V}_I(t'), \hat{\rho}_I(t')\right]\right]\right) dt'. \end{aligned} \tag{1.63}$$

Equation (1.63) still involves the density operator of the composite system, $\hat{\rho}_I(t)$. By applying suitable approximations relevant to the specific scenario, it is possible to derive a differential equation that depends exclusively on the state of the subsystem S at time t. The approximations used are the following:

- **Born approximation:** the *Born approximation* (or *weak-coupling approximation*) assumes that the coupling between the system and the reservoir is weak enough that the state of the reservoir is only minimally perturbed by its interaction with the system. This means that the density operator of the composite system $S + R$ can be approximated as:

  $$\hat{\rho}(t) \approx \hat{\rho}_S(t)\otimes\hat{\rho}_R(0) \qquad \forall\, t, \tag{1.64}$$

  with the reservoir remaining approximately in its initial state $\hat{\rho}_R(0)$ throughout the interaction.

  By applying the Born approximation, equation (1.63) gets the form:

  $$\begin{aligned}\frac{d\hat{\rho}_{S,I}(t)}{dt} &\approx -\frac{i}{\hbar}\mathrm{Tr}_R\left(\left[\hat{V}_I(t), \hat{\rho}_S(0)\otimes\hat{\rho}_R(0)\right]\right) + \\ &- \frac{1}{\hbar^2}\int_0^t \mathrm{Tr}_R\left(\left[\hat{V}_I(t), \left[\hat{V}_I(t'), \hat{\rho}_{S,I}(t')\otimes\hat{\rho}_R(0)\right]\right]\right) dt'. \end{aligned} \tag{1.65}$$

- **Markov approximation:** the *Markov approximation* assumes that the reservoir's memory effects are negligible, meaning that the system's future evolution depends only on its current state and not on its past history. This approximation leads to a *memoryless* or *Markovian process*. This is valid when the reservoir has a much faster relaxation time τ_R compared to the system's timescale τ_S, i.e. $\tau_R \ll \tau_S$. Therefore, the influence of the system on the reservoir can be neglected after a short correlation time beyond which the reservoir "forgets" the interaction it has had with the system. Mathematically, this implies that the reservoir's correlation functions decay rapidly for $t - t' > \tau_R$, therefore the contribution to the integral from times $t' < t - \tau_R$ is negligible and the upper limit of the integral in equation (1.65), can be safely extended to infinity without significantly affecting the result:

  $$\begin{aligned} \frac{d\hat{\rho}_{S,I}(t)}{dt} &\approx -\frac{i}{\hbar}\mathrm{Tr}_R\left(\left[\hat{V}_I(t), \hat{\rho}_S(0) \otimes \hat{\rho}_R(0)\right]\right) + \\ &- \frac{1}{\hbar^2}\int_0^{\infty} \mathrm{Tr}_R\left(\left[\hat{V}_I(t), \left[\hat{V}_I(t'), \hat{\rho}_{S,I}(t) \otimes \hat{\rho}_R(0)\right]\right]\right) dt'. \qquad (1.66) \end{aligned}$$

  Under the Markov approximation, the equation governing the system's dynamics can be expressed in a time-local form, meaning that the rate of change of the system's density operator at time t depends only on its state at that same time t.

Equation (1.66), obtained by applying both the Born and Markov approximations, is a *Markovian quantum master equation*, commonly known as *Redfield* or *Bloch-Redfield equation*. The Bloch-Redfield equation, in its simplest form, does not always preserve the positivity of the density matrix $\hat{\rho}_{S,I}(t)$ [44–47]. The lack of positivity can lead to unphysical results, as negative populations within the system. Therefore, further approximations are often necessary to ensure the physical consistency of the reduced density operator. Typically, the *secular* or *Rotating Wave Approximation (RWA)* is applied to restore the positivity of $\hat{\rho}_{S,I}(t)$ [44, 45, 48, 49]. A brief description of the approximation is given, while the application to the case under consideration is discussed in the next section.

- **Secular approximation:** the secular approximation involves neglecting rapidly oscillating terms, that are assumed to average out over time. Specifically, in the Bloch-Redfield equation, those terms that oscillate with frequencies corresponding to differences between non-degenerate energy levels are dropped.

  Consider an open quantum system, as a multi-level atom, described by the reduced density operator $\hat{\rho}_{S,I}(t)$ interacting with a reservoir. This system exhibits atomic transitions with frequencies ω and ω', leading to energy differences $\hbar(\omega - \omega') = \hbar\Delta$, where $\Delta \equiv \omega - \omega'$. The oscillation timescale $\tau\omega$ associated to the smallest non-zero energy difference is given by $1/|\omega - \omega'|$ [29]. Three regimes can be distinguished: *degenerate*, *non-degenerate*, and *near-degenerate* [48]. In degenerate cases, where $\Delta = 0$, transitions do not generate rapidly oscillating terms. In non-degenerate cases, where Δ is large, the oscillation timescales τ_ω are much shorter than the system's evolution timescale τ_S and thus the corresponding oscillating terms can be discarded. Hence, the rotating wave approximation (RWA) is valid in both degenerate and non-degenerate regimes. After the application of the approximation, the remaining terms result in a simplified master equation that ensures the positivity of the density operator. In this way, a *Gorini-Kossakowski-Sudarshan-Lindblad master equation*, or simply a *Lindblad master equation* can be derived. The Lindblad master equation inherently preserves the positivity of the density operator along with its unitary trace, thereby ensuring a consistent and physically meaningful description of the open quantum system's dynamics [44, 45, 50]. The Lindblad master equation is expressed as:

$$\frac{d\hat{\rho}_S(t)}{dt} = -\frac{i}{\hbar}[\hat{H}_S + \hat{H}_{LS}, \hat{\rho}_S(t)] + \sum_{\omega,i} \left(\hat{L}_i(\omega)\hat{\rho}_S(t)\hat{L}_i^\dagger(\omega) - \frac{1}{2}\left\{ \hat{L}_i^\dagger(\omega)\hat{L}_i(\omega), \hat{\rho}_S(t) \right\} \right), \tag{1.67}$$

where $\hat{H}_S$ is the system Hamiltonian and $\hat{H}_{LS}$ is an Hamiltonian operator, known as *Lamb-shift Hamiltonian*, used to renormalize the unperturbed system energy levels induced by the system-reservoir coupling [44, 45]. Moreover, $\hat{L}_i(\omega)$ are the *Lindblad operators*, relative to the reservoir mode angular frequency ω, that represent the interaction with the environment. The terms involving $\hat{L}_i$ capture the dissipative effects and ensure that the reduced system dynamics are both completely positive and trace-preserving.

In the near-degenerate case, where $1/|\omega - \omega'| = \tau_\omega \gg \tau_S$, the RWA fails to accurately model the dynamics of the system [29, 48, 49]. Averaging out the rapidly oscillating terms, associated to the near-degenerate energy difference $\hbar\Delta$, can neglect important and interesting interference effects, particularly in multi-level systems driven by spectrally broadened or incoherent radiation [14, 23, 27, 29, 34, 51]. Therefore, the RWA must be applied carefully, considering both the specific scenario in which the system exists and its characteristics.

To accurately capture interference effects in the V-type three-level system driven by non-coherent radiation, RWA is not applied in this case-study. In the following section, further approximations are applied to the Bloch-Redfield equation (1.66). The aim is to obtain a quantum master equation that preserves both trace and positivity and is ideally in a form close to the Lindblad equation.

1.3 Derivation of the quantum master equation

This section derives the quantum master equation for a V-type three-level system from the Bloch-Redfield equation, applying approximations appropriate to the case study.

First, the interaction Hamiltonian $\hat{V}_I$ in the interaction picture is defined, which dictates the time evolution of the reduced density operator $\hat{\rho}_S(t)$. Relevant approximations are then applied to the Bloch-Redfield equation to obtain the quantum master equation. The latter is expressed as a set of linear differential equations for each element of the system's density operator. The analysis considers two types of incoherent radiation: isotropic and unpolarized, as well as anisotropic and polarized. The aim is to compare how Fano coherence is generated in these different scenarios, ultimately identifying the optimal conditions for implementing an experimental setup on atomic platforms for the detection of noise-induced Fano coherence.

1.3.1 Interaction Hamiltonian for a V-type three level system driven by incoherent radiation

The light-matter interaction of interest involves a multi-level atom driven by a non-coherent radiation source, such as a thermal or broadband laser radiation. This scenario is effectively modeled using the open quantum system formalism, as the multi-level system S interacts with a reservoir R.

The atomic system under consideration is a three-level system in a V configuration, consisting of two excited states and one ground state, as depicted in figure 1.1. In the figure, $|a\rangle$ and $|b\rangle$ represent the excited states, which decay to the ground state $|c\rangle$ with rates γ_a and γ_b, respectively. Additionally, both excited states are coupled to the ground via incoherent pumping, (*e.g.* thermal radiation), with rate r_a, r_b. Conversely, there is no coupling between excited states. The angular frequencies of the two atomic transitions are indicated as $\omega_{ac} \equiv \omega_a - \omega_c$ and $\omega_{bc} \equiv \omega_b - \omega_c$, while the upper levels splitting is $\Delta \equiv \omega_{\mathrm{ac}} - \omega_{\mathrm{bc}}$. This scenario is described by the interaction between the system and the radiation field, modelled as a thermal reservoir, and is studied using a fully quantum mechanical description. The time-independent Hamiltonian of the reduced system is expressed as:

$$\hat{H}_S = \sum_l \hbar\omega_{lc}\hat{\sigma}^+_{lc}\hat{\sigma}^-_{lc} = \hbar\left(\omega_{ac}\hat{\sigma}^+_{ac}\hat{\sigma}^-_{ac} + \omega_{bc}\hat{\sigma}^+_{bc}\hat{\sigma}^-_{bc}\right), \tag{1.68}$$

with the energy of ground level $|c\rangle$ set to zero. Equivalently, from Subsection 1.1.1, the Hamiltonian for the quantized electromagnetic field is:

$$\hat{H}_R = \sum_{\lambda=1,2}\sum_{\mathbf{k}} \hbar\nu_{\mathbf{k},\lambda}\hat{a}^\dagger_{\mathbf{k},\lambda}\hat{a}_{\mathbf{k},\lambda}. \tag{1.69}$$

As previously shown in equation (1.57), the Hamiltonian of the composite system $S+R$

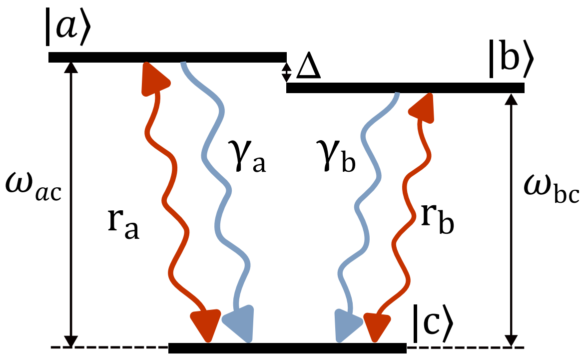

Figure 1.1: *The energy level configuration for the V-type three-level system under consideration consists of two nearly degenerate excited levels, denoted as $|a\rangle$ and $|b\rangle$ with a frequency splitting of Δ. These levels are incoherently pumped, at rates r_a and r_b respectively, from the ground level $|c\rangle$. Both $|a\rangle$ and $|b\rangle$ can decay to the ground level at rates γ_a and γ_b, respectively.*

includes the interaction Hamiltonian $\hat{V}(t)$, which describes the interaction between the atomic system and the electromagnetic field. The Hamiltonian $\hat{V}(t)$ can be derived by considering the coupling between the electric dipole moment operator of the atom, $\hat{\mu}$, and the electric field operator $\hat{E}(\mathbf{r}, t)$ [40, 41, 44]. In the interaction picture, the following expression is obtained:

$$\hat{V}_I(t) = -\hat{\mu}_I(t) \cdot \hat{E}_I(\mathbf{r}, t). \tag{1.70}$$

The dipole moment operator in the interaction picture, associated to the V-type three level system shown in figure 1.1, is given by:

$$\hat{\mu}_I(t) = \boldsymbol{\mu}_{ac}\left(\hat{\sigma}_{ac}^{+} e^{i\omega_{ac}t} + \hat{\sigma}_{ac}^{-} e^{-i\omega_{ac}t}\right) + \boldsymbol{\mu}_{bc}\left(\hat{\sigma}_{bc}^{+} e^{i\omega_{bc}t} + \hat{\sigma}_{bc}^{-} e^{-i\omega_{bc}t}\right), \tag{1.71}$$

where, equation (1.55) is used. Inserting equations (1.71) and (1.52) in equation (1.70) yields the following:

$$\begin{aligned}
\hat{V}_I(t) = & -i \sum_{\lambda=1,2} \sum_{\mathbf{k}} \sqrt{\frac{\hbar \nu_{\mathbf{k},\lambda}}{2\varepsilon_0 V}} \Big[(\boldsymbol{\mu}_{ac} \cdot \boldsymbol{\epsilon}_{\mathbf{k},\lambda}) \left(\hat{\sigma}_{ac}^{+} e^{i\omega_{ac}t} + \hat{\sigma}_{ac}^{-} e^{-i\omega_{ac}t}\right) \\
& \times \left(\hat{a}_{\mathbf{k},\lambda} e^{-i\nu_{\mathbf{k},\lambda}t + i\mathbf{k}\cdot\mathbf{r}} - \hat{a}_{\mathbf{k},\lambda}^{\dagger} e^{i\nu_{\mathbf{k},\lambda}t - i\mathbf{k}\cdot\mathbf{r}}\right) \Big] + \\
& - i \sum_{\lambda=1,2} \sum_{\mathbf{k}} \sqrt{\frac{\hbar \nu_{\mathbf{k},\lambda}}{2\varepsilon_0 V}} \Big[(\boldsymbol{\mu}_{bc} \cdot \boldsymbol{\epsilon}_{\mathbf{k},\lambda}) \left(\hat{\sigma}_{bc}^{+} e^{i\omega_{bc}t} + \hat{\sigma}_{bc}^{-} e^{-i\omega_{bc}t}\right) \\
& \times \left(\hat{a}_{\mathbf{k},\lambda} e^{-i\nu_{\mathbf{k},\lambda}t + i\mathbf{k}\cdot\mathbf{r}} - \hat{a}_{\mathbf{k},\lambda}^{\dagger} e^{i\nu_{\mathbf{k},\lambda}t - i\mathbf{k}\cdot\mathbf{r}}\right) \Big].
\end{aligned} \tag{1.72}$$

At this point, the *dipole approximation* is applied.

- **Dipole approximation:** the dipole approximation assumes that the wavelength of the field is larger than the size of the atom. This allows to disregard any spatial variations of the field over the spatial extent of the atom, meaning that the field can be considered approximately constant. The dipole approximation is particularly suitable for optical transitions, since atomic dimensions typically range in Angstroms, while optical wavelengths extend to hundreds of nanometers. The dipole approximation simplifies the electric field $\hat{E}(\mathbf{r}, t)$ to be nearly constant over the spatial extent of the atom. Consequently, the electric field can be evaluated at a reference point, chosen to be $\mathbf{r} = 0$. The electric field operator is then reformulated as follows:

$$\hat{E}(\mathbf{r}, t) \approx \hat{E}(0, t) = i \sum_{\lambda=1,2} \sum_{\mathbf{k}} \sqrt{\frac{\hbar \nu_{\mathbf{k},\lambda}}{2\varepsilon_0 V}} \boldsymbol{\epsilon}_{\mathbf{k},\lambda} \left[\hat{a}_{\mathbf{k},\lambda} e^{-i\nu_{\mathbf{k},\lambda}t} - \hat{a}_{\mathbf{k},\lambda}^{\dagger} e^{i\nu_{\mathbf{k},\lambda}t}\right]. \tag{1.73}$$

Hence, equation (1.72) becomes:

$$\begin{aligned}
&\hat{V}_I(t) = \\
&= -i \sum_{\lambda=1,2} \sum_{\mathbf{k}} \sqrt{\frac{\hbar \nu_{\mathbf{k},\lambda}}{2\varepsilon_0 V}} \Big[(\boldsymbol{\mu}_{ac} \cdot \boldsymbol{\epsilon}_{\mathbf{k},\lambda}) \left(\hat{\sigma}^{+}_{ac} e^{i\omega_{ac}t} + \hat{\sigma}^{-}_{ac} e^{-i\omega_{ac}t}\right) \left(\hat{a}_{\mathbf{k},\lambda} e^{-i\nu_{\mathbf{k},\lambda}t} - \hat{a}^{\dagger}_{\mathbf{k},\lambda} e^{i\nu_{\mathbf{k},\lambda}t}\right) \Big] + \\
&- i \sum_{\lambda=1,2} \sum_{\mathbf{k}} \sqrt{\frac{\hbar \nu_{\mathbf{k},\lambda}}{2\varepsilon_0 V}} \left[(\boldsymbol{\mu}_{bc} \cdot \boldsymbol{\epsilon}_{\mathbf{k},\lambda}) \left(\hat{\sigma}^{+}_{bc} e^{i\omega_{bc}t} + \hat{\sigma}^{-}_{bc} e^{-i\omega_{bc}t}\right) \left(\hat{a}_{\mathbf{k},\lambda} e^{-i\nu_{\mathbf{k},\lambda}t} - \hat{a}^{\dagger}_{\mathbf{k},\lambda} e^{i\nu_{\mathbf{k},\lambda}t}\right) \right].
\end{aligned} \tag{1.74}$$

Equation (1.74) can be simplified by applying RWA, that allows to discard the non-conserving energy terms contained in the equation.

- **Rotating Wave Approximation:** considering equation (1.74), not all the four terms arising from expanding the product $\left(\hat{\sigma}^{+}_{lc} e^{i\omega_{lc}} + \hat{\sigma}^{-}_{lc} e^{-i\omega_{lc}}\right) \left(\hat{a}_{\mathbf{k},\lambda} e^{-i\nu_{\mathbf{k}}t} - \hat{a}^{\dagger}_{\mathbf{k},\lambda} e^{i\nu_{\mathbf{k}}t}\right)$, with $l = a, b$, conserve the energy. Specifically, the term $\hat{\sigma}^{-}_{lc} \hat{a}_{\mathbf{k},\lambda}$ describes the transition of the atom from the excited state $|l\rangle$ to the ground state $|c\rangle$ and the destruction of one photon, resulting in a net energy loss (equal to the sum of the photon energy and the energy difference between the atomic states). Conversely, the term $\hat{\sigma}^{+}_{lc} \hat{a}^{\dagger}_{\mathbf{k},\lambda}$ represents the transfer of the atom's state to the excited state $|l\rangle$ and the creation of one photon, resulting in an energy gain. On the other hand, the remaining two terms conserve the energy of the light-matter interaction process [40]. Therefore, the non-conserving terms can be dropped by applying the RWA. As specified by McCauley *et al.* in [48], the application of the RWA at this stage should not to be confused with the secular approximation that could be applied later, which turns the Bloch-Redfield equation into a Lindblad master equation.

  Hence, equation (1.74) turns into:

$$\begin{aligned}
&\hat{V}_I(t) = \\
&= -i \sum_{\lambda=1,2} \sum_{\mathbf{k}} \sqrt{\frac{\hbar \nu_{\mathbf{k},\lambda}}{2\varepsilon_0 V}} \left[(\boldsymbol{\mu}_{ac} \cdot \boldsymbol{\epsilon}_{\mathbf{k},\lambda}) \left(\hat{\sigma}^{+}_{ac} \hat{a}_{\mathbf{k},\lambda} e^{i\left(\omega_{ac}t - \nu_{\mathbf{k},\lambda}t\right)} - \hat{\sigma}^{-}_{ac} \hat{a}^{\dagger}_{\mathbf{k},\lambda} e^{-i\left(\omega_{ac}t - \nu_{\mathbf{k},\lambda}t\right)} \right) \right] + \\
&- i \sum_{\lambda=1,2} \sum_{\mathbf{k}} \sqrt{\frac{\hbar \nu_{\mathbf{k},\lambda}}{2\varepsilon_0 V}} \left[(\boldsymbol{\mu}_{bc} \cdot \boldsymbol{\epsilon}_{\mathbf{k},\lambda}) \left(\hat{\sigma}^{+}_{bc} \hat{a}_{\mathbf{k},\lambda} e^{i\left(\omega_{bc}t - \nu_{\mathbf{k},\lambda}t\right)} - \hat{\sigma}^{-}_{bc} \hat{a}^{\dagger}_{\mathbf{k},\lambda} e^{-i\left(\omega_{bc}t - \nu_{\mathbf{k},\lambda}t\right)} \right) \right].
\end{aligned} \tag{1.75}$$

Equation (1.75) can be rewritten also in terms of the *coupling terms* $g^{(l)}_{\mathbf{k},\lambda}$, which have dimensions of an angular frequency:

$$g^{(l)}_{\mathbf{k},\lambda} \equiv -\frac{\boldsymbol{\mu}_{lc} \cdot \boldsymbol{\epsilon}_{\mathbf{k},\lambda}}{\hbar} \sqrt{\frac{\hbar \nu_k}{2\varepsilon_0 V}}, \tag{1.76}$$

with $l = a, b$, so that:

$$\begin{aligned}\hat{V}_I(t) =& i\hbar \sum_{\lambda=1,2} \sum_{\mathbf{k}} g^{(a)}_{\mathbf{k},\lambda} \left(\hat{\sigma}^+_{ac} \hat{a}_{\mathbf{k},\lambda} e^{i\left(\omega_{ac}t - \nu_{\mathbf{k},\lambda} t\right)} - \hat{\sigma}^-_{ac} \hat{a}^\dagger_{\mathbf{k},\lambda} e^{-i\left(\omega_{ac}t - \nu_{\mathbf{k},\lambda} t\right)} \right) + \\ &+ i\hbar \sum_{\lambda=1,2} \sum_{\mathbf{k}} g^{(b)}_{\mathbf{k},\lambda} \left(\hat{\sigma}^+_{bc} \hat{a}_{\mathbf{k},\lambda} e^{i\left(\omega_{bc}t - \nu_{\mathbf{k},\lambda} t\right)} - \hat{\sigma}^-_{bc} \hat{a}^\dagger_{\mathbf{k},\lambda} e^{-i\left(\omega_{bc}t - \nu_{\mathbf{k},\lambda} t\right)} \right).\end{aligned} \tag{1.77}$$

The coupling terms are real and quantify the strength of the interaction between subsystems S and R. These terms define also the *spectral density function* $J(\nu)$, which characterizes how the modes of the radiation field (reservoir) are distributed and how strongly these modes couple to the quantum system (atom). The spectral density is defined as:

$$J_l(\nu) \equiv \sum_{\lambda} \sum_{\mathbf{k}} |g^{(l)}_{\mathbf{k},\lambda}|^2 \delta(\nu - \nu_{\mathbf{k},\lambda}) \tag{1.78}$$

The presence of $\delta(\nu - \nu_{\mathbf{k},\lambda})$ ensures that only the modes of the radiation field that have a frequency $\nu_{\mathbf{k},\lambda}$ are considered.

Now that a simplified expression for $\hat{V}_I(t)$ has been obtained, it is possible to recover the Born-Redfield equation (1.66). The first term on the right-hand side of (1.66) is associated with the *coherent part* of the dynamics, since the commutator encapsulates the unitary evolution driven by the interaction Hamiltonian $\hat{V}_I(t)$. I denoted this term as $\frac{d\hat{\rho}_{S,I}(t)}{dt}|_{\text{coh}}$. By inserting $\hat{V}_I(t)$ in (1.66), the coherent term becomes:

$$\begin{aligned}\left.\frac{d\hat{\rho}_{S,I}(t)}{dt}\right|_{\text{coh}} &= -\frac{i}{\hbar} \mathrm{Tr}_R \left(\left[\hat{V}_I(t), \hat{\rho}_S(0) \otimes \hat{\rho}_R(0) \right] \right) = \\ &= -\sum_{\lambda=1}^{2} \sum_{\mathbf{k}} g^{a}_{\mathbf{k},\lambda} e^{i(\omega_{ac} - \nu_k)t} \langle \hat{a}_{\mathbf{k},\lambda} \rangle [\hat{\sigma}^+_{ac}, \hat{\rho}_S(0)] + \\ &\quad - \sum_{\lambda=1}^{2} \sum_{\mathbf{k}} g^{b}_{\mathbf{k},\lambda} e^{i(\omega_{bc} - \nu_k)t} \langle \hat{a}_{\mathbf{k},\lambda} \rangle [\hat{\sigma}^+_{bc}, \hat{\rho}_S(0)] + \text{h.c.},\end{aligned} \tag{1.79}$$

where $\langle \hat{a}_{\mathbf{k},\lambda} \rangle = \mathrm{Tr}_R \left(\hat{a}_{\mathbf{k},\lambda} \hat{\rho}_R(0) \right)$ are the expectation values of $\hat{a}_{\mathbf{k},\lambda}$ with respect to the state of the reservoir.

The R system is a thermal reservoir in equilibrium at temperature T. This implies that the modes of the reservoir are distributed as a mixture of uncorrelated thermal equilibrium states at temperature T. Hence, the state of the reservoir can be represented by the following reduced density operator [40, 44]:

$$\hat{\rho}_R(0) = \prod_{\mathbf{k},\lambda} \left[1 - \exp\left(-\frac{\hbar \nu_{\mathbf{k},\lambda}}{k_B T} \right) \right] \exp\left(-\frac{\hbar \nu_{\mathbf{k},\lambda} \hat{a}^\dagger_{\mathbf{k},\lambda} \hat{a}_{\mathbf{k},\lambda}}{k_B T} \right), \tag{1.80}$$

where k_B is the Boltzmann constant. In this way, the expectation value and the correlation function of the reservoir's operators, computed with respect to $\hat{\rho}_R(0)$, take the following values:

$$\begin{aligned}
\langle \hat{a}_{\mathbf{k},\lambda} \rangle &= \langle \hat{a}^{\dagger}_{\mathbf{k},\lambda} \rangle = 0 \qquad \forall \mathbf{k}, \lambda & (1.81)\\
\langle \hat{a}^{\dagger}_{\mathbf{k},\lambda} \hat{a}_{\mathbf{k}',\lambda'} \rangle &= \bar{n}_{\mathbf{k},\lambda} \delta_{\mathbf{k},\mathbf{k}'} \delta_{\lambda,\lambda'} & (1.82)\\
\langle \hat{a}_{\mathbf{k},\lambda} \hat{a}^{\dagger}_{\mathbf{k}',\lambda'} \rangle &= (\bar{n}_{\mathbf{k},\lambda} + 1) \delta_{\mathbf{k},\mathbf{k}'} \delta_{\lambda,\lambda'} & (1.83)\\
\langle \hat{a}_{\mathbf{k},\lambda} \hat{a}_{\mathbf{k}',\lambda'} \rangle &= \langle \hat{a}^{\dagger}_{\mathbf{k},\lambda} \hat{a}^{\dagger}_{\mathbf{k}',\lambda'} \rangle = 0 \qquad \forall \mathbf{k}, \mathbf{k}', \lambda, \lambda', & (1.84)
\end{aligned}$$

where

$$\bar{n}_{\mathbf{k},\lambda} = \frac{1}{\exp\left(\frac{\hbar \nu_{\mathbf{k},\lambda}}{k_B T}\right) - 1} \tag{1.85}$$

is the average photon (boson) number in the mode $\mathbf{k}, \lambda$ and δ denotes the Dirac delta function. These relations indicate that in thermal equilibrium, the expectation values of the annihilation and creation operators are equal to zero (equation (1.81)). Equations (1.82) and (1.83) give the average occupation numbers and the commutation relations of the creation and annihilation operators at thermal equilibrium. Finally, equation (1.84) shows that there are no correlations between modes.

Equation (1.81) implies that the coherent part of the reduced dynamics is equal to:

$$\left.\frac{d\hat{\rho}_{S,I}(t)}{dt}\right|_{\mathrm{coh}} = 0 \tag{1.86}$$

Consider now the second term on the right-hand side of equation (1.66), which is associated with the *incoherent part* of the reduced dynamics:

$$\left.\frac{d\hat{\rho}_{S,I}(t)}{dt}\right|_{\mathrm{incoh}} = -\frac{1}{\hbar^2} \int_0^{\infty} \mathrm{Tr}_R \left(\left[\hat{V}_I(t), \left[\hat{V}_I(t'), \hat{\rho}_{S,I}(t) \otimes \hat{\rho}_R(0) \right] \right] \right) dt'. \tag{1.87}$$

This term is related to the interaction between the system and the reservoir that leads to dissipation. This expression can be simplified by expanding the double commutator after substituting equation (1.77) and setting $t' = t - s$, where $s > \tau_R$ according to the Markov approximation. Each term in equation (1.87) is examined separately. The first term is:

$$\begin{aligned}
&- \int_0^{\infty} \sum_{\lambda,\lambda'} \sum_{\mathbf{k},\mathbf{k}'} g^{(l)}_{\mathbf{k},\lambda} g^{(l)}_{\mathbf{k}',\lambda'} \, e^{-i(\omega_{lc} - \nu_{\mathbf{k},\lambda})t + i(\omega_{lc} - \nu_{\mathbf{k}',\lambda'})(t-s)} \Big[\langle \hat{a}^{\dagger}_{\mathbf{k},\lambda} \hat{a}_{\mathbf{k}',\lambda'} \rangle \Big(\hat{\sigma}^{-}_{lc} \hat{\sigma}^{+}_{lc} \hat{\rho}_{S,I}(t) + \\
&- \sigma^{+}_{lc} \rho_{S,I}(t) \sigma^{-}_{lc} \Big) + \langle \hat{a}_{\mathbf{k}',\lambda'} \hat{a}^{\dagger}_{\mathbf{k}\lambda} \rangle \Big(\hat{\rho}_{S,I}(t) \hat{\sigma}^{+}_{lc} \hat{\sigma}^{-}_{lc} - \hat{\sigma}^{-}_{lc} \hat{\rho}_{S,I}(t) \hat{\sigma}^{+}_{lc} \Big) \Big] ds, \qquad (1.88)
\end{aligned}$$

that is associated with the atomic transition $|a\rangle \leftrightarrow |c\rangle$ with $l = a$ or $|b\rangle \leftrightarrow |c\rangle$ with $l = b$. Moreover, also the following crossing terms (namely involving both the levels $|a\rangle$ and $|b\rangle$) arise in equation (1.87):

$$\begin{aligned}
&- \int_0^{\infty} \sum_{\lambda,\lambda'} \sum_{\mathbf{k},\mathbf{k}'} g^{(a)}_{\mathbf{k},\lambda} g^{(b)}_{\mathbf{k}',\lambda'} \, e^{i(\omega_{ac} - \nu_{\mathbf{k},\lambda})t - i(\omega_{bc} - \nu_{\mathbf{k}',\lambda'})(t-s)} \Big[\langle \hat{a}^{\dagger}_{\mathbf{k}',\lambda'} \hat{a}_{\mathbf{k},\lambda} \rangle \Big(\hat{\rho}_{S,I}(t) \hat{\sigma}^{-}_{bc} \hat{\sigma}^{+}_{ac} + \\
&- \hat{\sigma}^{+}_{ac} \hat{\rho}_{S,I}(t) \hat{\sigma}^{-}_{bc} \Big) + \langle \hat{a}_{\mathbf{k},\lambda} \hat{a}^{\dagger}_{\mathbf{k}',\lambda'} \rangle \Big(\hat{\sigma}^{+}_{ac} \hat{\sigma}^{-}_{bc} \hat{\rho}_{S,I}(t) - \hat{\sigma}^{-}_{bc} \hat{\rho}_{S,I}(t) \hat{\sigma}^{+}_{ac} \Big) \Big] ds\,. \qquad (1.89)
\end{aligned}$$

Hence, from substituting the expectation values in equations (1.82)-(1.84), equations (1.88) and (1.89) simplify as:

$$\begin{aligned}
&-\int_0^\infty \sum_\lambda \sum_{\mathbf{k}} |g^{(l)}_{\mathbf{k},\lambda}|^2 e^{-i(\omega_{lc}-\nu_{\mathbf{k},\lambda})s}\Big[\bar{n}_{\mathbf{k},\lambda}\left(\hat{\sigma}^-_{lc}\hat{\sigma}^+_{lc}\hat{\rho}_{S,I}(t) - \hat{\sigma}^+_{lc}\hat{\rho}_{S,I}(t)\hat{\sigma}^-_{lc}\right) + \\
&+(\bar{n}_{\mathbf{k},\lambda}+1)\left(\hat{\rho}_{S,I}(t)\hat{\sigma}^+_{lc}\hat{\sigma}^-_{lc} - \hat{\sigma}^-_{lc}\hat{\rho}_{S,I}(t)\hat{\sigma}^+_{lc}\right)\Big]ds \qquad (1.90)
\end{aligned}$$

and

$$\begin{aligned}
&-\int_0^\infty \sum_\lambda \sum_{\mathbf{k}} g^{(a)}_{\mathbf{k},\lambda} g^{(b)}_{\mathbf{k},\lambda}\, e^{i(\omega_{ac}-\nu_{\mathbf{k},\lambda})t - i(\omega_{bc}-\nu_{\mathbf{k},\lambda})(t-s)}\Big[\bar{n}_{\mathbf{k},\lambda}\left(\hat{\rho}_{S,I}(t)\hat{\sigma}^-_{bc}\hat{\sigma}^+_{ac} - \hat{\sigma}^+_{ac}\hat{\rho}_{S,I}(t)\hat{\sigma}^-_{bc}\right) + \\
&+(\bar{n}_{\mathbf{k},\lambda}+1)\left(\hat{\sigma}^+_{ac}\hat{\sigma}^-_{bc}\hat{\rho}_{S,I}(t) - \hat{\sigma}^-_{bc}\hat{\rho}_{S,I}(t)\hat{\sigma}^+_{ac}\right)\Big]ds\,. \qquad (1.91)
\end{aligned}$$

In the above expression, the exponential terms can be recast as:

$$\begin{aligned}
&-\int_0^\infty \sum_\lambda \sum_{\mathbf{k}} g^{(a)}_{\mathbf{k},\lambda} g^{(b)}_{\mathbf{k},\lambda}\, e^{i\Delta t} e^{i(\omega_{bc}-\nu_{\mathbf{k},\lambda})s}\Big[\bar{n}_{\mathbf{k},\lambda}\left(\hat{\rho}_{S,I}(t)\hat{\sigma}^-_{bc}\hat{\sigma}^+_{ac} - \hat{\sigma}^+_{ac}\hat{\rho}_{S,I}(t)\hat{\sigma}^-_{bc}\right) + \\
&+(\bar{n}_{\mathbf{k},\lambda}+1)\left(\hat{\sigma}^+_{ac}\hat{\sigma}^-_{bc}\hat{\rho}_{S,I}(t) - \hat{\sigma}^-_{bc}\hat{\rho}_{S,I}(t)\hat{\sigma}^+_{ac}\right)\Big]ds\,. \qquad (1.92)
\end{aligned}$$

At this point the *Weisskopf-Wigner approximation* is applied.

- **Weisskopf-Wigner approximation:** the Weisskopf-Wigner approximation assumes that the electric field modes are densely packed in frequency, thus the summation over $\mathbf{k}$ can be replaced with an integral, performing the continuum limit [40, 44]:

$$\sum_{\mathbf{k}} \longrightarrow \frac{V}{(2\pi)^3}\int_0^{2\pi} d\phi \int_0^{\pi} d\theta \sin\theta \int_0^\infty |\mathbf{k}|^2 d|\mathbf{k}| \quad \text{with} \quad |\mathbf{k}| \equiv \frac{\nu_{\mathbf{k}}}{c}. \qquad (1.93)$$

The latter expression holds for a fixed polarization λ. In equation (1.93), the summation over Cartesian coordinates is replaced with an integral in spherical coordinates and the wavevector $\mathbf{k}$ can be expressed as $\mathbf{k} = |\mathbf{k}|(\sin\theta\cos\phi, \sin\theta\sin\phi, \cos\theta)$, varying over the spherical volume $d^3\mathbf{k} = |\mathbf{k}|^2 d|\mathbf{k}|\sin\theta d\theta d\phi$. The fact that the radiation field is contained in a sphere is an approximation that simplifies the mathematical treatment of the model. Nevertheless, the error introduced by this assumption is negligible, since the modes of the radiation field are uncorrelated due to the incoherence of the light source. The integration variable $|\mathbf{k}|$ is then replaced with $\frac{\nu_{\mathbf{k}}}{c}$ using the *dispersion relation*:

$$\frac{V}{(2\pi c)^3}\int_0^{2\pi} d\phi \int_0^{\pi} d\theta \sin\theta \int_0^\infty \nu_{\mathbf{k}}^2 d\nu_{\mathbf{k}} \qquad (1.94)$$

with fixed polarization λ.

Using the Weisskopf-Wigner approximation, the spectral density becomes:

$$\begin{aligned}
J_l(\nu) &\approx \frac{V}{(2\pi c)^3}\sum_\lambda \int_0^{2\pi} d\phi \int_0^{\pi} d\theta \sin\theta \int_0^\infty |g^{(l)}_{\mathbf{k},\lambda}|^2 \delta(\nu-\nu')\nu'^2 d\nu' = \\
&= \frac{\nu^3}{16\hbar\pi^3\varepsilon_o c^3}\sum_\lambda \int_0^{2\pi} d\phi \int_0^{\pi} |\boldsymbol{\mu}_{lc}\cdot\boldsymbol{\epsilon}_\lambda|^2 \sin\theta d\theta, \qquad (1.95)
\end{aligned}$$

where the properties of the Dirac delta function and definition (1.76) are used.

For an incoherent radiation source, the spectral density can often be approximated as flat near the atomic transitions, due to its broad frequency range, which implies the assumption $\nu_{\mathbf{k},\lambda} \approx \omega_{ac}, \omega_{bc}$ for any $\mathbf{k}, \lambda$ close to the transition frequencies. Consequently, the term ν^3 in equation (1.95) can be approximated by ω_{lc}^3, as ν^3 is slowly varying near ω_{lc}. Therefore, the spectral density can be considered approximately constant over the relevant frequency range: $J_l(\nu) \approx J_l(\omega_{lc})$ with $l = a, b$ [39, 40]. The spectral density is then:

$$J(\omega_{lc}) = \frac{\omega_{lc}^3}{16\hbar\pi^3\varepsilon_o c^3} \sum_\lambda \int_0^{2\pi} d\phi \int_0^{\pi} d\theta \sin\theta |\boldsymbol{\mu}_{lc} \cdot \boldsymbol{\epsilon}_\lambda|^2. \tag{1.96}$$

By applying the Weisskopf-Wigner approximation, terms (1.90) and (1.92) become:

$$\begin{aligned}&-\int_0^\infty \int_0^\infty J_l(\omega_{lc}) e^{-i(\omega_{lc}-\nu_{\mathbf{k},\lambda})s} \Big[\bar{n}_{\mathbf{k},\lambda} \left(\hat{\sigma}_{lc}^- \hat{\sigma}_{lc}^+ \hat{\rho}_{S,I}(t) - \hat{\sigma}_{lc}^+ \hat{\rho}_{S,I}(t) \hat{\sigma}_{lc}^-\right) + \\ &+(\bar{n}_{\mathbf{k},\lambda} + 1) \left(\hat{\rho}_{S,I}(t) \hat{\sigma}_{lc}^+ \hat{\sigma}_{lc}^- - \hat{\sigma}_{lc}^- \hat{\rho}_{S,I}(t) \hat{\sigma}_{lc}^+\right) \Big] d\nu_{\mathbf{k},\lambda} ds\end{aligned} \tag{1.97}$$

and

$$\begin{aligned}&-\int_0^\infty \int_0^\infty \sqrt{J_a(\omega_{ac}) J_b(\omega_{bc})} e^{i\Delta t} e^{i(\omega_{bc}-\nu_{\mathbf{k},\lambda})s} \Big[\bar{n}_{\mathbf{k},\lambda} \left(\hat{\rho}_{S,I}(t) \hat{\sigma}_{bc}^- \hat{\sigma}_{ac}^+ - \hat{\sigma}_{ac}^+ \hat{\rho}_{S,I}(t) \hat{\sigma}_{bc}^-\right) + \\ &+(\bar{n}_{\mathbf{k},\lambda} + 1) \left(\hat{\sigma}_{ac}^+ \hat{\sigma}_{bc}^- \hat{\rho}_{S,I}(t) - \hat{\sigma}_{bc}^- \hat{\rho}_{S,I}(t) \hat{\sigma}_{ac}^+\right) \Big] d\nu_{\mathbf{k},\lambda} ds \,,\end{aligned} \tag{1.98}$$

where the spectral density function is used. Notice that when $\nu_{\mathbf{k},\lambda} \neq \omega_{lc}$, the exponential terms $e^{i(\omega_{lc}-\nu_{\mathbf{k},\lambda})s}$ in equations (1.97) and (1.98) oscillate rapidly. By applying the Weisskopf-Wigner approximation, the only relevant frequency modes are those close to the atomic transition. The result of this approximation in equations (1.97) and (1.98) is to set the following integral computations:

$$\begin{aligned}&\int_0^\infty e^{-i(\omega_{lc}-\nu_{\mathbf{k},\lambda})s} d\nu_{\mathbf{k},\lambda} = e^{-i\omega_{lc}s} \int_0^\infty e^{i\nu_{\mathbf{k},\lambda}s} d\nu_{\mathbf{k},\lambda} \approx \\ &\approx \frac{e^{-i\omega_{lc}s}}{2} \int_{-\infty}^\infty e^{i\nu_{\mathbf{k},\lambda}s} d\nu_{\mathbf{k},\lambda} = e^{-i\omega_{lc}s} \left(\pi\delta s + i\mathbb{P}\frac{1}{s}\right)\end{aligned} \tag{1.99}$$

and

$$\begin{aligned}&\int_0^\infty e^{i\Delta t} e^{i(\omega_{bc}-\nu_{\mathbf{k},\lambda})s} d\nu_{\mathbf{k},\lambda} = e^{i\Delta t} e^{i\omega_{bc}s} \int_0^\infty e^{-i\nu_{\mathbf{k},\lambda}s} d\nu_{\mathbf{k},\lambda} \approx \\ &\approx e^{i\Delta t} \frac{e^{i(\omega_{bc}-\nu_{\mathbf{k},\lambda})s}}{2} \int_{-\infty}^\infty e^{-i\nu_{\mathbf{k},\lambda}s} d\nu_{\mathbf{k},\lambda} = e^{i\Delta t} e^{i\omega_{bc}s} \left(\pi\delta(s) - i\mathbb{P}\frac{1}{s}\right),\end{aligned} \tag{1.100}$$

where in both equations the one-side Fourier transform of the Dirac delta function is exploited:

$$\int_0^\infty e^{\pm i\nu s} d\nu \equiv \pi\delta(s) \pm i\mathbb{P}\frac{1}{s}. \tag{1.101}$$

The term $\mathbb{P}$ denotes the Cauchy principal value of the integral. The Cauchy principal value is a mathematical technique used to handle integrals that would otherwise diverge, as in this case, due to the singularity at $s = 0$. This term gives rise to the *Lamb shift effect*, which origins from the interaction of the atom with the vacuum fluctuations of the electromagnetic field, causing a slight shift in the energy levels of the atom [44, 48]. In this treatment, the Lamb shift term is neglected, as in references [27, 30, 52], since it is negligible for weak system-radiation couplings, being much smaller than the atomic transition frequencies.

Substituting expressions (1.99) and (1.100) in the terms (1.97) and (1.98) yields:

$$\begin{aligned}&-\pi J_l(\omega_{lc})\int_0^\infty e^{-i\omega_{lc}s}\Big[\bar{n}_{\mathbf{k},\lambda}\left(\hat{\sigma}^-_{lc}\hat{\sigma}^+_{lc}\hat{\rho}_{S,I}(t)-\hat{\sigma}^+_{lc}\hat{\rho}_{S,I}(t)\hat{\sigma}^-_{lc}\right)+\\&+(\bar{n}_{\mathbf{k},\lambda}+1)\left(\hat{\rho}_{S,I}(t)\hat{\sigma}^+_{lc}\hat{\sigma}^-_{lc}-\hat{\sigma}^-_{lc}\hat{\rho}_{S,I}(t)\hat{\sigma}^+_{lc}\right)\Big]\delta(s)ds\end{aligned} \tag{1.102}$$

and

$$\begin{aligned}&-\pi\sqrt{J_a(\omega_{ac})J_b(\omega_{bc})}\int_0^\infty e^{i\Delta t}e^{i\omega_{bc}s}\Big[\bar{n}_{\mathbf{k},\lambda}\left(\hat{\rho}_{S,I}(t)\hat{\sigma}^-_{bc}\hat{\sigma}^+_{ac}-\hat{\sigma}^+_{ac}\hat{\rho}_{S,I}(t)\hat{\sigma}^-_{bc}\right)+\\&+(\bar{n}_{\mathbf{k},\lambda}+1)\left(\hat{\sigma}^+_{ac}\hat{\sigma}^-_{bc}\hat{\rho}_{S,I}(t)-\hat{\sigma}^-_{bc}\hat{\rho}_{S,I}(t)\hat{\sigma}^+_{ac}\right)\Big]\delta(s)ds\,.\end{aligned} \tag{1.103}$$

By evaluating the integral, the terms become:

$$-\pi J(\omega_{lc})\Big[\bar{n}_{\mathbf{k},\lambda}\left(\hat{\sigma}^-_{lc}\hat{\sigma}^+_{lc}\hat{\rho}_{S,I}(t)-\hat{\sigma}^+_{lc}\hat{\rho}_{S,I}(t)\hat{\sigma}^-_{lc}\right)+(\bar{n}_{\mathbf{k},\lambda}+1)\left(\hat{\rho}_{S,I}(t)\hat{\sigma}^+_{lc}\hat{\sigma}^-_{lc}-\hat{\sigma}^-_{lc}\hat{\rho}_{S,I}(t)\hat{\sigma}^+_{lc}\right)\Big] \tag{1.104}$$

and

$$\begin{aligned}&-\pi\sqrt{J(\omega_{ac})J(\omega_{bc})}e^{i\Delta t}\Big[\bar{n}_{\mathbf{k},\lambda}\left(\hat{\rho}_{S,I}(t)\hat{\sigma}^-_{bc}\hat{\sigma}^+_{ac}-\hat{\sigma}^+_{ac}\hat{\rho}_{S,I}(t)\hat{\sigma}^-_{bc}\right)+\\&+(\bar{n}_{\mathbf{k},\lambda}+1)\left(\hat{\sigma}^+_{ac}\hat{\sigma}^-_{bc}\hat{\rho}_{S,I}(t)-\hat{\sigma}^-_{bc}\hat{\rho}_{S,I}(t)\hat{\sigma}^+_{ac}\right)\Big]\,.\end{aligned} \tag{1.105}$$

The term shown in (1.105) includes an oscillatory component at the frequency difference Δ between the two excited states. If the two excited states are nearly degenerate, the oscillation period $1/\Delta$ can exceed the system's characteristic timescale. In this case, applying the secular approximation, which is suitable for large or zero Δ, becomes inappropriate. The reason is that the secular approximation could ignore interesting interference effects by averaging the oscillatory component. To account for these effects the *partial secular approximation* is used.

- **Partial secular approximation:** this approximation maintains the coupling between populations and coherences that arise from the terms in the master equation that oscillate with frequencies proportional to Δ. The partial secular approximation allows to observe the creation of coherence and non-monotonic excited states population dynamics, which result from interference effects between closely spaced levels [27, 29, 53, 54].

  This approximation states that, since $\omega_{ac}-\omega_{bc}=\Delta\ll\omega_{\mathrm{ac}},\omega_{\mathrm{bc}}$, then $\omega_{ac}\simeq\omega_{bc}$. This is valid, for example, in the context of optical transitions, where $\omega_{ac},\omega_{bc}\sim$ hundreds of THz. The condition $\Delta\ll\omega_{\mathrm{ac}},\omega_{\mathrm{bc}}$ justifies the use of the partial secular approximation as it ensures that terms oscillating at transition frequencies, except those oscillating at frequency Δ, average out over the system's timescale.

After the application of this approximation, crossing terms as (1.105) become:

$$\begin{aligned}-\pi\sqrt{J_a(\omega_{ac})J_b(\omega_{ac})}\Big[&\bar{n}\left(\hat{\rho}_{S,I}(t)\hat{\sigma}^-_{bc}\hat{\sigma}^+_{ac}-\hat{\sigma}^+_{ac}\hat{\rho}_{S,I}(t)\hat{\sigma}^-_{bc}\right)+\\ &+(\bar{n}+1)\left(\hat{\sigma}^+_{ac}\hat{\sigma}^-_{bc}\hat{\rho}_{S,I}(t)-\hat{\sigma}^-_{bc}\hat{\rho}_{S,I}(t)\hat{\sigma}^+_{ac}\right)\Big]\,. \end{aligned} \tag{1.106}$$

Note that the application of the Weisskopf-Wigner approximation first and the partial-secular approximation then imply that:

$$\bar{n}=\frac{1}{\exp\left(\frac{\hbar\omega_{ac}}{k_BT}\right)-1} \tag{1.107}$$

since only the modes close to the atomic transitions are relevant, and $\omega_{ac}\approx\omega_{bc}$.

At the end of the calculations, the Born-Redfield equation (1.66) transforms into:

$$\begin{aligned}&\frac{d\hat{\rho}_{S,I}(t)}{dt}=\left.\frac{d\hat{\rho}_{S,I}(t)}{dt}\right|_{\text{incoh}}=\\ &-\pi J_a(\omega_{ac})\Big[\bar{n}\big(\hat{\sigma}^-_{ac}\hat{\sigma}^+_{ac}\hat{\rho}_S(t)-\hat{\sigma}^+_{ac}\hat{\rho}_S(t)\hat{\sigma}^-_{ac}\big)+(\bar{n}+1)\big(\hat{\rho}_S(t)\hat{\sigma}^+_{ac}\hat{\sigma}^-_{ac}+-\hat{\sigma}^-_{ac}\hat{\rho}_S(t)\hat{\sigma}^+_{ac}\big)\Big]\\ &-\pi J_b(\omega_{ac})\Big[\bar{n}\big(\hat{\sigma}^-_{bc}\hat{\sigma}^+_{bc}\hat{\rho}_S(t)-\hat{\sigma}^+_{bc}\hat{\rho}_S(t)\hat{\sigma}^-_{bc}\big)+(\bar{n}+1)\big(\hat{\rho}_S(t)\hat{\sigma}^+_{bc}\hat{\sigma}^-_{bc}-\hat{\sigma}^-_{bc}\hat{\rho}_S(t)\hat{\sigma}^+_{bc}\big)\Big]\\ &-\pi\sqrt{J_a(\omega_{ac})J_b(\omega_{ac})}\Big[\bar{n}\big(\hat{\rho}_S(t)\hat{\sigma}^-_{bc}\hat{\sigma}^+_{ac}-\hat{\sigma}^+_{ac}\hat{\rho}_S(t)\hat{\sigma}^-_{bc}\big)+(\bar{n}+1)\big(\hat{\sigma}^+_{ac}\hat{\sigma}^-_{bc}\hat{\rho}_S(t)-\hat{\sigma}^-_{bc}\hat{\rho}_S(t)\hat{\sigma}^+_{ac}\big)\Big]\\ &-\pi\sqrt{J_a(\omega_{ac})J_b(\omega_{ac})}\Big[\bar{n}\big(\hat{\rho}_S(t)\hat{\sigma}^-_{ac}\hat{\sigma}^+_{bc}-\hat{\sigma}^+_{bc}\hat{\rho}_S(t)\hat{\sigma}^-_{ac}\big)+(\bar{n}+1)\big(\hat{\sigma}^+_{bc}\hat{\sigma}^-_{ac}\hat{\rho}_S(t)-\hat{\sigma}^-_{ac}\hat{\rho}_S(t)\hat{\sigma}^+_{bc}\big)\Big]+\\ &+\text{h.c.}.\end{aligned} \tag{1.108}$$

Equation (1.108) deviates from the standard Lindblad master equation due to the inclusion of the mixed terms (the last two lines), which account for quantum interference effects. However, as shown by McCauley *et al.* [48], when the spectral density is sufficiently flat and transitions are close enough to share the same spectral density value, the Bloch-Redfield equation closely approximates a Lindblad master equation, thereby maintaining positivity. Indeed, Jeske *et al.* in [53] explain that these conditions lead to the degenerate Lindblad master equation case, described in the reference. For this reason the issue of losing positive semi-definiteness of $\hat{\rho}_S(t)$ does not occur, as also observed in this case study, and equation (1.108) consistently provides accurate predictions, as also remarked in previous works on the subject [26, 28, 29].

Equation (1.108) is general, regarding the type of incoherent radiation considered. In the next sections, the specific case of isotropic, unpolarized radiation and anisotropic, polarized radiation are described in detail.

1.3.2 Interaction with an isotropic, unpolarized non-coherent source

In this section I consider an *isotropic unpolarized* incoherent radiation interacting with the three-level system. I start the calculation by expanding equation (1.108) by inserting equation (1.96). As previously done, I perform the calculation on just two representative terms:

$$\frac{\omega_{lc}^3}{16\hbar\pi^2\varepsilon_0 c^3}\int_0^{2\pi} d\phi \int_0^{\pi} \sin\theta d\theta \sum_\lambda |\boldsymbol{\mu}_{lc}\cdot\boldsymbol{\epsilon}_\lambda|^2 \Big[\bar{n}\left(\hat{\sigma}_{ac}^{-}\hat{\sigma}_{ac}^{+}\hat{\rho}_{S,I}(t') - \hat{\sigma}_{ac}^{+}\hat{\rho}_{S,I}(t')\hat{\sigma}_{ac}^{-}\right) + \\ + (\bar{n}+1)\left(\hat{\rho}_{S,I}(t')\hat{\sigma}_{ac}^{+}\hat{\sigma}_{ac}^{-} - \hat{\sigma}_{ac}^{-}\hat{\rho}_{S,I}(t')\hat{\sigma}_{ac}^{+}\right)\Big] \tag{1.109}$$

and

$$\frac{\omega_{ac}^3}{16\hbar\pi^2\varepsilon_0 c^3}\int_0^{2\pi} d\phi \int_0^{\pi} \sin\theta d\theta \sum_\lambda (\boldsymbol{\mu}_{ac}\cdot\boldsymbol{\epsilon}_\lambda)(\boldsymbol{\mu}_{bc}\cdot\boldsymbol{\epsilon}_\lambda) \Big[\bar{n}\left(\hat{\rho}_{S,I}(t')\hat{\sigma}_{bc}^{-}\hat{\sigma}_{ac}^{+} - \hat{\sigma}_{ac}^{+}\hat{\rho}_{S,I}(t')\hat{\sigma}_{bc}^{-}\right) + \\ + (\bar{n}+1)\left(\hat{\sigma}_{ac}^{+}\hat{\sigma}_{bc}^{-}\hat{\rho}_{S,I}(t') - \hat{\sigma}_{bc}^{-}\hat{\rho}_{S,I}(t')\hat{\sigma}_{ac}^{+}\right)\Big]. \tag{1.110}$$

At this point, the wave vector and the polarization vector can be expressed in spherical coordinates in order to evaluate the angular integrals and then the sum over the polarizations [30, 39]. Following the methodology used in [30, 39, 55], I rewrite the wave vector in spherical coordinates: $\boldsymbol{k} = |\boldsymbol{k}|[\sin\theta\cos\phi, \sin\theta\sin\phi, \cos\theta]$. The polarization and wave vector must be orthogonal, thus two possible instances $\boldsymbol{\epsilon}_{\lambda=1}$, $\boldsymbol{\epsilon}_{\lambda=2}$ of the polarization vector for $\lambda = 1, 2$ are given by the following expressions:

$$\boldsymbol{\epsilon}_{\lambda=1} = [-\cos\theta\cos\phi, -\cos\theta\sin\phi, \sin\theta] \tag{1.111}$$

$$\boldsymbol{\epsilon}_{\lambda=2} = [\sin\phi, -\cos\phi, 0]. \tag{1.112}$$

Then, the scalar products $(\boldsymbol{\mu}_{lc}\cdot\boldsymbol{\epsilon}_{\lambda=1})$ and $(\boldsymbol{\mu}_{lc}\cdot\boldsymbol{\epsilon}_{\lambda=2})$, with $l = a, b$, for arbitrary electric dipole moments $\boldsymbol{\mu}_{ac}$ and $\boldsymbol{\mu}_{bc}$, are computed as long with the evaluation of the integrals over the spherical polar angles θ,ϕ, obtaining:

$$\int_0^{2\pi} d\phi \int_0^{\pi} \sin\theta d\theta \sum_\lambda |\boldsymbol{\mu}_{lc}\cdot\boldsymbol{\epsilon}_\lambda|^2 = \frac{8}{3}\pi\,|\boldsymbol{\mu}_{lc}|^2 \tag{1.113}$$

and

$$\int_0^{2\pi} d\phi \int_0^{\pi} \sin\theta d\theta \sum_\lambda (\boldsymbol{\mu}_{ac}\cdot\boldsymbol{\epsilon}_\lambda)(\boldsymbol{\mu}_{bc}\cdot\boldsymbol{\epsilon}_\lambda) = \frac{8}{3}\pi\,(\boldsymbol{\mu}_{ac}\cdot\boldsymbol{\mu}_{bc}). \tag{1.114}$$

As a result, substituting (1.113) and (1.114) in (1.109) and (1.110) leads to:

$$\frac{\omega_{lc}^3|\boldsymbol{\mu}_{lc}|^2}{6\hbar\pi\varepsilon_0 c^3}\Big[\bar{n}\left(\hat{\sigma}_{ac}^{-}\hat{\sigma}_{ac}^{+}\hat{\rho}_S(t') - \hat{\sigma}_{ac}^{+}\hat{\rho}_S(t')\hat{\sigma}_{ac}^{-}\right) + (\bar{n}+1)\left(\hat{\rho}_S(t')\hat{\sigma}_{ac}^{+}\hat{\sigma}_{ac}^{-} - \hat{\sigma}_{ac}^{-}\hat{\rho}_S(t')\hat{\sigma}_{ac}^{+}\right)\Big] \tag{1.115}$$

and

$$\frac{\omega_{ac}^3(\boldsymbol{\mu}_{ac}\cdot\boldsymbol{\mu}_{bc})}{6\hbar\pi\varepsilon_0 c^3}\Big[\bar{n}\left(\hat{\rho}_S(t')\hat{\sigma}_{bc}^{-}\hat{\sigma}_{ac}^{+} - \hat{\sigma}_{ac}^{+}\hat{\rho}_S(t')\hat{\sigma}_{bc}^{-}\right) + (\bar{n}+1)\left(\hat{\sigma}_{ac}^{+}\hat{\sigma}_{bc}^{-}\hat{\rho}_S(t') - \hat{\sigma}_{bc}^{-}\hat{\rho}_S(t')\hat{\sigma}_{ac}^{+}\right)\Big]. \tag{1.116}$$

The fact that I am evaluating the integrals in (1.113) and (1.114) means that an *isotropic* and *unpolarized radiation* is assumed, i.e., the modes of the radiation are uniformly distributed along all the spatial directions, without a specific polarization.

Equation (1.108) then assumes the form:

$$
\begin{aligned}
&\frac{d\hat{\rho}_{S,I}(t)}{dt} = \left.\frac{d\hat{\rho}_{S,I}(t)}{dt}\right|_{\text{incoh}} = \\
&-\frac{\gamma_a}{2}\Big[\bar{n}\big(\hat{\sigma}^-_{ac}\hat{\sigma}^+_{ac}\hat{\rho}_S(t) - \hat{\sigma}^+_{ac}\hat{\rho}_S(t)\hat{\sigma}^-_{ac}\big) + (\bar{n}+1)\big(\hat{\rho}_S(t)\hat{\sigma}^+_{ac}\hat{\sigma}^-_{ac} + -\hat{\sigma}^-_{ac}\hat{\rho}_S(t)\hat{\sigma}^+_{ac}\big)\Big] \\
&-\frac{\gamma_b}{2}\Big[\bar{n}\big(\hat{\sigma}^-_{bc}\hat{\sigma}^+_{bc}\hat{\rho}_S(t) - \hat{\sigma}^+_{bc}\hat{\rho}_S(t)\hat{\sigma}^-_{bc}\big) + (\bar{n}+1)\big(\hat{\rho}_S(t)\hat{\sigma}^+_{bc}\hat{\sigma}^-_{bc} - \hat{\sigma}^-_{bc}\hat{\rho}_S(t)\hat{\sigma}^+_{bc}\big)\Big] \\
&-p\frac{\sqrt{\gamma_a\gamma_b}}{2}\Big[\bar{n}\big(\hat{\rho}_S(t)\hat{\sigma}^-_{bc}\hat{\sigma}^+_{ac} - \hat{\sigma}^+_{ac}\hat{\rho}_S(t)\hat{\sigma}^-_{bc}\big) + (\bar{n}+1)\big(\hat{\sigma}^+_{ac}\hat{\sigma}^-_{bc}\hat{\rho}_S(t) - \hat{\sigma}^-_{bc}\hat{\rho}_S(t)\hat{\sigma}^+_{ac}\big)\Big] \\
&-p\frac{\sqrt{\gamma_a\gamma_b}}{2}\Big[\bar{n}\big(\hat{\rho}_S(t)\hat{\sigma}^-_{ac}\hat{\sigma}^+_{bc} - \hat{\sigma}^+_{bc}\hat{\rho}_S(t)\hat{\sigma}^-_{ac}\big) + (\bar{n}+1)\big(\hat{\sigma}^+_{bc}\hat{\sigma}^-_{ac}\hat{\rho}_S(t) - \hat{\sigma}^-_{ac}\hat{\rho}_S(t)\hat{\sigma}^+_{bc}\big)\Big] + \text{h.c..}
\end{aligned}
\tag{1.117}
$$

In Eq. (1.117),

$$
\begin{aligned}
\gamma_l &\equiv \frac{\omega_{lc}^3\,|\mu_{lc}|^2}{\hbar 3\pi\varepsilon_0 c^3} &(1.118)\\
p &\equiv \frac{\boldsymbol{\mu}_{ac}\cdot\boldsymbol{\mu}_{bc}}{|\boldsymbol{\mu}_{ac}|\,|\boldsymbol{\mu}_{bc}|} = \cos\Theta, &(1.119)
\end{aligned}
$$

where γ_l denotes the *spontaneous decay rate* from level $|l\rangle$ to the ground level $|c\rangle$. The parameter p is the *alignment parameter* between the transition dipole moments of the transitions $|a\rangle \leftrightarrow |c\rangle$, $|b\rangle \leftrightarrow |c\rangle$, and Θ is the angle between the two electric dipole moments. The parameter p ranges from -1 to $+1$, where $p = +1$ indicates that the transition dipole moments $\boldsymbol{\mu}_{ac}$ and $\boldsymbol{\mu}_{bc}$ are parallel, $p = -1$ means they are anti-parallel, and $p = 0$ corresponds to orthogonal dipole moments.

Finally, the equation of motion for $\hat{\rho}_S(t)$ in the Schrödinger picture is derived by adding the Hamiltonian $\hat{H}_S$ of the three-level system in the coherent part of the differential equation of $\hat{\rho}_S(t)$. Formally, it entails to solve the differential equation

$$
\begin{aligned}
\frac{d\hat{\rho}_S(t)}{dt} &= -\frac{i}{\hbar}\mathrm{Tr}_R\left[\hat{V}_I(t) + \hat{H}_S\otimes\hat{I}_R, \hat{\rho}_S(0)\otimes\hat{\rho}_R(0)\right] + \\
&- \frac{1}{\hbar^2}\int_0^t \mathrm{Tr}_R\left[\hat{V}_I(t), \left[\hat{V}_I(t'), \hat{\rho}_S(t')\otimes\hat{\rho}_R(0)\right]\right] dt'.
\end{aligned}
\tag{1.120}
$$

Hence, by incorporating the explicit expression of $\hat{H}_S$ into the differential equation (1.120) and decomposing $\hat{\rho}_S(t)$ in its elements $\langle l|\hat{\rho}_S(t)|j\rangle \equiv \rho_{lj}(t)$ with $l, j = a, b, c$, the set of differential equations for each $\rho_{lj}(t)$ is obtained, upon following the same steps already performed in the interaction picture, as reported below [55]:

$$
\begin{cases}
\dfrac{d\rho_{aa}(t)}{dt} = -\gamma_a\left(\bar{n}+1\right)\rho_{aa}(t) + \gamma_a\bar{n}\rho_{cc}(t) - p\sqrt{\gamma_a\gamma_b}\left(\bar{n}+1\right)\mathrm{Re}[\rho_{\mathrm{ab}}(\mathrm{t})] \\
\dfrac{d\rho_{bb}(t)}{dt} = -\gamma_b\left(\bar{n}+1\right)\rho_{bb}(t) + \gamma_b\bar{n}\rho_{cc}(t) - p\sqrt{\gamma_a\gamma_b}\left(\bar{n}+1\right)\mathrm{Re}[\rho_{\mathrm{ab}}(\mathrm{t})] \\
\dfrac{d\rho_{cc}(t)}{dt} = -\left(\gamma_a+\gamma_b\right)\bar{n}\rho_{cc}(t) + \left(\bar{n}+1\right)\left(\gamma_a\rho_{aa}(t) + \gamma_b\rho_{bb}(t)\right) + 2p\sqrt{\gamma_a\gamma_b}\left(\bar{n}+1\right)\mathrm{Re}[\rho_{\mathrm{ab}}(\mathrm{t})] \\
\dfrac{d\rho_{ab}(t)}{dt} = -p\dfrac{\sqrt{\gamma_a\gamma_b}}{2}\left(\bar{n}+1\right)\left(\rho_{aa}(t)+\rho_{bb}(t)\right) + p\sqrt{\gamma_a\gamma_b}\bar{n}\rho_{cc}(t) - \left[\dfrac{\gamma_a+\gamma_b}{2}\left(\bar{n}+1\right) + i\Delta\right]\rho_{ab}(t)
\end{cases}
\tag{1.121}
$$

together with

$$\begin{cases} \dfrac{d\rho_{ac}(t)}{dt} = -p\dfrac{\sqrt{\gamma_a\gamma_b}}{2}\left(\bar{n}+1\right)\rho_{bc}(t) - \left[\dfrac{\gamma_b}{2}\bar{n} + \dfrac{\gamma_a}{2}\left(2\bar{n}+1\right) + i\dfrac{\omega_{ac}}{2}\right]\rho_{ac}(t) \\ \dfrac{d\rho_{bc}(t)}{dt} = -p\dfrac{\sqrt{\gamma_a\gamma_b}}{2}\left(\bar{n}+1\right)\rho_{ac}(t) - \left[\dfrac{\gamma_a}{2}\bar{n} + \dfrac{\gamma_b}{2}\left(2\bar{n}+1\right) + i\dfrac{\omega_{bc}}{2}\right]\rho_{bc}(t)\,. \end{cases} \tag{1.122}$$

The incoherent pumping rates $r_l \equiv \bar{n}\gamma_l$ of the transitions $|l\rangle \leftrightarrow |c\rangle$ $(l = a, b)$ are associated with the absorption and stimulated emission processes due to the incoherent light source. Note that, if $p = 0$, thus the transition dipole moments are orthogonal, then equation (1.121) and (1.122) for the quantum system dynamics simplify to the standard Pauli rate equations [28, 29].

Equations (1.121) and (1.122) correspond to two independent sub-processes of the quantum system's evolution [14]. Equation (1.121) comprise the time-evolution of the quantum coherence between the two nearly degenerate excited levels $|a\rangle, |b\rangle$, which arises thanks to the interference both between the two decay paths and between the two pumping paths (see Fig. 1.1). This kind of coupling gives rise to an effective one-photon coherence that makes indistinguishable the transition $|a\rangle \leftrightarrow |c\rangle$ or $|b\rangle \leftrightarrow |c\rangle$ along which the decay and pumping processes occur. On the other hand, the sub-process (1.122) returns the time-evolutions of the quantum coherence between each excited level and the ground state, which are not affected by how the system populations vary. This decoupling is a consequence of applying the partial secular approximation, which averaged out the oscillating terms at the single atomic transition frequencies, while retaining the terms oscillating at the frequency splitting Δ [30, 55]. It is important to note that equations (1.121) and (1.122) apply to single atoms and do not account for interactions between atoms or collective behaviors. The mathematical model remains valid for theoretical predictions in the proof-of-principle experiment since the atomic densities are low enough to treat the atoms as non-interacting, as it is shown in Section 3.2.

In subsection 1.4.1, I present the simulations for the isotropic unpolarized case scenario, which are obtained by numerically solving equations (1.121) and (1.122). These simulations analyze the influence of the governing parameters Δ, $\bar{n}$ and p.

1.3.3 Interaction with a polarized non-coherent source

In this section, the case of an *anisotropic* and *polarized* incoherent radiation is considered. Differently from the isotropic and unpolarized case presented in the previous section, the anisotropy of the radiation affects only the incoherent pumping, thereby influencing the absorption and stimulated emission processes. The spontaneous emission process, instead, remains isotropic due to interaction with vacuum fluctuations. As explained by Dodin *et al.* in [29], this condition can be described by the interaction of the system with two distinct photon baths: the isotropic radiative environment for the spontaneous decay and the directional excitation beam inducing the absorption and stimulated emission.

In the polarized case, the integration over the spherical volume $d^3\mathbf{k} = |\mathbf{k}|^2 d|\mathbf{k}| \sin\theta d\theta d\phi$ is performed solely on the magnitude of the wavevector $|\mathbf{k}|^2 d|\mathbf{k}|$, since the direction of $\mathbf{k}$ is defined. Consequently, the spectral density $J_l(\nu)$ is given by:

$$J_l(\nu) = \frac{\nu^3}{16\hbar\pi^3\varepsilon_o c^3} \sum_{\lambda} |\boldsymbol{\mu}_{lc} \cdot \boldsymbol{\epsilon}_{\lambda}|^2. \tag{1.123}$$

At this point, it is necessary to define the polarization vector $\boldsymbol{\epsilon}_{\lambda}$ as well as the transition dipole moments vectors $\boldsymbol{\mu}_{ac}$ and $\boldsymbol{\mu}_{bc}$ of the atomic transitions. The discussion focuses on the case of the atomic transitions with $\Delta m_F = m_{F'} - m_F = \pm 1$, where the quantum number m_F identifies the hyperfine magnetic sublevel within the ground manifold F, while the subscript F' indicates the excited manifold. In particular, the quantum number m_F specifies the projection of the total angular momentum F, which is given by the sum of the electronic total angular momentum J and the nuclear spin I along a chosen quantization axis, typically the z axis [41, 56]. This specific case is used in the implementation of the V-type three-level system in the hyperfine structure of ^{87}Rb atoms, described in Chapter 3.

For $\Delta m_F = +1$, the corresponding transition involves coupling with circularly polarized light in the x-y plane, according to the selection rules. The unitary transition dipole moment vector for this transition is defined as:

$$\boldsymbol{\mu} = \boldsymbol{\mu}_+ = \left[-\frac{1}{\sqrt{2}}, -i\frac{1}{\sqrt{2}}, 0\right]. \tag{1.124}$$

Conversely, for $\Delta m_F = -1$ the transition involves the coupling with circularly polarized light in the x-y plane, but rotated in the opposite sense respect to the previous case. The unitary dipole moment vector for this transition is:

$$\boldsymbol{\mu} = \boldsymbol{\mu}_- = \left[\frac{1}{\sqrt{2}}, -i\frac{1}{\sqrt{2}}, 0\right]. \tag{1.125}$$

The atomic transition $|a\rangle \leftrightarrow |c\rangle$ is described by the transition dipole moment vector $\boldsymbol{\mu}_{ac} = |\boldsymbol{\mu}_{ac}|\boldsymbol{\mu}_-$, while the atomic transition $|b\rangle \leftrightarrow |c\rangle$ is described by the transition dipole moment vector $\boldsymbol{\mu}_{bc} = |\boldsymbol{\mu}_{bc}|\boldsymbol{\mu}_+$. Note that $\boldsymbol{\mu}_{ac} \perp \boldsymbol{\mu}_{bc}$. If the polarization of the light is oriented along the x axis, the corresponding unitary polarization vector is given by:

$$\boldsymbol{\epsilon}_{\lambda} = \boldsymbol{\epsilon}_x = [1, 0, 0] \tag{1.126}$$

or as the linear combination:

$$\boldsymbol{\epsilon}_x = \sqrt{2}\left(\boldsymbol{\mu}_- - \boldsymbol{\mu}_+\right). \tag{1.127}$$

The last expression indicates that a linear polarization can drive both $\boldsymbol{\mu}_-$ and $\boldsymbol{\mu}_+$ transitions.

Starting from the equation (1.108) and using equation (1.123), the following terms are obtained:

$$\begin{aligned} &\frac{\omega_{lc}^3 |\boldsymbol{\mu}_{lc} \cdot \boldsymbol{\epsilon}_x|^2}{16\hbar\pi^2\varepsilon_0 c^3} \left[\bar{n}\left(\hat{\sigma}_{ac}^-\hat{\sigma}_{ac}^+\hat{\rho}_S(t') - \hat{\sigma}_{ac}^+\hat{\rho}_S(t')\hat{\sigma}_{ac}^-\right) + \bar{n}\left(\hat{\rho}_S(t')\hat{\sigma}_{ac}^+\hat{\sigma}_{ac}^- - \hat{\sigma}_{ac}^-\hat{\rho}_S(t')\hat{\sigma}_{ac}^+\right)\right] + \\ &+ \frac{\omega_{lc}^3 |\boldsymbol{\mu}_{lc}|^2}{6\hbar\pi\varepsilon_0 c^3} \left(\hat{\rho}_S(t')\hat{\sigma}_{ac}^+\hat{\sigma}_{ac}^- - \hat{\sigma}_{ac}^-\hat{\rho}_S(t')\hat{\sigma}_{ac}^+\right) \end{aligned} \tag{1.128}$$

and

$$\begin{aligned}
&\frac{\omega_{ac}^3\left(\boldsymbol{\mu}_{ac}\cdot\boldsymbol{\epsilon}_x\right)\left(\boldsymbol{\mu}_{bc}\cdot\boldsymbol{\epsilon}_x\right)}{16\hbar\pi^2\varepsilon_0 c^3}\Big[\bar{n}\left(\hat{\rho}_S(t')\hat{\sigma}_{bc}^{-}\hat{\sigma}_{ac}^{+}-\hat{\sigma}_{ac}^{+}\hat{\rho}_S(t')\hat{\sigma}_{bc}^{-}\right)+\bar{n}\left(\hat{\sigma}_{ac}^{+}\hat{\sigma}_{bc}^{-}\hat{\rho}_S(t')-\hat{\sigma}_{bc}^{-}\hat{\rho}_S(t')\hat{\sigma}_{ac}^{+}\right)\Big]+\\
&+\frac{\omega_{ac}^3\left(\boldsymbol{\mu}_{ac}\cdot\boldsymbol{\mu}_{bc}\right)}{6\hbar\pi\varepsilon_0 c^3}\left(\hat{\sigma}_{ac}^{+}\hat{\sigma}_{bc}^{-}\hat{\rho}_S(t')-\hat{\sigma}_{bc}^{-}\hat{\rho}_S(t')\hat{\sigma}_{ac}^{+}\right),
\end{aligned}\tag{1.129}$$

where the terms related to the spontaneous emission phenomenon are the last two in each equation. Then, calculating the scalar products:

$$\begin{aligned}
&\frac{\omega_{lc}^3|\boldsymbol{\mu}_{lc}|^2}{32\hbar\pi^2\varepsilon_0 c^3}\Big[\bar{n}\left(\hat{\sigma}_{ac}^{-}\hat{\sigma}_{ac}^{+}\hat{\rho}_S(t')-\hat{\sigma}_{ac}^{+}\hat{\rho}_S(t')\hat{\sigma}_{ac}^{-}\right)+\bar{n}\left(\hat{\rho}_S(t')\hat{\sigma}_{ac}^{+}\hat{\sigma}_{ac}^{-}-\hat{\sigma}_{ac}^{-}\hat{\rho}_S(t')\hat{\sigma}_{ac}^{+}\right)\Big]+\\
&+\frac{\omega_{lc}^3|\boldsymbol{\mu}_{lc}|^2}{6\hbar\pi\varepsilon_0 c^3}\left(\hat{\rho}_S(t')\hat{\sigma}_{ac}^{+}\hat{\sigma}_{ac}^{-}-\hat{\sigma}_{ac}^{-}\hat{\rho}_S(t')\hat{\sigma}_{ac}^{+}\right)
\end{aligned}\tag{1.130}$$

and

$$\begin{aligned}
&\frac{\omega_{ac}^3\left|\boldsymbol{\mu}_{ac}\right|\left|\boldsymbol{\mu}_{bc}\right|}{32\hbar\pi^2\varepsilon_0 c^3}\Big[\bar{n}\left(\hat{\rho}_S(t')\hat{\sigma}_{bc}^{-}\hat{\sigma}_{ac}^{+}-\hat{\sigma}_{ac}^{+}\hat{\rho}_S(t')\hat{\sigma}_{bc}^{-}\right)+\bar{n}\left(\hat{\sigma}_{ac}^{+}\hat{\sigma}_{bc}^{-}\hat{\rho}_S(t')-\hat{\sigma}_{bc}^{-}\hat{\rho}_S(t')\hat{\sigma}_{ac}^{+}\right)\Big]+\\
&+\frac{\omega_{ac}^3\left(\boldsymbol{\mu}_{ac}\cdot\boldsymbol{\mu}_{bc}\right)}{6\hbar\pi\varepsilon_0 c^3}\left(\hat{\sigma}_{ac}^{+}\hat{\sigma}_{bc}^{-}\hat{\rho}_S(t')-\hat{\sigma}_{bc}^{-}\hat{\rho}_S(t')\hat{\sigma}_{ac}^{+}\right).
\end{aligned}\tag{1.131}$$

Using unpolarized and isotropic radiation, the incoherent pumping rate $r_l/2=\bar{n}\gamma_l/2$ is given by:

$$\frac{r_l^{iso}}{2}=\bar{n}\frac{\gamma_l^{iso}}{2}=\frac{\omega_{lc}^3\left|\mu_{lc}\right|^2}{6\hbar\pi\varepsilon_0 c^3}\bar{n}.\tag{1.132}$$

On the contrary, for the case of polarized radiation, the incoherent pumping rate is:

$$\frac{r_l^{pol}}{2}=\bar{n}\frac{\gamma_l^{pol}}{2}=\frac{\omega_{lc}^3\left|\mu_{lc}\right|^2}{32\hbar\pi^2\varepsilon_0 c^3}\bar{n}=\bar{n}\frac{\gamma_l^{iso}}{2}\frac{3}{16\pi}\Rightarrow\bar{n}\gamma_l^{pol}=\frac{3}{16\pi}\bar{n}\gamma_l^{iso}.\tag{1.133}$$

As also demonstrated in [30], the anisotropic pumping rate r_l^{pol} is smaller by a factor of $16\pi/3$ than the isotropic pumping rate r_l^{iso}.

Overall, the master equation in the context of polarized radiation is:

$$\begin{cases}
\dfrac{d\rho_{aa}(t)}{dt}=-\left(\gamma_a^{pol}\bar{n}+\gamma_a^{iso}\right)\rho_{aa}(t)+\gamma_a^{pol}\bar{n}\rho_{cc}(t)-\left(\sqrt{\gamma_a^{pol}\gamma_b^{pol}}\bar{n}+p\sqrt{\gamma_a^{iso}\gamma_b^{iso}}\right)\mathrm{Re}[\rho_{\mathrm{ab}}(\mathrm{t})]\\
\dfrac{d\rho_{bb}(t)}{dt}=-\left(\gamma_b^{pol}\bar{n}+\gamma_b^{iso}\right)\rho_{bb}(t)+\gamma_b^{pol}\bar{n}\rho_{cc}(t)-\left(\sqrt{\gamma_a^{pol}\gamma_b^{pol}}\bar{n}+p\sqrt{\gamma_a^{iso}\gamma_b^{iso}}\right)\mathrm{Re}[\rho_{\mathrm{ab}}(\mathrm{t})]\\
\dfrac{d\rho_{cc}(t)}{dt}=-\left(\gamma_a^{pol}+\gamma_b^{pol}\right)\bar{n}\rho_{cc}(t)+\bar{n}\left(\gamma_a^{pol}\rho_{aa}(t)+\gamma_b^{pol}\rho_{bb}(t)\right)+\left(\gamma_a^{iso}\rho_{aa}(t)+\gamma_b^{iso}\rho_{bb}(t)\right)+\\
\qquad\qquad+2\left(\sqrt{\gamma_a^{pol}\gamma_b^{pol}}\bar{n}+p\sqrt{\gamma_a^{iso}\gamma_b^{iso}}\right)\mathrm{Re}[\rho_{\mathrm{ab}}(\mathrm{t})]\\
\dfrac{d\rho_{ab}(t)}{dt}=-\dfrac{1}{2}\left(\sqrt{\gamma_a^{pol}\gamma_b^{pol}}\bar{n}+p\sqrt{\gamma_a^{iso}\gamma_b^{iso}}\right)\left(\rho_{aa}(t)+\rho_{bb}(t)\right)+\sqrt{\gamma_a^{pol}\gamma_b^{pol}}\bar{n}\rho_{cc}(t)+\\
\qquad\qquad-\left[\dfrac{\gamma_a^{pol}+\gamma_b^{pol}}{2}\bar{n}+\dfrac{\gamma_a^{iso}+\gamma_b^{iso}}{2}+i\Delta\right]\rho_{ab}(t)
\end{cases}\tag{1.134}$$

together with

$$\left\{\begin{aligned} \frac{d\rho_{ac}(t)}{dt} &= -\frac{1}{2}\left(\sqrt{\gamma_a^{pol}\gamma_b^{pol}}\bar{n} + p\sqrt{\gamma_a^{iso}\gamma_b^{iso}}\right)\rho_{bc}(t) - \left[\frac{\gamma_b^{pol}}{2}\bar{n} + \gamma_a^{pol}\bar{n} + \frac{\gamma_a^{iso}}{2} + i\frac{\omega_{ac}}{2}\right]\rho_{ac}(t) \\ \frac{d\rho_{bc}(t)}{dt} &= -\frac{1}{2}\left(\sqrt{\gamma_a^{pol}\gamma_b^{pol}}\bar{n} + p\sqrt{\gamma_a^{iso}\gamma_b^{iso}}\right)\rho_{ac}(t) - \left[\frac{\gamma_a^{pol}}{2}\bar{n} + \gamma_b^{pol}\bar{n} + \frac{\gamma_b^{iso}}{2} + i\frac{\omega_{bc}}{2}\right]\rho_{bc}(t). \end{aligned}\right. \tag{1.135}$$

The structure of equations (1.134) and (1.135) mirrors that of equations (1.121) and (1.122), with the key difference that the system interacts with two distinct thermal baths, identified through the quantities γ_l^{pol} and γ_l^{iso}. Specifically, the interaction can be decomposed into two parts: the modes of the field with wavevector $\mathbf{k}$ and polarization $\boldsymbol{\epsilon}_x$ act as a hot bath, that supply energy to the V-system, while the remaining vacuum modes act as a cold bath, to which the system dissipates energy [29]. Notice that the selected transitions have orthogonal electric dipole moments. This implies $p = 0$ for the isotropic process of spontaneous emission.

The experimental realization of a proof-of-principle experiment to detect noise-induced Fano coherences in a V-type three-level system, described in Section 3.2, employs polarized incoherent radiation. The reasons behind this choice are explained in the following section.

1.4 Theoretical prediction for V-type three-level systems

Recent works have extensively investigated the driving of multi-level systems, in particular V-type three-level systems, by isotropic, unpolarized, non-coherent radiation sources [23, 26–28, 51]. These studies provide analytic solutions to equations (1.121), revealing two distinct dynamical regimes based on the ratio between the excited state splitting Δ and the average radiative decay rate $\bar{\gamma}$ between the two decay rates γ_a and γ_b. The solutions are also influenced by the source's average photon number $\bar{n}$, whose value is determined by the ratio between the average incoherent excitation rate $\bar{r}$ and the average spontaneous decay rate $\bar{\gamma}$ [26, 28, 51]. Subsequently, also the case of polarized radiation has been examined in [29, 30]. Analytic solutions to equations (1.122) and (1.135) are still not provided in prior literature.

This section examines and discusses the dynamical regimes associated with an unpolarized an polarized incoherent radiation. Rather than relying on analytical solutions, as in previous works, this thesis presents numerically obtained solutions to understand the behavior of all elements of the system's density operator. In particular, the solutions of equations (1.121) for unpolarized radiation and (1.134) for polarized radiation are analyzed separately in Subsections 1.4.1 and 1.4.2, respectively. This analysis is crucial for determining the conditions needed for a proof-of-principle experiment with atoms to detect Fano coherence, treated in Chapter 3. The solutions of equations (1.122) are used in the quantum thermodynamic analysis in Chapter 2.

1.4.1 Dynamical regimes with isotropic unpolarized radiation

The dynamics of a V-type three level system interacting with a continuum of radiation modes, uniformly distributed along all the spatial directions without a specific polarization, is described by equations (1.121) and (1.122). I remind that the above equations correspond to two independent sub-processes for the quantum system's evolution. The first set of differential equations in (1.121) describes the time-evolution of the coupling between the quantum coherence between the nearly degenerate excited levels $|a\rangle, |b\rangle$, and the system's populations. On the other hand, the sub-process (1.122) captures the time-evolution of the quantum coherences between each excited level and the ground state, which are not affected by how the system populations vary. This decoupling is a consequence of applying the partial secular approximation.

The differential equations in (1.121) and (1.122) can be reformulated using the Liouville representation, as done in [28, 30, 51, 52]. In this representation, the reduced density operator $\hat{\rho}_S$ is expressed in matrix-vector form:

$$\mathbf{x}(t) = [\rho_{aa}(t), \rho_{ab}(t), \rho_{ac}(t), \rho_{ba}(t), \rho_{bb}(t), \rho_{bc}(t), \rho_{ca}(t), \rho_{cb}(t)\rho_{cc}(t)]^T. \tag{1.136}$$

In this way, the elements of a $N \times N$ density operator are represented by a vector of dimension N^2 [57]. Differently from [28, 30, 51, 52], the state vector $\mathbf{x}(t)$ includes all the elements of the system's density operator, allowing to numerically solve both sub-processes in equations (1.121) and (1.122) simultaneously. In Section 2.2 a different method is adopted, by solving the two sub-processes separately. Both approaches ultimately yield the same results.

The coefficient matrix of the linear differential equations is represented by the Liouville super-operator $\hat{\mathcal{L}}$. The latter is decomposed in the "coherent" term $\hat{\mathcal{L}}_H$, comprising the coherent evolution of the dynamics, and the "dissipative" term $\hat{\mathcal{L}}_{\mathcal{D}}$ that encapsulates the effects of dissipation on the density matrix. In formulas:

$$-\frac{i}{\hbar}\left[\hat{H}_S, \hat{\rho}_S(t)\right] \rightarrow \hat{\mathcal{L}}_H \mathbf{x}(t) \qquad \text{with} \qquad \hat{\mathcal{L}}_H = \hat{H}_S \otimes \hat{\mathbb{I}}_S - \hat{\mathbb{I}}_S \otimes \hat{H}_S^T. \tag{1.137}$$

Here $\hat{\mathbb{I}}_S$ is the identity operator in the Hilbert space of the system S. The term $\hat{\mathcal{L}}_{\mathcal{D}}$, instead, can be further divided for simplicity in three contributions:

1. $\hat{\mathcal{L}}_{\mathcal{D}_1}$, that describes the decay and pumping processes relative to transition $|a\rangle \leftrightarrow |c\rangle$.
2. $\hat{\mathcal{L}}_{\mathcal{D}_2}$, that describes the decay and pumping processes relative to transition $|b\rangle \leftrightarrow |c\rangle$.
3. $\hat{\mathcal{L}}_{\mathcal{D}_{12}}$, that describes Fano interference terms.

The procedure used to obtain all the above dissipative terms can be found in [58]. The following linear homogeneous differential equation is then obtained:

$$\frac{d\mathbf{x}(t)}{dt} = \hat{\mathcal{L}}\mathbf{x}(t) \qquad \text{with} \qquad \hat{\mathcal{L}} = \hat{\mathcal{L}}_H + \hat{\mathcal{L}}_{\mathcal{D}_1} + \hat{\mathcal{L}}_{\mathcal{D}_2} + \hat{\mathcal{L}}_{\mathcal{D}_{12}}. \tag{1.138}$$

The advantages of the Liouville super-operator are several, among which is the ability to represent the master equation formalism in a compact and more manageable form. Moreover, it is possible to numerically solve the set of equations in (1.138) via exponentiation:

$$\mathbf{x}(t) = e^{\hat{\mathcal{L}}t}\mathbf{x}(0), \tag{1.139}$$

with $\mathbf{x}(0)$ denoting the initial state. The exponential of the super-operator is computed using the Matlab function `expm`, which employs the scaling and squaring algorithm of Higham [59]. The numerical solution of equation (1.139) is valid under the assumption that all terms composing the super-operator remain constant over time, which is the case treated in this and in the following subsection. Subsequently, a time-dependent incoherent radiation is also evaluated, being useful for the implementation of the proof-of-principle experiment of Fano coherence generation.

To properly analyse the generation of Fano coherence induced by incoherent driving, I choose a coherence-free initial state. Specifically, as in [26, 28, 30, 51] , I initialize the system in the ground state, meaning the initial state vector $\mathbf{x}(0)$ has only $\rho_{cc}(0) = 1$ as the non-zero element. This initial condition guarantees the existence of positive populations at all times, as discussed in [26, 28, 51]

The analytical and numerical solutions reveal two critical physical regimes for the evolution of the Fano-coherence ρ_{ab}: an *overdamped regime* and an *underdamped regime*, separated by a *transition regime* [26, 28, 51]. The regimes are determined by different values of the excited states splitting Δ, of the average spontaneous decay rate $\bar{\gamma} = (\gamma_a + \gamma_b)/2$, of the alignment parameter p and of the radiation average photon number $\bar{n}$. The latter can be interpreted also as the radiation intensity. For simplicity, $\gamma_a > \gamma_b$ is assumed, though the results hold for the reverse condition $\gamma_a < \gamma_b$ as well.

First, consider the *weak pumping condition*, where $\bar{n} \ll 1$. In the following, I report the results found by Dodin *et al.* in [51] and previously by Tscherbul *et al.* [26]. The following parameter is defined [51]:

$$\Delta_p \equiv \sqrt{\Delta^2 - (1 - p^2)\gamma_a\gamma_b}\,, \tag{1.140}$$

that can be interpreted as a generalized excited state splitting. Focusing on the case $p = +1$, the two main regimes are identified by the ratio $\Delta_p/\bar{\gamma} = \Delta/\bar{\gamma}$ [26, 51]:

(i) **Underdamped regime,** $\Delta_p/\bar{\gamma} \gg 1$: in presence of a large excited state splitting, the real and imaginary parts of the coherence ρ_{ab} oscillate at frequency Δ, as depicted in figure 1.2. These oscillations are damped by interactions with the incoherent field, through spontaneous and stimulated emission processes, and they reach zero on the time scale $\tau_{\text{coh}} \approx 1/\bar{\gamma}$ [26].

   When the V-system transitions from symmetrical ($\gamma_a = \gamma_b$) to asymmetrical ($\gamma_a/\gamma_b > 1$), distinct behaviors in the real and imaginary parts of the coherence can be observed. In particular, the real part decays more rapidly than the imaginary part, because the real part of the coherence couples to system's populations via the interference terms of the master equations. Once the faster decaying population (ρ_{aa}) reaches equilibrium, the real part of the coherence is suppressed. In contrast, the imaginary part, which is independent from the populations, persists until the slower decaying population (ρ_{bb}) also reaches equilibrium [51]. Furthermore, the oscillation amplitude of both Re$[\rho_{ab}]$ and Im$[\rho_{ab}]$ decreases as γ_a/γ_b increases. The ground state population ρ_{cc} is not reported in the graphs, since its behavior can be retrieved by applying the constraint $\rho_{cc} = 1 - \rho_{aa} - \rho_{bb}$.

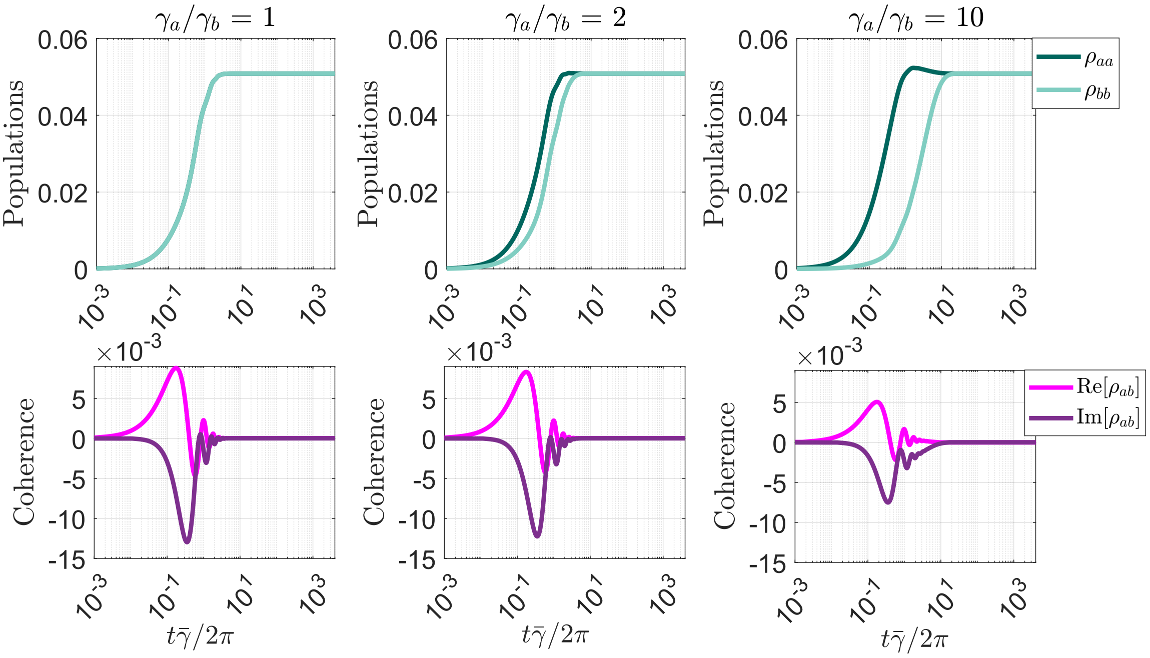

Figure 1.2: *Dimensionless time evolution of excited states populations and real and imaginary part of quantum coherence between levels $|a\rangle$ and $|b\rangle$. The radiation intensity is set to fulfill the weak pumping regime ($\bar{n} = 0.06$), with a large splitting between excited states ($\Delta/\bar{\gamma} = 10$). Different ratios of decay rates γ_a/γ_b are shown, with $p = 1$ in all panels of the figure.*

In figure 1.3 the parameter p is decreased to $p = 0.5$ to show its influence on the amplitude of coherence. The amplitude decreases as the absolute value of p decreases,

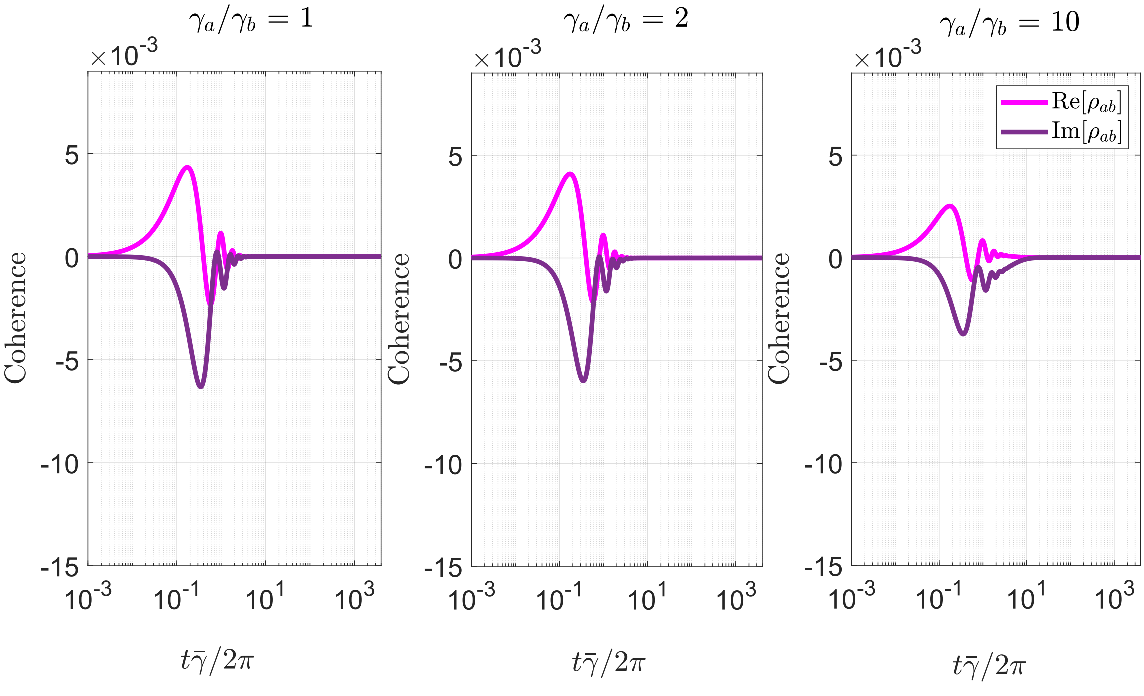

Figure 1.3: *Dimensionless time evolution of real and imaginary part of quantum coherence ρ_{ab} with $p = 0.5$. The radiation intensity is set to fulfill the weak pumping regime ($\bar{n} = 0.06$), with a large splitting between excited states ($\Delta/\bar{\gamma} = 10$).*

without affecting the overall time dynamics. Hence, parallel or anti-parallel transition dipole moments maximise the amplitude of Re$[\rho_{ab}]$, while the sign of p only affects the sign of imaginary and real parts.

(ii) **Overdamped regime, $\Delta_p/\bar{\gamma} \ll 1$:** assume now that the excited states are very close in frequency. In this regime, the real and imaginary parts of ρ_{ab} reach a quasi-stationary state as depicted in figure 1.4.

In this scenario, the time scale of coherence dynamics is given by $\tau_{\text{coh}} = 2\bar{\gamma}/\Delta_p^2$ [26, 51]. Thus, in the limit $\Delta_p \to 0$, the coherence lifetime approaches infinity . The condition $\Delta_p = 0$ is achieved with degenerate excited levels ($\Delta = 0$) and with parallel (or anti-parallel) transition dipoles moments ($p = \pm 1$). Under these conditions, noise-induced Fano coherence can become stationary, which is advantageous for possible attaining quantum heat engines or photocells [23, 33, 34], as well as its detection. Therefore, by tuning the splitting Δ, the coherence lifetime can be made in principle arbitrarily long.

The excited state populations evolve non-monotonically, showing a quasi-stationary state as well. As long as $t \leq \tau_{\text{coh}}$, the system evolves to a state that involves an in-phase coherent superposition between the excited energy eignestates [51]. During this period, the populations of the excited levels reach a first saturation level, which is lower than that of thermal equilibrium, as long as Re$[\rho_{ab}] \neq 0$. In this scenario, the real part of the

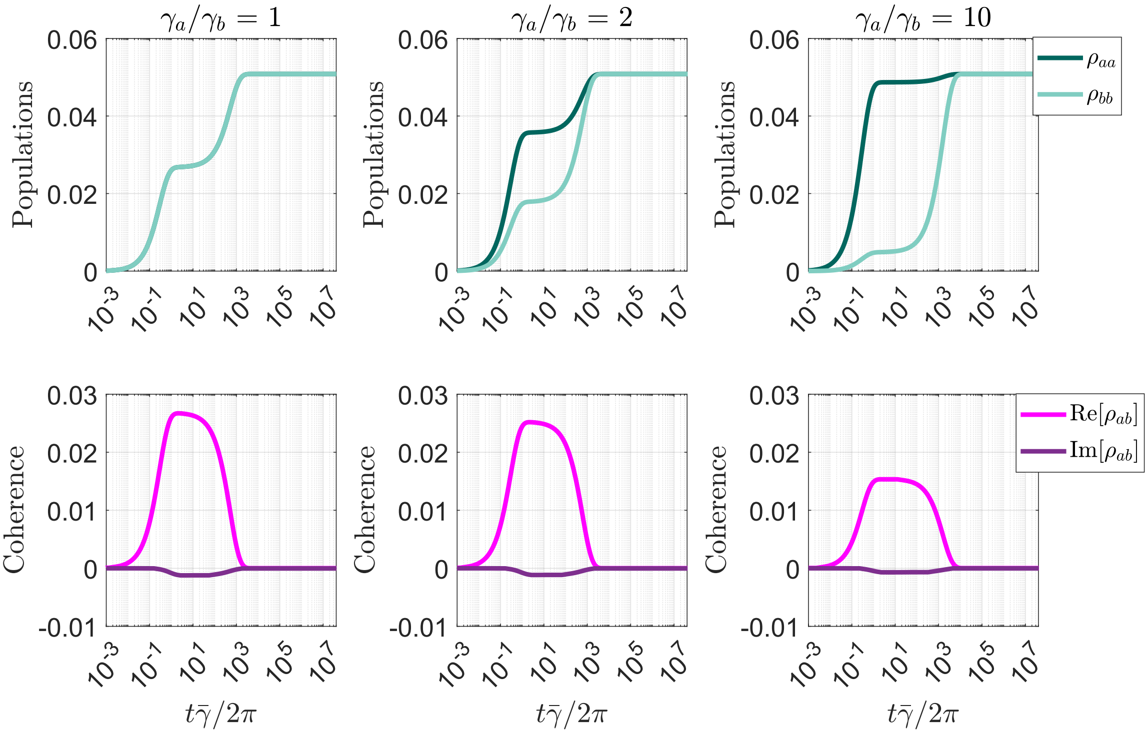

Figure 1.4: *Dimensionless time evolution of excited states populations as well as of real and imaginary part of quantum coherence between levels $|a\rangle$ and $|b\rangle$. The radiation intensity is set to fulfill the weak pumping regime ($\bar{n} = 0.06$), with a small splitting between excited states ($\Delta/\bar{\gamma} = 0.1$). Different ratios of decay rates γ_a/γ_b are shown, with $p = 1$ in all panels of the figure.*

coherence can be interpreted as a decay channel for populations. As time progresses and $\mathrm{Re}[\rho_{ab}]$ decays to zero, the in-phase coherent superposition component of the system state diminishes due to the population-coherence coupling term in equations (1.121). Eventually, the system reaches the equilibrium state predicted by Pauli rate-law equations, where the excited state populations attain a second saturation level, corresponding to the thermal equilibrium state, and $\mathrm{Re}[\rho_{ab}] = 0$.

As seen in the previous regime, also in the overdamped regime the asymmetry of the system leads to a decrease in the value of both the real and imaginary part of ρ_{ab}. On the other hand, increasing γ_a/γ_b results in longer dynamics for ρ_{ab}.

Figure 1.5 shows that if p is decreased to $p = 0.5$ the maximum value of $\mathrm{Re}[\rho_{ab}]$ reduces. More precisely, if $|p| < 1$, the quasi-stationary condition is lost. In this case, the lifetime of the coherence is no longer dependent from Δ, but is given by $\tau_{\mathrm{coh}} = 1/(1 - |p|)\bar{\gamma}$ [28]. Again, the sign of p, only affects the sign of imaginary and real parts.

For the detection of noise-induced Fano coherence, achieving a stationary or a quasi-stationary state with high coherence values is preferable to having an oscillating state. Therefore, the overdamped regime is the favourable condition. I show now that, using strong pumping, the overdamped regime can be easily achieved, as the requirement $\Delta_p/\bar{\gamma} \ll 1$ can be relaxed, thus allowing Δ to be much larger than $\bar{\gamma}$ without compromising quasi-stationarity.

The *strong-pumping regime*, where $\bar{n} \gg 1$, is particularly relevant in the context of quantum heat engines [33]. As clarified by Koyu *et al.* in [28], the condition $\bar{n} = r_l/\gamma_l \gg 1$, with $l = a, b$, does not violate the weak-coupling assumption, as long as $r_l \ll \omega_{ac}$, for all $l = a, b$, meaning the pumping rate is much smaller than the atomic transition frequency.

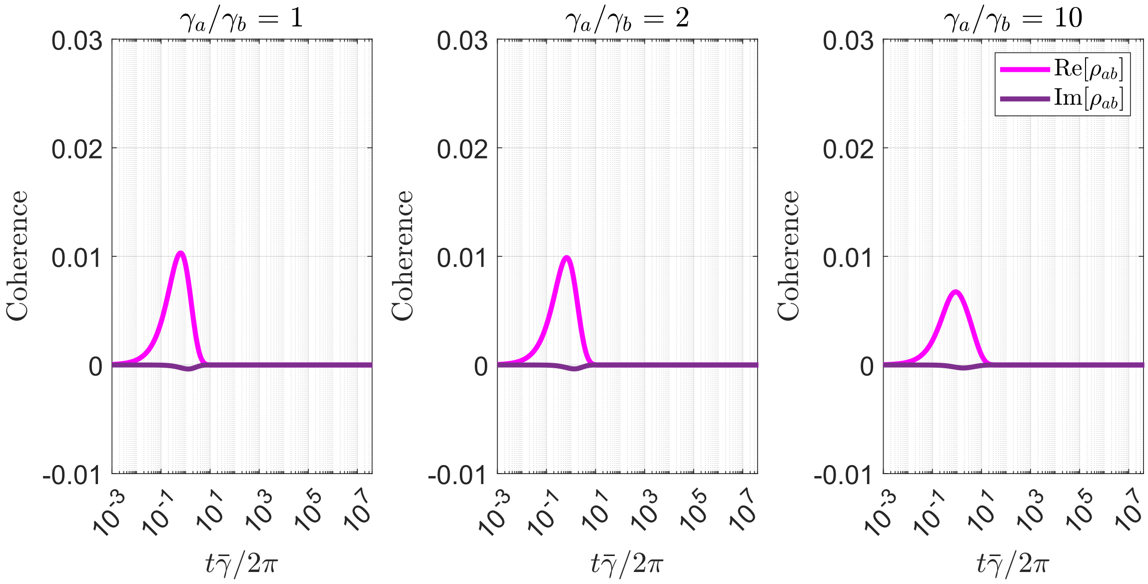

Figure 1.5: *Dimensionless time evolution of real and imaginary part of quantum coherence ρ_{ab} with $p = 0.5$. The radiation intensity is set to fulfill the weak pumping regime ($\bar{n} = 0.06$), with a small splitting between excited states ($\Delta/\bar{\gamma} = 0.1$).*

If ω_{ac} corresponds to an optical transition (thus, $\omega_{ac} \approx 100$ THz) and γ_l to an atomic linewidths (thus, $\gamma_l \approx 10$ MHz) then $\bar{n}$ can assume values up to $10^3 - 10^4$. Regarding Markovianity, it is mantained if the pumping rate r_l is smaller than the inverse of the reservoir correlation time τ_R. Typically, in the optical regime $\tau_R \approx 10$ fs, then $\bar{n} \leq 10^3 - 10^4$ is acceptable.

Below, I report the findings of Koyu *et al.* in [28], where they examine the interaction between a V-type three-level system and a strong intensity incoherent radiation. Differently from their work, I also provide cases of asymmetric V-type systems. The solutions can be classified again into two physical regimes: underdamped and overdamped regimes, depending on the ratio $\Delta/\bar{\gamma}$ and $\bar{n}$. As discussed in detail in [28], the underdamped regime is found if $\Delta/\bar{\gamma} > f(p)\bar{n}$, where $f(p)\bar{n}$ is a straight line whose slope depends solely on p, in the large $\Delta/\bar{\gamma}$ and $\bar{n}$ limit. The function $f(p)$ is derived in detail in [28]. Conversely, when $\Delta/\bar{\gamma} < f(p)\bar{n}$, the solutions to the differential equations are overdamped. I focus solely on this case, as it is the most interesting for experimental validation of the phenomenon.

(i) **Overdamped regime, $\Delta/\bar{\gamma} < f(p)\bar{n}$:** I set $\bar{n} = 100$, $\Delta/\bar{\gamma} = 0.1$ and $p = 1$. As depicted in figure 1.6, the quasi-stationarity for the real part of ρ_{ab} is obtained. The coherence lifetime is significantly longer with $\bar{n} \gg 1$ compared to the case with $\bar{n} \ll 1$ (see also figure 1.4). As demonstrated in [28], for $p = 1$, $\tau_{\text{coh}} = 1.34\,\bar{n}\bar{\gamma}/\Delta^2$. Hence, larger $\bar{n}$ implies longer-lived Fano coherence, as long as Δ remains small. Eventually, for $\Delta \to 0$ then $\tau_{\text{coh}} \to \infty$, thus achieving a stationary condition.

In figure 1.6, also the case of large state splitting, $\Delta/\bar{\gamma} = 10$ is shown, which in the weak-pumping regime corresponds to the underdamped scenario. As can be seen, with strong pumping, the configuration $\Delta/\bar{\gamma} = 10$ attains quasi-steady state for $\text{Re}[\rho_{ab}]$, while the imaginary part is approximately zero. By increasing the intensity $\bar{n}$, it is possible to relax the condition of small splittings Δ to achieve overdamped solutions. However, the larger Δ, the shorter τ_{coh}. The populations ρ_{aa}, ρ_{bb} behave in the same way when the system is symmetrical ($\gamma_a = \gamma_b$). In the case $\gamma_a = 2\,\gamma_b$, the two different values of Δ do not affect the population ρ_{aa}, so the solid and dashed lines overlap. In contrast, ρ_{bb} reaches steady state faster for larger values of Δ.

Setting $p = 0.5$ yields the results shown in figure 1.7. Similar to the case with $\bar{n} \ll 1$, the quasi-stationarity of $\text{Re}[\rho_{ab}]$ is lost. As explained in [28], when $|p| < 1$, e.g. $p = 0.5$, the coherence life-time deacreases as $\bar{n}$ increases. Moreover, $\text{Re}[\rho_{ab}], \text{Im}[\rho_{ab}]$ become insensitive to $\Delta/\bar{\gamma}$. For this reason, in the panels of figure 1.7, exclusively the behaviors with different values of $\bar{n}$ are compared.

To conclude this subsection, I compare τ_{coh} in the weak and strong pumping conditions. For $p = 1$, their ratio is equal to [28]:

$$\frac{\tau_{\text{coh}}\big|_{\bar{n}\gg 1}}{\tau_{\text{coh}}\big|_{\bar{n}\ll 1}} = \frac{1.34\,\bar{n}\bar{\gamma}/\Delta^2}{2\bar{\gamma}/\Delta^2} = 0.67\bar{n} \approx \frac{2}{3}\bar{n}. \tag{1.141}$$

Hence, for $\bar{n} > 3/2$ there is an enhancement of τ_{coh} that may facilitate the experimental observation of noise-induced coherence.

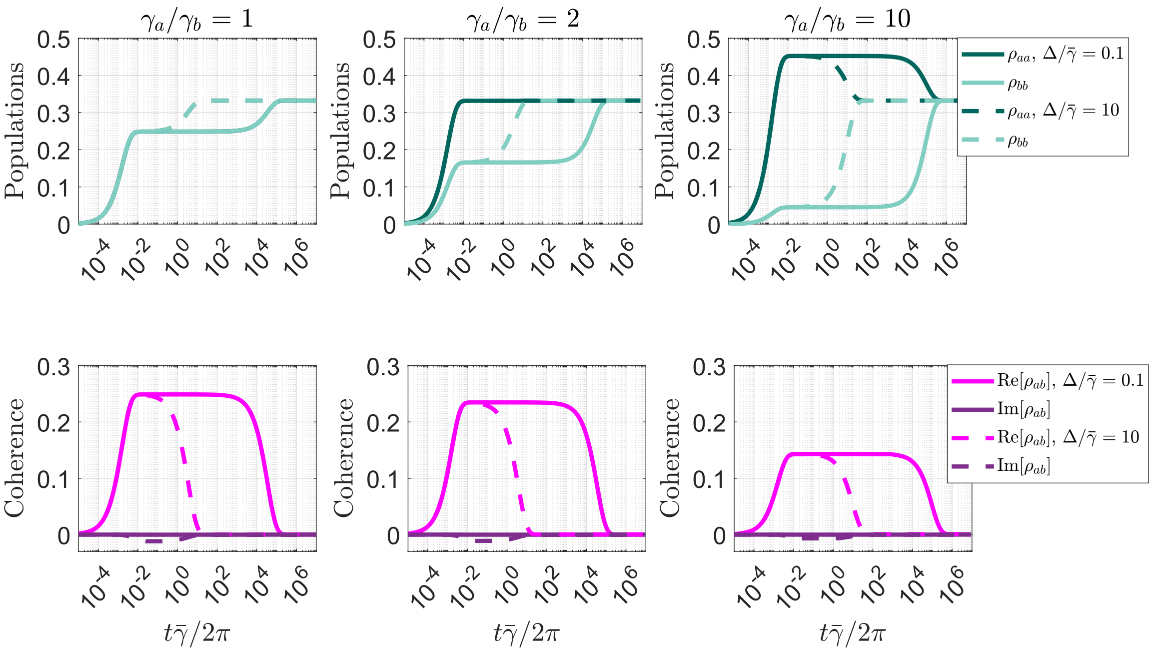

Figure 1.6: *Dimensionless time evolution of excited states populations and real and imaginary part of quantum coherence between levels* $|a\rangle$ *and* $|b\rangle$*. The radiation intensity is set to fulfill the strong pumping regime* ($\bar{n} = 100$)*, with small* ($\Delta/\bar{\gamma} = 0.1$*, solid lines) and large splitting* ($\Delta/\bar{\gamma} = 10$*, dashed lines) between excited levels. Different ratios of decay rates* γ_a/γ_b *are shown, with* $p = 1$ *in all panels of the figure.*

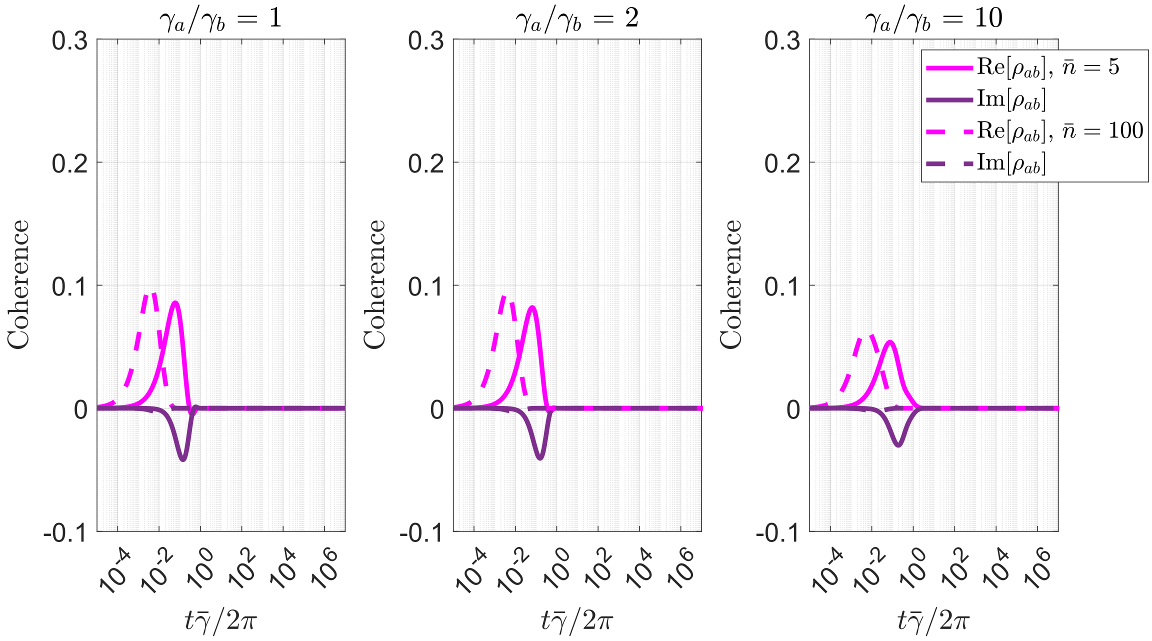

Figure 1.7: *Dimensionless time evolution of real and imaginary part of quantum coherence* ρ_{ab}*, with* $p = 0.5$*. The radiation intensity is set to fulfill the strong pumping regime* ($\bar{n} = 5$*, solid lines and* $\bar{n} = 100$*, dashed lines), with* $\Delta/\bar{\gamma} = 10$*.*

1.4.2 Dynamical regimes with anisotropic polarized radiation

In Subsection 1.3.3 I focused on deriving the differential equations for anisotropic and polarized radiation. This type of incoherent radiation source can be beneficial in a V-type three-level system with orthogonal transition dipole moments. In such a system, no interference effects occur with an isotropic and unpolarized source, as p would be zero for all radiative processes. However, using polarized radiation can allow for interference during the absorption and stimulated processes. On the other hand, if the transition dipole moments are orthogonal, no Fano interference is present during spontaneous emission, which involves the interaction between the system and the isotropic modes of the vacuum.

I consider the case already introduced in Subsection 1.3.3, where the V-system comprises $\Delta m_F = \pm 1$ atomic transitions. The transition dipole moments are $\boldsymbol{\mu}_{ac} = |\boldsymbol{\mu}_{ac}|\boldsymbol{\mu}_-$ and $\boldsymbol{\mu}_{bc} = |\boldsymbol{\mu}_{bc}|\boldsymbol{\mu}_+$, with $\boldsymbol{\mu}_+$, $\boldsymbol{\mu}_-$ being the unitary vectors expressed in equations (1.124) and (1.125), respectively. The polarization of the radiation is set linear and along the x-axis: $\boldsymbol{\epsilon}_{\mathbf{k},\lambda} = \boldsymbol{\epsilon}_x$. I analyze the dynamical behaviour of populations and coherence ρ_{ab} by numerically solving equations (1.134) and (1.135), after reformulating them in the Liouville representation, similarly to the isotropic and unpolarized case. Again, the reduced density operator $\hat{\rho}_S$ is expressed as the state vector in equation (1.136). The "coherent" term $\hat{\mathcal{L}}_H$ of Liouville super-operator is the same of the one reported in equation (1.137). However, the "dissipative" term changes, due to the interaction with polarized radiation and the vacuum. Again, the term $\hat{\mathcal{L}}_{\mathcal{D}}$ can be further divided into the three contributions $\hat{\mathcal{L}}_{\mathcal{D}_1}$, $\hat{\mathcal{L}}_{\mathcal{D}_2}$ and $\hat{\mathcal{L}}_{\mathcal{D}_12}$, as previously done in Subsection 1.4.1. I numerically solve equation (1.138) via exponentiation with initial condition $\rho_{cc}(0) = 1$.

First, both underdamped and overdamped regimes under the weak-pumping condition are analyzed. Differently from the case with isotropic and unpolarized radiation, when $\bar{n} \ll 1$, the underdamped and overdamped regimes are identified not by the ratio $\Delta_p/\bar{\gamma}$, but simply by the ratio $\Delta/\bar{\gamma}$. Indeed, in the context of polarized radiation, the alignment parameter p can no longer influence the coupling between radiation and the discrete system, being replaced by the scalar product $\boldsymbol{\mu}_{lc} \cdot \boldsymbol{\epsilon}_\lambda$, as derived in Subsection 1.3.3. In this case, the p parameter can only influence the isotropic process of spontaneous emission. However, if the transitions involved possess orthogonal dipole vectors, $p = 0$ and thus the alignment parameter has no impact on the dynamics. The results I show below are based on works by Dodin *et al.* in [29] and by Koyu *et al.* in [30].

(i) **Underdamped regime,** $\Delta/\bar{\gamma} \gg 1$: as already seen with unpolarized and isotropic light, in the large excited levels splitting scenario, the real and imaginary parts of the coherence ρ_{ab} oscillate at frequency Δ, as depicted in figure 1.8. They eventually reaches the stationary state on the time scale $\tau_{\text{coh}} \approx 1/\bar{\gamma}$. Surprisingly, both $\text{Re}[\rho_{ab}]$ and $\text{Im}[\rho_{ab}]$ exhibit a nonzero stationary value, indicating that Fano coherence does not decay to zero over time under the influence of polarized incoherent light. Albeit counterintuitive, this result does not contradict thermodynamic principles, since the driving of the system with polarized light can be viewed as an interaction with two distinct reservoirs [29]: one at high-temperature, represented by polarized field modes, coupling to both atomic transitions, and the other as a cold reservoir, consisting of isotropic vacuum modes responsible for dissipation. These interactions keep the system out of equilibrium, thus enabling stationary coherences to persist.

Koyu *et al.* [30] explain this behavior differently. They illustrate that the polarized incoherent radiation creates an in-phase superposition of energy eigenstates. This

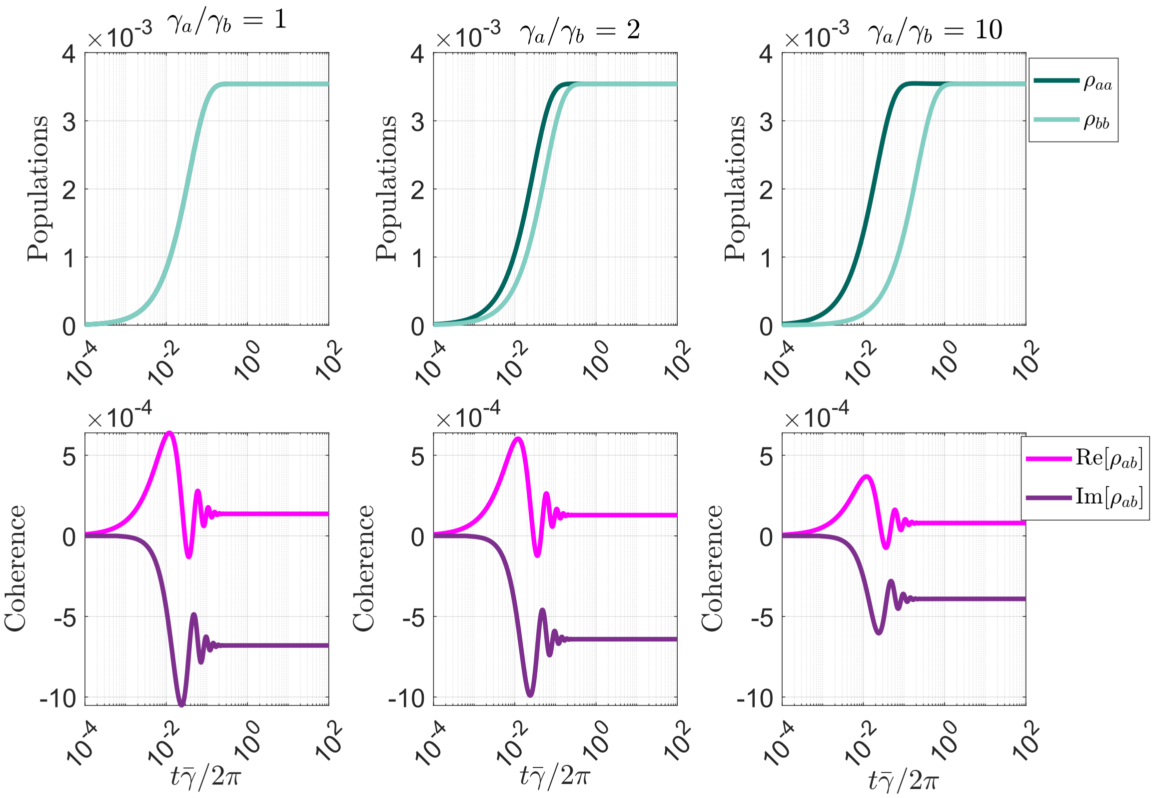

Figure 1.8: *Dimensionless time evolution of excited states populations and real and imaginary part of quantum coherence between levels $|a\rangle$ and $|b\rangle$. The radiation intensity is set to fulfill the weak pumping regime ($\bar{n} = 0.06$), with a large splitting between excited states ($\Delta/\bar{\gamma} = 10$). The polarization of the radiation is linear and along the x-axis. Different ratios of decay rates γ_a/γ_b are shown.*

excitation evolves gaining a periodic relative phase over time. The continuous action of the incoherent source generates new excitations at every moment, each starting in-phase but evolving with different phases as generated at different times. Summing together all these phases results in an ensemble dephasing, where different phases from various excitations average out to *nearly* zero.

Compared to the case with isotropic radiation, it can be observed a significant reduction in the values of coherence and populations, approximately by one order of magnitude. This reduction is attributable to the fact that the anisotropic pumping rate is smaller by a factor of $16\pi/3$ compared to the isotropic one, as discussed in Subsection 1.3.3, while the rates of spontaneous emission remain the same. Despite the difference in the pumping rate r, the system's behavior with different ratios of decay rates remains consistent with the scenario where $\Delta \gg \bar{\gamma}$. Additionally, the populations dynamics in this regime can be accurately described using the secular (no interference) approximation.

(ii) **Overdamped regime,** $\Delta/\bar{\gamma} \ll 1$: in the regime with a small splitting Δ between the excited energy levels, both the real and imaginary parts of ρ_{ab} reach a nonzero stationary state, as depicted in figure 1.9. This behavior contrasts with the isotropic case, where Fano coherence persists in the long-time limit only when $\Delta = 0$ (degenerate configuration).

Moreover, figure 1.9 indicates that Re$[\rho_{ab}]$ is of the same order of magnitude as the excited populations, differently from the scenario where $\Delta/\bar{\gamma} \gg 1$. However, the maximum values of both populations and coherence are smaller than those shown in figure 1.4, due to the reduced anisotropic pumping rate, $r^{pol} = \frac{3}{16\pi} r^{iso}$. As in the case of large Δ, the population dynamics here can be described by the Pauli rate-law equations, differently from the isotropic scenario.

Under polarized radiation in the strong-pumping condition, there is no clear identification of the regimes based on the parameters. Instead, I distinguish between the regimes by observing the numerical solutions: non-oscillatory solutions indicate the overdamped regime. I focus on this type of dynamics.

(i) **Overdamped regime:** I set $\bar{n} = 100$, $\Delta/\bar{\gamma} = 0.1$. As depicted in figure 1.10, higher values for the stationary state of Re$[\rho_{ab}]$ are obtained, suggesting that the signal for a proof-of-principle experiment could be enhanced by increasing $\bar{n}$, i.e. the intensity of the radiation source.

Figure 1.10 also shows the scenario of large state splitting, $\Delta/\bar{\gamma} = 10$, which corresponds to the underdamped regime in the weak-pumping condition. Interestingly,

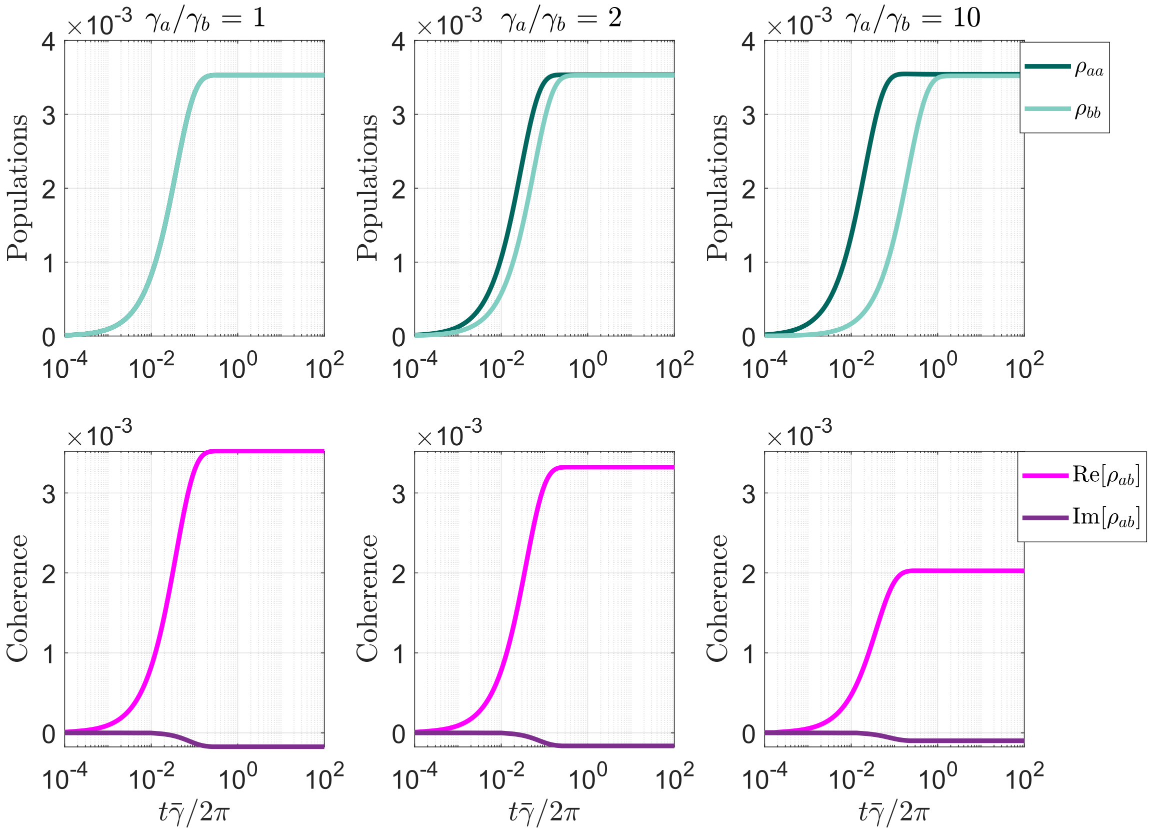

Figure 1.9: *Dimensionless time evolution of excited states populations and real and imaginary part of quantum coherence between levels $|a\rangle$ and $|b\rangle$. The radiation intensity is set to fulfill the weak pumping regime ($\bar{n} = 0.06$), with a small splitting between excited states ($\Delta/\bar{\gamma} = 0.1$). The polarization of the radiation is linear and along the x-axis. Different ratios of decay rates γ_a/γ_b are shown.*

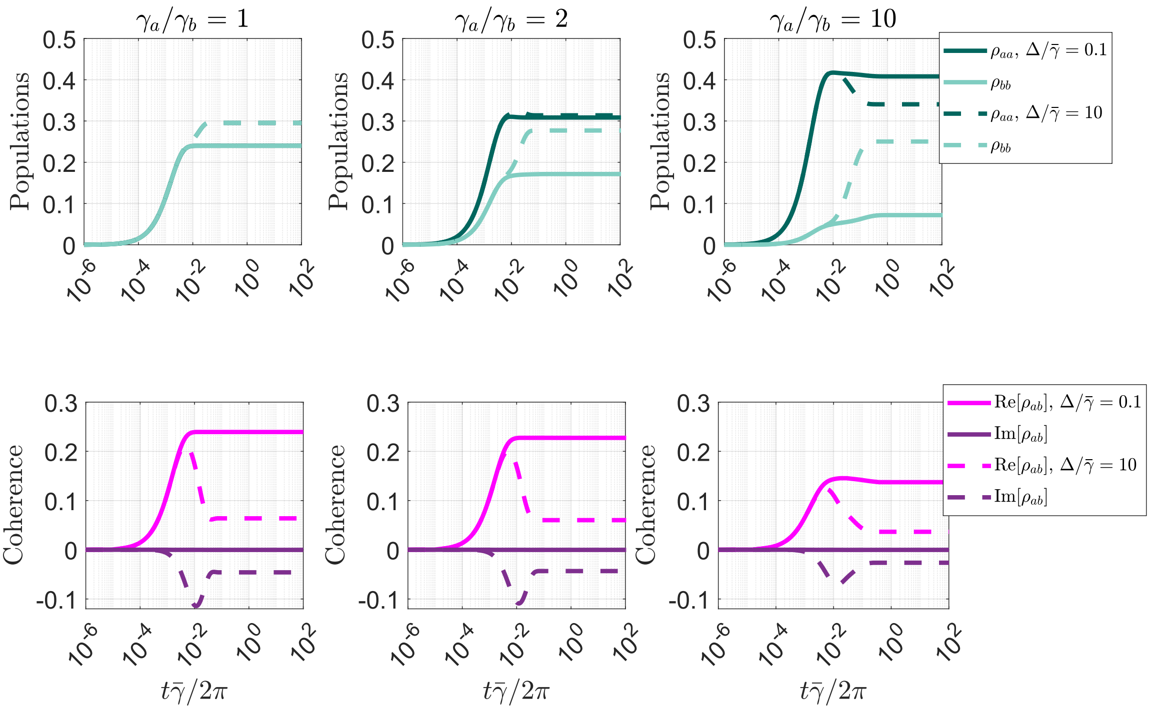

Figure 1.10: *Dimensionless time evolution of excited states populations and real and imaginary part of quantum coherence between levels $|a\rangle$ and $|b\rangle$. The radiation intensity is set to fulfill the strong pumping regime ($\bar{n} = 100$), with small ($\Delta/\bar{\gamma} = 0.1$, solid lines) and large splitting ($\Delta/\bar{\gamma} = 10$, dashed lines) between excited levels. The polarization of the radiation is linear and along the x-axis. Different ratios of decay rates γ_a/γ_b are shown.*

> even in this case, a nonzero stationary state for Re[ρ_{ab}] can be observed, whose value, however, is smaller than the maximum value reached during the time evolution.
>
> Hence, it is possible to observe again that with $\bar{n} \gg 1$ the condition of small splitting Δ to achieve overdamped solutions can be relaxed. However, increasing Δ results in lower stationary values of the real part of Fano coherence [30]. The latter can be enhanced by increasing $\bar{n}$ as shown in figure 1.11. The figure illustrates the impact of $\bar{n}$ and $\Delta/\bar{\gamma}$ on the stationary value of Re[ρ_{ab}], comparing symmetric ($\gamma_a/\gamma_b = 1$) and strongly asymmetric V-type systems ($\gamma_a/\gamma_b = 10$). For the optimal detection of Fano coherence, it is beneficial to tune the splitting Δ around small values, where the coherence is high. Moreover, it is advantageous to implement a symmetric system rather than an asymmetric one.

It is important to clarify that the solutions presented in this and the previous Subsection are based on the assumption of an instantaneous activation of the interaction between the system and incoherent radiation. Dodin *et al* in [52] discuss time-dependent incoherent radiation, showing that if the turn-on time exceeds the system's fastest characteristic time scale τ_S, the magnitude of induced Fano coherence can significantly decrease. However, in atomic systems excited by a broadband laser, as the one described later for coherence detection, sufficiently rapid activation of the source can be achieved using acousto-optic modulators. Therefore, the result of these simulations remain relevant in our context.

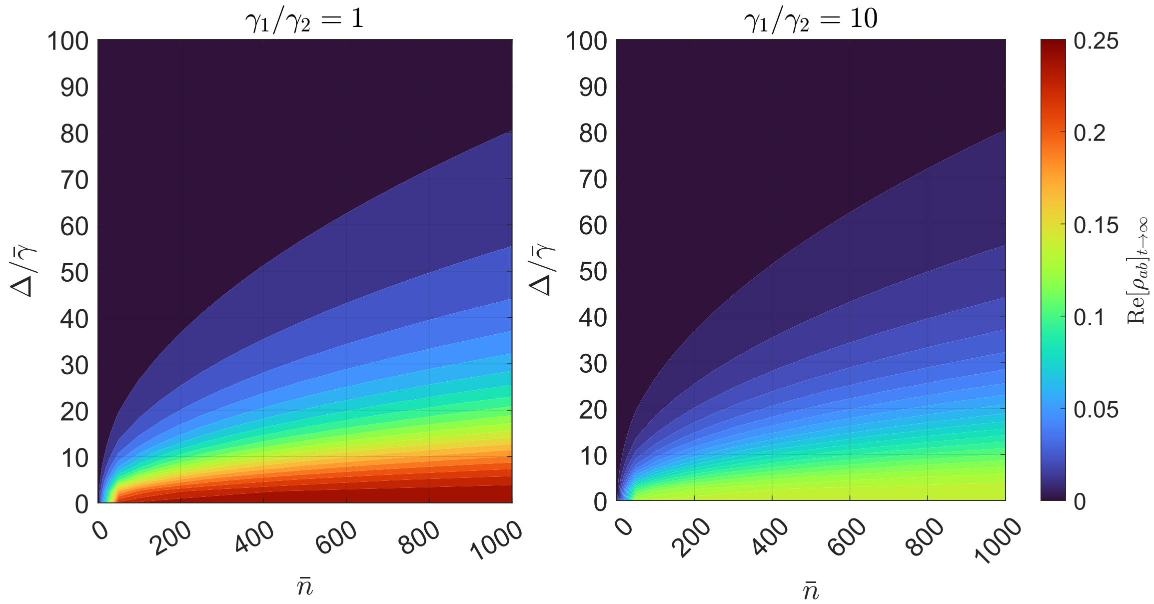

Figure 1.11: *Stationary value of* $\mathrm{Re}[\rho_{ab}]$ *as a function of* $\bar{n}$ *and* $\Delta/\bar{\gamma}$ *with linearly polarized light along the x-axis. Comparison between symmetric* ($\gamma_a/\gamma_b = 1$) *and asymmetric* ($\gamma_a/\gamma_b = 10$) *V-type three-level system is shown.*

In Chapter 3 I present simulations specific to the atomic system used in the experiment, evaluating the effects of a time-dependent field due to the rapid switching of acousto-optic modulators.

2 | Energetics and quantumness of noise -induced Fano coherences

In the previous chapter, I examined how Fano interference can emerge from the interaction between a discrete multi-level system and the continuum of modes characterizing a non-coherent source. This interaction leads to the formation of quasi-stationary or stationary states for the Fano coherence between the excited levels. Thermodynamically, the generation of Fano coherence results in a non-negligible amount of excess energy in the V-type system, characterized by a residual energy in comparison with the initial state of the system at the beginning of the transformation. Given their origin, it is natural to ask ourselves whether noise-induced Fano coherences exhibit distinct non-classical traits. To address this aspect, it is necessary to employ specific tools that adequately capture the quantum features of the system and the process under investigation.

Consider to measure a quantum system with respect to two observables that commute, meaning they can be measured simultaneously. In classical physics, measurement outcomes are considered to reflect the inherent properties of a system and are independent of any additional observables that may be measured simultaneously. This concept is referred to as *non-contextuality* [60]. However, in quantum mechanics, the outcome of a measurement can depend on other measurements performed simultaneously, even if these measurements do not disturb the system. This dependence is termed *contextuality*. Contextuality implies that the value of an observable does not exist independently of the measurement context, challenging the classical notion of objective reality. More formally, the measurement result of a quantum observable is dependent upon which other observables, even commuting, are within the same measurement set. Non-classical features of a system can be identified by the presence of contextuality, where the incompatibility of physical observables reveals the quantum nature of the system [61].

In quantum mechanics, it is possible to use a probability-like framework to represent quantum states in phase space. The *Wigner distribution* is a widely known tool for this task. Introduced by Eugene Wigner in 1932, the Wigner function is defined for position and momentum and allows for the calculation of quantum mechanical averages similarly to classical probability distributions, but with the significant difference that it can take on negative values, highlighting the non-classical nature of quantum states [62, 63]. A probability that can assume negative and/or non-real values is defined as a *quasiprobability*.

The Wigner distribution is not the only quasiprobability distribution used in quantum mechanics. Indeed, generalizing the Wigner function to multi-time statistics for multi-level systems or in cases where the position and momentum do not have proper analogs, the *Kirkwood-Dirac quasiprobability (KDQ) distribution* can be used [64, 65]. Originally formulated by John G. Kirkwood in 1933 and further extended by Paul A. M. Dirac, this distribution provides insights into the joint properties of outcomes pairs from non-commuting observables, resulting also in this case to non-real values [66, 67].

In the physical scenario addressed in the thesis, I employ the KDQ distribution of the stochastic energy changes to identify contextuality in the generation of noise-induced Fano coherences, as well as excess energy that could be further exploited as work by an external load. This is achieved by examining the loss of positivity in the KDQ distribution, indicated by the presence of negative real parts or non-zero imaginary parts [68, 69]. KD quasiprobabilities are evaluated at the initial and final times of the transformation under scrutiny leading to the emergence of Fano coherences. This approach allows to demonstrate that, despite their origin from interaction with an incoherent source, these coherences are linked with intrinsic quantum traits.

Throughout this chapter, I explore how KD quasiprobabilities can be applied to analyze the coherence properties in the system under scrutiny. Section 2.1 covers the mathematical formulation of these quasiprobabilities. Moreover, I discuss how KDQ helps to understand energy fluctuations in systems interacting with the environment and their role in defining thermodynamic quantities, as work distribution. In Section 2.2 I analyze the energetics of the case study, i.e. the interaction of the V-type three-level system with an unpolarized, isotropic incoherent radiation source, by proving the quantum nature of noise-induced Fano coherence. I also explore the potential of the process generating Fano coherences for energy conversion purposes. In particular, I present numerical simulations to optimize both the initial quantum state of the three-level system (before interaction with the light source) and the parameters of the system, including the coupling strength with the light field, to enhance the non-positivity of certain quasiprobabilities. Enhancing negativity yields thermodynamic benefits, as quantum coherence results in a greater extractable work [36–38].

2.1 Non-equilibrium quantum thermodynamics in a finite - dimensional system

Quantum thermodynamics is a rapidly growing field that seeks to generalize classical thermodynamics and non-equilibrium statistical physics to small-scale systems that operate far from equilibrium, incorporating quantum mechanical principles [70, 71]. This field offers a comprehensive framework for examining energy dynamics and coherence properties in quantum systems, such as V-type three-level systems.

In this section, I introduce the fundamental physical quantities of quantum thermodynamics, which set the stage for the discussion of Kirkwood-Dirac quasiprobabilities and their significance.

2.1.1 Energy and heat exchange in closed and open quantum systems

Quantum thermodynamics, similarly to classical thermodynamics, focuses on energy and its transformations, distinguishing between *heat* Q and *work* W. In quantum system, random energy fluctuations become more pronounced compared to macroscopic systems, where average quantities dominate. The field of statistical physics at the microscopic scale is essential for understanding this random behavior, as it characterizes the statistical properties of these fluctuations and associates probability distributions to them [72].

Consider a closed quantum system initially in the state $\hat{\rho}_S(0)$ that evolves into the state $\hat{\rho}_S(t)$ over a time interval t. The Hamiltonian for the system at time t is denoted by $\hat{H}_S(t)$. The average internal energy of the system at time t is expressed as:

$$\langle \mathrm{E_S}(t) \rangle \equiv \mathrm{Tr}\left(\hat{\rho}_S(t)\hat{H}_S(t)\right). \tag{2.1}$$

Thus, from equation (2.1) the average change in energy $\langle \Delta \mathrm{E_S}(t) \rangle$ over the time interval $[0, t]$ is:

$$\langle \Delta \mathrm{E_S}(t) \rangle = \mathrm{Tr}\left(\hat{\rho}_S(t)\hat{H}_S(t)\right) - \mathrm{Tr}\left(\hat{\rho}_S(0)\hat{H}_S(0)\right). \tag{2.2}$$

As observed, the internal energy difference depends solely on the initial and final states of the system. Therefore, internal energy is a state function, meaning it is independent of the specific thermodynamic process performed on the system.

Energy changes within the system arise from two distinct processes: heat and work. Heat pertains to changes in the system's density operator due to the interactions with the environment [70, 73]. Heat is quantified by the expression:

$$\langle Q(t) \rangle \equiv \int_0^t \mathrm{Tr}\left(\frac{d\hat{\rho}_S(t')}{dt}\hat{H}_S(t')\right) dt'. \tag{2.3}$$

Conversely, work is associated with the time variation of the Hamiltonian, and it is defined as:

$$\langle W(t) \rangle \equiv \int_0^t \mathrm{Tr}\left(\hat{\rho}_S(t')\frac{d\hat{H}_S(t')}{dt}\right) dt'. \tag{2.4}$$

The convention on the sign follows the familiar principles of classical thermodynamics: if $\langle W \rangle < 0$, work is extracted from the system. On the contrary, $\langle W \rangle > 0$, work is done on the system by the environment. For heat transfer, $\langle Q \rangle < 0$ indicates heat dissipation to the environment, while $\langle Q \rangle > 0$ represents heat absorbed by the system. It is crucial to stress that work and heat are path-dependent quantities, unlike state functions as internal energy. This means that they depends on the specific process or path taken by the system during the thermodynamic transformation.

The sum of average heat and work, defined by equations (2.3) and (2.4) respectively, yields:

$$\begin{aligned}\langle Q(t)\rangle + \langle W(t)\rangle &= \int_0^t \left[\mathrm{Tr}\left(\frac{d\hat{\rho}_S(t')}{dt'}\hat{H}_S(t')\right) + \mathrm{Tr}\left(\hat{\rho}_S(t')\frac{d\hat{H}_S(t')}{dt'}\right)\right] dt = \\ &= \int_0^t \frac{d}{dt}\mathrm{Tr}\left(\hat{\rho}_S(t')\hat{H}_S(t')\right) dt' = \mathrm{Tr}\left(\hat{\rho}_S(t)\hat{H}_S(t)\right) - \mathrm{Tr}\left(\hat{\rho}_S(0)\hat{H}_S(0)\right) = \\ &= \langle \Delta \mathrm{E}_{\mathrm{S}}(t)\rangle.\end{aligned} \tag{2.5}$$

Equation 2.5 represents the *first law of thermodynamics*, which states that the sum of the average heat and work transfer equals the average energy change in the system. As highlighted in [70], since heat and work are process-dependent quantities, no observables are associated to them, differently the average energy change that depends only on the initial and final states. It is thus possible to associate an observable to the average energy change. Hence, the latter can be represented by an Hermitian operator while the former can not.

The exchange of heat and work in thermodynamic processes can be either reversible or irreversible, depending on the physical quantity, ascribable as *entropy* S. For a process P involving the system and its environment, the change in the system's entropy follows the inequality:

$$\Delta S \geq \int_P \frac{\langle \delta Q\rangle}{T}, \tag{2.6}$$

where $\Delta S = S(\hat{\rho}_S(t)) - S(\hat{\rho}_S(0))$. If the system is in thermal equilibrium state at temperature T, i.e. $\hat{\rho}_S = \hat{\rho}_{S,\mathrm{th}} = e^{-\beta \hat{H}_S}/\mathrm{Tr}\left(e^{-\beta\hat{H}_S}\right)$, where $\beta = 1/k_B T$, and $\hat{H}_S$ is the Hamiltonian of the system, then the thermodynamic entropy $S(\hat{\rho}_S(t))$ equals the *Shannon* or *information theory entropy* times the Boltzmann constant k_B, i.e.:

$$S(\hat{\rho}_S(t)) \equiv k_B \mathrm{Tr}(\hat{\rho}_{S,\mathrm{th}} \log \hat{\rho}_{S,\mathrm{th}}), \tag{2.7}$$

The above definition is valid provided the interaction between the system and the environment is weak [70]. Moreover, in equation (2.6), $\langle \delta Q\rangle$ represents the infinitesimal amount of heat exchanged during the process P, and T denotes the temperature at which this heat exchange occurs. Equation (2.6) is known as the *Clausius inequality*, and it embodies the *second law of thermodynamics* for all processes. In the context of non-equilibrium thermodynamics, a process is considered irreversible if it satisfies the inequality. Conversely, a process is defined reversible if the change in entropy precisely equals to:

$$\Delta S = \int_{\mathrm{reversible}} \frac{\langle \delta Q\rangle}{T}. \tag{2.8}$$

The thermodynamic quantities discussed so far arise from fluctuations in the internal energy of a closed quantum system with a potentially time-dependent Hamiltonian. Heat and work are derived from the evolution of the system's density operator and Hamiltonian, respectively. For the case of a closed quantum system, as outlined in Subsection 1.2.1, the dynamics of the system is governed by the Schrödinger-Von Neumann equation, as expressed in equation (1.38). Using the first law of thermodynamics, expressed in equation (2.5), and applying the Schrödinger-Von Neumann equation yields:

$$\begin{aligned}\langle \Delta \mathrm{E}_S(t)\rangle &= \int_0^t \mathrm{Tr}\left(\frac{d\hat{\rho}_S(t')}{dt'}\hat{H}_S(t')\right) dt' + \int_0^t \mathrm{Tr}\left(\hat{\rho}_S(t')\frac{d\hat{H}_S(t')}{dt'}\right) dt' = \\ &= -\frac{i}{\hbar}\int_0^t \mathrm{Tr}\left(\left[\hat{H}_S(t'),\hat{\rho}_S(t')\right]\hat{H}_S(t')\right) dt' + \int_0^t \mathrm{Tr}\left(\hat{\rho}_S(t')\frac{d\hat{H}_S(t')}{dt'}\right) dt' = \\ &= \int_0^t \mathrm{Tr}\left(\hat{\rho}_S(t')\frac{d\hat{H}_S(t')}{dt'}\right) dt' = \langle W(t)\rangle\,. \end{aligned} \tag{2.9}$$

Indeed,

$$\mathrm{Tr}\left(\left[\hat{H}_S(t),\hat{\rho}_S(t)\right]\hat{H}_S(t)\right) = \mathrm{Tr}\left(\hat{H}^2_S(t)\hat{\rho}_S(t)\right) - \mathrm{Tr}\left(\hat{H}^2_S(t)\hat{\rho}_S(t)\right) = 0. \tag{2.10}$$

This result follows from the linearity and cyclic properties of the trace: $\mathrm{Tr}\,(A \pm B) = \mathrm{Tr}\,(A) \pm \mathrm{Tr}\,(B)$ and $\mathrm{Tr}\,(AB) = \mathrm{Tr}\,(BA)$. As demonstrated by Alicki, this shows that coherent excitation produces work, and in a closed quantum system, there is no heat exchange [70, 71, 73].

Consider the case of an open quantum system, whose dynamics are governed by a Lindblad-type quantum master equation, which ensures the positivity and trace preservation of the system's density operator:

$$\frac{d\hat{\rho}_S(t)}{dt} = -\frac{i}{\hbar}[\hat{H}_S,\hat{\rho}_S(t)] + \hat{\mathcal{L}}[\hat{\rho}_S(t)]. \tag{2.11}$$

Here, the Lindblad superoperator $\hat{\mathcal{L}}$ is given by:

$$\hat{\mathcal{L}}[\hat{\rho}_S(t)] = \sum_{\omega,i}\left(\hat{L}_i(\omega)\hat{\rho}_S(t)\hat{L}_i^\dagger(\omega) - \frac{1}{2}\left\{\hat{L}_i^\dagger(\omega)\hat{L}_i(\omega),\hat{\rho}_S(t)\right\}\right). \tag{2.12}$$

By following the same procedure as in equation (2.9), I obtain:

$$\begin{aligned}\langle \Delta \mathrm{E}_S(t)\rangle &= \int_0^t \mathrm{Tr}\left(\frac{d\hat{\rho}_S(t')}{dt'}\hat{H}_S(t')\right) dt' + \int_0^t \mathrm{Tr}\left(\hat{\rho}_S(t')\frac{d\hat{H}_S(t')}{dt'}\right) dt' = \\ &= -\frac{i}{\hbar}\int_0^t \mathrm{Tr}\left(\left[\hat{H}_S(t'),\hat{\rho}_S(t')\right]\hat{H}_S(t')\right) dt' + \int_0^t \mathrm{Tr}\left(\hat{\mathcal{L}}(\hat{\rho}_S(t'))\hat{H}_S(t')\right) dt' + \\ &+ \int_0^t \mathrm{Tr}\left(\hat{\rho}_S(t')\frac{d\hat{H}_S(t')}{dt'}\right) dt' = \int_0^t \mathrm{Tr}\left(\hat{\mathcal{L}}(\hat{\rho}_S(t'))\hat{H}_S(t')\right) dt' + \\ &+ \int_0^t \mathrm{Tr}\left(\hat{\rho}_S(t')\frac{d\hat{H}_S(t')}{dt'}\right) dt' = \langle Q(t)\rangle + \langle W(t)\rangle\,. \end{aligned} \tag{2.13}$$

The Lindblad terms, represented by the operator $\hat{\mathcal{L}}$, are associated with the net heat provided by the environment [71, 73].

I emphasize again that work and heat are path-dependent quantities and for this reason they are not associated in general with single-time events. In classical physics, this is addressed by tracking the system's state over time, defined by its position and momentum, forming its trajectory in phase space. These trajectories delineate how energy is exchanged as work or heat throughout a process [71]. In microscopic systems, the scenario is more intricate due to fluctuations of thermodynamic quantities, leading to a statistical distribution of values. In quantum mechanics, one approach to evaluate work and heat involves constructing a quantum trajectory through two *projective measurements* at different times. A projective measurement of an observable, represented by an Hermitian operator, extracts an outcome corresponding to one of the observable's eigenvalues and causes the collapse of the system's wave function to the corresponding eigenstate. This approach is commonly known as the *Two-Point Measurement (TPM) scheme.* However, these measurements affect the statistics of the observables, evaluated at previous times. Thus, the challenge lies in developing a stochastic framework for quantum processes that accurately reflects these fluctuations while considering the effects of quantum measurements and coherence, even in case of non-commuting observables at different times [37, 71, 72, 74].

In the next section I briefly describe the TPM scheme and its limitations, paving the way for the introduction of KD quasiprobabilities to describe work and heat distributions.

2.1.2 Two-Point Measurement scheme and no-go theorem

As discussed in the previous subsection, work and heat in quantum systems can not be represented by Hermitian operators, meaning there are no observables that can be directly measured through a single projective measurement [72, 75].

The established method for estimating these thermodynamic quantities in the quantum regime is the *Two-Point Measurement (TPM) scheme.* The TPM protocol involves measuring the system's internal energy at two distinct times during the thermodynamic process, typically at the initial and final times. In doing so, it generates a stochastic sequence of outcomes, from which the corresponding thermodynamic quantities can be derived [37, 71, 72, 75–79].

Consider a closed quantum system in the initial state $\hat{\rho}_S(0)$ and with a time-dependent Hamiltonian. At $t = 0$, the Hamiltonian is given by:

$$\hat{H}_S(0) = \sum_j \mathrm{E}_j(0)|\mathrm{E}_j(0)\rangle\langle \mathrm{E}_j(0)| = \sum_j \mathrm{E}_j(0)\hat{\Pi}_j(0), \tag{2.14}$$

where $\hat{\Pi}_j(0) = |\mathrm{E}_j(0)\rangle\langle \mathrm{E}_j(0)|$ is the j-th projector operator onto the eigenstate $|\mathrm{E}_j(0)\rangle$ associated to the energy eigenvalue $\mathrm{E}_j(0)$.

After the system undergoes a unitary evolution described by the operator $\hat{U}(\tau, 0)$ from time 0 to time τ, as the one reported in equation (1.36), the final state of the system is $\hat{\rho}_S(\tau) = \hat{U}(\tau, 0)\hat{\rho}_S(0)\hat{U}^\dagger(\tau, 0)$, to which is associated the Hamiltonian

$$\hat{H}_S(\tau) = \sum_l \mathrm{E}_l(\tau)|\mathrm{E}_l(\tau)\rangle\langle \mathrm{E}_l(\tau)| = \sum_l \mathrm{E}_l(\tau)\hat{\Pi}_l(\tau). \tag{2.15}$$

Following references [37, 70, 71], the TPM protocol is such that the first projective measurement of $\hat{H}_S(0)$ on $\hat{\rho}_S(0)$ yields the outcome $\mathrm{E}_j(0)$ and the post-measurement state $|\mathrm{E}_j(0)\rangle\langle \mathrm{E}_j(0)|$. The closed system then evolves unitarily, according to: $\hat{\rho}_S(0) \to \hat{\rho}_S(\tau) =$

$\hat{U}(\tau,0)|\mathrm{E}_j\rangle\langle\mathrm{E}_j|\hat{U}^\dagger(\tau,0)$. The second projective measurement is performed on $\hat{H}_S(\tau)$, resulting in the outcome $\mathrm{E}_l(\tau)$. The difference between the initial and final measured energies corresponds to the fluctuating work

$$W_{l,j} \equiv \mathrm{E}_l(\tau) - \mathrm{E}_j(0). \tag{2.16}$$

Since the system is closed and evolves unitarily, no heat dissipation occurs, as detailed previously in Subsection 2.1.1.

Given that work is a fluctuating quantity, the described procedure must be repeated multiple times to obtain the average value $\langle W(t)\rangle$. Each iteration of the procedure yields a pair of outcomes $(\mathrm{E}_j(0), \mathrm{E}_l(\tau))$. The joint probability distribution $p^\tau_{j,l}$ of finding the initial energy value $\mathrm{E}_j(0)$ and the final energy value $\mathrm{E}_l(\tau)$, associated to any outcome pair, is determined by:

$$p^\tau_{j,l} \equiv p^0_j \, p^\tau_{l|j} \tag{2.17}$$

with:

$$p^0_j \equiv \langle\mathrm{E}_j(0)|\hat{\rho}_S(0)|\mathrm{E}_j(0)\rangle \tag{2.18}$$

$$p^\tau_{l|j} \equiv |\langle\mathrm{E}_l(\tau)|\hat{U}(\tau,0)|\mathrm{E}_j(0)\rangle|^2. \tag{2.19}$$

Here, p^0_j is the probability of measuring the initial energy $\mathrm{E}_j(0)$, and $p^\tau_{l|j}$ is the conditional probability to measure the energy $\mathrm{E}_l(\tau)$ at $t=\tau$ conditioned to have measured the energy $\mathrm{E}_j(0)$ at $t=0$. Equation (2.17) can be formulated also as in [37]:

$$p^\tau_{j,l} = \mathrm{Tr}\left[\hat{U}^\dagger(\tau,0)\hat{\Pi}_l(\tau)\hat{U}(\tau,0)\hat{\Pi}_j(0)\hat{\rho}_S(0)\hat{\Pi}_j(0)\right]. \tag{2.20}$$

The work probability distributions is then described by the following expression:

$$p\left(W\right) \equiv \sum_{j,l} p^\tau_{j,l}\, \delta\left(W - \left[\mathrm{E}_l(\tau) - \mathrm{E}_j(0)\right]\right), \tag{2.21}$$

where the Dirac delta ensures that the distribution only has values where the fluctuating variable W coincides with $W_{l,j}$. In this way, the average work is computed as the expectation value of the work probability distribution:

$$\langle W(t)\rangle = \sum_W p\left(W\right) W. \tag{2.22}$$

The TPM scheme,while widely used in quantum thermodynamics, has several limitations when applied to quantum systems. As highlighted in various studies [37, 71, 80, 81], one significant drawback is the invasiveness of the first projective measurement. In fact, if a system starts in a superposition of energy eigenstates, represented by a density operator $\hat{\rho}_S(0)$ with non-zero off-diagonal elements, the first energy measurement will collapse the initial state of the system into the energy eigenbasis. This process cancels the quantum coherence originally present in $\hat{\rho}_S(0)$, thereby preventing all interference effects resulting from the initial coherence. Moreover, this loss of coherence can lead to a reduction in the maximum average work that can be extracted or absorbed, given that coherent contributions are not accounted for [37, 71, 80].

In contrast, for quantum systems initially in a statistical mixture of energy eigenstates, where the density operator $\hat{\rho}_S(0)$ is diagonal, the TPM protocol is effective in describing work fluctuations. Specifically, if $\left[\hat{\rho}_S(0), \hat{H}_S(t)\right] = 0$ and $\left[\hat{H}_S(0), \hat{U}^{\dagger}(\tau,0)\hat{H}_S(\tau)\hat{U}(\tau,0)\right] = 0$ the average energy change predicted by the TPM protocol matches the average energy change due to the unitary evolution of $\hat{\rho}_S$, i.e. [37, 70, 71, 81]:

$$\begin{aligned}\langle W(\tau)\rangle &= \sum_W p\,(W)\,W = \sum_W \sum_{j,l} p^{\tau}_{j,l}\,\delta\left(W - [\mathrm{E}_l(\tau) - \mathrm{E}_j(0)]\right) = \sum_{j,l} p^0_j\, p^{\tau}_{l|j}[\mathrm{E}_l(\tau) - \mathrm{E}_j(0)] = \\ &= \sum_l p^{\tau}_l \mathrm{E}_l(\tau) - \sum_j p^0_j \mathrm{E}_j(0) = \mathrm{Tr}\left(\hat{\rho}_S(\tau)\hat{H}_S(\tau)\right) - \mathrm{Tr}\left(\hat{\rho}_S(0)\hat{H}_S(0)\right) = \langle \Delta \mathrm{E}_\mathrm{S}(\tau)\rangle.\end{aligned} \tag{2.23}$$

Here, $p^{\tau}_l = \sum_j p^{\tau}_{j,l}$ is the marginal of the joint probability distribution over the initial energies. Only with an initial diagonal state the so-called *unperturbed marginals* are obtained; sufficient condition for the latter circumstance is that the measurement of the system's state is non-invasive [37]. Indeed, in such a case, p^{τ}_l becomes $p^{\tau}_l = \langle \mathrm{E}_l(\tau)|\hat{\rho}_S(\tau)|\mathrm{E}_l(\tau)\rangle$, which is the probability of measuring the outcome $\mathrm{E}_l(\tau)$ at the final time $t = \tau$, as it is valid in the classical limit.

However, when at least one between $\left[\hat{\rho}_S(0), \hat{H}_S(t)\right]$ or $\left[\hat{H}_S(0), \hat{U}^{\dagger}(\tau,0)\hat{H}_S(\tau)\hat{U}(\tau,0)\right]$ is non-zero, meaning non-commuting or incompatible observables, the measurement process becomes invasive. Specifically, the statistics of measuring $\hat{H}_S(\tau)$ after $\hat{H}_S(0)$ differs if the initial measurement at $t = 0$ is not conducted [37, 71, 81].

To have a satisfactory analogy with the classical physics, where non-invasivity of the measurement procedure is given for granted, one would like the following requirements to be met by a work protocol [37, 65, 71, 81]:

1. **Positive, real and linear work distribution:** the work probability distribution $p(W)$ must be positive, real, linear with respect to the initial state $\hat{\rho}_S(0)$, and normalized to 1: $\sum_W p(W) = 1$.

2. **Unperturbed average energy change:** the protocol must ensure that the disturbance induced by the measurement is such that the generic joint probabilities $d_{j,l}$ lead to the unperturbed marginals:

$$\sum_j d^{\tau}_{j,l} = p^{\tau}_l \tag{2.24}$$

$$\sum_l d^{\tau}_{j,l} = p^0_j, \tag{2.25}$$

which implies unperturbed average energy change:

$$\langle \Delta \mathrm{E}_\mathrm{S}(\tau)\rangle = \mathrm{Tr}\left(\hat{\rho}_S(\tau)\hat{H}_S(\tau)\right) - \mathrm{Tr}\left(\hat{\rho}_S(0)\hat{H}_S(0)\right) = \sum_{j,l} d^{\tau}_{j,l}[\mathrm{E}_l(\tau) - \mathrm{E}_j(0)], \tag{2.26}$$

with $\hat{\rho}_S(0)$ generic initial density operator. I stress that $\sum_j d^{\tau}_{j,l}$ and $\sum_l d^{\tau}_{j,l}$ correspond to the single-time probability p_l^τ, p_j^0, associated to the outcomes $\mathrm{E}_l(\tau), \mathrm{E}_j(0)$ respectively.

These conditions are met only if $\left[\hat{\rho}_S(0), \hat{H}_S(t)\right] = 0$ or $\left[\hat{H}_S(0), \hat{U}^\dagger(\tau,0)\hat{H}_S(\tau)\hat{U}(\tau,0)\right] = 0$ holds, whereby the work probability distribution can be correctly obtained by means of the TPM scheme [37]. However, when commutation conditions are violated, the resulting incompatibility between observables leads to the so-called *no-go theorem* [37, 65, 71]:

Theorem 1. *A work protocol that satisfies the aforementioned requirements does not exist for any combinations of* $\hat{\rho}_S(0), \hat{H}_S(0), \hat{H}_S(\tau), \hat{U}(\tau,0)$.

In other words, when the state and the measurement observables do not commute, no measurement scheme can simultaneously satisfy these conditions for any work process and quantum states. The no-go theorem highlights the intrinsic difficulty in accounting for quantum coherence and measurement disturbances. As a result, approaches beyond TPM, such as the use of quasiprobabilities, are often explored to address this challenge in quantum thermodynamics, as I show in the next section.

2.1.3 Kirkwood-Dirac quasiprobabilities approach

Quasiprobabilities are built by relaxing part of the two requirements in Subsection 2.1.2. In particular, the requirement of positivity of the work probability distribution is relaxed [37, 65, 71, 80, 82, 83]. Notably, the occurrence of negative values in quasiprobability distributions is closely related to the concept of contextuality, which highlights the non-classical behavior of quantum systems [68, 69, 83–85]. Quasiprobabilities do not constitute the sole method to describe energy fluctuation in thermodynamic processes, as discussed in [71] and references therein. This approach is particularly advantageous because it preserves the linearity of probability theory while incorporating the distinctive quantum mechanical feature of contextuality [65].

I now introduce the Kirkwood-Dirac quasiprobability (KDQ) distribution that can lead to negative real values or even complex values to describe fluctuations of thermodynamic quantities defined at two or multiple times. I start from a closed quantum system undergoing unitary evolution from $t = 0$ to $t = \tau$, whereby the KDQ distribution is defined as follows [37, 65]:

$$q_{j,l} \equiv \mathrm{Tr}\left(\hat{U}^\dagger(\tau,0)\hat{\Pi}_l(\tau)\hat{U}(\tau,0)\hat{\Pi}_j(0)\hat{\rho}_S(0)\right), \tag{2.27}$$

where I remind that $\hat{\Pi}_l(\tau) = |\mathrm{E}_l(\tau)\rangle\langle\mathrm{E}_l(\tau)|$ is the projector for the measurement at time $t = \tau$ and $\hat{\Pi}_j(0) = |\mathrm{E}_j(0)\rangle\langle\mathrm{E}_j(0)|$ is the projector for the measurement at time $t = 0$. Definition (2.27) is not unique; another valid expression is:

$$q_{j,l} \equiv \mathrm{Tr}\left(\hat{\rho}_S(0)\hat{\Pi}_j(0)\hat{U}^\dagger(\tau,0)\hat{\Pi}_l(\tau)\hat{U}(\tau,0)\right), \tag{2.28}$$

which differs from the first just in the sign of the imaginary part, as discussed in [37]. In the following I use the expression in the equation (2.27). The real part of the KDQ is known as the *Margenau-Hill quasiprobability (MHQ)* [86].

Both quasiprobabilities in equations (2.27) and (2.28) satisfy the requirement 2 of the no-go theorem. Specifically, they yield the correct marginal probabilities:

$$\begin{aligned}\sum_j q_{j,l} &= \mathrm{Tr}\left(\hat{U}^\dagger(\tau,0)\hat{\Pi}_l(\tau)\hat{U}(\tau,0)\hat{\rho}_S(0)\right) &(2.29)\\ \sum_l q_{j,l} &= \mathrm{Tr}\left(\hat{\Pi}_j(0)\hat{\rho}_S(0)\right). &(2.30)\end{aligned}$$

Moreover, a KDQ distribution is linear and this entails that the TPM protocol is recovered when the state and the measurement observables commute, as when the initial state is diagonal. Indeed, if $[\hat{\rho}_S(0),\hat{H}_S(t)]=0$, the KDQ are equal to the joint probabilities of the TPM scheme:

$$\begin{aligned}&q_{j,l} =\\ &\quad = \mathrm{Tr}\left(\hat{U}^\dagger(\tau,0)\hat{\Pi}_l(\tau)\hat{U}(\tau,0)\hat{\Pi}_j(0)\hat{\rho}_S(0)\right) = \mathrm{Tr}\left(\hat{U}^\dagger(\tau,0)\hat{\Pi}_l(\tau)\hat{U}(\tau,0)\hat{\Pi}_j(0)\hat{\Pi}_j(0)\hat{\rho}_S(0)\right) =\\ &\quad = \mathrm{Tr}\left(\hat{U}^\dagger(\tau,0)\hat{\Pi}_l(\tau)\hat{U}(\tau,0)\hat{\Pi}_j(0)\hat{\rho}_S(0)\hat{\Pi}_j(0)\right) = p^\tau_{j,l}\end{aligned} \tag{2.31}$$

returned by the TPM scheme. In equation (2.31) I have made use of the idempotence property of projectors, i.e. $(\hat{\Pi}_j)^2 = \hat{\Pi}_j$, and of the commutativity condition.

For the sake of completeness, I specify all the properties of KDQ, which are meaningful in the following sections [55, 65]:

(i) The sum of KDQ is equal to 1: $\sum_{j,l} q_{j,l} = 1$.

(ii) The unperturbed marginals are obtained:

$$\begin{aligned}\sum_j q_{j,l} &= p^\tau_l = \mathrm{Tr}\left(\hat{\Pi}_l(\tau)\hat{\rho}_S(\tau)\right) &(2.32)\\ \sum_l q_{j,l} &= p^0_j = \mathrm{Tr}\left(\hat{\Pi}_j(0)\hat{\rho}_S(0)\right). &(2.33)\end{aligned}$$

I remind that, if $[\hat{\rho}_S(0),\hat{H}_S(0)] \neq 0$ for some $\hat{\rho}_S(0)$ and $\hat{H}_S(0)$, then the unperturbed marginal p^τ_l at time τ is not obtained by the TPM scheme. The latter, indeed, cancels the off-diagonal terms of $\hat{\rho}_S(0)$ with respect to the eigenbasis of $\hat{H}_S(0)$ due to the initial projective measurement at time 0.

(iii) The KDQ are linear in the initial density operator $\hat{\rho}_S(0)$. This means that, given any admissible decomposition of $\hat{\rho}_S(0)$ [say $\hat{\rho}_S(0) = \hat{\rho}^{(1)}_S(0) + \hat{\rho}^{(2)}_S(0)$], equation (2.27) splits in two terms, one linearly dependent on $\hat{\rho}^{(1)}_S(0)$ and the other on $\hat{\rho}^{(2)}_S(0)$, i.e.,

$$q_{j,l} = q^{(1)}_{j,l} + q^{(2)}_{j,l} \tag{2.34}$$

with $q^{(n)}_{j,l} = \mathrm{Tr}\left(\hat{U}^\dagger(\tau,0)\hat{\Pi}_l\hat{U}(\tau,0)\hat{\Pi}_j\hat{\rho}^{(n)}_S(0)\right)$, $n = 1,2$. A choice that is commonly adopted is to take $\hat{\rho}^{(1)}_S(0)$ as the matrix that solely contains the diagonal terms of $\hat{\rho}_S(0)$, and $\hat{\rho}^{(2)}_S(0)$ as the matrix comprising only the off-diagonal terms.

(iv) KDQ are in general complex numbers and thus can lose positivity, i.e., they can admit negative real parts and imaginary parts different from zero. The presence of non-positivity is a proof of quantum contextuality: its explanation requires taking into account non-classical features like the presence of quantum coherence in the state of the system or the incompatibility of the measurement observables. For a two-time statistics (here, of energy outcomes), non-positivity can be regarded as a form of non-classicality [87]. I quantify the non-positivity of KDQ, and thus non-classicality in the statistics of energy outcomes, by means of the *non-positivity functional* [36, 55, 64, 65, 88]

$$\aleph \equiv -1 + \sum_{j,l} |q_{j,l}|. \tag{2.35}$$

If $\aleph > 0$, then negative real parts and/or imaginary parts of $q_{j,l}$ are present, while $\aleph = 0$ when all the quasiprobabilities are positive real numbers.

All the aforementioned properties illustrate that the KDQ can be an effective tool for capturing quantum characteristics of energetic processes. Specifically, I explore how KDQ distributions can be applied to key thermodynamic quantities such as internal energy and work. These quantities fluctuate at the microscopic level, making KDQ distributions ideal for describing their statistics.

For a closed quantum system $\hat{\rho}_S(t)$, evolving from an initial time 0 to a final time τ under the Hamiltonian $\hat{H}_S(t)$, the average work is given by:

$$\langle W(t) \rangle = \sum_W p\,(W)\,W = \sum_W \sum_{j,l} q_{j,l}\,\delta\,(W - [\mathrm{E}_l(\tau) - \mathrm{E}_j(0)]) = \sum_{j,l} q_{j,l}\,\left[\mathrm{E}_l(\tau) - \mathrm{E}_j(0)\right]. \tag{2.36}$$

According to the sign convention, a negative $\langle W(t) \rangle$ means that the final energy is less than the initial energy, with the consequence that work could be extracted from the system. In quantum processes, the quasiprobability distribution may contain negative real values. Thus, $\langle W(t) \rangle$ can be negative even exploiting energy transitions with $\mathrm{E}_l(\tau) > \mathrm{E}_j(0)$. Indeed, this is possible only if the corresponding quasiprobability is $q_{j,l} < 0$. Such a circumstance, indicates the presence of system's quantum traits and can also enable enhanced work extraction beyond classical limits. It can be proven that negative quasiprobabilities are associated with "anomalous" internal energy variations [36–38].

I conclude this subsection by emphasizing that in quantum processes, a quasiprobability distribution *may* contain negative real values, under operators' commutativity. However, the presence of positive real values, $\mathrm{Re}[q_{j,l}] > 0$, does not necessarily indicate that the underlying process is classical. The positivity of the MHQ, indeed, suggests a weaker form of classicality compared to the classicality defined by the TPM scheme. If the state does not commute with the measurement observable, but the MHQ is positive, it does not necessarily imply that there is no classical statistical probability distribution capable of reproducing the same results as those obtained with quasiprobabilities. Nevertheless, this classical statistics will be built on a different thermodynamic process potentially having entirely different conditions $(\hat{\rho}_S, \hat{H}_S, \dots)$. Conversely, the measurement statistics associated to a quantum system is considered classical in a stricter sense if the MHQ is positive and the TPM scheme applied under the same conditions gives the same results.

2.2 Energy fluctuations of a three-level system generating Fano-coherence

In this section, I present my recent results reported in [55], Donati *et al.*. The objective is to investigate the energetics involved in generating Fano coherences due to the interaction with an isotropic unpolarized radiation and to evaluate the role of energy fluctuations beyond average values. To achieve this, I employ KD quasiprobabilities. This approach enables to describe the time statistics of energy outcomes by evaluating the Hamiltonian of the quantum system at distinct times. In this regard, notice that the concepts discussed in the previous section can be extended to an open quantum system, such as the one under scrutiny, that is described by a Markovian quantum master equation. I therefore formalize the physical context in which I am working.

2.2.1 KDQ distribution for the V-type three-level system

I consider the V-type three-level system already described in Subsection 1.3.1, with time-independent Hamiltonian $\hat{H}_S = \sum_{k=1}^{3} \mathrm{E}_k \hat{\Pi}_k$. Here, $\mathrm{E}_k = \hbar\omega_k$ with $k = a, b, c$ denotes the energies of the system and $\hat{\Pi}_k \equiv |\mathrm{E}_k\rangle\langle\mathrm{E}_k| = |k\rangle\langle k|$ the corresponding projectors. Initially, the three-level system is prepared in the density operator $\hat{\rho}_S(0)$ and subsequently interacts with an isotropic, unpolarized non-coherent source. The interaction is modeled by the Markovian quantum master equation derived in Section 1.3.2, which ensures both the positivity and trace preservation of the system's density operator, as I have already explained. In particular, the time evolution of the reduced density operator elements is governed by equations (1.121) and (1.122). The solution to the latter can be achieved by solving two distinct systems of linear equations, as I did in [55]:

$$\frac{d\mathbf{x}(t)}{dt} = A\mathbf{x}(t) \quad \text{and} \quad \frac{d\mathbf{z}(t)}{dt} = C\mathbf{z}(t) \tag{2.37}$$

with state vectors

$$\mathbf{x}(t) \equiv \Big(\rho_{aa}(t), \rho_{bb}(t), \rho_{cc}(t), \mathrm{Re}[\rho_{ab}(t)], \mathrm{Im}[\rho_{ab}(t)]\Big)^T \tag{2.38}$$

$$\mathbf{z}(t) \equiv \Big(\mathrm{Re}[\rho_{ac}(t)], \mathrm{Im}[\rho_{ac}(t)], \mathrm{Re}[\rho_{bc}(t)], \mathrm{Im}[\rho_{bc}(t)]\Big)^T . \tag{2.39}$$

Differently from previous approaches [28, 51, 52], the vector $\mathbf{x}$ includes the population of the ground level $\rho_{cc}(t)$ rather than imposing the constraint $\rho_{cc}(t) = 1 - \rho_{aa}(t) - \rho_{bb}(t)$. This choice is needed to get at any time t the correct density operator $\hat{\rho}_S(t)$, solution of equations (1.121),(1.122) altogether, from the direct exponentiation of the two differential equations in (2.37). It is thus required to determine the solution of the whole process by solving separately the sub-processes in equations (1.121),(1.122) that composed it. In equation (2.37), the matrices A, C of coefficients are equal to

$$A = \begin{pmatrix} -\gamma_a\left(\bar{n}+1\right) & 0 & \gamma_a\bar{n} & -p\sqrt{\gamma_a\gamma_b}\left(\bar{n}+1\right) & 0 \\ 0 & -\gamma_b\left(\bar{n}+1\right) & \gamma_b\bar{n} & -p\sqrt{\gamma_a\gamma_b}\left(\bar{n}+1\right) & 0 \\ \gamma_a\left(\bar{n}+1\right) & \gamma_b\left(\bar{n}+1\right) & -\left(\gamma_a+\gamma_b\right)\bar{n} & 2p\sqrt{\gamma_a\gamma_b}\left(\bar{n}+1\right) & 0 \\ -\frac{p}{2}\sqrt{\gamma_a\gamma_b}\left(\bar{n}+1\right) & -\frac{p}{2}\sqrt{\gamma_a\gamma_b}\left(\bar{n}+1\right) & p\sqrt{\gamma_a\gamma_b}\bar{n} & -\frac{\gamma_a+\gamma_b}{2}\left(\bar{n}+1\right) & \Delta \\ 0 & 0 & 0 & -\Delta & -\frac{\gamma_a+\gamma_b}{2}\left(\bar{n}+1\right) \end{pmatrix} \tag{2.40}$$

$$C = \begin{pmatrix} -\left[\bar{n}\left(\gamma_a+\frac{\gamma_b}{2}\right)+\frac{\gamma_a}{2}\right] & \omega_{ac} & -\frac{p}{2}\sqrt{\gamma_a\gamma_b}\left(\bar{n}+1\right) & 0 \\ -\omega_{ac} & -\left[\bar{n}\left(\gamma_a+\frac{\gamma_b}{2}\right)+\frac{\gamma_a}{2}\right] & 0 & -\frac{p}{2}\sqrt{\gamma_a\gamma_b}\left(\bar{n}+1\right) \\ -\frac{p}{2}\sqrt{\gamma_a\gamma_b}\left(\bar{n}+1\right) & 0 & -\left[\bar{n}\left(\gamma_b+\frac{\gamma_a}{2}\right)+\frac{\gamma_b}{2}\right] & \omega_{bc} \\ 0 & -\frac{p}{2}\sqrt{\gamma_a\gamma_b}\left(\bar{n}+1\right) & -\omega_{bc} & -\left[\bar{n}\left(\gamma_b+\frac{\gamma_a}{2}\right)+\frac{\gamma_b}{2}\right] \end{pmatrix} \tag{2.41}$$

I numerically solve the homogeneous differential equations (2.37) via exponentiation, namely

$$\mathbf{x}(t) = e^{At}\mathbf{x}(0) \tag{2.42}$$

$$\mathbf{z}(t) = e^{Ct}\mathbf{z}(0) \tag{2.43}$$

with $\mathbf{x}(0)$, $\mathbf{z}(0)$ denoting the initial states. The exponential of the matrices A, C is computed using the MATLAB function `expm`, which employs the scaling and squaring algorithm of Higham [59].

As already discussed in Section 1.4, analytical solutions of equations (1.121) have been demonstrated in previous studies [28, 51]. These solutions exhibit different behaviors depending on the value of the ratio $\Delta/\bar{\gamma}$ (between the energy splitting Δ among the excited states and the average decay rate $\bar{\gamma}$), as well as on the average photon number $\bar{n}$ and on the alignment parameter p. Specifically, two main regimes emerge: the overdamped and the underdamped regimes, separated by the critical regime. As I have shown in Subsection 1.4.1, only in the overdamped regime quasi-stationary Fano coherences can be established, thus resulting in a prolonged coherence lifetime. In the large-time limit, the quantum system tends towards a nonequilibrium steady states with vanishing coherences $\rho_{ab}, \rho_{ac}, \rho_{bc}$ and constant populations, apart the peculiar case with $|p| = 1$ and a superposition of energy eigenstates as initial state. Being linked to populations, the quantum coherence ρ_{ab} exponentially decays on a fast time scale, contrarily to ρ_{ac}, ρ_{bc} that, when initially different from zero, tend to zero following a damped oscillatory trend. During the decay, after a sufficiently large time, the real and imaginary parts of ρ_{ac}, ρ_{bc} come into phase. These behaviours are thus dependent on both the initial state, and the model's parameters. Under the weak pumping condition ($\bar{n} < 1$) with $p \leq |1|$, achieving the overdamped regime is possible when $\Delta/\bar{\gamma} \ll 1$. However, under the strong pumping condition ($\bar{n} > 1$), the requirement $\Delta/\bar{\gamma} \ll 1$ can be relaxed, which means a value of Δ much larger than $\bar{\gamma}$, without compromising the quasi-stationarity of coherences. This rationale guides the selection of $\Delta/\bar{\gamma} \ll 1$ in the analyses presented in the next subsection, representing the condition to obtain quasi-stationary states for ρ_{ab} in all the pumping regimes.

Time evolution of the system's density operator can be efficiently described in a compact form using *open quantum maps* $\Phi[\cdot]$ [44]. An open quantum map yields the system's density operator at time t, i.e., $\hat{\rho}_S(t) = \Phi[\hat{\rho}_S(0)]$. In this case, it represents the solution to the Bloch-Redfield quantum master equation describing the interaction. For this reason, $\Phi[\cdot]$ is a *Completely Positive Trace Preserving (CPTP)* map, meaning that it maintains the physical integrity of the system's density operator throughout the evolution.

The KDQ describing the statistics of the energy changes, corresponding to the internal energy variation within the open system, over the interval $[t_1, t_2]$, is defined as

$$q_{j,l} \equiv \mathrm{Tr}\left(\hat{\Pi}_l\, \Phi\left[\hat{\Pi}_j\, \hat{\rho}_S(0)\right]\right), \tag{2.44}$$

where $\hat{\Pi}_l$ and $\hat{\Pi}_j$ are the l-th and j-th projectors of $\hat{H}_S$ evaluated at times t_2 and t_1 respectively. This definition is derived from the expression for closed systems. Indeed, applying the cyclic property of trace to equation (2.27) yields:

$$q_{j,l} = \mathrm{Tr}\left(\hat{U}^\dagger(\tau,0)\hat{\Pi}_l\hat{U}(\tau,0)\hat{\Pi}_j\hat{\rho}_S(0)\right) = \mathrm{Tr}\left(\hat{\Pi}_l\hat{U}(\tau,0)\hat{\Pi}_j\hat{\rho}_S(0)\hat{U}^\dagger(\tau,0)\right), \tag{2.45}$$

where the term $\hat{U}(\tau,0)\hat{\Pi}_j\hat{\rho}_S(0)\hat{U}^\dagger(\tau,0)$ represents the time evolution of the operator $\hat{\Pi}_j\hat{\rho}_S(0)$. Then, for an open system, the correspondence $\hat{U}(\tau,0)\hat{\Pi}_j\hat{\rho}_S(0)\hat{U}^\dagger(\tau,0) \rightarrow \Phi\left[\hat{\Pi}_j\, \hat{\rho}_S(0)\right]$ holds, leading to equation (2.44).

Each quasiprobability $q_{j,l}$ is associated to the (j,l)-th realization $\Delta\mathrm{E}_{j,l} \equiv \mathrm{E}_l(t_2) - \mathrm{E}_j(t_1)$ of the energy change $\Delta\mathrm{E}$, which is given by the difference of the system energies evaluated at times t_2 and t_1. All the properties listed in Subesection 2.1.3 hold for open quantum systems as well, with the substitution $\hat{U}(\tau,0)A\hat{U}^\dagger(\tau,0) \rightarrow \Phi[A]$.

2.2.2 Quantumness certification

In this subsection I demonstrate that the generation of Fano coherences are linked to a quasiprobability distribution for the energy changes in a V-type three-level system, which exhibits negativity in its values, with the imaginary parts being zero. The presence of negativity results from initializing the three-level system in a superposition of the wavefunctions comprising the energy eigenbasis, meaning that in such a basis quantum coherences have to be included. This occurs for specific parameter settings that I analyze in more details in Subsection 2.2.3. Interestingly, there is also a subset of parameters' values such that solely the quantum coherence in the initial state of the system (leading to negativity) is responsible for an amount of excess energy

$$-\langle\Delta\mathrm{E}(t)\rangle = -\sum_{j,l} q_{j,l}\Delta\mathrm{E}_{j,l}(t) = \sum_{j,l} q_{j,l}\left(\mathrm{E}_j(0) - \mathrm{E}_l(t)\right) = \mathrm{Tr}\left(\hat{H}_S\left(\hat{\rho}_S(0) - \hat{\rho}_S(t)\right)\right) \tag{2.46}$$

larger than zero for any time t, with $\hat{H}_S$ time-independent. It is important to note that in the context of open quantum systems, internal energy variations result from heat and work exchanges, as discussed in Subsection 2.1.1. Nonetheless, negative values of $\langle\Delta\mathrm{E}(t)\rangle$ can be interpreted as extractable work, which means that this excess energy could be harnessed as work, provided an appropriate load or storage system is in place.

One example of these quantum behaviours involving the generation of Fano coherences is shown. For this purpose, the following parameters' setting are taken:

(i) **V-type three-level system:** spontaneous decay rates (from $|a\rangle, |b\rangle$ to $|c\rangle$) $\gamma_a = \gamma_b \equiv \gamma \approx 3 \cdot 10^7$ [rad/s]; energies $\mathrm{E}_3 = \hbar\omega_a$, $\mathrm{E}_2 = \hbar\omega_b$, $\mathrm{E}_1 = \hbar\omega_c$ with $\mathrm{E}_1 \leq \mathrm{E}_2 \leq \mathrm{E}_3$; $\omega_a = D + \Delta/2$, $\omega_b = D - \Delta/2$ and $\omega_c = 0$, with $D \approx 10^{15}$ [rad/s] (optical transition). Thus, $\omega_{ac} = \omega_a$, $\omega_{bc} = \omega_b$ and $\omega_{ac} \approx \omega_{bc}$, according to the approximations described in Section 1.3. Moreover, $\Delta \ll \gamma$, i.e. $\Delta = 0.1\gamma \ll D$. In the following, the units of measurement of the plotted quantities are re-scaled such that $\hbar = 1$.

(ii) **Incoherent source:** average photons number $\bar{n} = 3$; alignment parameter (between the dipole moments of the transitions $|a\rangle \leftrightarrow |c\rangle, |b\rangle \leftrightarrow |c\rangle$) $p = \cos\Theta = -1, -0.75, -0.5, -0.25, 0$. The incoherent source can represent a broadband laser or even sunlight radiation.

(iii) **The bare Hamiltonian:** $\hat{H}_S$ of the V-type three-level system is given by:

$$\hat{H}_S = \hbar \sum_k \omega_k |k\rangle\langle k| = \hbar\left(\omega_a \hat{\Pi}_a + \omega_b \hat{\Pi}_b + \omega_c \hat{\Pi}_c\right),$$

where $k = a, b, c$.

(iv) **Initial quantum state of the three-level system:** $\hat{\rho}_S(0) = |\psi_0\rangle\langle\psi_0|$ with

$$|\psi_0\rangle = \alpha_a|a\rangle + \alpha_b\, e^{i\phi_b}|b\rangle + \alpha_c|c\rangle \tag{2.47}$$

and $\alpha_a = \sqrt{0.3}$, $\alpha_b = \sqrt{0.3}$, $\phi_b = \pi$, and $\alpha_c = \sqrt{0.4}$; note that $\alpha_a^2 + \alpha_b^2 + \alpha_c^2 = 1$ to ensure probability conservation. As previously anticipated, the initial density operator of the three-level system contains quantum coherence along the eigenbasis of $\hat{H}_S$.

Now, using this parameters setting, I show two distinct plots: one concerning the average energy change $\langle\Delta\mathrm{E}\rangle$ as a function of the dimensionless time $t\gamma/(2\pi)$ (figure 2.1), and the other regarding the underlying KDQ distribution (figure 2.2). For both plots I numerically solve the linear differential equations (2.37) that describe the dynamics responsible for the generation of Fano coherence in Markovian regime. The values of the parameters inserted in equations (2.37) are those provided at points (i)-(iv) above. Moreover, I consider the results given by splitting the KDQ as in equation (2.34), where $\hat{\rho}_S(0) = |\psi_0\rangle\langle\psi_0|$ is linearly decomposed in the sum of two matrices: $\hat{\rho}_S(0) = \mathrm{diag}(\hat{\rho}_S(0)) + \chi_S(0)$. The term $\mathrm{diag}(\hat{\rho}_S(0))$ contains the diagonal elements of $\hat{\rho}_S(0)$, while $\chi_S(0)$ contains the off-diagonal elements. I denote the two contributions of the KDQ

$$q_{j,l} = \mathrm{Tr}\Big[|l\rangle\langle l|\,\Phi\big[|j\rangle\langle j|\psi_0\rangle\langle\psi_0|\big]\Big] = \langle j|\psi_0\rangle\,\langle l|\,\Phi\big[|j\rangle\langle\psi_0|\big]\,|l\rangle \tag{2.48}$$

with $j, l = a, b, c$, as $q_{j,l}^{\mathrm{diag}}$ and $q_{j,l}^{\mathrm{coh}}$ respectively. In (2.48), the quantum map $\Phi[\cdot]$ is derived from equations of motion (2.42) and (2.43).

The ranges of parameters at points (i)-(iv) are such that $\langle\Delta\mathrm{E}\rangle = 0$, as long as the initial density operator $\hat{\rho}_S(0)$ of the three-level system does not contain quantum coherence χ_S (with respect to the basis diagonalizing $\hat{H}_S$). I stress that, by construction, such a result can not be provided by the TPM scheme. On the contrary, by including quantum

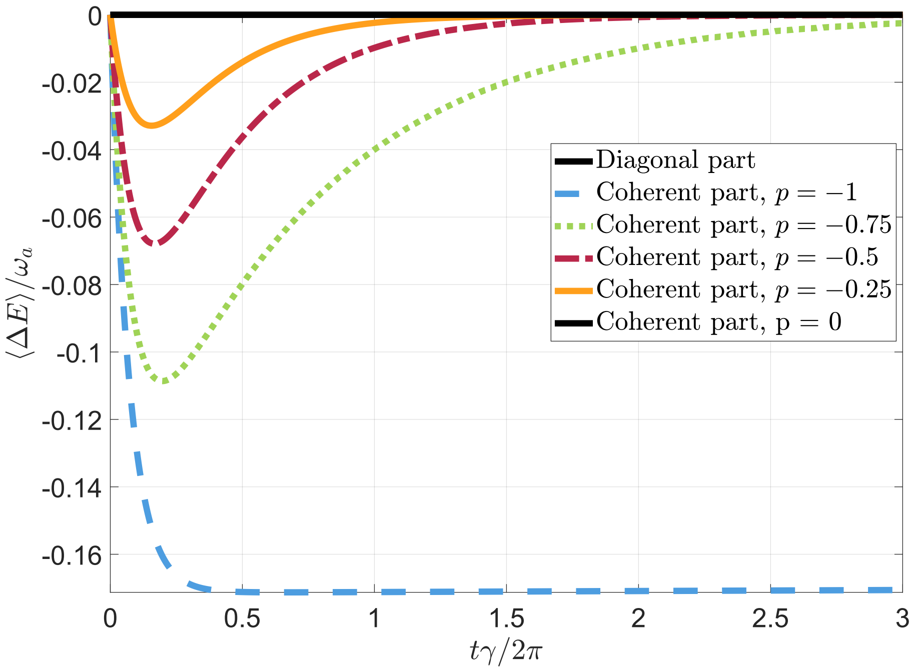

Figure 2.1: *Average energy change* $\langle\Delta\mathrm{E}\rangle$, *re-scaled by* ω_a, *as a function of the dimensionless time* $t\gamma/(2\pi)$, *which we obtain by numerically computing the corresponding KDQ distribution. The dynamics of the three-level system subjected to an incoherent light source, entering in the quasiprobabilities, is provided by equations* (2.37). *The black solid line denotes the contribution* $\langle\Delta E\rangle_{\mathrm{diag}}$ *of the average energy change that corresponds solely to the diagonal elements, contained in* $\mathrm{diag}(\hat{\rho}_S(0))$, *of the initial state* $\hat{\rho}_S(0)$. *It can be verified that* $\langle\Delta\mathrm{E}\rangle_{\mathrm{diag}}$ *is equal to zero for any value of* p. *On the other hand, all the other curves in the figure refer to the contribution* $\langle\Delta\mathrm{E}\rangle_{\mathrm{coh}}$ *of the average energy change depending on* χ_S, *matrix containing the off-diagonal elements of* $\hat{\rho}_S(0)$, *for* $p=0,-0.25,-0.5,-0.75,-1$. *Notice that the black solid line is used also for* $\langle\Delta\mathrm{E}\rangle_{\mathrm{coh}}$ *with* $p=0$ *since in this case* $\langle\Delta\mathrm{E}\rangle_{\mathrm{coh}}=0$.

coherences as given by equation (2.47), $\langle\Delta\mathrm{E}\rangle=\langle\Delta\mathrm{E}\rangle_{\mathrm{coh}}\leq 0$, as shown in figure 2.1. In fact, $\langle\Delta\mathrm{E}\rangle=\langle\Delta\mathrm{E}\rangle_{\mathrm{diag}}+\langle\Delta\mathrm{E}\rangle_{\mathrm{coh}}$ but $\langle\Delta\mathrm{E}\rangle_{\mathrm{diag}}=0$ in this case study. Indeed, the contribution from the off-diagonal elements of $\hat{\rho}_S$ is analyzed. This entails a non-negligible amount of excess energy assisted from initializing the quantum system in a superposition state of the energy eigenstates. Moreover, both the magnitude of $|\langle\Delta\mathrm{E}\rangle|$ and the time interval in which $|\langle\Delta\mathrm{E}\rangle|\neq 0$ can be linearly enhanced by increasing the value (with sign) of the alignment parameter $p\in[-1,1]$. Such an effect is maximized for $p=-1$, whereby $\max[-\langle\Delta\mathrm{E}\rangle/\omega_a]\approx 0.17$ and remains quasi-stationary as long as the incoherent light source is active. This finding is related (and thus consistent) with the already-known fact that $|p|=1$ implies quasi-stationary Fano coherences, ideally for an arbitrarily large time t [28, 30, 51]. It is worth noting the sign of p is not relevant for the solution $\hat{\rho}_S(t)$ of the quantum system dynamics, but it matters for the sign of $\langle\Delta\mathrm{E}\rangle$ and thus for the nature of the thermodynamics process under investigation. In fact, using the ranges of parameters at point (i)-(iv), p negative entails energy in excess, while p positive means absorbed energy.

In the panels of figure 2.2 the full distribution of KDQ (dashed black lines) $q_{j,l}$ with $j,l=a,b,c$, is plotted. Such a quasiprobability distribution underlies the energy change statistics and thus the average energy change shown in figure 2.1. In doing this, I use again

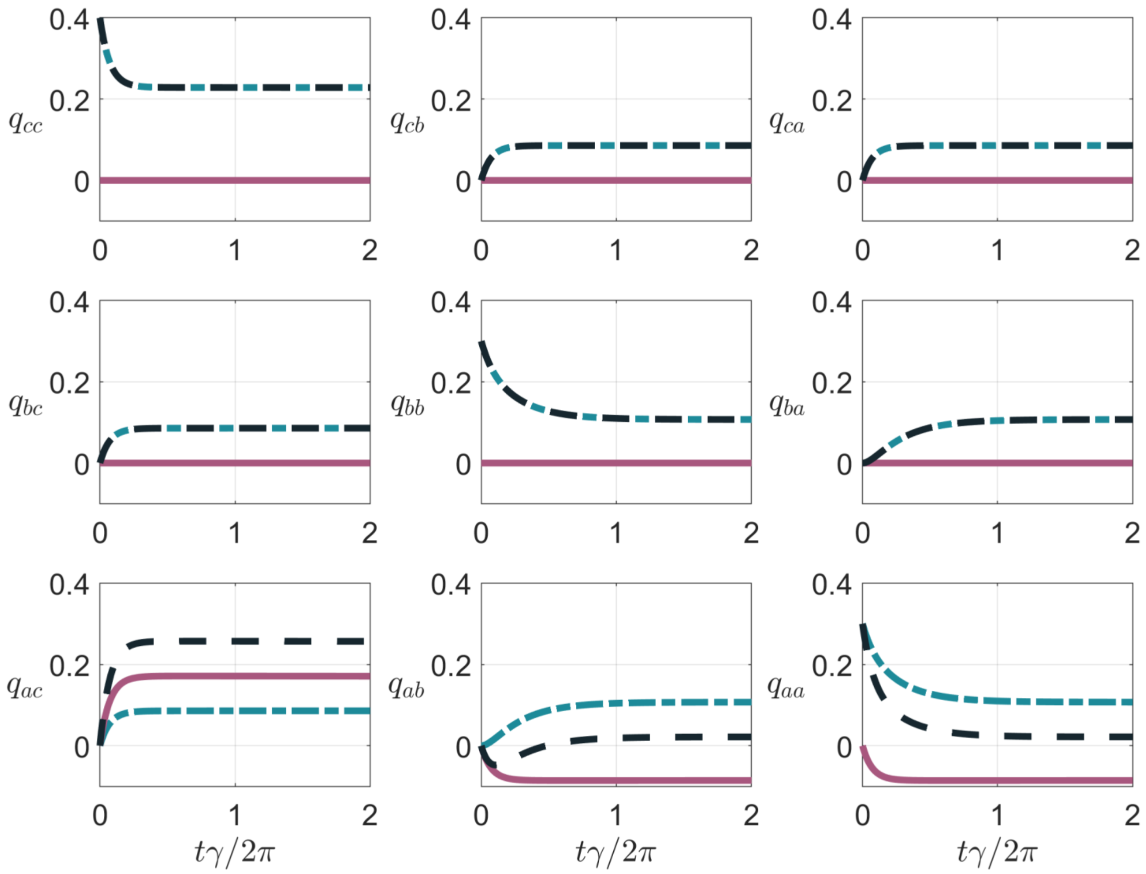

Figure 2.2: *Kirkwood-Dirac quasiprobabilities (dashed black lines), quantifying the energy change statistics of the V-type three-level system subjected to incoherent light source, as a function of the dimensionless time* $t\gamma/(2\pi)$. *The quasiprobabilities refer to the (energy) transitions between the levels* $|a\rangle, |b\rangle, |c\rangle$ *of the system. Here, the imaginary parts of all the quasiprobabilities are equal to zero. For all the panels, the parameter setting at points (i)-(iv) is used with* $p = -1$, *and I distinguish between the contributions* $q_{j,l}^{\rm diag}$ *and* $q_{j,l}^{\rm coh}$ *depending respectively on* χ_S *(solid red lines) and* $\mathrm{diag}(\hat{\rho}_S(0))$ *(dash-dotted blue lines), where* $\mathrm{diag}(\hat{\rho}_S(0)), \chi_S$ *linearly decompose the initial density operator* $\hat{\rho}_S(0)$.

the parameters setting at points (i)-(iv) but with $p = -1$, whereby the imaginary parts of all the plotted KDQ are equal to zero. In the figure, I distinguish between $q_{j,l}^{\rm diag}$ and $q_{j,l}^{\rm coh}$ of $q_{j,l}$, which I recall are the contributions stemming respectively from the matrices containing the diagonal and off-diagonal elements of $\hat{\rho}_S(0)$. It can be observed that q_{ac}, q_{ab}, q_{aa} have a contribution of $q_{j,l}^{\rm coh} \neq 0$ (solid red lines in the figure), which is due to initializing the system in a state with quantum coherence (with respect to the eigenbasis of $\hat{H}_S$). Notably, the quasiprobability q_{ab} is globally negative in a transient time interval. In this regard, it is worth recalling that the Fano coherence can arise between the excited levels $|a\rangle$, $|b\rangle$ of the three-level system. Hence, the presence of negativity in the corresponding KDQ describing energy change fluctuations is an hallmark of Fano coherence generation occurring in a non-classical regime. I complete this analysis by showing in figure 2.3 that:

(i) the real part of $q_{a,b}^{\rm coh}$ (plotted as a function of time) monotonically grows by increasing the value of the alignment parameter p that effectively represents a control knob to enhance the negativity of the corresponding KDQ [panel (a)], and thus the amount of

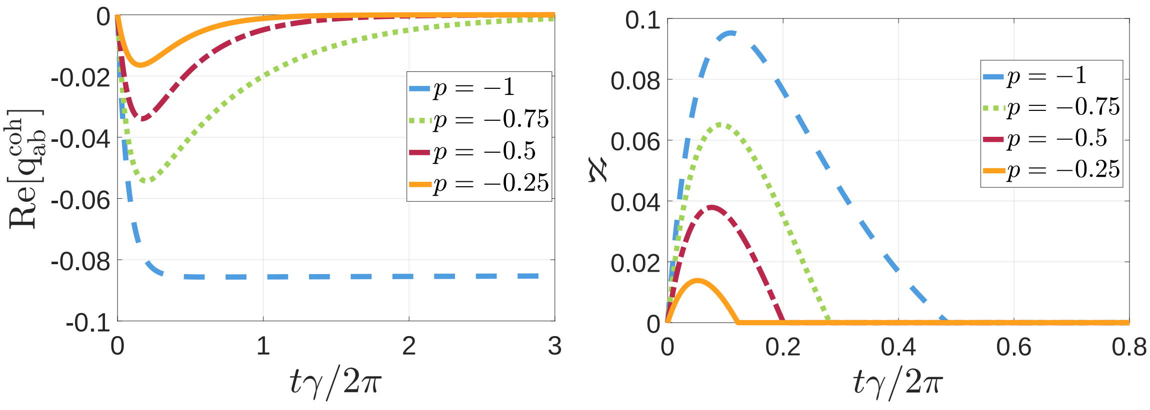

(a) (b)

Figure 2.3: *(a) Real part of $q^{\mathrm{coh}}_{a,b}$ [panel (a)] and the non-positivity functional $\aleph$ [panel (b)], as a function of the dimensionless time $t\gamma/(2\pi)$, for $p = -1, -0.75, -0.5, -0.25$. For both panels, the ranges of parameters at point (i)-(iv) are considered.*

the excess energy in several cases as detailed below.

(ii) The non-positivity functional $\aleph$ of the KDQ distribution of energy changes is > 0 in a transient time interval, at least in the parameters setting at points (i)-(iv). This aspect certifies the presence of negative real parts of quasiprobabilities, as observed in figure 2.3a, and thus non-classicality. Moreover, $\aleph$ is maximized for $p = -1$.

As a final remark, notice that initializing a V-system in a superposition of all the three energy eigenstates (as in equation (2.47)) is not a necessary condition for observing a quasiprobability distribution with negative values ($\aleph \neq 0$), since the main factor appears to be the presence of coherence between the excited states.

2.2.3 Optimization of excess energy

In the previous section, I have introduced a case study in which $\langle \Delta \mathrm{E} \rangle_{\mathrm{diag}}$, dependent on the diagonal elements of $\hat{\rho}_S(0)$, is zero for any time t. In this section the focus shifts to optimizing some key parameters of the model, including the initial quantum state of the three-level system, in order to maximize the value of $-\langle \Delta \mathrm{E} \rangle_{\mathrm{coh}}$ arising from the off-diagonal elements of $\hat{\rho}_S(0)$. As mentioned earlier, such an optimization also leads to an enhancement of negativity.

Achieving the condition $\langle \Delta \mathrm{E} \rangle_{\mathrm{diag}} = 0$ relies solely on specific values of $\bar{n}$ and $\rho_{cc}(0) = |\alpha_c|^2$, under the assumption that the initial state of the system is given by Eq. (2.47). The analytical formula returning the values of $\bar{n}, \rho_{cc}(0)$ such that $\langle \Delta \mathrm{E} \rangle_{\mathrm{diag}} = 0$ is unknown. However, to attain $\langle \Delta \mathrm{E} \rangle_{\mathrm{diag}} = 0$ with an increased value of $\bar{n}$, one needs to decrease $\rho_{cc}(0)$, and vice-versa. For instance, in the weak pumping regime ($\bar{n} < 1$), the condition $\langle \Delta \mathrm{E} \rangle_{\mathrm{diag}} = 0$ is satisfied for $\bar{n} = 0.5$ and $\rho_{cc}(0) = 0.6$. Conversely, in the strong pumping regime ($\bar{n} > 1$), the condition $\langle \Delta \mathrm{E} \rangle_{\mathrm{diag}} = 0$ holds for $\bar{n} = 3$ and $\rho_{cc}(0) = 0.4$ that are the values used in Subsection 2.2.2. Choosing $\bar{n}$ above (below) the value allowing for $\langle \Delta \mathrm{E} \rangle_{\mathrm{diag}} = 0$, for a given $\rho_{cc}(0)$, leads to $\langle \Delta \mathrm{E} \rangle_{\mathrm{diag}}$ being nonzero and either positive (negative). These considerations are valid for any values of p, but in what follows I specifically select $p = -0.5$.

Once the condition $\langle \Delta \mathrm{E} \rangle = \langle \Delta \mathrm{E} \rangle_{\mathrm{coh}}$ is established, the optimization of $\langle \Delta \mathrm{E} \rangle_{\mathrm{coh}}$ is determined by the initial state $|\psi_0\rangle = \alpha_a\, e^{i\phi_a}|a\rangle + \alpha_b\, e^{i\phi_b}|b\rangle + \alpha_c\, e^{i\phi_c}|c\rangle$, where I consider a more general state featuring also the relative phases ϕ_a, ϕ_c in addition to ϕ_b.

Setting the values $\bar{n} = 3$ and $\rho_{cc}(0) = 0.4$, I take the populations $\rho_{aa} = |\alpha_a|^2 = \rho_{bb} = |\alpha_b|^2 = 0.3$, and the relative phases ϕ_a, ϕ_b, ϕ_c of $|\psi_0\rangle$ are varied within the range $[0, 2\pi]$. Interestingly, setting one of the relative phases to zero does not impact the maximum attainable value for $\langle \Delta \mathrm{E} \rangle$. Moreover, by using $\phi_a = 0$ or $\phi_b = 0$ and $\phi_c = 0$, I identify two distinct scenarios:

(i) $\boldsymbol{\phi_a} = 0$ or $\boldsymbol{\phi_b} = 0$.
Setting $\phi_a = 0$, the two relative phase vary within the range $[0, 2\pi]$, and I then record the corresponding values of $\langle \Delta \mathrm{E} \rangle$. Figure 2.4a highlights the maximum values of $\langle \Delta \mathrm{E} \rangle_{\mathrm{coh}}$ by varying the value of the phases ϕ_b, ϕ_c. From the figure it can be observed that, in this setting, ϕ_c does not affect neither the magnitude nor the sign of $|\langle \Delta \mathrm{E} \rangle_{\mathrm{coh}}|$. Conversely, the relative phase ϕ_b significantly influences the quantity $|\langle \Delta \mathrm{E} \rangle_{\mathrm{coh}}|$. The magnitude $|\langle \Delta \mathrm{E} \rangle_{\mathrm{coh}}|$ is zero for $\phi_b = \pi/2$, and increases in both directions either towards $\phi_b = 0$ or $\phi_b = \pi$, but with opposite sign. The value $\phi_b = \pi$ represents a line of mirroring symmetry. The results depicted in figure 2.4a are the same if $\phi_b = 0$ instead of $\phi_a = 0$ and the relative phases ϕ_a, ϕ_c are varied.

(ii) $\boldsymbol{\phi_c} = 0$.
In this scenario I explore how the largest values of $\langle \Delta \mathrm{E} \rangle_{\mathrm{coh}}$, with sign, modify by varying the values of the phases ϕ_a and ϕ_b across the range $[0, 2\pi]$; see figure 2.4b. Unlike the symmetry observed in figure 2.4a, a different pattern emerges, whereby the mirroring symmetry line is given by the condition $\phi_a = \phi_b$.

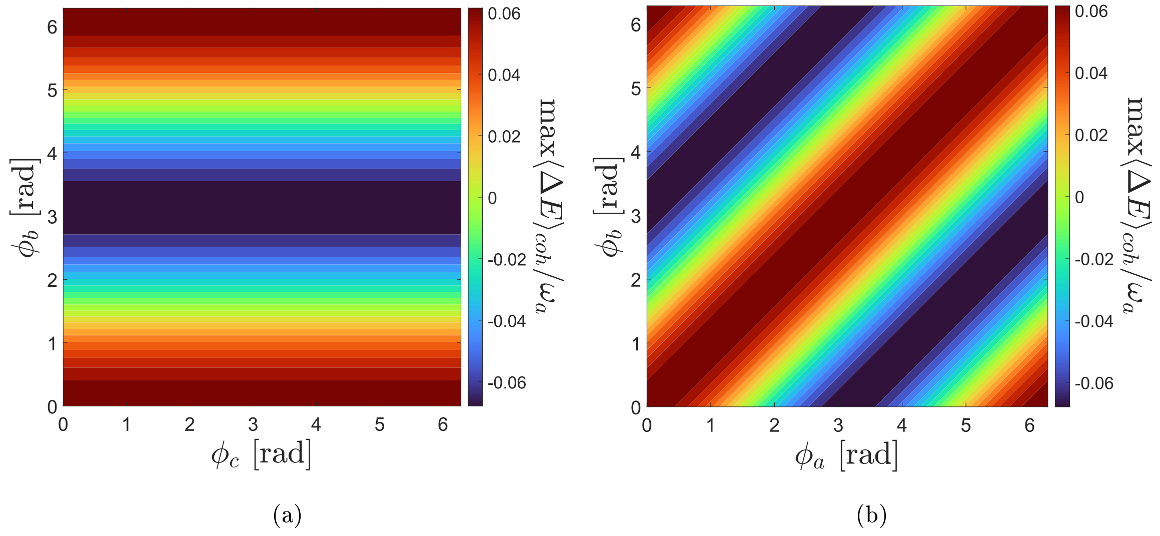

(a) (b)

Figure 2.4: *Largest values of $\langle \Delta \mathrm{E} \rangle_{\mathrm{coh}}$ including its sign, re-scaled by ω_a, as a function of the relative phases ϕ_b, ϕ_c [panel (a)], and ϕ_a, ϕ_b [panel (b)]. In both panels the value of p has been set to -0.5, $\bar{n} = 3$, $\rho_{cc} = 0.4$, and $\rho_{aa} = \rho_{bb} = 0.3$.*

I recall that in figure 2.4 the value of p has been set to -0.5. However, if one is free to also vary p, then it would be observed that the sign of p is responsible to affect the sign of $\langle \Delta \mathrm{E} \rangle$, such that whenever $p < 0$ the sign of $\langle \Delta \mathrm{E} \rangle$ is the same in figure 2.4, while for $p > 0$ the condition is reversed. Similarly, the magnitude of p is responsible to modify the magnitude of $\langle \Delta \mathrm{E} \rangle$, such that decreasing the magnitude of p decreases the largest value of $|\langle \Delta \mathrm{E} \rangle|$. This behaviour has been previously noticed in figure. 2.1. Before proceeding, it is also worth stressing that selecting $\phi_a = 0$, $\phi_b = \pi$, $\phi_c = 0$ in $|\psi_0\rangle$ leads to the maximization of $-\langle \Delta \mathrm{E} \rangle$ in figure 2.4.

I now analyze how $\langle \Delta \mathrm{E} \rangle$ varies for different values of the populations $\rho_{aa}(0)$ and $\rho_{bb}(0)$ pertaining to the excited states $|a\rangle$ and $|b\rangle$. The population in the ground level $\rho_{cc}(0)$ is not directly considered, as it is predetermined by $\bar{n}$, in order to satisfy the condition $\langle \Delta \mathrm{E} \rangle_{\mathrm{diag}} = 0$. For instance, in the scenario with $p = -0.5, \bar{n} = 3 \Rightarrow \rho_{cc}(0) = 0.4$, I vary only the value of the population $\rho_{aa}(0)$; indeed, $\rho_{bb}(0)$ changes according to the constraint $\rho_{bb}(t) = 1 - \rho_{aa}(t) - \rho_{cc}(t)$ for any t. The results depicted in figure 2.5 illustrate $\max\langle \Delta \mathrm{E} \rangle_{\mathrm{coh}}$ as a function of $\rho_{aa}(0)$, with $\phi_b = 0, \pi/4, \pi/2, 3\pi/4, \pi$. While $\rho_{cc}(0)$ may affect $\langle \Delta \mathrm{E} \rangle_{\mathrm{diag}}$, the initial populations $\rho_{aa}(0), \rho_{bb}(0)$ of the excited states impact $\langle \Delta \mathrm{E} \rangle_{\mathrm{coh}}$. Specifically, $\langle \Delta \mathrm{E} \rangle_{\mathrm{coh}}$ is zero when the three-level system is initialized with one among $\rho_{aa}(0), \rho_{bb}(0)$ is set to zero. Additionally, it can be observed that the maximum value of $\langle \Delta \mathrm{E} \rangle_{\mathrm{coh}}$ is obtained when $\rho_{aa}(0) = \rho_{bb}(0)$. The imbalance in favor of one over the other decreases $\max\langle \Delta \mathrm{E} \rangle_{\mathrm{coh}}$. As

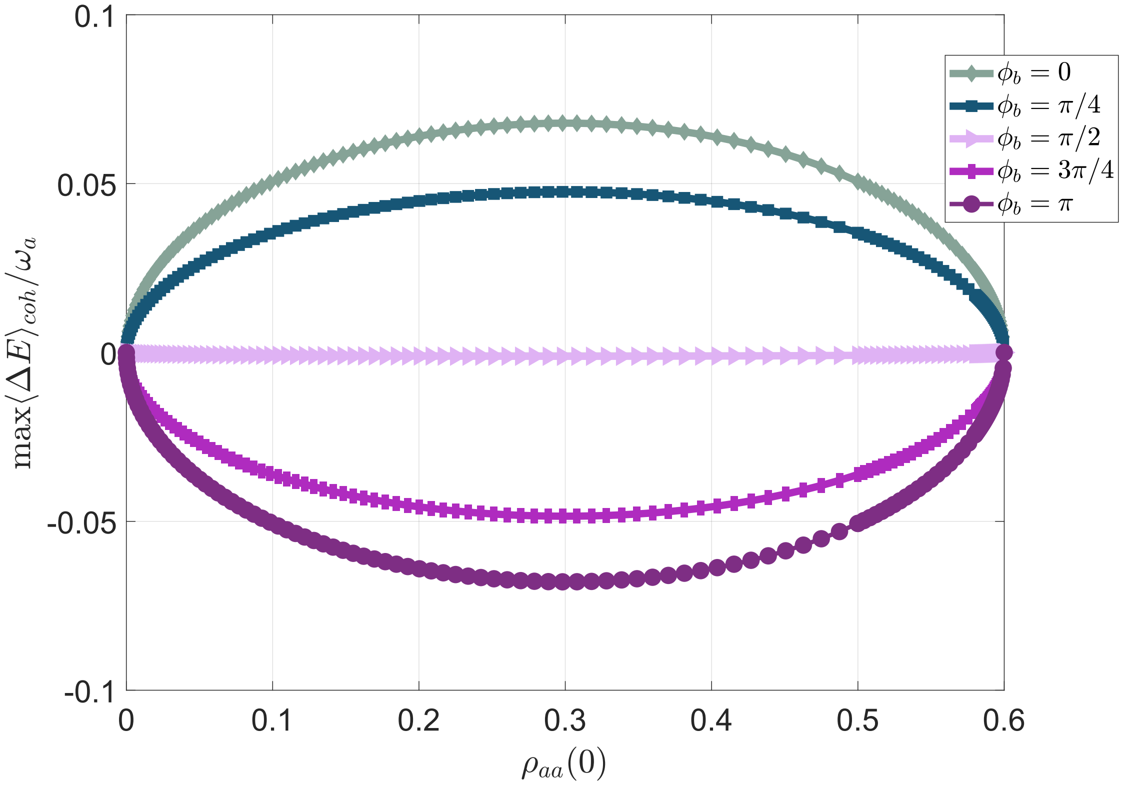

Figure 2.5: *Maximum value of $\langle \Delta \mathrm{E} \rangle_{\mathrm{coh}}$ as a function of $\rho_{aa}(0)$, initial population of the excited state $|a\rangle$. The ground state is fixed at $\rho_{cc}(0) = 0.4$ and the relative phases are $\phi_a = \phi_c = 0$, while $\rho_{bb}(0) = 1 - \rho_{cc}(0) - \rho_{aa}(0)$. The alignment parameter p is set to $p = -0.5$. Different values of ϕ_b are taken into account.*

p	$\eta_{\max}$	$\dfrac{\widetilde{t}\gamma}{2\pi}$
-1	6%	> 0.40
-0.75	4%	0.20
-0.5	2%	0.17
-0.25	1%	0.16

Table 2.1: *Achievable maximum thermodynamic efficiency of the process and time instants at which it is obtained, for various values of p.*

in figure 2.4a, varying ϕ_b from 0 to π enables a transition from the condition of maximum absorbed energy ($\phi_b = 0$) to maximum energy in excess ($\phi_b = \pi$), passing through a regime where $\langle \Delta \mathrm{E} \rangle_{\mathrm{coh}} = \langle \Delta \mathrm{E} \rangle_{\mathrm{diag}} = \langle \Delta \mathrm{E} \rangle = 0$ ($\phi_b = \pi/2$).

To sum-up, the optimal initial state configuration is achieved by setting the populations $\rho_{aa}(0), \rho_{bb}(0) \neq 0$ and $\rho_{aa}(0) = \rho_{bb}(0)$, while the value of $\rho_{cc}(0)$ is dictated by the $\bar{n}$ that allows for $\langle \Delta \mathrm{E} \rangle = \langle \Delta \mathrm{E} \rangle_{\mathrm{coh}}$. Finally, regarding the relative phases ϕ_a, ϕ_b, ϕ_c entering the initial wave-function $|\psi_0\rangle$, setting all the three to zero means maximum absorbed energy, whereas choosing $\phi_b = \pi$ (with $\phi_a = \phi_c = 0$) entails the maximum amount of excess energy.

2.2.4 Efficiency of the process

The assessment of the thermodynamic efficiency is crucial in any energy conversion process, to gauge the performance in transforming a form of energy (the input energy $\mathcal{E}_{\mathrm{in}}$) in another (energy in excess $\mathcal{E}_{\mathrm{exc}}$) for practical uses. The efficiency is generally defined as follows:

$$\eta \equiv \frac{\mathcal{E}_{\mathrm{exc}}}{\mathcal{E}_{\mathrm{in}}} \,. \tag{2.49}$$

In this case study, the excess energy is given by the quantity $-\langle \Delta \mathrm{E}(t) \rangle > 0$, where only the contribution from the off-diagonal elements of $\hat{\rho}_S$ accounts. Conversely, the energy that drives the system, which originates from the incoherent field, is $\mathcal{E}_{\mathrm{in}} = \bar{n}\hbar\omega_{ac}$ that corresponds to the average energy of the photons impinging on the system. Indeed, as previously done, I assume $\omega_{ac} \approx \omega_{bc}$. Hence,

$$\eta(t) = \frac{-\langle \Delta \mathrm{E}(t) \rangle}{\bar{n}\hbar\omega_{ac}} \,. \tag{2.50}$$

Equation (2.50) reveals that the time dependence of the efficiency follows the one of $\langle \Delta \mathrm{E} \rangle$ depicted in figure 2.1. Consequently, the efficiency reaches its peak when $\langle \Delta \mathrm{E} \rangle$ is maximized with sign, which occurs at a specific instant t denoted as $\widetilde{t}$. Notably, in the scenario with $p = -1$, both η and $-\langle \Delta \mathrm{E} \rangle$ attain a maximum quasi-stationary value.

Based on the optimization analysis in Subsection 2.2.3, I focus on the condition yielding the maximum amount of energy in excess, given by $\rho_{aa}(0) = \rho_{bb}(0) = 0.3$ with $\rho_{cc}(0) = 0.4$, $\bar{n} = 3$ and $\phi_a = \phi_c = 0, \phi_b = \pi$. In table 2.1 the achievable maximum efficiency is reported together with the time instants at which it is obtained, for various values of p. I conclude by emphasising that the energy for preparing the initial state of the three-level system was not included among the costs in the calculation of the efficiency. This is because I am implicitly assuming to work in a condition where the preparation of a superposition of Hamiltonian eigenstates as the initial state is given for granted. However, this assumptions shall be properly calibrated when dealing with the experimental realization of a process for Fano coherence generation.

2.2.5 Discussion

Throughout this chapter, I analyzed the energetics of a V-type three-level system exhibiting noise-induced Fano coherence due to interaction with a non-coherent source. The motivation for this analysis arises from the question: "To what extent the process generating Fano coherence can be considered genuinely quantum?" The answer to this question would constitute a first attempt to certify the quantumness of a process driven by an incoherent field that induces quantum effects in a nonequilibrium regime.

To address this, I determined the Kirkwood-Dirac quasiprobability distribution associated to the time-dependent energy changes in the system while exposed to incoherent radiation. If the real part of some quasiprobability is negative, or even some quasiprobability is complex, then one can witness the onset of a genuine quantum effect linked to quantum interferences. Necessary condition for that is the non-commutativity of the initial state of the quantum system with the Hamiltonian $\hat{H}_S$ at the beginning of the dynamical transformation (recall that in the process generating Fano coherence, the Hamiltonian is time-independent). Thus, as expected, initializing the three-level system in a superposition of the Hamiltonian eigenstates leads to negative quasiprobabilities with zero imaginary parts for a precise set of parameters. Initializing the system in the ground state of $\hat{H}_S$ does not lead to the same result. In this regard, further studies are essential to understand the interplay between the generation of Fano coherences and the presence of quantum coherences in the initial state. These investigations will elucidate how different types of coherences impact the quantum dynamics of the open system and contribute to the negativity in the KDQ distribution characterizing energy change fluctuations.

Under the same parameter setting and initial state choice (with $\bar{n} = 3$ and $\rho_{cc}(0) = 0.4$), I found that $\langle \Delta \mathrm{E} \rangle = \langle \Delta \mathrm{E} \rangle_{\mathrm{coh}} \leq 0$ within a certain time interval for any value of the alignment parameter p, except $p = 0$. Interestingly, despite the incoherence of the input light source, the maximum efficiency of the thermodynamic process goes up to 6%, and becomes quasi-stationary for $p = -1$. These findings motivate further investigation into designing and optimizing (coherent or incoherent) coupling with an external load, which could function as an energy battery [89] or quantum flywheel [90]. The latter can be minimally modeled by using a two-level system either coherently or incoherently "connected" to the V-type three-level system. This approach could align the thermodynamic study of this thesis with the research described by Svidzinsky *et al.* in [34], which contemplates a five-level system where the presence of Fano coherence in the V-type system enhances the photocurrent that passes through a two-level system representing the external load.

Finally, the results presented in this chapter could be experimentally validated via reconstructing quasiprobabilities for the energy change statistics. As recently shown in [36, 65], reconstruction procedures based on projective measurements or interferometric schemes can be employed for this purpose. Implementing a V-type three-level system conducive to Fano coherence is, in principle, feasible using an atomic platform, such as a gas of a suitable atomic species maintained at a constant temperature, as shown in the next chapter. Preparing the system's initial state in a superposition of Hamiltonian eigenstates can be achieved using independent coherent light sources that are quasi-resonant with the two dipole transitions before interacting with the incoherent radiation. The choice between a cold or hot gas can be crucial, since lower temperatures may enhance parameter tunability. Additionally, generating Fano coherence might require the polarization of the incoherent radiation field, depending on the selected atomic species [30, 51].

3 | Implementation on ^{87}Rb atoms: theoretical and experimental results

Despite extensive research conducted on the topic, an experiment proving the existence of Fano coherences produced by the interplay of incoherent pumping and spontaneous emission is still missing, based on current knowledge. This phenomenon has a broad field of applicability, spanning from quantum heat engines to photoconversion devices and biological systems that interact with the environment and radiation. All these systems could potentially benefit from the presence of Fano coherences, which might enable more efficient exploitation of the energy supplied by external driving.

Currently, an atomic platform stands as the most suitable candidate for realizing a proof-of-principle experiment, given the possibility to finely adjust the parameters that define a three-level V-type system. In Chapter 1, for example, the role of the splitting Δ between excited levels has been investigated as well as its influence on the dynamics of populations and coherences. Implementing the V-type system on magnetic sublevels in an atomic structure allows for tuning the splitting by simply varying a uniform magnetic field. Previous proposals, such as those by Dodin *et al.* [29] and subsequently by Koyu *et al.* [30], suggested experiments with beams of Calcium atoms excited by a broadband polarized laser within a uniform magnetic field. According to their proposal schemes, coherence can be observed through resolved detection of the fluorescence signal [29] or by measuring the difference in the fluorescence signals emitted by the atoms driven by x-polarized versus isotropic incoherent light [30]. Similarly, in [32] the authors propose an experimental scenario for measuring steady-state noise-induced Fano coherences in a Λ-type three-level system, using metastable He(2^3S_1) atoms. Additionally, recent experiments in a magneto-optical trap of Rubidium atoms have detected an increase in beat amplitude due to collective light emission, analogous to Fano coherences from interactions with vacuum modes, as reported in [35].

In my case study I chose to implement the V-type three-level system in the hyperfine structure of Rubidium-87 (^{87}Rb) atoms. There are several compelling reasons for selecting ^{87}Rb as one of ideal candidate for a proof-of-principle experiment to detect Fano coherence. Firstly, the isotope ^{87}Rb has a well-documented atomic structure, with detailed knowledge of its energy levels and transition properties [41, 91]. Moreover, it features a rich hyperfine structure due to its nuclear spin ($I = 3/2$), providing multiple energy levels suitable for creating the V-system. From a technical standpoint, the transitions between the $5^2S_{1/2}$

ground state manifold and the $5^2P_{1/2}$ and $5^2P_{3/2}$ excited state manifolds, known as $D1$ and $D2$ lines respectively, are well-matched to commercially available diode lasers ($\lambda = 795$ nm and $\lambda = 780$ nm, respectively). This accessibility simplifies the experimental setup involving laser excitation and control.

Although Rubidium's cooling and trapping technologies are well-developed, enabling cold atom experiments, the designed setup utilizes hot atomic ensembles. This approach is driven by several factors: it simplifies the experimental design and reduces costs compared to ultra-cold conditions. The main objective at this stage is to establish the feasibility of detecting Fano coherence. Hot atomic ensembles offer a practical and robust initial validation before transitioning to more sophisticated cold atom configurations. Additionally, conducting the experiment in less-controlled environmental conditions better simulates the real-world scenarios of future applications.

The detection of noise-induced Fano coherence is performed by driving the V-type system with a polarized broadband laser and measuring the spatial anisotropy in the fluorescence emitted by the atoms, a method proposed in [29]. The measurement is compared with one conducted under conditions of no Fano coherence. Section 3.1 introduces the hyperfine atomic structure of ^{87}Rb, where the V-type three-level system is realized. Moreover, it presents an optimization analysis focused on maximizing ρ_{ab} by adjusting the parameters that influence atomic dynamics. Subsequently, the relationship between Fano coherence and the anisotropic fluorescence emission is thoroughly examined, providing a theoretical foundation for the experimental observations. In Section 3.2, the experimental setup designed to detect Fano coherence is described in detail. This includes the arrangement of optical components and atomic sample, the configuration of the coils for uniform magnetic field along z-axis, and the methodologies employed to excite the atoms and measure their fluorescence. Finally, Section 3.3, outlines preliminary measurements obtained from initial trials, highlighting the feasibility and effectiveness of the proposed detection technique. These preliminary findings are crucial as they offer insights into potential adjustments and refinements needed to optimize the experimental conditions for observing Fano coherence in future experiments.

3.1 ^{87}Rb atoms as V-type three level sysyems

Rubidium (Rb) is a chemical element, belonging to the group of *alkali metals*, along with lithium (Li), sodium (Na), potassium (K), caesium (Cs) and francium (Fr). These elements are categorized under group 1 in the periodic table, each possessing a single electron in their outermost s-orbital. Natural rubidium on Earth consists primarily of two isotopes: 72% is the stable isotope ^{85}Rb, while 28% is the slightly radioactive ^{87}Rb. The atomic structure of rubidium is rather complex and it is briefly described in this section as long as the choice of the levels for the implementation of the V-system. Once these atomic parameters are defined, the next step involves optimizing the system dynamics parameters to achieve the optimal coherence signal in the emission spectrum.

3.1.1 V-type three level systems in the hyperfine structure of ^{87}Rb atoms

The atomic structure of ^{87}Rb atoms can be treated in different energy description. The ground energy level of the outer electron of this atomic species is denoted as $5^2S_{1/2}$. In this notation:

- the principal quantum number is $n = 5$;
- S identify the s-orbital angular momentum number, that is $L = 0$;
- the superscript (2) indicates the multiplicity of the state, which is given by $2S + 1$. Here, S is the total spin quantum number, related to the spin angular momentum $\mathbf{S}$. For a single electron, as in this case, S is equal to $S = 1/2$. Thus, $2S + 1 = 2$, indicating a doublet state, with two possible spin orientations.
- The subscript (1/2) specifies the total angular momentum $\mathbf{J}$, which is the vector sum of the orbital angular momentum $\mathbf{L}$ and the spin angular momentum $\mathbf{S}$:

  $$\mathbf{J} = \mathbf{L} + \mathbf{S} \tag{3.1}$$

  and the corresponding quantum number J is in the range [91]:

  $$|L - S| \leq J \leq L + S. \tag{3.2}$$

In this context, the usual quantum numbers $n, l, m, \ldots$ are expressed with capital letters to refer to the more general case of multi-electron atoms, where atomic quantities represent total electron values. Hence, L is the quantum number for the total electron orbital angular momentum [41].

The interaction between the electron's spin angular momentum $\mathbf{S}$ and its orbital angular momentum $\mathbf{L}$, which arises from the electron's motion around the nucleus, results in what is known as *spin-orbit coupling*. This coupling causes the apparent degenerate energy levels to split into multiple closely spaced levels, giving rise to the *fine structure* of the atom. An illustrative example of the fine structure splitting is observed in the first excited state of the ^{87}Rb atom. In the ground state of ^{87}Rb, where $L = 0$ and $S = 1/2$, the total angular momentum J is 1/2, showing no splitting. However, in the first excited state 5^2P, where $L = 1$ and $S = 1/2$, J can take the values 1/2 or 3/2. Consequently, the 5^2P state splits into two fine structure levels: $5^2P_{1/2}$ and $5^2P_{3/2}$. The energy levels shift according to the value of J, causing the $L = 0 \rightarrow L = 1$ transition, known as the D line, to split into two components: the *D1 line* ($5^2S_{1/2} \rightarrow 5^2P_{1/2}$) and the *D2 line* ($5^2S_{1/2} \rightarrow 5^2P_{3/2}$) [91].

At a deeper level, the interaction between the magnetic field generated by the electron's total angular momentum $\mathbf{J}$ and the magnetic moment of the nucleus (due to its nuclear spin $\mathbf{I}$) leads to the formation of the *hyperfine structure*. For ^{87}Rb, the nuclear spin quantum number is $I = 3/2$. This interaction is much weaker than the spin-orbit coupling responsible for the fine structure, but still causes additional splitting of the energy levels based on the nuclear spin. This hyperfine splitting is characterized by the total atomic angular momentum **F** [91]:

$$\mathbf{F} = \mathbf{J} + \mathbf{I}. \tag{3.3}$$

The possible values of the quantum number F are:

$$|J - I| \leq F \leq J + I. \tag{3.4}$$

For the ground state of ^{87}Rb, where $J = 1/2$ and $I = 3/2$, F can be either 1 or 2. In the case of the excited state for the $D2$ line ($5^2P_{3/2}$), F can take values of 0, 1, 2, or 3, whereas for the $D1$ line ($5^2P_{1/2}$), F is either 1 or 2. The detailed fine and hyperfine structures for the $D1$ and $D2$ lines are comprehensively depicted in reference [91].

Each hyperfine energy levels contains $2F + 1$ magnetic sublevels, distinguished by the magnetic quantum number m_F. In the absence of external magnetic fields, these sublevels are degenerate. However, applying an external magnetic field along one axis (e.g. the z-axis) breaks this degeneracy. The energy shift of the levels due to a weak magnetic field is linear and can be described as [41, 91]:

$$\Delta \mathrm{E}_{|F\ m_F\rangle} = \mu_B\, g_F\, m_F\, B_z, \tag{3.5}$$

where μ_B is the Bohr magneton and g_F is the hyperfine Landé g-factor. When the energy shift is small compared to the hyperfine splittings the regime is called *anomalous Zeeman effect*, and the linearity expressed in equation (3.5) holds. For stronger magnetic fields, the regimes are known as the *Paschen-Back effect* and *normal Zeeman regimes* for fine structure. In these regimes equation (3.5) no longer applies and the calculation of the energy shift becomes more complex [41, 91].

To implement a V-type three-level system interacting with an optical field, it is crucial to identify the allowed atomic transitions. This involves understanding the *selection rules* that determine "dipole allowed" transitions, ensuring that the dipole matrix element $\boldsymbol{\mu}_{lj} = \langle l|e\mathbf{r}|j\rangle$ is non-zero. The selection rules can be summarized as follows:

(i) **Fine-structure selection rules:** for transitions between fine-structure states of the form $|J\ m_J\rangle \rightarrow |J'\ m_{J'}\rangle$ the rules are:

$$J = J' \quad \text{or} \quad J = J' + 1 \tag{3.6}$$

$$m_J = m'_J \quad \text{or} \quad m_J = m_{J'} + 1 \tag{3.7}$$

$$J \neq J' \quad \text{if} \quad m_J = m_{J'} = 0. \tag{3.8}$$

Transitions where $J = J' = 0$ are forbidden, and any transitions not obeying to these rules have vanishing dipole matrix elements, making them dipole forbidden.

(ii) **Hyperfine-structure selection rules:** for transitions between hyperfine-structure states of the form $|F\ m_F\rangle \rightarrow |F'\ m_{F'}\rangle$ the selection rules are:

$$F = F' \quad \text{or} \quad F = F' + 1 \tag{3.9}$$

$$m_F = m_F' \quad \text{or} \quad m_F = m_{F'} + 1 \tag{3.10}$$

$$F \neq F' \quad \text{if} \quad m_F = m_{F'} = 0. \tag{3.11}$$

Again, $F = F' = 0$ is a forbidden transition. Any transitions not adhering to these rules have vanishing dipole matrix elements, making them dipole forbidden.

Assuming a magnetic field $\mathbf{B}$ along the z-axis, the degeneracy between magnetic sublevels (both in the fine and hyperfine structure) is broken. When light interacts with transitions between these magnetic sublevels, the selection rules in equations (3.7) and (3.11) must be observed. It's important to note that the driving radiation must also comply polarization rules to properly excite the selected transitions. Transitions where $\Delta m_F = m_{F'} - m_F = 0$, i.e., $m_F = m_{F'}$, are known as π *transitions.* The latter are coupled by linearly polarized radiation parallel to the magnetic field (along the z-axis in this case), i.e., $\boldsymbol{\epsilon}_{\mathbf{k},\lambda} = \boldsymbol{\epsilon}_z = [0, 0, 1]$, with the wavevector $\mathbf{k}$ oriented orthogonal to $\mathbf{B}$. Transitions where $\Delta m_F = m_{F'} - m_F = +1$ are referred to as σ^+ *transitions.* These transitions are coupled by circularly polarized light in the x-y plane, whose unitary vector is:

$$\boldsymbol{\epsilon}_+ = \left[-\frac{1}{\sqrt{2}}, -i\frac{1}{\sqrt{2}}, 0\right] \tag{3.12}$$

and the wavevector $\mathbf{k}$ is parallel to the magnetic field. Lastly, transitions where $\Delta m_F = m_{F'} - m_F = -1$ are referred to as σ^- transitions, and they are coupled by circularly polarized light in the x-y plane, whose unitary vector is:

$$\boldsymbol{\epsilon}_- = \left[\frac{1}{\sqrt{2}}, -i\frac{1}{\sqrt{2}}, 0\right] \tag{3.13}$$

and the wavevector $\mathbf{k}$ is again parallel to the magnetic field.

The hyperfine structure is particularly suitable for implementing V-type systems to detect Fano coherence. Hyperfine levels are responsive to low magnetic fields, enabling precise control of energy levels through the anomalous Zeeman effect, where hyperfine energy levels shift linearly with the applied field. Additionally, the smaller hyperfine splittings facilitate the use of microwave or radiofrequency fields for manipulation and preparation. Nonetheless, it is crucial to ensure that the hyperfine transitions are sufficiently isolated, meaning the hyperfine ground and excited manifolds must be spaced far enough from other hyperfine manifolds to prevent the involvement of additional transitions. On this point, the broadband radiation used should not be excessively broad to avoid exciting other hyperfine or fine levels. The $D1$ line is ideal for this purpose, with just well separated two hyperfine manifolds ($F = 1$, $F = 2$) in the ground state, with 6.83 GHz frequency splitting, and two hyperfine manifolds ($F' = 1$, $F' = 2$) in the excited state separated by 814 MHz. Notably, both the excited and ground manifolds can be resolved even at high temperatures, despite Doppler broadening due to atomic motion.

Among the four possible $F \rightarrow F'$ transitions, the hyperfine transition $F = 1 \rightarrow F' = 1$

is selected, since it contains the least number of magnetic sublevels, specifically $2F+1=3$ sublevels. Within this transition, the V-scheme is implemented as illustrated in figure 3.1. The ground state $|c\rangle$ corresponds to the $|F=1\ m_F=0\rangle$ atomic level, while the two excited states $|a\rangle$ and $|b\rangle$ are represented by the $|F'=1\ m_{F'}=-1\rangle$ and $|F'=1\ m_{F'}=+1\rangle$ levels, respectively. The selected transitions $|a\rangle \leftrightarrow |c\rangle$ and $|b\rangle \leftrightarrow |c\rangle$ have $\Delta m_F=-1$ and $\Delta m_F=+1$, respectively. Thus, they are driven by circularly polarized light in the x-y plane, with the wavevector $\mathbf{k}$ along the z-axis, adhering to the selection rules. The transition dipole moment vectors are:

$$\boldsymbol{\mu}_{ac} = |\boldsymbol{\mu}_{ac}| \left[\frac{1}{\sqrt{2}}, -i\frac{1}{\sqrt{2}}, 0\right] \tag{3.14}$$

$$\boldsymbol{\mu}_{bc} = |\boldsymbol{\mu}_{bc}| \left[-\frac{1}{\sqrt{2}}, -i\frac{1}{\sqrt{2}}, 0\right]. \tag{3.15}$$

Here, $|\boldsymbol{\mu}_{ac}|$ and $|\boldsymbol{\mu}_{bc}|$ are the electric dipole moment matrix element. Their values can be found in [91], where all the dipole matrix elements for specific $|F\ m_F\rangle \rightarrow |F'\ m_{F'}\rangle$ are listed. In this case study, $|\boldsymbol{\mu}_{ac}| = |\boldsymbol{\mu}_{bc}|$ and their values are reported in table 3.1.

The vectors $\boldsymbol{\mu}_{ac}$ and $\boldsymbol{\mu}_{bc}$ are orthogonal, thus $p=0$ and no interference between the pumping paths and decaying paths occurs when using an isotropic unpolarized radiation. To induce Fano interference between the pumping paths, polarized radiation is required. For this purpose, I have chosen the polarization to be aligned along the x-axis, in an horizontal-vertical basis, which is represented by the unitary vector:

$$\boldsymbol{\epsilon}_\lambda = \boldsymbol{\epsilon}_x = [1, 0, 0] \tag{3.16}$$

or as a linear combination:

$$\boldsymbol{\epsilon}_x = \sqrt{2}\left(\left[\frac{1}{\sqrt{2}}, -i\frac{1}{\sqrt{2}}, 0\right] - \left[-\frac{1}{\sqrt{2}}, -i\frac{1}{\sqrt{2}}, 0\right]\right). \tag{3.17}$$

The last expression indicates that linearly polarized light can drive both $\boldsymbol{\mu}_{ac}$ and $\boldsymbol{\mu}_{bc}$ transitions.

The selected V-type three-level system is symmetric, implying that $\gamma_a = \gamma_b$. As discussed in [41, 91], all the excited state hyperfine sublevels decay at the same rate Γ, which is the decay rate of the $D1$ line, with population decay branching into various ground state

Quantity	Magnitude
Transition $F=1 \rightarrow F'=1$ frequency, ω_0 [THz]	377.11226
Dipole matrix element for D1 line, $\lvert\langle J\|\boldsymbol{\mu}\|J'\rangle\rvert^2$ [C·m]	2.537×10^{-29}
Dipole matrix elements, $\lvert\boldsymbol{\mu}_{ac}\rvert, \lvert\boldsymbol{\mu}_{bc}\rvert$ [C·m]	$\sqrt{\frac{1}{12}}\,\lvert\langle J\|\boldsymbol{\mu}\|J'\rangle\rvert^2$
Decay rate D1 line, Γ [MHz]	$2\pi \cdot 5.75$
Landé g-factor $F'=1$ manifold $D1$ line, $g_{F'}$ [-]	$-1/6$

Table 3.1: *Values of relevant physical quantities for* ^{87}*Rb.*

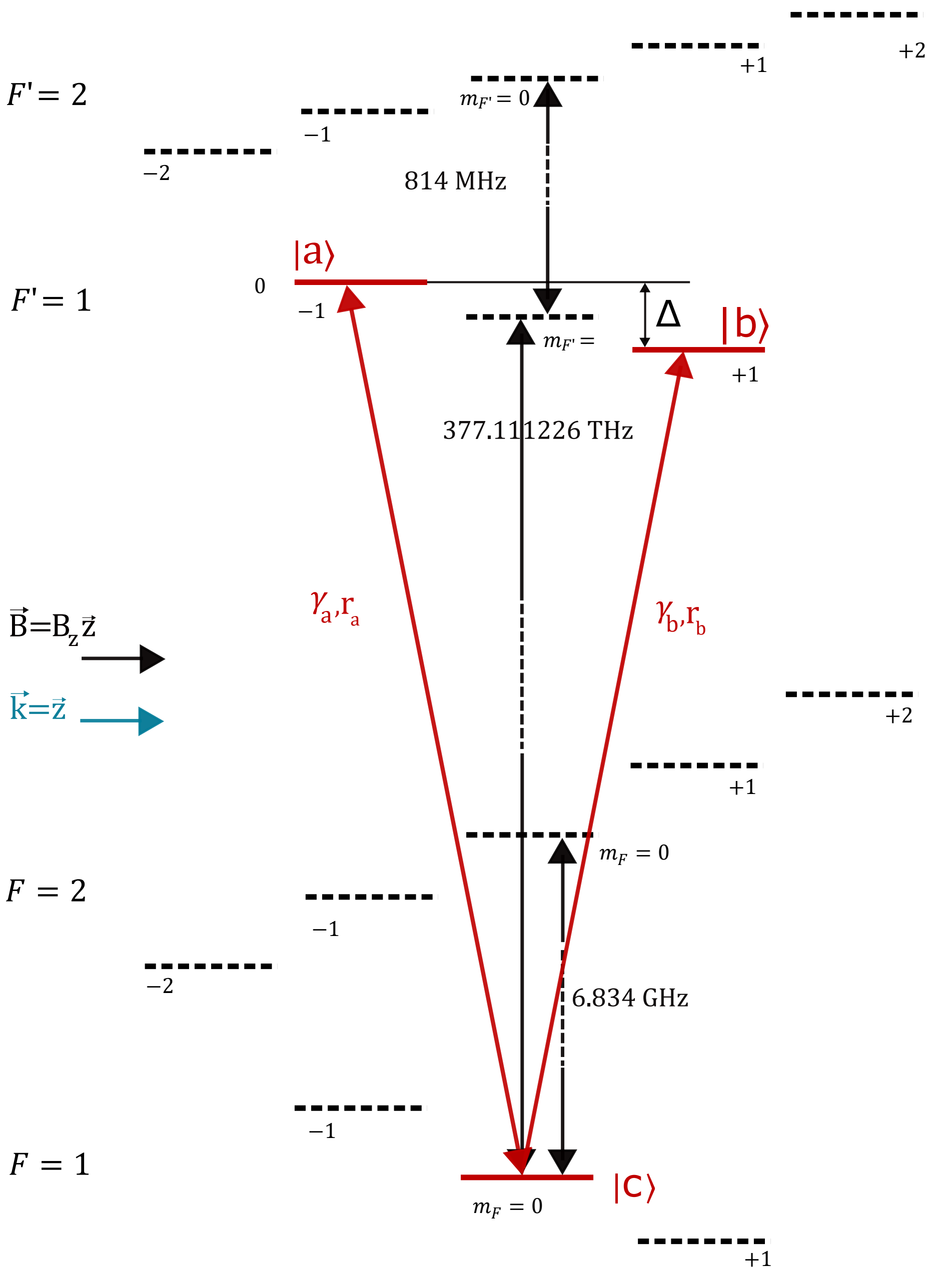

Figure 3.1: *V-type three level system within the D1 line transition of ^{87}Rb. The ground state $|c\rangle$ corresponds to the hyperfine magnetic sublevel $|F = 1\ m_F = 0\rangle$, while the two excited states $|a\rangle$ and $|b\rangle$ are represented by the $|F' = 1\ m_{F'} = -1\rangle$ and $|F' = 1\ m_{F'} = +1\rangle$, respectively. The red arrows represents the radiation processes involved: spontaneous emission from levels $|a\rangle$ and $|b\rangle$ to level $|c\rangle$ at rates γ_a, γ_b respectively; incoherent pumping and stimulated emission involving transitions $|a\rangle \leftrightarrow |c\rangle$ and $|b\rangle \leftrightarrow |c\rangle$ at rates r_a, r_b, respectively. The parameter Δ is the splitting between the excited levels: $\Delta = \omega_{ac} - \omega_{bc}$. In the figure the wavevector* **k** *of the radiation and the uniform magnetic field vector* **B** *are reported, as well as the frequency difference between the hyperfine manifolds of D1 line.*

sublevels. Hence:

$$\Gamma = \frac{\omega_0^3}{\hbar 3\pi\varepsilon_0 c^3}\frac{2J+1}{2J'+1}\left|\langle J||\boldsymbol{\mu}||J'\rangle\right|^2 = \gamma_a = \gamma_b \tag{3.18}$$

where $J = J' = 1/2$ for $D1$ line and $\langle J||\boldsymbol{\mu}||J'\rangle$ is the $D1$ matrix element, found in [91], and whose values is reported in table 3.1. Here, the definition of the decay rate expressed in equation (1.118) is used. From equation (3.18) it follows that $\bar{\gamma} = (\gamma_a + \gamma_b)/2 = \gamma_a = \gamma_b$.

The incoherent pumping rate r_l, with $l = a, b$, depends on both atomic properties and the radiation source used. In particular, it can be expressed in two ways: either as $r_l = \bar{n}\gamma_l$ or as $r_l = B_l \rho_\nu(\nu_{ac})$. In the latter, $\rho_\nu(\nu_{ac})$ is the spectral energy density of the broadband laser at the transition frequency $\omega_{ac} = 2\pi\nu_{ac} \approx \omega_{bc}$ and B_l is the Einstein B-coefficient, given by:

$$B_l = \frac{\pi|\boldsymbol{\mu}_{lc}|^2}{3\varepsilon_0}, \tag{3.19}$$

where $l = a, b$. Since $|\boldsymbol{\mu}_{ac}| = |\boldsymbol{\mu}_{bc}|$, it follows that $B_a = B_b$ and $r_a = r_b$, consistent with the symmetry of the system. For a broadband laser, the intensity can be approximated as follows [92]:

$$I_{laser} = c\int \rho_\nu(\nu)d\nu \approx c\rho_\nu(\nu_{ac})\Delta\nu_{laser}, \tag{3.20}$$

where the spectral density of the source is assumed to be relatively flat around the atomic transitions. The quantity $\Delta\nu_{laser}$ is the spectral width of the laser. This approximation holds when the laser's has a broader spectral width compared to the frequency separations Δ of the atomic transitions, aligning with the assumptions in the mathematical model. By selecting a value for $\bar{n}$ and knowing the bandwidth of the broadband laser $\Delta\nu_{laser}$, one can relate the average photon number to the laser intensity:

$$I_{laser} = c\rho_\nu(\nu_{ac})\Delta\nu_{laser} = c\frac{r_a}{B_a}\Delta\nu_{laser} = c\frac{\bar{n}\gamma_a}{B_a}\Delta\nu_{laser}. \tag{3.21}$$

Hence, the average photon number $\bar{n}$ results proportional to the intensity of the broadband source, as anticipated in Chapter 1. It is crucial to ensure that the laser intensity remains below the *saturation intensity* of the atomic transition, which is defined as [41, 91]:

$$I_{sat} = \frac{c\varepsilon_0\Gamma^2\hbar^2}{4|\boldsymbol{\epsilon}_x \cdot \boldsymbol{\mu}_{ac}|^2}. \tag{3.22}$$

If the laser intensity absorbed by the $|a\rangle \leftrightarrow |c\rangle$ transition exceeds saturation intensity, the atomic population levels involved can become saturated, leading to a range of effects, such as reduced absorption, altered emission properties and thus to the disruption of the noise-induced Fano coherence phenomenon. The same applies to the transition $|b\rangle \leftrightarrow |c\rangle$. Note that I_{sat} is the same for both transitions. Hence, there exists a maximum value of $\bar{n}$, above which the effects of saturation come into play.

Finally, the control on Δ is performed by manipulating a uniform magnetic field $\mathbf{B} = B_z\mathbf{z}$ along the z-axis. For a weak magnetic field, equation (3.5), can be expressed in terms of frequency, resulting in:

$$\hbar(\omega_{ac} - \omega_{bc}) = \hbar\Delta = \mu_B\, g_{F'}\,(m_{F'_{ac}} - m_{F'_{bc}})\,B_z = 2\mu_B\, g_{F'}B_z. \tag{3.23}$$

Hence,

$$\Delta = 2\frac{\mu_B}{\hbar}\, g_{F'}B_z, \tag{3.24}$$

where the Landé g-factor for the $F' = 1$ excited state manifold of the $D1$ line is listed in table 3.1 and can be found in [91].

In this subsection all the governing parameters have been defined as depending on the atomic species, the incoherent radiation source, and the external magnetic field. In the next subsection I analyze these parameters to determine the optimal conditions for maximizing Fano coherence and provide the corresponding solutions to the differential equations.

3.1.2 Theoretical prediction with ^{87}Rb atoms

The V-type three-level system, implemented in the hyperfine structure of ^{87}Rb atoms, interacts with a broadband laser, with the wavevector **k** along the z-axis and linear polarization along the x-axis. The dynamical regimes with anisotropic polarized radiation were analyzed in Subsection 1.4.2 of this thesis. It was observed that in the overdamped regime Fano coherence has a nonzero stationary values, which need to be maximized for effective detection.

Using the governing parameters specific to the implemented atomic system, I conduct an analysis based on the approach used in Subsection 1.4.2 for a general V-system. The parameters $\Delta/\bar{\gamma}$ and $\bar{n}$ are varied in the overdamped solutions region, to find where $\mathrm{Re}[\rho_{ab}]$ is maximized. In figure 3.2, the stationary values of $\mathrm{Re}[\rho_{ab}]$ are shown for different values of $\Delta/\bar{\gamma}$ and $\bar{n}$. The maximum value of $\bar{n}$ in this scenario is $\bar{n}_{\max} = 345$, above which the intensity exceeds the saturation intensity. It can be observed that large excited states splittings are detrimental to stationary Fano coherence. For this reason $0 < \Delta/\bar{\gamma} < 1$ is selected as the range of interest. Regarding the intensity $\bar{n}$, higher values result in greater stationary values of $\mathrm{Re}[\rho_{ab}]$. However, beyond a certain level, the increase in $\mathrm{Re}[\rho_{ab}]_{t\to\infty}$ becomes less significant. For example, $\mathrm{Re}[\rho_{ab}]_{t\to\infty}$ at $\bar{n} = 100$ differs by only 4% from its value at $\bar{n}_{\max} = 345$, whereas $\mathrm{Re}[\rho_{ab}]_{t\to\infty}$ at $\bar{n} = 5$ differs by 45% from its value at $\bar{n} = 100$.

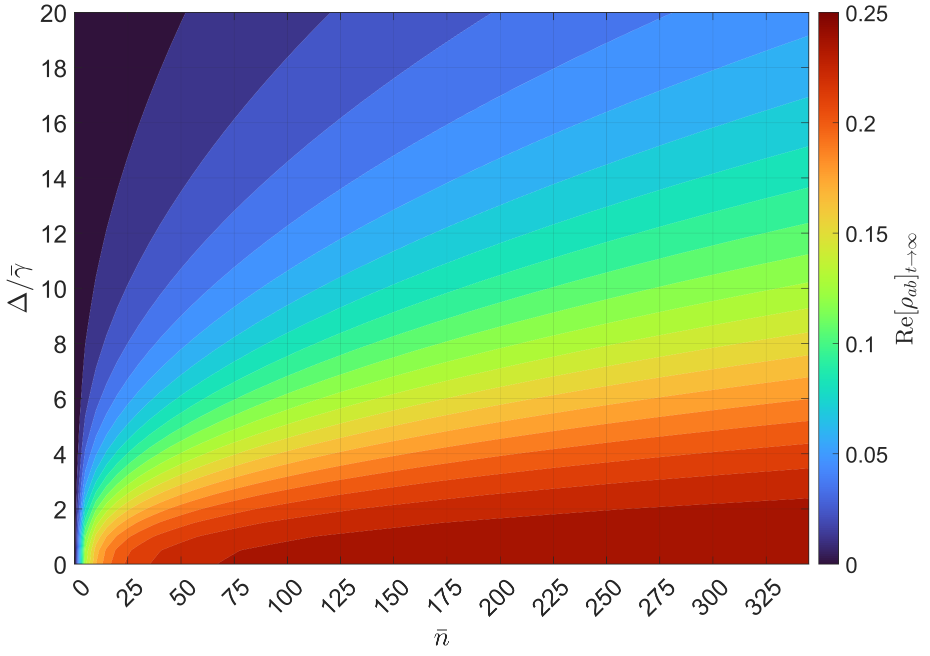

Figure 3.2: *Stationary value of* $\mathrm{Re}[\rho_{ab}]$ *as a function of* $\bar{n}$ *and* $\Delta/\bar{\gamma}$ *with linearly polarized light along the x-axis.*

Therefore, preliminary measurements are restricted to values of $\bar{n}$ below 100.

Up to this point, I considered a sudden turn-on of radiation to generate Fano coherence. It is important to explore the effect of time-dependent radiation on $\rho_{ab}(t)$, particularly the impact of a slow turn-on. In the experimental setup, I periodically turn on the incoherent beam for a time interval $[0, t_1]$, and then turn it off for a time interval $[t_1, t_2]$ to allow the system to reinitialize to the ground state through relaxation processes. After the interval $[t_1, t_2]$ the radiation is turned on again, repeating the cycle. Turning off the radiation allows the system to return to the ground state, ensuring that each measurement cycle starts from the same initial conditions. This approach enhances the reliability and reproducibility of the results by ensuring that the observed phenomena originate from consistent starting conditions. The detection of the signal is performed with a photodiode, whose dynamics is slower than that of the system. In this way it is possible to average the signal over multiple cycles of turn-on and turn-off, reducing noise and improving the signal-to-noise ratio, leading to clearer and more accurate measurements of the coherence effects. Consequently, this technique provides a robust method for observing and analyzing Fano coherence in the experimental setup.

I modeled the incoherent time-dependent field following the theory discussed in [52]. The time dependency is incorporated into the average photon number as $\bar{n}(t) = \bar{n}f(t)$, where, differently from [52], I selected $f(t)$ to have the form of a sigmoid function:

$$f(t) = \frac{1}{1 + \exp\left[-20\,\frac{t-\tau_{on}/2}{\tau_{on}}\right]}, \tag{3.25}$$

where τ_{on} is the turn-on time scale. The choice of a sigmoid function ensures a smooth and gradual increase in the photon number, which is essential for avoiding abrupt changes in the field and for better reproducing realistic experimental conditions.

Dodin *et al.* in [52] explored the dynamics of an isotropic and unpolarized radiation field, comparing the effects of different turn-on time scales relative to the system's characteristic time scale τ_S. They found that in the overdamped regime, with $p = 1$ and $\tau_{on} \gg \tau_S$, the Fano coherence significantly diminishes, losing its quasi-stationary nature. Conversely, when $\tau_{on} \ll \tau_S$, the system's behavior aligns with the solutions derived under a time-independent field. In the latter scenario, the field reaches its steady state much faster than the system evolves, meaning the transient behavior of the field does not impact the system's dynamics. Thus, the V-system's evolution is governed predominantly by the steady state field rather than the transient field.

In the case of anisotropic polarized radiation with time-dependency, different behaviors are observed. By selecting values for $\Delta/\bar{\gamma}$ and $\bar{n}$ that yield overdamping solutions for the density operator elements, specifically $\Delta/\bar{\gamma} = 0.1$ and $\bar{n} = 25$, I examined scenarios where $\tau_{on} \ll \tau_S \approx 1/\bar{\gamma}$ and $\tau_{on} \gg \tau_S$, as illustrated in figure 3.3. It is evident that the stationary value of $\rho_{ab}(t)$ remains unaffected by a slow turn-on process, although the dynamics exhibit a slower evolution. By repeatedly switching on and off the radiation, an excessively slow switching process would result in a considerable loss of signal since the dynamics of coherence are significantly slower. Therefore, in the realized experimental

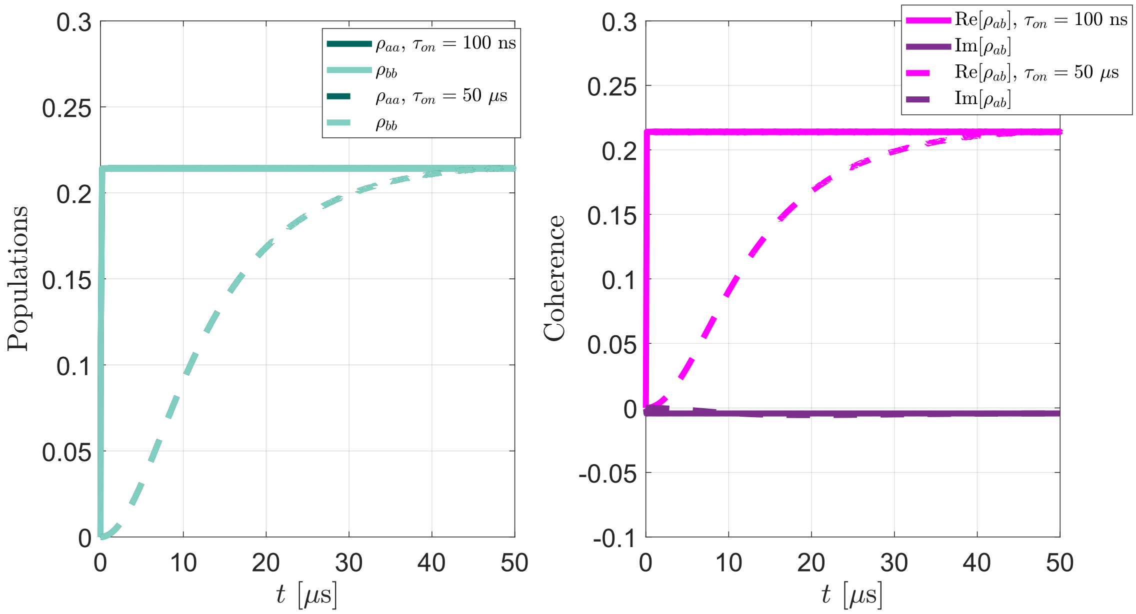

Figure 3.3: *Time evolution of excited states populations and real and imaginary part of quantum coherence between levels* $|a\rangle$ *and* $|b\rangle$*. The radiation intensity is set to fulfill the strong pumping regime* ($\bar{n} = 25$)*, with small splitting* ($\Delta/\bar{\gamma} = 0.1$)*. The turn-on time scale* τ_{on} *is varied as* $\tau_{on} \ll \tau_S$ *(solid line) and* $\tau_{on} \gg \tau_S$ *(dashed line).*

setup, acousto-optic modulators (AOMs) have been chosen to control the radiation, since they have on/off times around a hundred nanoseconds for small beam diameters. For the turning off process, the sigmoid function is modified as follows:

$$f(t) = 1 - \frac{1}{1 + \exp\left[-20\,\frac{t-(\tau_{\text{pulse}}-\tau_{on}/2)}{\tau_{on}}\right]} \tag{3.26}$$

with τ_{pulse} as the time duration of the single pulse. For example, a train of pulses with $\tau_{\text{pulse}} = 3\mu$s is realized, with light-off period of 2μs. The time scale for both turning on and off processes, τ_{on} and τ_{off} respectively, is set to 100 ns. Using these pulses, I obtain the signals shown in figure 3.4.

The challenge of how to detect noise-induced Fano coherence remains an open question. The following subsection addresses this aspect by detailing the angle-resolved fluorescence measurement technique. This method enables the isolation and analysis of specific contributions to the radiated emission from the atoms, directly linked to $\rho_{ab}(t)$.

3.1.3 Angle-resolved fluorescence detection

The detection of Fano coherence is related to the detection of resonance fluorescence from the excited atoms. Following the scheme proposed in [29], consider a fraction of ^{87}Rb atoms that are excited from the ground state $|c\rangle = |F = 1\ m_F = 0\rangle$, after the initial turn-on of the anisotropic and polarized incoherent radiation. As observed previously, the turn-on time can influence the values of Fano coherence. In particular, if the turn-on time is much longer than the time-scale of the system, $\tau_S \approx 1/\bar{\gamma}$, the Fano coherence exhibits slow dynamics, thereby decreasing the average detectable signal. To adress this issue, AOMs are used.

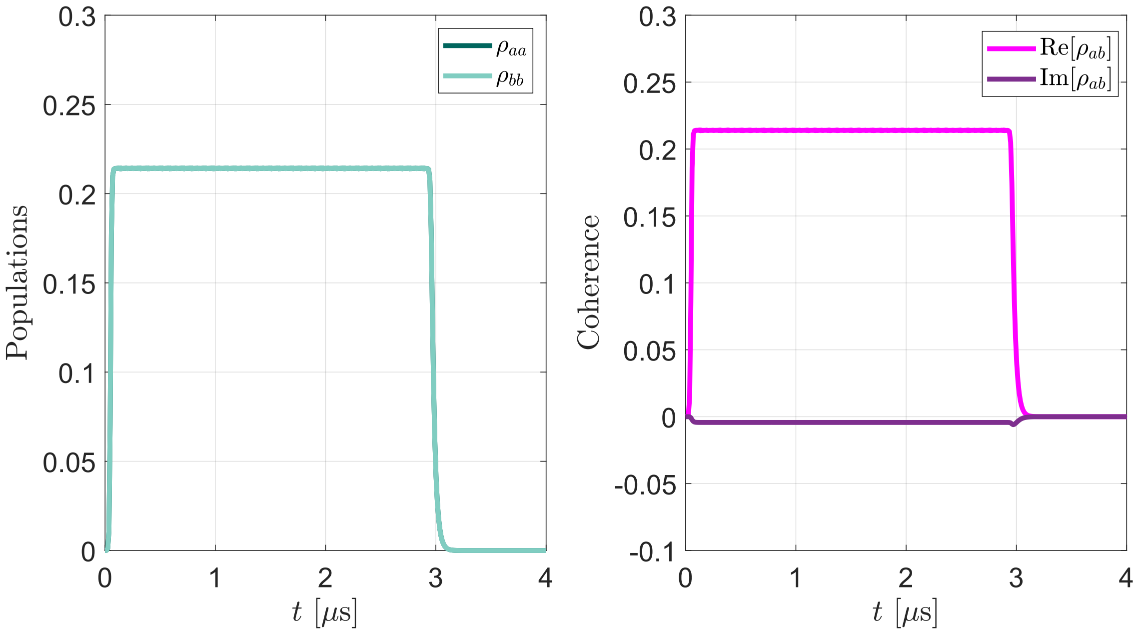

Figure 3.4: *Time evolution of excited states populations and real and imaginary part of coherence between level $|a\rangle$ and $|b\rangle$. The radiation excites the system with a train of pulses with $\tau_{\text{pulse}} = 3\mu s$ and a light-off period of $2\mu s$. In the picture, the effect of a single pulse is shown. The intensity is set to fulfill the strong pumping regime ($\bar{n} = 25$), with small splitting ($\Delta/\bar{\gamma} = 0.1$). The turn-on and off time scale $\tau_{on} = \tau_{off} = 100$ ns.*

Assuming the excited atoms are in the state $|a\rangle = |F' = 1\ m_{F'} = -1\rangle$, they can then decay to the ground level emitting photons and thus producing resonance fluorescence radiation. The intensity expectation value of resonance fluorescence can be calculated as follows [39–41]:

$$\langle I_{ac}(\mathbf{R},t)\rangle = \frac{\varepsilon_0 c}{2}\langle \hat{E}^{-}_{ac}(\mathbf{r},t)\hat{E}^{+}_{ac}(\mathbf{r},t)\rangle, \tag{3.27}$$

where $\hat{E}^{\pm}_{ac}(\mathbf{r},t)$ is the electric field operator emitted from transition $|a\rangle \leftrightarrow |c\rangle$ and its conjugate, while $\mathbf{R}$ is the distance vector from the emitting source. For an oscillating dipole, as the atom emitting radiation, the electric field operator can be approximated according to [41]:

$$\hat{E}^{+}_{ac}(\mathbf{R},t) \approx -\frac{1}{4\pi\varepsilon_0 c^2}\left[(\boldsymbol{\mu}_{ac}\cdot\mathbf{R})\,\mathbf{R} - \boldsymbol{\mu}_{ac}\right]\omega^2_{ac}|\boldsymbol{\mu}_{ac}|\frac{\hat{\sigma}^{-}_{ac}(t)}{\mathbf{R}}. \tag{3.28}$$

Here, ω_{ac} is the atomic transition frequency, $\boldsymbol{\mu}_{ac}$ is the transition dipole moment vector and its module is the transition dipole moment matrix element. Finally, $\hat{\sigma}^{-}_{ac}(t)$ is the lowering operator. Substituting equation (3.28) in equation (3.27) I obtain:

$$\langle I_{ac}(\mathbf{R},t)\rangle = \frac{\omega^4_{ac}|\boldsymbol{\mu}_{ac}|^2}{32\pi^2\varepsilon_0 c^3}\left|\frac{\left[(\boldsymbol{\mu}_{ac}\cdot\mathbf{R})\,\mathbf{R} - \boldsymbol{\mu}_{ac}\right]}{\mathbf{R}}\right|^2\langle\hat{\sigma}^{+}_{ac}(t)\hat{\sigma}^{-}_{ac}(t)\rangle. \tag{3.29}$$

In the above expression, the order of the electric field operators is crucial. In the expectation value on the right hand side, the lowering operator is to the right, meaning that if the atom is in the ground state the intensity is zero. This order is known as *normal ordering* [39, 41].

The atoms can also be excited to the state $|b\rangle = |F' = 1\ m_{F'} = +1\rangle$, where all the steps described previously apply. The total intensity of the radiation emitted is then given by:

$$\langle I(\mathbf{R},t)\rangle = \langle \hat{E}^{-}(\mathbf{r},t)\hat{E}^{+}(\mathbf{r},t)\rangle, \tag{3.30}$$

where the electric field operators $\hat{E}^{+}(\mathbf{R},t)$ and $\hat{E}^{-}(\mathbf{R},t)$ are composed of the sum of the two electric fields emitted from transitions $|a\rangle \rightarrow |c\rangle$ and $|b\rangle \rightarrow |c\rangle$:

$$\hat{E}^{+}(\mathbf{r},t) = \hat{E}^{+}_{ac}(\mathbf{r},t) + \hat{E}^{+}_{bc}(\mathbf{r},t). \tag{3.31}$$

The same applies for the complex conjugate. Hence:

$$\begin{aligned}\langle I(\mathbf{R},t)\rangle =& \frac{\varepsilon_0 c}{2}\Big(\langle \hat{E}^{-}_{ac}(\mathbf{r},t)\hat{E}^{+}_{ac}(\mathbf{r},t)\rangle + \langle \hat{E}^{-}_{bc}(\mathbf{r},t)\hat{E}^{+}_{bc}(\mathbf{r},t)\rangle + & (3.32)\\ &+ \langle \hat{E}^{-}_{ac}(\mathbf{r},t)\hat{E}^{+}_{bc}(\mathbf{r},t)\rangle + \langle \hat{E}^{-}_{bc}(\mathbf{r},t)\hat{E}^{+}_{ac}(\mathbf{r},t)\rangle\Big). & (3.33)\end{aligned}$$

Considering the following equalities [41]:

$$\langle \hat{\sigma}^{+}_{lc}(t)\hat{\sigma}^{-}_{lc}(t)\rangle = \mathrm{Tr}\left(\hat{\sigma}^{+}_{lc}(t)\hat{\sigma}^{-}_{lc}(t)\hat{\rho}_S(t)\right) = \rho_{lc}(t) \tag{3.34}$$

$$\left|\frac{\left[\left(\boldsymbol{\mu}_{lc}\cdot\mathbf{R}\right)\mathbf{R} - \boldsymbol{\mu}_{lc}\right]}{\mathbf{R}}\right|^2 = \frac{1-|\boldsymbol{\mu}_{lc}\cdot\mathbf{R}|^2}{|\mathbf{R}|^2}, \tag{3.35}$$

with $l = a, b$. By writing the vector $\mathbf{R}$ in spherical coordinates:

$$\mathbf{R} = |\mathbf{R}|\left[\sin\theta\cos\varphi, \sin\theta\sin\varphi, \cos\theta\right], \tag{3.36}$$

the fluorescence intensity is finally equal to:

$$\begin{aligned}\langle I(\theta,\varphi,,t)\rangle =& \frac{1}{32\pi^2\varepsilon_0 c^3|\mathbf{R}|^2}\Bigg[\frac{1+\cos^2\theta}{2}\left(\omega_{ac}^4|\boldsymbol{\mu}_{ac}|^2\rho_{aa}(t') + \omega_{bc}^4|\boldsymbol{\mu}_{bc}|^2\rho_{bb}(t')\right) +\\ &+ \omega_{ac}^2\omega_{bc}^2|\boldsymbol{\mu}_{ac}||\boldsymbol{\mu}_{bc}|\sin^2\theta\left(\cos(2\varphi)\mathrm{Re}[\rho_{ab}(t')] - \sin(2\varphi)\mathrm{Im}[\rho_{ab}(t')]]\right)\Bigg]. \end{aligned} \tag{3.37}$$

Here $t' = t + |\mathbf{R}|/c$. Since the selected V-type three-level system has $\boldsymbol{\mu}_{ac} = \boldsymbol{\mu}_{bc}$ and $\omega_{ac} \approx \omega_{bc}$, then:

$$\begin{aligned}\langle I(\theta,\varphi,t)\rangle =& \frac{\omega_{ac}^4|\boldsymbol{\mu}_{ac}|^2}{32\pi^2\varepsilon_0 c^3|\mathbf{R}|^2}\Bigg[\frac{1+\cos^2\theta}{2}\left(\rho_{aa}(t') + \rho_{bb}(t')\right) +\\ &+ \sin^2\theta\left(\cos(2\varphi)\mathrm{Re}[\rho_{ab}(t')] - \sin(2\varphi)\mathrm{Im}[\rho_{ab}(t')]]\right)\Bigg]. \end{aligned} \tag{3.38}$$

Equations (3.37) and (3.38) directly relate the real and imaginary parts of Fano coherence to an observable quantity: the intensity of the emitted fluorescence, as a function of angular coordinates. Both equations can be reformulated as follows:

$$\langle I(\theta,\varphi,t)\rangle = \frac{\omega_{ac}^4|\boldsymbol{\mu}_{ac}|^2}{32\pi^2\varepsilon_0 c^3|\mathbf{R}|^2}\left[\frac{1+\cos^2\theta}{2}\big(\rho_{aa}(t')+\rho_{bb}(t')\big)+\sin^2\theta\cos(2\varphi+\alpha)\right]$$
$$\text{with} \qquad \tan\alpha = \frac{\mathrm{Im}[\rho_{ab}]}{\mathrm{Re}[\rho_{ab}]}. \tag{3.39}$$

This formulation highlights that the ratio between the imaginary and real parts of the coherence produces a phase shift in the φ dependent term. This phase shift α must be accounted for during measurement. Specifically, the fluorescence component dependent on φ might not be oriented precisely at a given φ, but could be slightly deviated due to α.

By placing detectors around the atoms, it is possible to select specific ranges of solid angles to isolate the contribution from each term of equation (3.38). As detailed in [29], if the following integrals are computed:

$$I_1(t) = \int_0^\pi\int_{-\pi/4}^{\pi/4} I(\theta,\varphi,t)d\varphi d\theta + \int_0^\pi\int_{3\pi/4}^{5\pi/4} I(\theta,\varphi,t)d\varphi d\theta \tag{3.40}$$

$$I_2(t) = \int_0^\pi\int_{\pi/4}^{3\pi/4} I(\theta,\varphi,t)d\varphi d\theta + \int_0^\pi\int_{5\pi/4}^{7\pi/4} I(\theta,\varphi,t)d\varphi d\theta \tag{3.41}$$

their difference $I_2(t) - I_1(t)$ is directly proportional to $\mathrm{Re}[\rho_{ab}(t)]$. These specific ranges of solid angles are chosen to maximize the sensitivity to the spatial anisotropy caused by the real part of the coherence term. By integrating over these two angular regions and taking their difference, the symmetric contributions from $\rho_{aa}(t)$ and $\rho_{bb}(t)$ cancel out, isolating a signal dependent solely on $\mathrm{Re}[\rho_{ab}(t)]$. This detection technique, known as *angle-resolved*, allows for the selection of specific angular ranges to isolate the contributions of individual terms in the fluorescence intensity.

The real and imaginary parts of Fano coherence are responsible for spatial anisotropy in the x-y plane, as also illustrated in figure 3.5, that can be detected. This results in the characteristic "doughnut-shaped" radiation pattern, typical of an oscillating dipole. To detect the presence of Fano coherence in the V-system, I place two photodetectors along the x-axis and y-axis in a differential configuration. If Fano coherence is present, a non-zero signal should be measured. Using a short focal length lens with $f_{\text{lens}} = D_{\text{lens}} = 25.4$ mm, where f_{lens} is the focal length and D_{lens} is the diameter, an angle aperture of $\pi/2$ is obtained. The integration ranges for θ and φ are:

- For fluorescence around the x-axis: $\theta \in [\pi/4, 3\pi/4]$, $\varphi \in [-\pi/4, \pi/4]$.
- For fluorescence around the y-axis: $\theta \in [\pi/4, 3\pi/4]$, $\varphi \in [\pi/4, 3\pi/4]$.

The intensities $I_1(t)$ and $I_2(t)$ are then given by:

$$I_1(t) = \int_{\pi/4}^{3\pi/4}\int_{-\pi/4}^{\pi/4} I(\theta,\varphi,t)d\varphi d\theta \tag{3.42}$$

$$I_2(t) = \int_{\pi/4}^{3\pi/4}\int_{\pi/4}^{3\pi/4} I(\theta,\varphi,t)d\varphi d\theta. \tag{3.43}$$

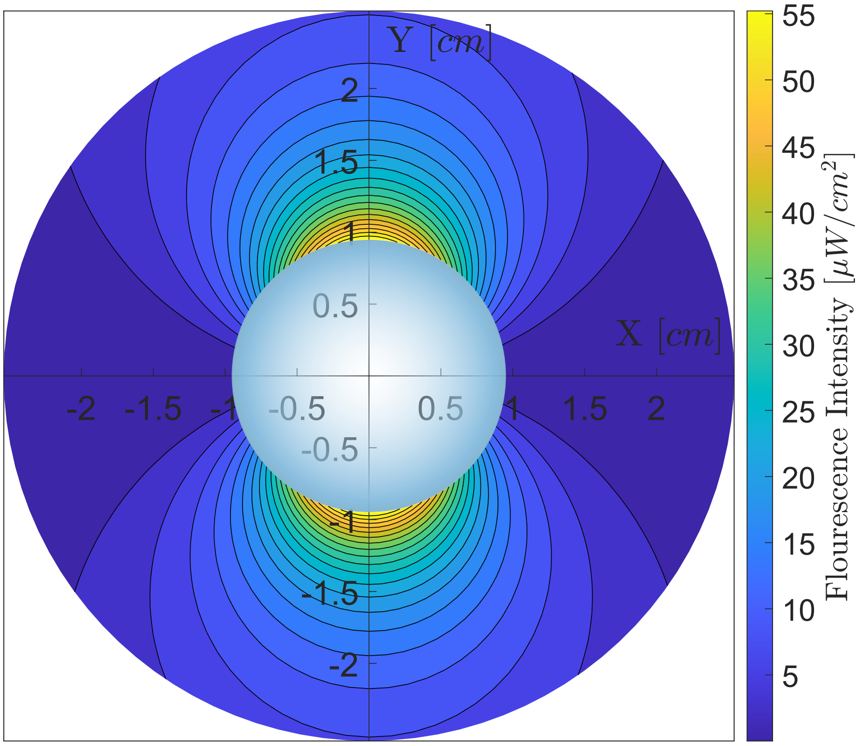

Figure 3.5: *Fluorescence intensity around the atomic vapor cell when stationary coherence is reached. The polarized radiation intensity is set to* $\bar{n} = 25$, *with small splitting* $\Delta/\bar{\gamma} = 0.1$. *At* $(x, y) = (0, 0)$ *is the vapor cell, whose diameter is* 19 *mm.*

The chosen range of angles ensures that the signal difference $I_2(t) - I_1(t)$ is merely dependent on $\mathrm{Re}[\rho_{ab}]$.

By driving the three-level system with the same train pulses described previously, with excited states splitting set to $\Delta/\bar{\gamma} = 0.1$ and the intensity radiation to $\bar{n} = 25$, whose turning on and off time are $\tau_{on} = \tau_{off} = 100$ ns, the time evolution of $I_1(t), I_2(t)$ and their difference are illustrated in figure 3.6. To distinguish the fluorescence signal influenced by Fano coherence, it is essential to establish a reference value, denoted as I_0, representing the signal obtained under isotropic conditions. An isotropic fluorescence pattern occurs when interference effects are absent, such as when the frequency separation between the two excited states Δ significantly exceeds the laser bandwidth $\Delta\nu_{\text{laser}}$. In this scenario, the source can no longer excite both transitions, making them distinguishable and minimizing interference in the pumping process. As a result, Fano coherence vanishes, and the populations and coherences of the atomic system evolve according to the Pauli rate equations. The resulting fluorescence pattern becomes isotropic in the x-y plane, as described by:

$$\langle I(\theta, t)\rangle = \frac{\omega_{ac}^4 |\boldsymbol{\mu}_{ac}|^2}{32\pi^2 \varepsilon_0 c^3 |\mathbf{R}|^2} \left[\frac{1 + \cos^2\theta}{2} \left(\rho_{aa}(t') + \rho_{bb}(t')\right) \right], \tag{3.44}$$

where the angular dependence arises solely from the θ angle. The radiation pattern in the x-z plane (or equivalently in the y-z plane) in this case is “peanut-shaped”, typical of a rotating dipole.

In figure 3.6, the difference $I_2(t) - I_1(t)$ of the equations (3.42) and (3.43), is normalized

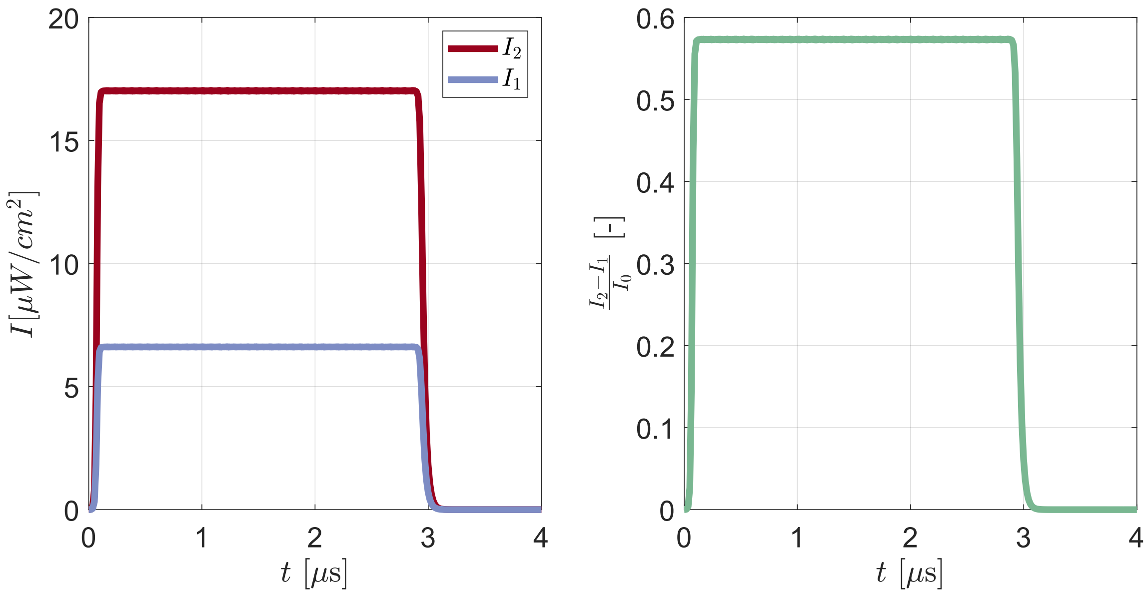

Figure 3.6: *Fluorescence intensities around the x-axis ($I_1(t)$) and around y-axis ($I_2(t)$) varying with time. The values of angles θ and φ are those of equations (3.42) and (3.43). On the right, their difference is shown, scaled by I_0, which is the isotropic fluorescence intensity obtained when $\rho_{ab}(t) = 0$. The radiation intensity is set to $\bar{n} = 25$, with small splitting $\Delta/\bar{\gamma} = 0.1$.*

by the isotropic fluorescence intensity I_0. The latter is collected over the same angular range and can be expressed as:

$$\begin{aligned} I_0 &= \int_{\pi/4}^{3\pi/4}\int_{-\pi/4}^{\pi/4} \langle I(\theta,\varphi,t)\rangle d\varphi d\theta = \\ &= \int_{\pi/4}^{3\pi/4}\int_{-\pi/4}^{\pi/4} \frac{\omega_{ac}^4|\boldsymbol{\mu}_{ac}|^2}{32\pi^2\varepsilon_0 c^3|\mathbf{R}|^2}\left[\frac{1+\cos^2\theta}{2}\left(\rho_{aa}(t')+\rho_{bb}(t')\right)\right] d\varphi d\theta. \end{aligned} \tag{3.45}$$

Since the fluorescence is isotropic, I_0 is calculated just around the x-axis, where φ varies between $-\pi/4$ and $+\pi/4$. The time evolution of excited state populations and coherence associated to $I_1(t)$ and $I_2(t)$ were depicted in figure 3.4.

To accurately distinguish between the fluorescence measured under isotropic and anisotropic conditions, it is necessary to continuously vary the splitting Δ. This can be accomplished by sinusoidally modulating the magnetic field along the z-axis. By slowly varying the magnetic field such that $\Delta/\bar{\gamma} \approx 0.1$ at minimum and $\Delta > 2\Delta\nu_{laser}$ at maximum, the difference signal from the two photodiodes should exhibit a similar modulation pattern. In particular, it should oscillate between a maximum value at $\Delta/\bar{\gamma} \approx 0.1$ and a minimum value (ideally approximately zero) when the splitting is greater than the laser bandwidth.

For a laser bandwidth $\Delta\nu_{laser} \leq 10$ MHz, the required splitting Δ should be $\Delta > 2\Delta\nu_{laser} = 20$ MHz. This ensures that the laser selectively excites only one of the two transitions, causing the loss of interference. Having selected the V-type three-level system and established how to control the key parameters Δ and $\bar{n}$ via magnetic fields and laser intensity, I describe in the next section the experimental setup designed for detecting noise-induced Fano coherence in a hot rubidium vapor cell. In the setup, atoms are excited using a linearly polarized broadband laser. This experimental arrangement is essential for validating the theoretical predictions discussed.

3.2 Proof-of-principle experiment for Fano-coherence detection

The previous sections explored the dynamics of excited state populations and noise-induced Fano coherence within a three-level system realized in the hyperfine structure of ^{87}Rb atoms. I utilized anisotropic polarized radiation that can be switched on and off. Additionally, I introduced the angle-resolved fluorescence technique to detect coherence. By measuring the fluorescence with photodetectors placed along the x and y-axes, any non-zero $\rho_{ab}(t)$ should result in a measurable difference between these two signals.

To achieve this measurement, a well-designed optical setup is required. Specifically, the setup must include magnetic field control, laser source control for adjusting the frequency and frequency band, as well as the intensy, an atomic source, and a detection system. The next subsections describe each of these main components in detail.

3.2.1 Rb vapor cell and magnetic cage

As previously discussed, the platform for implementing the V-type three-level system is a hot atomic ensemble in a vapor cell. Specifically, I decided to use a quartz vapor reference cell from Thorlabs, in the enhanced version with 98% pure ^{87}Rb (model: GC19075-RB87). The standard cells typically have the natural abundance of the two isotopes ^{85}Rb and ^{87}Rb, where the latter constitutes only 27.85%. Using the enhanced version ensures that there is minimal influence from ^{85}Rb isotopes.

The Thorlabs enhanced vapor cell is long 75 mm with a diameter of 19 mm. The vapor pressure inside the cell depends on the temperature according to the following empirical vapor pressure model [91, 93]:

$$\log_{10} P_v = 2.881 + 4.857 - \frac{4215}{T} \quad \text{solid phase} \tag{3.46}$$

$$\log_{10} P_v = 2.881 + 4.312 - \frac{4040}{T} \quad \text{liquid phase} \tag{3.47}$$

where P_v is the vapor pressure in torr and T is the temperature in K. The melting point of ^{87}Rb is at $T = 39.30\,°C$. The subsequent measurements are taken at temperature up to $T = 40\,°C$. At this temperature, the atomic density is $n_{\text{atomic}} = 5.92 \cdot 10^{16}\,\text{m}^{-3}$, which means that the atomic density is low enough that interactions between atoms do can be neglected in the mathematical model. Having established the atomic density, the optical density (OD) of the medium can be calculated as follows:

$$\text{OD} = n_{\text{atomic}}\, \sigma_{\text{abs}}\, L_{\text{cell}} \tag{3.48}$$

$$\sigma_{\text{abs}} = \frac{3\lambda^2}{2\pi}, \tag{3.49}$$

where σ_{abs} is the absorption cross-section on resonance and L_{cell} is the length of the vapor cell. At $T = 40°C$ OD $= 1338$.

The temperature of the vapor cell is controlled putting it in thermal contact with resistors housed in aluminum casings, each with a resistance of 15Ω and a power rating of $15W$. Temperature regulation is achieved with a $10\,k\Omega$ NTC thermistor connected to a Thorlabs TC300 temperature controller, which utilizes a Proportional-Integral-Derivative (PID) feedback loop for precise temperature management.

The cell with the heating resistors is then placed inside a cage, which is composed of coils holders, as illustrated in figure 3.7. Inside the cage there are two pairs of rectangular-shaped coils in the Helmholtz configuration, whose axis are along the x and y-axis. These coils are used to cancel the x and y-components of the magnetic field around the center of the cage, where the vapor cell is located. An additional pair of Helmholtz coils, aligned with the z-axis, is placed outside the cage to generate a uniform magnetic field along the z-axis at the cage's center. The latter establishes the quantization axis and tunes the excited states splitting.

The coils along the z-axis were custom-designed to be placed outside the cage. A square shape was chosen for its superior field homogeneity compared to circular coils, despite offering a lower maximum field intensity [94, 95]. The design and implementation follow the methodology outlined in [95], starting with calculations based on the Biot-Savart law, where the conductor is approximated as an infinitesimally small element to derive the magnetic field components $\mathbf{B} = B_x\mathbf{x} + B_y\mathbf{y} + B_z\mathbf{z}$. Due to the necessity of achieving a higher field magnitude than what a single turn can provide, multiple turns are used, resulting in a coil with a cross-section that is thick relative to the diameter of the conductor, as illustrated in figure 3.8. Therefore, it is not possible to consider the conductor as infinitesimal; the dimensions of the cross-section must be taken into account to accurately model the magnetic

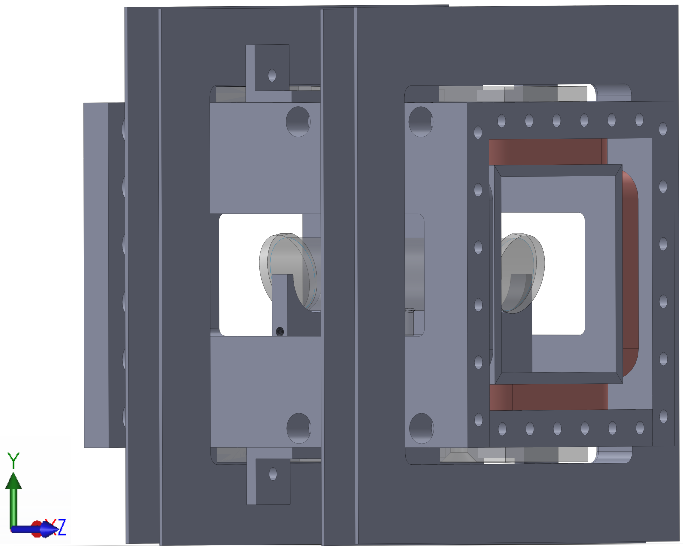

Figure 3.7: *Coils cage with the vapor cell at its center. The cage consists of two pairs of coils aligned along the x and y-axis, while an additional pair of square-shaped coils is positioned outside the cage along the z-axis.*

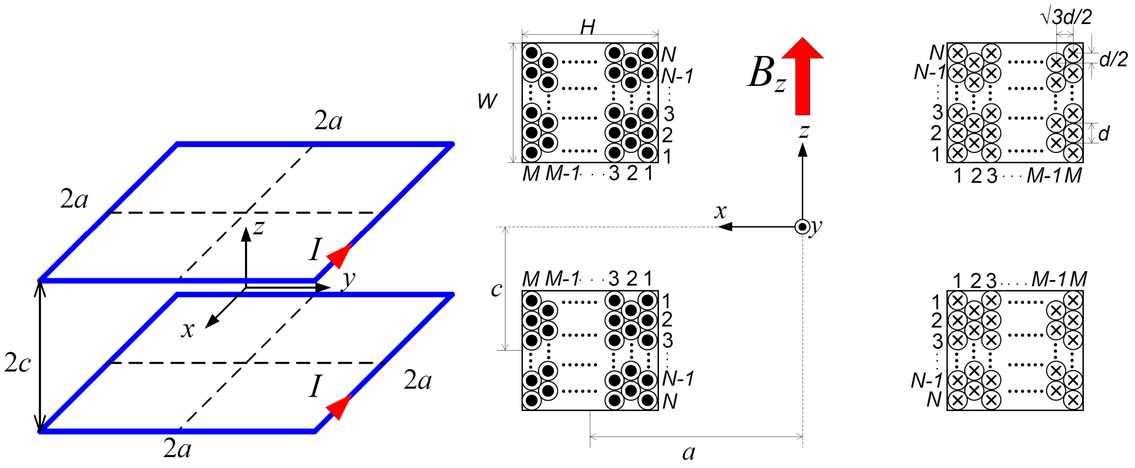

Figure 3.8: *Left: A filamentary square Helmholtz coil pair. Right: Cross-section of a thick Helmholtz coil pair, composed of M layers and N turns for odd layers, $N-1$ turns for even layers (figure reproduced from [95], without any modification).*

field.

Considering the cross-section of the thick Helmholtz coils as the ones shown in figure 3.8, where each coil consists of M layers of round conductors, with a diameter d. The odd layers contain N turns, while the even layers have $N-1$ turns. This coil configuration can be modeled as an assembly of individual pairs of single-turn square loops positioned at turn n and layer m. The origin of the reference system is placed at the center between the two coils and the axial magnetic field generated by each pair of single-turn square loops can be computed using the following formula:

$$\begin{aligned} B_{z_{mn}}(x,y,z) =& \frac{\mu_0 I}{4\pi}\sum_{i=1}^{2}\sum_{j=1}^{2}(-1)^{(i+j+1)}\sum_{k=1}^{2}\frac{x-x_i}{\sqrt{(x-x_i)^2+(y-y_j)^2+(z-z_k)^2}+(y-y_j)} \\ & \times\frac{1}{\sqrt{(x-x_i)^2+(y-y_j)^2+(z-z_k)^2}}+ \\ & -\frac{\mu_0 I}{4\pi}\sum_{i=1}^{2}\sum_{j=1}^{2}(-1)^{(i+j)}\sum_{k=1}^{2}\frac{y-y_j}{\sqrt{(x-x_i)^2+(y-y_j)^2+(z-z_k)^2}+(x-x_i)} \\ & \times\frac{1}{\sqrt{(x-x_i)^2+(y-y_j)^2+(z-z_k)^2}} \end{aligned} \tag{3.50}$$

Here, the coordinates of the single-turn square loop are defined as: $x_1 = y_1 = a_m$, $x_2 = y_2 = -a_m$, $z_1 = c_n$, $z_2 = -c_n$. The parameters a_m and c_n are determined by the following expressions from [95]:

$$a_m = a - \frac{H}{2} + \frac{d}{2} + (m-1)\frac{\sqrt{3}}{2}d \tag{3.51}$$

$$c_n = c - \frac{W}{2} + d\left(n - \frac{1}{2}\right) \quad \text{for } m \text{ odd values} \tag{3.52}$$

$$c_n = c - \frac{W}{2} + dn \quad \text{for } m \text{ even values} \tag{3.53}$$

where, H, W are the width and height of the thick cross-section, and a and c are the

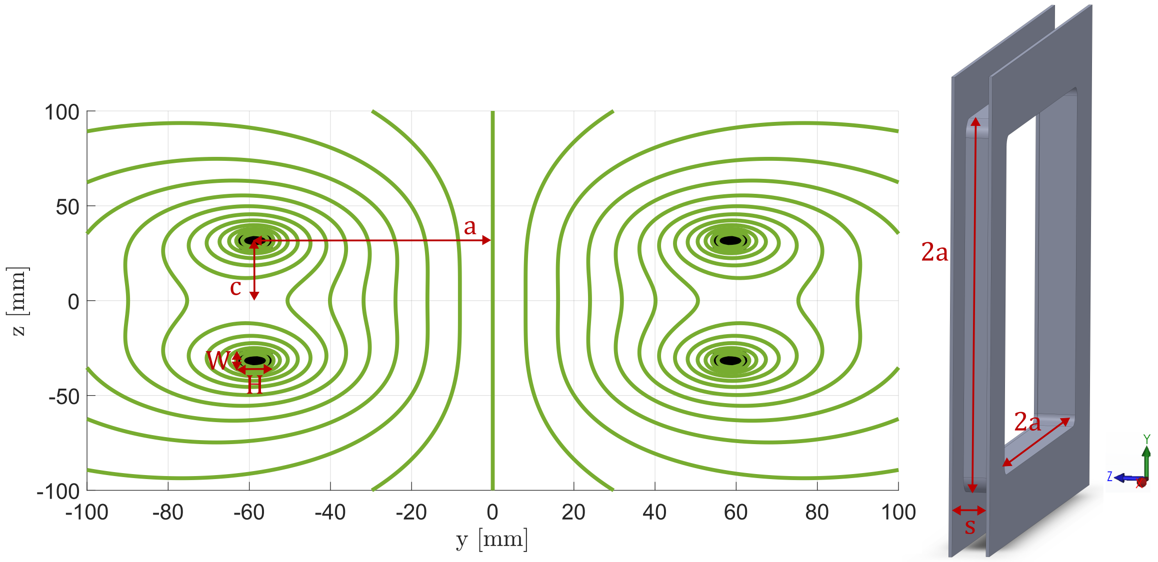

Figure 3.9: *Left: 2D magnetic field streamlines on the y-z plane generated by the designed pair of thick coils. The cross-sectional values W, H and the average distances a, c are shown in the figure and listed in table 3.2. Right: Coils holder with dimensions detailed in 3.2.*

average coil width and coil space respectively, as depicted in figure 3.8. The relationship $c = 0.544506a$ ensures a uniform magnetic field at the center (0,0,0) according to the Helmholtz condition [94, 95].

The coils and their holders are designed to produce a uniform magnetic field up to 50 G. To achieve this, the coils are constructed with $N = 6$ turns in $M = 6$ layers resulting in a total of $MN - M/2 = 33$ turns. The copper conductor chosen has a diameter of $d = 1.5$ mm, which supports a high current flux of up to 10 A. Based on these parameters, the holders were designed as depicted in figure 3.9, and both the holder and coil dimensions are listed in table 3.2.

By applying a current of $I = 6$ A, the generated magnetic field along the z-axis varies with the y and z positions around the center as shown in figure 3.10. Due to the symmetry of the square Helmholtz coil configuration, the variation with the x position is identical to the variation along the y position. The magnetic field remains uniform within the range

Quantity	Magnitude
Side of the coil support, a [mm]	54.5
Width of the coil support, s [mm]	10
Conductor diameter, d [mm]	1.5
Number of layers, M [-]	6
Number of turns, N [-]	6
Total number of turns $MN - M/2$ [-]	33
Coils cross-section width W [mm]	9
Coils cross-section height W [mm]	8

Table 3.2: *Designed values for the z-axis coils holder and coils pair.*

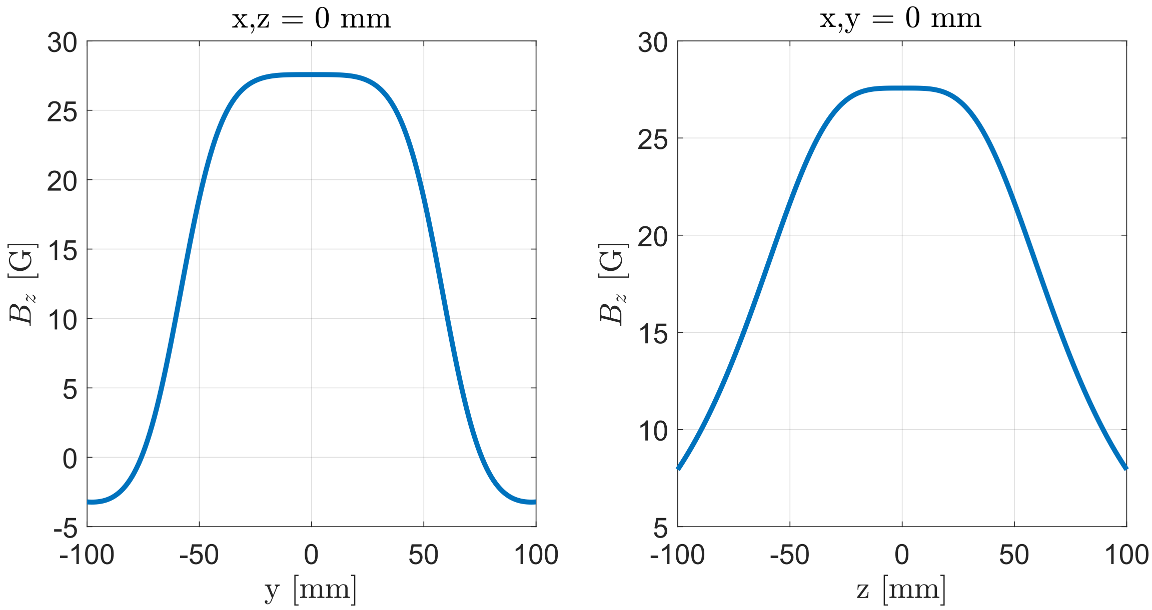

Figure 3.10: *Magnetic field B_z generated by the designed square Helmholtz coils. The figure illustrates the field's variation with respect to the y and z positions around the central point. The variation respect to the x direction equals the variation along y. The field is uniform to within 0.01% over the range $x = y \in [-22, 22]$ mm and $z \in [-20, 20]$ mm. A current of $I = 6$ A is considered.*

$x = y \in [-22, 22]$ mm and $z \in [-20, 20]$ mm. Given that the vapor cell has a cylindrical shape with a diameter of 19 mm, the uniform field radially covers the entire space around the cell. Along its length, equal to 75 mm, only the portion of the cell within the range $z \in [-20, 20]$ mm experiences a uniform magnetic field.

To ensure precise monitoring and control of the magnetic field within the cage, a three-axis magnetometer (Adafruit Magnetometer MMC5603) is placed inside the cage under the vapor cell. The magnetometer provides real-time measurements of the magnetic field along the x, y, and z directions. The smallest change in the magnetic field that the sensor can detect is 0.0625 mG and the total RMS noise is 2 mG. The data from the magnetometer is acquired using an Arduino Nano 33 IoT, enabling accurate current adjustments to maintain the desired magnetic field conditions.

The magnetic field along the z-axis is modulated by adjusting the current through the coils using a function generator. The current is varied sinusoidally with a frequency of less than 10 Hz. The low frequency ensures that the magnetic field can be considered approximately constant on the time scale of the system, and accounts for the inertia of the coils. When $B_z \approx 50$ G the corresponding splitting Δ is $\Delta \approx 23$ MHz, as given by equation (3.24). If the laser's bandwidth is less than this value, modulations in the fluorescence signal should be detectable.

3.2.2 Detection scheme

To detect Fano coherence, the angle-resolved fluorescence scheme, outlined in Subsection 3.1.3, is employed. As previously described, two photodetectors are arranged along the x and y-axes in a differential configuration.

To enhance the detection of fluorescence, a lens system is placed in front of each photodetector. This optical setup focuses the fluorescence emitted from the sample onto the photodiodes, thereby increasing both the intensity and sensitivity of the measurements, which is essential for accurately detecting weak fluorescence signals. The first lens has a short focal length of $f_{\text{lens}_1} = 25.4$ mm, and a diameter of $D_{\text{lens}} = 25.4$ mm, providing an angular aperture of $\pi/2$. The short focal length allows to capture a large amount of light emitted from the atom and the diameter is appropriately sized to cover the portion of the vapor cell along the z-axis where the magnetic field is uniform, specifically within the range $z \in [-20, 20]$ mm.

The two photodetectors utilized are silicon PIN photodiodes (HAMAMATSU S6967) featuring a large photosensitive area of $A_{\text{ph}} = 5.5 \times 4.8$ mm^2. The large area enhances the signal detection capability by capturing more light. The lens system and the photodiode define the fluorescence-emitting volume of interest within the vapor cell. The transverse photodiode dimension that is imaged into the vapor cell can be calculated as follows: $L_{\text{fluor}} = L_{\text{ph}} f_{\text{lens}_1} / f_{\text{lens}_2}$. To determine the volume, the cross-section area of the beam and the dimension L_{fluor} are used, yielding a fluorescence volume of $V_{\text{fluor}} = L_{\text{fluor}} \pi d_{\text{beam}}^2 / 4$.

Photodiodes with such a large photosensitive area generally exhibit higher capacitance, which can degrade their electronic performance. To address this, a transimpedance amplifier, which includes an inverting operational amplifier paired with a feedback resistor, is typically employed to convert the photodiode current into a voltage signal, as the one realized for my setup, whose electrical circuit is shown in figure 3.11. In the design of low-noise amplifiers, particular care is needed to minimize the input voltage noise of the operational amplifier to ensure optimal signal-to-noise ratio with large-area photodiodes [96]. In my case, the junction capacitance C_{ph} of the photodiode is $C_{\text{ph}} = 50$ pF. Its high value significantly affects the noise performance of the circuit, especially the input voltage noise of the operational amplifier. To address this, a *bootstrapping technique*, described in [96], is employed. Using a low-noise depletion-mode N-channel Junction Field-Effect Transistor (JFET) (NXP Semiconductors BF862) effectively reduces the photodiode's capacitance and the associated noise. Indeed, this configuration substitutes the operational amplifier noise with the JFET's lower noise. Additionally, this approach can enhance the circuit's band-

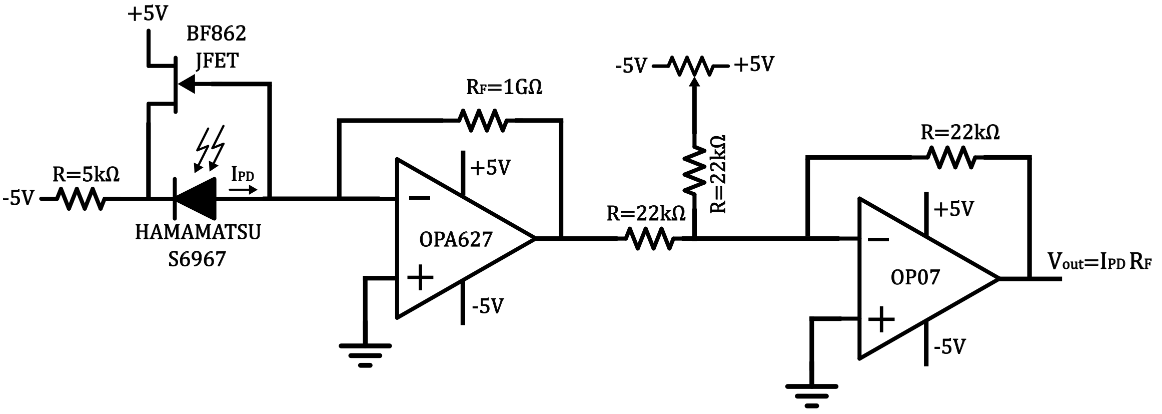

Figure 3.11: *Electronic circuit of the two transimpedence amplifiers photodiodes in the bootstrap configuration.*

width by minimizing the compensating feedback capacitance. This substantial improvement in both noise performance and bandwidth is achieved by making the feedback resistor R_F interact with the much lower capacitance of the JFET gate rather than the large capacitance of the photodiode.

To enhance the transimpedance gain, a feedback resistor of $R_\mathrm{F} = 1\,\mathrm{G}\Omega$ is used. This high resistance value, however, reduces the -3dB bandwidth of the transimpedance amplifier, which results in $\nu_{-3dB} \approx 9$ kHz for the photodiodes used in this setup. The bandwidth of the photodiode defines the time over which the electrical signal is integrated. Consequently, in this configuration, dynamic events occurring within time scales shorter than $110\,\mu$s are effectively integrated and averaged. A second operational amplifier stage with unity gain is incorporated into the transimpedance photodiode circuit, as shown in figure 3.11. This stage is used to add an offset to the photodiode signal, enabling the balance between the two photodiodes under dark conditions.

Finally, the two photodiodes are arranged in a differential configuration using a differential amplifier circuit. The latter not only measures the difference signal resulting from the anisotropy of fluorescence but also helps reducing low-frequency noise. Figure 3.12 illustrates the Power Spectral Density (PSD) of the electronic signal difference between the two photodiodes: the first oriented along the x-axis ($\mathrm{PD_x}$) and the other along the y-axis ($\mathrm{PD_y}$). The PSD of each individual photodiode is also shown in the figure. The differential configuration effectively cancels out low-frequency common noise. This is particularly advantageous when the magnetic field is modulated at frequencies below 10 Hz, as the fluorescence modulation is expected at this frequency and its harmonics. The peak at 10 Hz, that can be seen in the figure, corresponds to the frequency of a modulation applied to the laser beam to balance the signals from the two photodiodes, before the measurement.

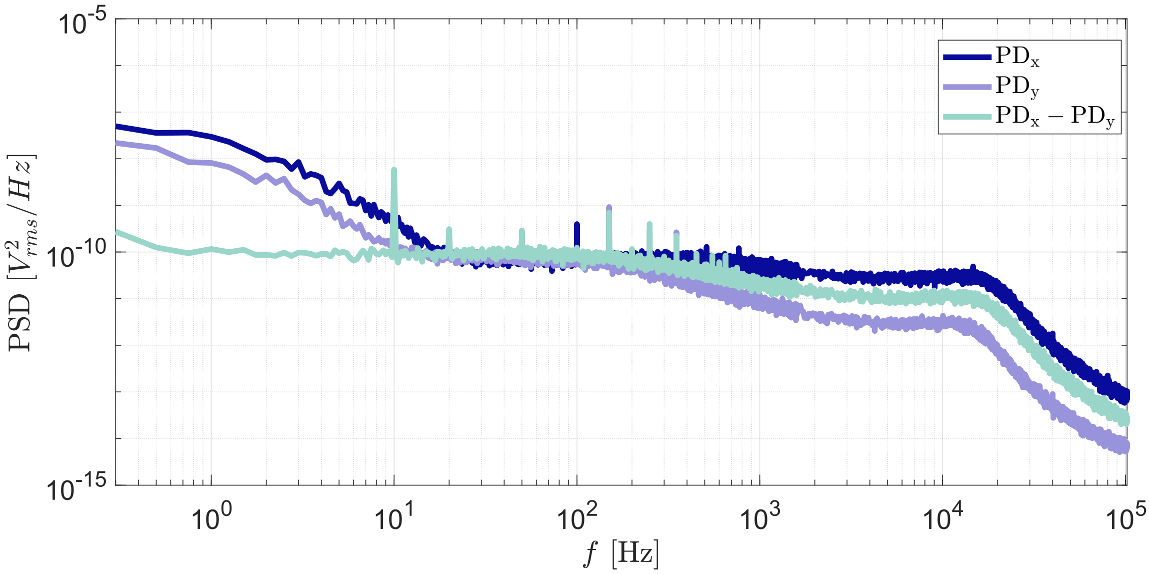

Figure 3.12: *Power spectral density (PSD) of the electronic signal from the photodiodes placed transverse to the x-axis ($\mathrm{PD_x}$) and y-axis ($\mathrm{PD_y}$). The PSD of the signal difference ($\mathrm{PD_x}$ - $\mathrm{PD_y}$), obtained using a differential amplifier circuit, is also shown.*

3.2.3 Laser system and control

The incoherent source is realized with a Distributed-Feedback (DFB) diode laser at $\lambda = 795$ nm (TOPTICA Eagleyard EYP-DFB-0795-00080-1500-BFW01-0005) with a specified maximum linewidth of 1 MHz. To broaden this source and make it approximately incoherent, the driving current is modulated with Gaussian noise, generated by a function generator, and defined by amplitude and offset. The effect of the noise on the linewidth is estimated by observing the beat note with a locked reference Distributed Bragg Reflector (DBR) laser (Thorlabs DBR795PN), which has a linewidth of 1 MHz. The linewidth of the beat note is the square root of the sum of the squares of the individual linewidths of the two lasers. When one laser has a linewidth significantly greater than the other, the beat note linewidth is primarily influenced by the broader laser. Hence, the DFB linewidth can be approximated with the beat note linewidth.

To evaluate the Full Width at Half Maximum (FWHM) of the beat note I employ the Line-Profile Analysis Software (LIPRAS) [97]. The fitting process utilizes the *pseudo-Voigt profile*, which is a linear combination of Gaussian and Lorentzian distributions. The pseudo-Voigt profile is commonly used for fitting diffraction data. It is defined as:

$$V_p(x, f) = \eta \cdot L(x, f) + (1 - \eta) \cdot G(x, f). \tag{3.54}$$

Here η represents a weighting factor that depends on the FWHM, f, while $L(x, f)$ and $G(x, f)$ denote the Lorentzian and Gaussian profiles, respectively. To achieve an accurate fit between the model and the experimental data, LIPRAS employs a least squares optimization routine, which is a component of the Curve Fitting Toolbox$^{\text{TM}}$ from MathWorks®. To assess the goodness-of-fit, LIPRAS employs several statistical metrics, including the root mean squared error, and the following measures [97]:

$$R_p = \frac{\sum |y_{\text{obs}} - y_{\text{calc}}|}{\sum y_{\text{obs}}} \times 100 \tag{3.55}$$

$$R_{wp} = \left[\frac{\sum w(y_{\text{obs}} - y_{\text{calc}})^2}{\sum w(y_{\text{obs}})^2} \right]^{1/2} \times 100 \tag{3.56}$$

$$GOF = \frac{\sum w(y_{\text{obs}} - y_{\text{calc}})^2}{v}, \tag{3.57}$$

where y_{obs} are the experimental data, y_{calc} are the fit data, w denotes the fit weights and $v = \text{n. of data points} - \text{n. of variables}$.

Figure 3.13 displays the experimental data of the beat note between the broadband DFB laser and the locked reference DBR laser, acquired with a spectrum analyzer. The pseudo-Voigt profile calculated using LIPRAS, along with the background fit, is also shown. The noise amplitude applied to the laser driving current was $250\,\text{mV}_{\text{pp}}$ with an offset of $-75\,\text{mV}_{\text{DC}}$. The fitted FWHM is 7.5 MHz, with the peak located at 114.5 MHz. The error metrics are: $R_p = -0.2853\%$, $R_{wp} = -0.3606\%$ and $GOF = -0.0009$, indicating a good fit to the data. The beat note without Gaussian noise applied to the laser driving current is also shown in the inset of the figure.

Since the DBR laser is expected to have a linewidth 1 MHz, the assumption that the

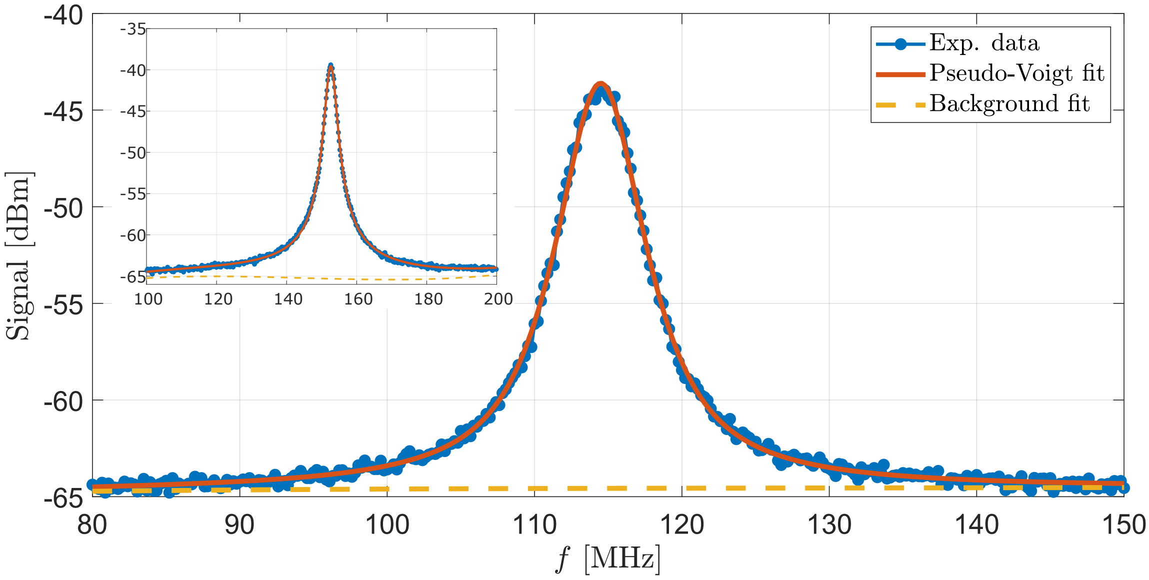

Figure 3.13: *Experimental data (blue line with markers) of the beat note between the broadband DFB laser and the locked reference DBR laser, acquired with a spectrum analyzer. The pseudo-Voigt profile is shown (solid red line) as well as the background fit (yellow dashed line). The amplitude of the gaussian noise signal is* $250\,\mathrm{mV_{pp}}$ *and the offset is* $-75\,\mathrm{mV_{DC}}$. *Inset: beat note without Gaussian noise applied to the DFB laser current.*

bandwidth of the DFB laser $\Delta\nu_{\text{laser}}$ is equal to the FWHM of the beat note is justified. This equivalence allows for a fast estimation of the DFB laser's bandwidth in the experimental setup. The DBR laser is also used to calibrate the frequency of the DFB laser to match the hyperfine transition $F = 1 \to F' = 1$. However, due to the noise introduced into the driving current, the DFB laser is not locked, as the noise complicates locking it with a standard PID feedback loop.

To periodically reset the dynamics of the three-level system, as discussed in Subsection 3.1.2, the broadband laser is switched on and off. This rapid switching is achieved using a 80 MHz Acousto-Optic Modulator (AOM). The 80 MHz radiofrequency, required for the acousto-optic effect, is combined with a pulse train in a frequency mixer. The pulse train comprises an active duration of $22\,\mu$s and an inactive duration of $3\,\mu$s. These time intervals are chosen to ensure that Fano coherence reaches and maintains its stationary value for a duration considerably longer than the $3\,\mu$s off period, which is designed to allow complete relaxation of the excitation. The pulse train is detected in the transmission signal after the vapor cell, measured by a fast photodiode and shown in figure 3.14.

3.2.4 Optical setup

The integration of the various components described above results in the experimental setup illustrated in figure 3.15. The setup was designed to perform measurements of Fano coherence through fluorescence signals. Included in the setup is a repumper laser, which is phase-locked to a reference laser using a Phase Lock Loop (PLL) through a beat note. The repumper laser is designed to excite atoms that have decayed to the $F = 2$ ground

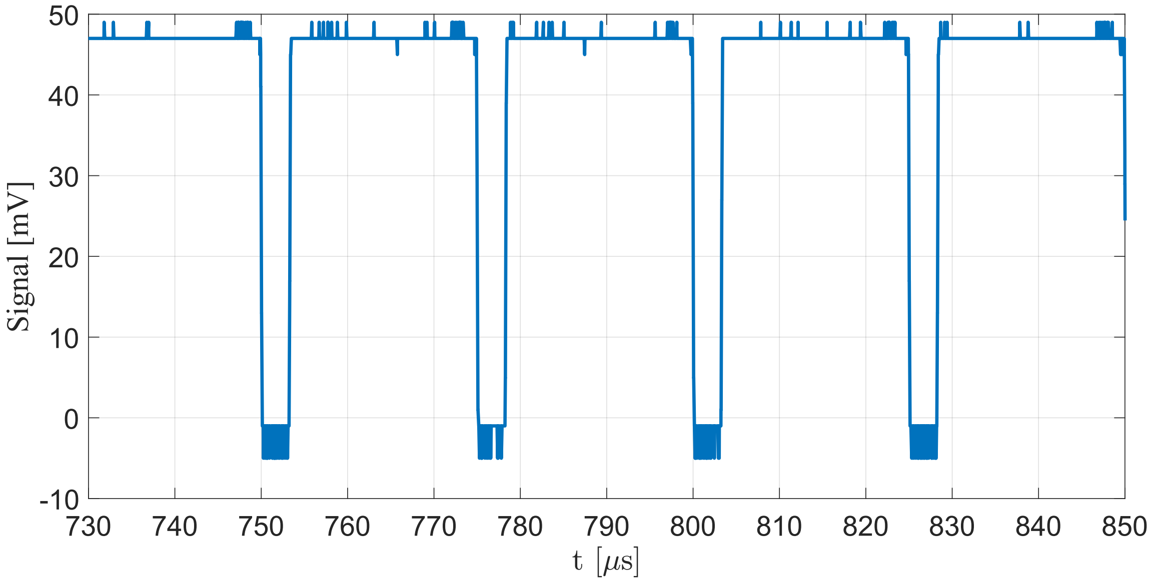

Figure 3.14: *Transmission signal of the modulated light with on and off activation of the AOM. The pulse train consists of* $22\,\mu$s *pulses with a* $3\,\mu$s *off interval. The intensity of the incoherent source is set to* $\bar{n} = 30$.

state, making them unavailable for excitation by the broadband laser. Recall that the ground state manifolds $F = 1$ and $F = 2$ are separated by approximately 6.8 GHz and are not coupled by the broadband radiation source. The repumper laser addresses this by exciting atoms in the $F = 2$ ground state to the $F' = 1$ excited state manifold of the $D2$ line at a wavelength of 780 nm. This process allows the atoms to decay back to the $F = 1$ ground state, effectively enabling repumping and maintaining a continuous cycle of excitation. Initial fluorescence measurements unexpectedly showed only a slight increase in the amplitude of the fluorescence signal when the repumper was active. Instead, the repumper introduced a significant offset in the fluorescence measurements, despite the presence of a 10-nm narrowband filter centered at 795 nm in front of the two photodiodes. This suggests that the repumper was ineffective in enhancing signal clarity. Consequently, the decision was made to remove the repumper and focus on significantly enhancing the signal through precise temperature control.

Figure 3.16 illustrates the experimental setup implemented in the laboratory. On the right is the beatnote detection setup for the master laser. The central part of the setup features the coils cage, which houses the vapor cell and is flanked by two photodiodes positioned to collect fluorescence signals along the vertical (y-axis) and horizontal (x-axis) directions. Initially, only one photodiode was used along with two beams with orthogonal polarizations, where the change in polarization simulated the change in the photodiode's position. However, due to the high noise levels associated with a single photodetector setup, the design was modified to incorporate a differential configuration using two photodiodes. This adjustment significantly improved the signal-to-noise ratio by mitigating low-frequency noise.

In the next section, I present preliminary experimental measurements. These results hint at the presence of Fano coherence, however further investigation is needed to determine the

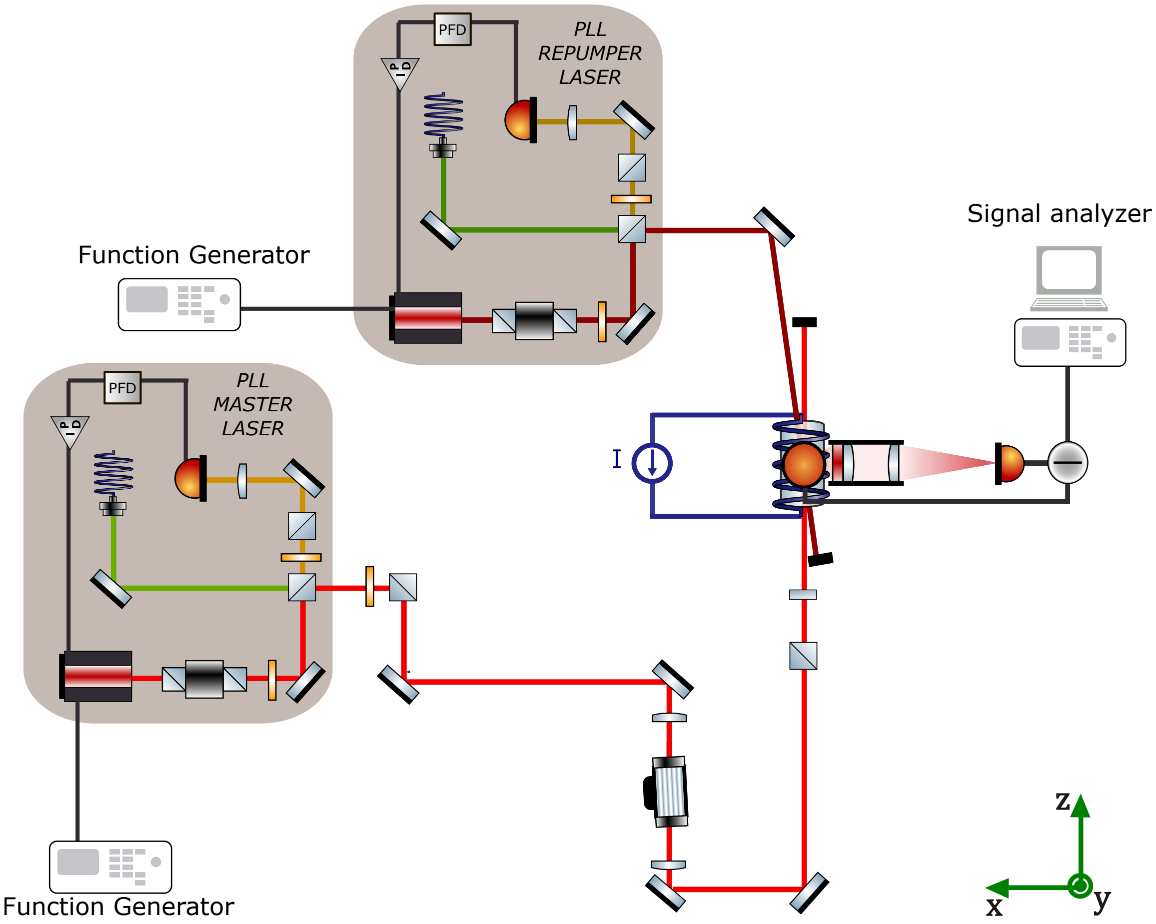

Figure 3.15: *Experimental setup scheme. The repumper and master laser are designed to be locked in a Phase Lock Loop (PLL) scheme. The master laser beam then passes through an AOM and impinges on the vapour cell. Two photodiodes, placed orthogonally around the vapour cell, detect the fluorescence emitted by the atoms. The cell is surrounded by pairs of magnetic coils. The difference signal spectrum of the two photodiodes is then analysed.*

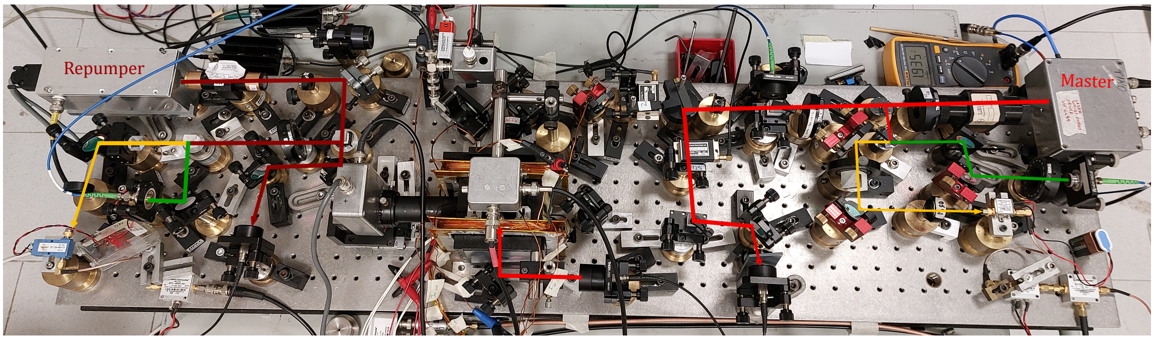

Figure 3.16: *Experimental setup.*

direct association of the observed signals to the Fano coherence.

3.3 Experimental results

The experimental setup, thoroughly described in section 3.2, was designed with precise control of the governing parameters of the dynamics equations relevant to the study. This setup is fundamentally structured to measure the fluorescence anisotropy when Fano coherence is present and compare it to the isotropic fluorescence, observed when such coherence is absent. The design of the setup has undergone numerous iterations, each addressing specific challenges inherent to the detection of weak fluorescence signals.

Initially, a single photodiode was employed with orthogonally polarized beams to simulate changes in photodiode positions. However, this configuration resulted in excessive noise levels, necessitating the adoption of a differential configuration with two photodiodes. The evolution of the setup also included efforts to implement a PLL for the master broadband laser, although the complexity introduced by noisy current driving led to maintaining the laser in a free-running state. Furthermore, early fluorescence measurements indicated minimal signal amplification from the repumper, accompanied by an undesirable offset in measurements. Consequently, the repumper was excluded, and signal improvement was pursued achieved through stringent temperature control.

In the finalized version, the coils cage is centrally positioned, with two photodiodes aligned along the vertical (y-axis) and horizontal (x-axis) directions to capture the emitted fluorescence, as shown in figure 3.15 and 3.16. The magnetic field is modulated at low frequency in such a way to drive the V-type three-level system in and out the anisotropic fluorescence scenario and capturing the same modulation in the difference signal from photodiodes. The measurements obtained thus far are preliminary but indicate potential success in detecting the weak fluorescence signals associated with Fano coherence. However, further studies are needed to validate these results.

3.3.1 Towards Fano coherence detection: preliminary measurements

The weak electronic signal coming from the two photodiodes is measured and analyzed using a Dynamic Signal Analyzer (Keysight 35670A) and the signal spectrum is obtained through a Fast Fourier Transform-based measurement, whose frequency range can span from $122\,\mu$Hz to 102.4 kHz. In particular, the Power Spectral Density (PSD) of the signal is calculated to understand its frequency components.

The measurement begins by setting the temperature of the vapor cell to $T = 40,{}^\circ$C and introducing noise into the driving current of the DFB master laser. It is verified that the frequency beat note aligns with the atomic transition $F = 1 \rightarrow F' = 1$. The noise applied has an amplitude of $250\,\mathrm{mV_{pp}}$ and an offset of $-75\,\mathrm{mV_{DC}}$, resulting in a laser's bandwidth of $\Delta\nu_{\mathrm{laser}} = 7.5,\mathrm{MHz}$, as determined from the fitting shown in figure 3.13. To modulate the magnetic field, a sinusoidal signal at $f = 5$Hz is sent to the power supply controlling the z-axis coils. B_z varies between $B_{z_{\min}} \approx 1$ G and $B_{z_{\max}} \approx 50$ G. These values correspond to an excited states splitting of $\Delta/\bar{\gamma} = 0.1$ and $\Delta/\bar{\gamma} = 4$, respectively. The x and y-axis coils are adjusted to cancel out the magnetic field along their respective axes, ensuring that only the z-axis component remains.

In figure 3.17, the average PSD signals over 20 traces are depicted within the range of $[0, 40]$ Hz. When the laser is active, peaks at 5 Hz and its higher harmonics are observed. The 5 Hz peak is also present when the laser is inactive, indicating that the magnetic field modulation impacts the electronic circuit of the photodiodes, generating electrical

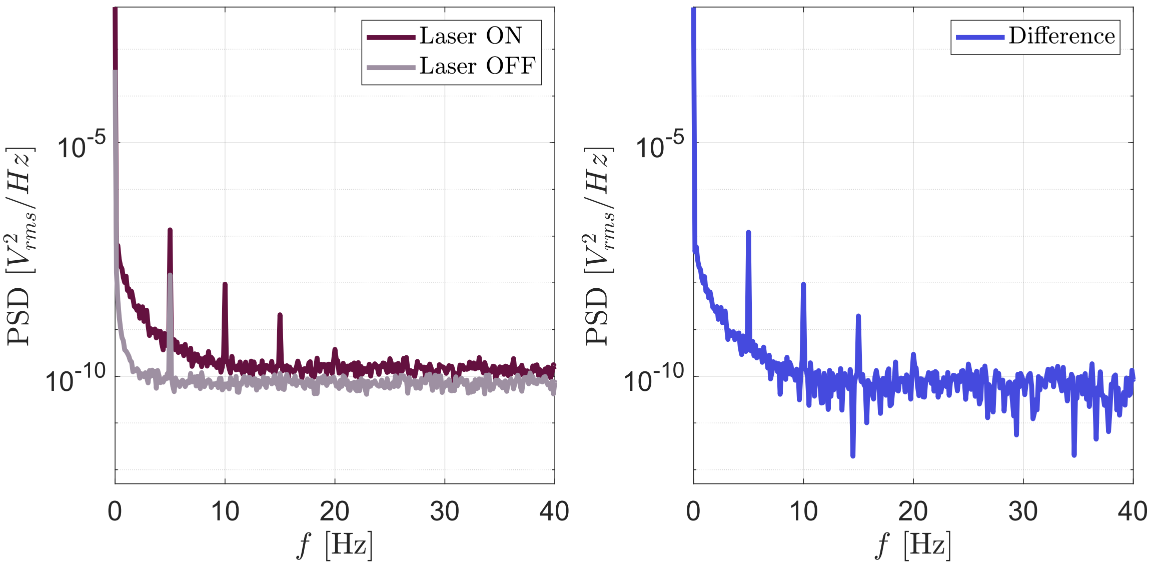

Figure 3.17: *Left: PSD of the difference signal between the two photodiodes, with the master laser on and off. Right: PSD of the difference between these two traces. The laser power is set to* $P_{\text{laser}} \approx 2\,\mu\text{W}$*, corresponding to* $\bar{n} = 9$*. The magnetic field is sinusoidally modulated at* $f = 5\text{Hz}$ *with* $B_{z_{\text{min}}} \approx 1$ *G and* $B_{z_{\text{max}}} \approx 50$ *G. The traces represent the average of 20 measurements.*

noise. The difference signal, obtained by subtracting the laser-off scenario from the laser-on scenario, still exhibits a peak at 5 Hz (picture on the right in figure 3.17), demonstrating that the magnetic field modulation is also reflected in the fluorescence signal. I want to remark that the signal labeled “laser off” refers to a continuous turn-off of the laser light, not the intermittent off periods within the pulse train. The pulse train, characterized by pulses lasting $22\,\mu\text{s}$ with $3\,\mu\text{s}$ off intervals, is applied only when the laser is on.

I subsequently examined the behavior of the 5 Hz peak value and its higher harmonics (10, 15, 20 Hz) by varying the laser power within the range $P_{\text{laser}} \in [0.5, 30]\,\mu\text{W}$, which corresponds to $\bar{n} \in [2, 125]$. The result is shown in figure 3.18. For each peak, the associated signal is expressed relative to the noise floor of the signal, as both the signal and the noise level increase with laser power. At lower power levels, there is a notable enhancement of the signal, which begins to saturate as the power increases. This observation aligns with the theoretical predictions illustrated in figure 3.2, where, for a fixed low Δ, a significant increase in signal is seen at low $\bar{n}$, followed by a saturation trend at very high $\bar{n}$. The exception is the peak at 5 Hz, which shows a distinct behavior: at P_{laser} below $5\,\mu\text{W}$, the signal reaches a maximum, followed by a decrease. However, for P_{laser} above $10\,\mu\text{W}$, the signal starts to increase again, exhibiting a saturation behavior. This suggests that different mechanisms may dominate the signal generation at low and high power levels, with potential implications for optimizing the detection of Fano coherence.

Based on the results illustrated in figure 3.18, I chose a laser power below the saturation point, specifically $P_{\text{laser}} = 5\,\mu\text{W}$, corresponding to $\bar{n} = 21$. With the amplitude of the modulated magnetic field set to 20 G, I varied the offset, thus $B_{z_{\text{min}}}$ and $B_{z_{\text{max}}} = B_{z_{\text{min}}} + 20$ G. The range of $B_{z_{\text{min}}}$ is adjusted between 0.5 and 30 G. The frequency peaks measured varying the magnetic field offset are presented in figure 3.19. As $B_{z_{\text{min}}}$ increases, a significant

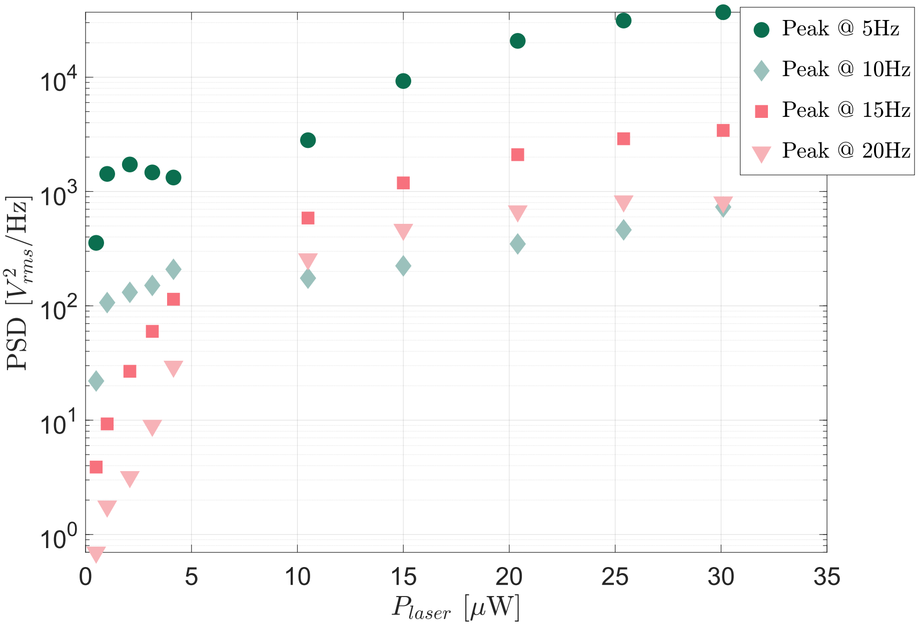

Figure 3.18: *PSD of the frequency peaks* $(5, 10, 15, 20$ *Hz) as the laser power is varied. The values of the peaks are relative to the noise floor of the associated signal. The magnetic field is sinusoidally modulated at* $f = 5\mathrm{Hz}$ *with* $B_{z_{\min}} \approx 1$ *G and* $B_{z_{\max}} \approx 50$ *G.*

reduction is observed across all main harmonics. An increment of $B_{z_{\min}}$ increases the ratio $\Delta/\bar{\gamma}$, at which the interference effect should be present. For the values of $B_{z_{\min}}$ selected, the range of $\Delta/\bar{\gamma}$ spans from 0.04 to 2.4. According to figure 3.2, for $\Delta/\bar{\gamma} \ll 1$, the steady-

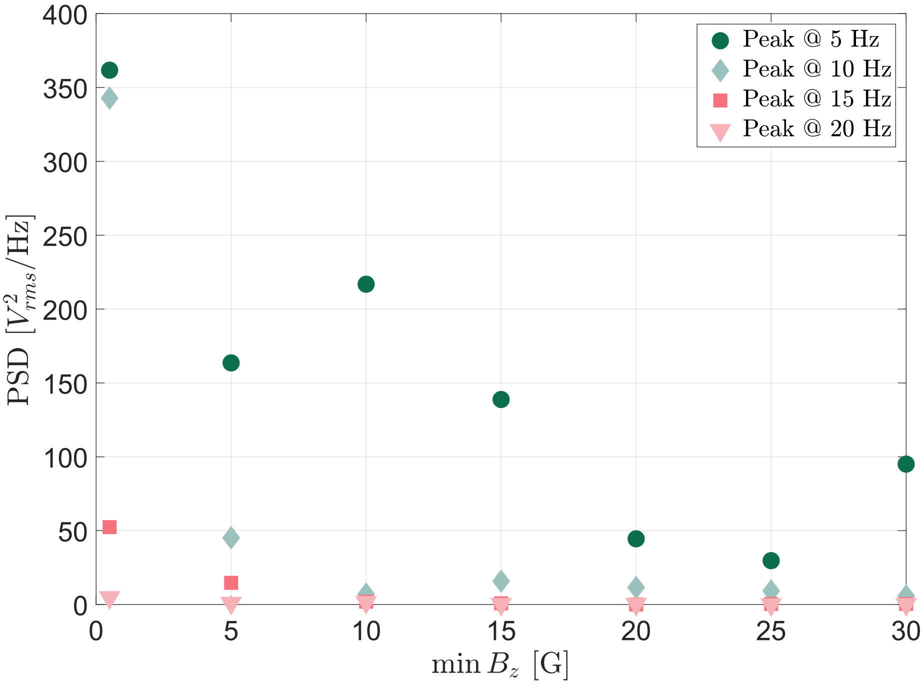

Figure 3.19: *PSD of the frequency peaks* $(5, 10, 15, 20$ *Hz) as the offset of the magnetic field is varied. This variation is reported as a variation of* $B_{z_{\min}}$*, since* $B_{z_{\max}} = B_{z_{\min}} + 20G$*. The amplitude of the modulated field is constant at 20 G. The frequency modulation is at* $f = 5\mathrm{Hz}$*. The values of the peaks are relative to the noise floor of the associated signal.*

state value of the real part of Fano coherence at $\bar{n} = 21$ is higher than for $\Delta/\bar{\gamma} > 1$ at the same $\bar{n}$. Therefore, the behavior observed in Figure 3.19 aligns well with the theoretical predictions. However, the 5 Hz peak exhibits again anomalous behavior, showing a decrease at $B_{z_{\mathrm{min}}} = 5$ G and an increase at $B_{z_{\mathrm{min}}} = 10$ G. It is crucial to note that this frequency might be influenced by electrical noise, which could be contributing to these observed anomalies.

With these data, the preliminary results appear to align well with theoretical predictions. Further measurements are planned to investigate whether the observed behaviors are independent of the modulation frequency of the magnetic field. Moreover, I planned to investigate the influence of applying a stronger noise to broaden the laser spectrum further, and examining the effect of the direction of linear polarization. The current measurements lack sufficient statistical analysis, as they are intended as preliminary observations. Comprehensive statistical evaluation will be conducted in subsequent investigations to strengthen the conclusions.

3.3.2 Discussion

The experimental results, obtained with the optical setup presented, seem promising towards a validation of Fano coherence presence inside a V-type three-level system driven by a broadband laser. Here, the angled-resolved fluorescence scheme for Fano coherence detection is enriched with a slow modulation of the B_z magnetic field, between values that produce a small and large excited state splitting, moving the fluorescence from to be spatially anisotropic to isotropic. This slow modulation is retrieved effectively in the fluorescence signal, which present peaks at the frequency of the field modulation and the subsequent three harmonics.

The behavior of the difference signal between photodiodes is measured evaluating its spectrum and was analysed changing the power of the laser and the offset of the magnetic field modulation. The data show a notable enhancement of the signal at low power levels, which subsequently reaches a saturation point as the laser power increases. This observation aligns well with theoretical predictions where, for a fixed low Δ, significant signal enhancement is expected at low $\bar{n}$, followed by a saturation trend at higher $\bar{n}$.

In terms of the magnetic field, the observed reduction in signal strength with increasing $B_{z_{\mathrm{min}}}$, and thus $\Delta/\bar{\gamma}$, suggests that the interference effects diminish as the magnetic field modulation becomes less favorable for coherent interactions.

The behavior of the 5 Hz peak is particularly noteworthy, displaying anomalous behavior. The peak's deviation from the expected pattern could be indicative of the influence of electrical noise. This noise might affect the photodiode measurements, particularly at this specific frequency, which justifies further investigation, as measurements changing the magnetic field modulation frequency.

The preliminary nature of these experimental results indicates the need for additional measurements to confirm and expand upon these results. Moreover, a statistical analysis is also required. As such, a comprehensive statistical evaluation will be carried out in subsequent investigations to validate these observations and provide a more robust understanding of the underlying phenomenon. Overall, the initial results appear consistent with theoretical predictions.

Conclusions

In this thesis, I investigated the generation of noise-induced Fano coherence within a V-type three-level system excited by an incoherent radiation source. Despite the inherent incoherence of the radiation, its broad spectrum interacts with the discrete energy levels of the system, remarkably leading to significant interference effects in both the excitation and spontaneous emission processes. This interaction ultimately results in the creation of a coherent superposition state of the system, specifically in the creation of coherence between the two excited states, i.e. Fano coherence. To the best of my knowledge, the observation of Fano coherence in such systems has not yet been reported.

I derived the quantum master equation for the system dynamics under two distinct conditions: one involving an isotropic unpolarized source and the other involving an anisotropic polarized source. The polarized source allows for the recovery of interference effects in the excitation process, especially in systems where the electric dipole moments are orthogonal. The orthogonality of the transition dipole moments makes them distinguishable, thereby eliminating the associated interference. By employing an appropriately polarized source capable of exciting both dipole moments, the interference is restored. However, the spontaneous emission process remains isotropic by nature, as it arises from interactions with vacuum modes, thus no interference between the decay paths can emerge if the transition dipole moments are orthogonal.

For both scenarios, the solutions were analyzed by identifying two regimes: the overdamped regime and the underdamped regime in the weak and strong pumping conditions. Adequate Fano coherence values, characterized by quasi-stationary and stationary behaviors over time, were only achievable within the overdamped regime. The key parameters governing these equations—namely, the splitting between the excited levels Δ, the radiation intensity $\bar{n}$, and the alignment factor between the electric dipole moments p—were investigated to ensure that the solutions fall within the overdamped regime. Stationarity or quasi-stationarity of coherence facilitates its detection in practical experimental setups.

From a thermodynamic perspective, generating Fano coherences in a V-type system implies an excess of energy relative to the system's initial state before the process. Given their origin, I investigated whether noise-induced Fano coherences exhibit distinctive non-classical properties. For this purpose, I employed the Kirkwood-Dirac Quasiprobability distribution to analyze stochastic energy fluctuations within the system. The presence of negative real parts in the KDQ distribution indicates genuine quantum features for the generation of noise-induced Fano coherences.

I calculated the Kirkwood-Dirac quasiprobability distribution to study time-dependent energy variations in the system under incoherent radiation. My analysis revealed that initializing the three-level system in a superposition of the Hamiltonian eigenstates results in negative real parts of the quasiprobability associated to the coherence between the excited states. Furthermore, the observed energy changes arise exclusively from the off-diagonal elements of the system's density matrix and exhibit negative values. This suggests that the excess energy could be interpreted as extractable work, potentially harnessed by an external load. Notably, despite the incoherent nature of the input light source, the thermodynamic process achieved a thermodynamic efficiency of up to 6%.

Finally, the V-type three-level system was designed to be implemented on an atomic platform for a proof-of-principle experiment aimed at detecting noise-induced Fano coherence. The atomic platform is particularly advantageous due to its ability to precisely control the key parameters, namely Δ and $\bar{n}$. The system was identified in the D1 line $F = 1 \rightarrow F' = 1$ hyperfine atomic transition of ^{87}Rb atoms, involving the magnetic sublevels $\Delta m_F = \pm 1$. By exciting the system with a broadband polarized laser, Fano coherence can be detected through the angle-resolved fluorescence technique. This method isolates the contribution of the coherence between the excited states to the emitted radiation, revealing a spatial anisotropy around the atomic vapor cell.

I designed and realized an optical setup for the detection, which includes a controllable uniform magnetic field to precisely adjust the splitting Δ, and a laser whose spectrum can be broadened by introducing Gaussian noise into its driving current. The fluorescence signal is detected using two photodiodes aligned orthogonally around the cell in a differential configuration. By modulating the magnetic field between small and large splitting configurations, the fluorescence transitions from anisotropic to isotropic conditions. Preliminary measurements indicated that the modulation of the magnetic field is reflected in the photodiode signals' spectrum, indicating a promising presence of coherence. By conducting the same measurement with different laser intensities ($\bar{n}$) and magnetic field modulation offsets (Δ) I observed a consistent behavior with theoretical predictions. Further measurements are planned to comprehensively validate the presence of Fano coherence.

Future developments

Building on the insights gained from this study, several possibilities for future research and development present themselves. The following areas are identified as promising for further investigation and refinement:

- **Cold atoms experiment:** the transition to experiments with cold atoms can offer significant improvements in signal-to-noise ratios and sensitivity, particularly for detecting subtle phenomena as Fano coherence. By mitigating the influence of thermal noise and Doppler broadening, cold atom systems enhance the precision of measurements. Additionally, the lower temperatures of cold atom ensembles allow for more precise control over atomic energy levels and enable the exploration of various initial atomic states through advanced state preparation techniques. However, the implementation of cold atom experiments involves increased complexity in the experimental setup.

- **Validation on different platforms:** the V-type three-level system can also be implemented on alternative platforms, such as solid-state platforms. In these systems, incoherence may arise not only from the radiation but also from lattice vibrations, which can be modeled as interactions with a thermal phonon reservoir. As discussed in [34], the incoherent phonon interaction can couple the three level system with a two-level system, representing the lower and upper states in the conduction and valence bands, respectively, at which an external load can be connected. By interpreting this system as a photoconversion device, the current, and thus electrical power, can be in principle enhanced by Fano interference. On this regard, two-dimensional materials like semiconducting Transition Metal Dichalcogenides (TMDs) offer a promising avenue for exploration. As two-dimensional materials, TMDs offer unique opto-electronic properties and the low-dimensional nature enables better control and facilitates the integration into nanoscale devices. A first approach to this material occurred during my collaboration with Prof. Niek van Hults' group at ICFO. During this period, I conducted an analysis of tungsten diselenide (WSe_2) at room temperature. This analysis employed microscopic photo-current and luminescence detection techniques within a Fourier-transform excitation spectroscopy framework. The objective was to investigate the role of excitons in the material's photoresponse. To achieve this, we spatially resolved the excitation spectrum of WSe_2, by examining both its current and luminescence responses. This experience proved invaluable for understanding the optical behavior of two-dimensional materials under broad excitation as well as how to perform current measurements on these materials. However, further in-depth studies are required to explore how to implement multi-level systems on solid-state platforms and to precisely control the key parameters. Testing these systems could advance the research on the topic towards practical technological applications.

List of Pubblications

During my PhD, I contributed to the following scientific publications:

- J. Wragg, L. Bolzonello, **L. Donati**, K. Soundarapandian, R. Bertini, F. Koppens and N. van Hulst, *The Bright and Dark Excitons of Room Temperature WSe2 Distinguished by Photo-Current and Luminescence Spectroscopy Mapping*, (2024); submitted for revision to the international journal *Nature Nanotechnology*;
- **L. Donati**, F. S. Cataliotti and S. Gherardini, *Energetics and quantumness of Fano coherence generation*, Sci. Rep. **14**, 20145, (2024);
- I. Gianani, I. Mastroserio, L. Buffoni, N. Bruno, **L. Donati**, V. Cimini, M. Barbieri, F. S. Cataliotti and F. Caruso, *Experimental Quantum Embedding for Machine Learning*, Adv. Quantum Technol. **5**, 2100140, (2022).

Bibliography

[1] A. Kastler. *Quelques suggestions concernant la production optique et la détection optique d'une inégalité de population des niveaux de quantifigation spatiale des atomes. Application a l'expérience de Stern et Gerlach et a la résonance magnétique. J. Phys. Radium*, 11:255, (1950).

[2] F.G. Major. 5. optical pumping. In *Atomic and Electron Physics*, volume 7 of *Methods in Experimental Physics*, pages 1–28. Academic Press, (1968).

[3] C. Cohen-Tannoudji. *Reviews of Modern Physics*, 70(3), (1998).

[4] W. Hanle. *Über magnetische Beeinflussung der Polarisation der Resonanzfluoreszenz. Zeitschrift für Physik*, 30(1):93–105, (1924).

[5] F. D. Colegrove, P. A. Franken, R. R. Lewis, and R. H. Sands. *Novel Method of Spectroscopy With Applications to Precision Fine Structure Measurements. Phys. Rev. Lett.*, **3**(9):420, (1959).

[6] A. T. Forrester, W. E. Parkins, and E. Gerjuoy. *On the Possibility of Observing Beat Frequencies between Lines in the Visible Spectrum. Phys. Rev.*, **72**:728, (1947).

[7] S. Haroche. *Quantum beats and time resolved spectroscopy In: Shimoda, K. (eds) High Resolution Laser Spectroscopy*, volume **13**. Topics in Applied Physics, Springer, Berlin, Heidelberg, (1976).

[8] W. Demtröder. *Laser Spectroscopy Vol. 1: Technology.* Springer-Verlag Berlin Heidelberg, (2008).

[9] E. Arimondo and G. Orriols. *Nonabsorbing atomic coherences by coherent two-photon transitions in a three-level optical pumping. Lett. Nuovo Cimento*, **17**:333–338, (1976).

[10] H. R. Gray, R. M. Whitley, and C.R. Stroud. *Coherent trapping of atomic populations. Opt. Lett.*, **3**:218–220, (1978).

[11] E. Arimondo. *Relaxation processes in coherent-population trapping. Opt. Lett.*, **54**:2216–2223, (1996).

[12] S. E. Harris, J. E. Field, and A. Imamoğlu. *Nonlinear optical processes using electromagnetically induced transparency. Phys. Rev. Lett.*, **64**:1107–1110, (1990).

[13] S. E. Harris. *Electromagnetically Induced Transparency. Physics Today*, **50**:36–42, (1997).

[14] G. S. Agarwal. *Quantum Statistical Theories of Spontaneous Emissions and Their Relation to other Approaches. Springer Tracts in Modern Physics*, Vol. **70**, Springer Berlin, (1974).

[15] G. C. Hegerfeldt and M. B. Plenio. *Coherence with incoherent light: A new type of quantum beat for a single atom. Phys. Rev. A*, **47**:2186, (1993).

[16] S.-Q. Gong, E. Paspalakis, and P. L. Knight. *Effects of spontaneous emission interference on population inversions of a V-type atom. J. Mod. Opt.*, **45**:2433–2442, (1998).

[17] S.-Q. Gong, Y. Li, S.-D. Du, and Z.-Z. Xu. *Unexpected population inversion via spontaneously generated coherence of a* Λ*-system. Phys. Lett. A*, **259**:43–48, (1999).

[18] S.-Y. Zhu, L. Narducci, and M. O. Scully. *Quantum-mechanical interference effects in the spontaneous-emission spectrum of a driven atom. Phys. Rev. A*, **52**:4791–4802, (1995).

[19] S.Y. Zhu, R. C. F. Chan, and C. P. Lee. *Spontaneous emission from a three-level atom. Phys. Rev. A*, **52**:710–716, (1995).

[20] P. Zhou P. and S. Swain. *Ultranarrow Spectral Lines via Quantum Interference. Phys. Rev. Lett.*, **77**:3995–3998, (1996).

[21] D. A. Cardimona, M. G. Raymer, and C. R. Stroud Jr. *Steady-state quantum interference in resonance fluorescence. J. Phys. B: Atom. Mol. Phys.*, **15**:55, (1982).

[22] K. T. Kapale, M. O. Scully, S.-Y. Zhu, and S. Zubairy. *Quenching of spontaneous emission through interference of incoherent pump processes. Phys. Rev. A*, **67**:023804, (2003).

[23] V. V. Kozlov, Y. Rostovtsev, and M. O. Scully. *Inducing quantum coherence via decays and incoherent pumping with application to population trapping, lasing without inversion, and quenching of spontaneous emission. Phys. Rev. A*, **74**:063829, (2006).

[24] U. Fano. *Sullo spettro di assorbimento dei gas nobili presso il limite dello spettro d'arco. Nuovo Cim.*, **12**:154–161, (1935).

[25] U. Fano. *Effects of configuration interaction on intensities and phase shifts. Phys. Rev.*, **124**:1886, (1961).

[26] T. V. Tscherbul and P. Brumer. *Long-Lived Quasistationary Coherences in a V-type System Driven by Incoherent Light. Phys. Rev. Lett.*, **113**:113601, (2014).

[27] T. V. Tscherbul and P. Brumer. *Partial secular Bloch-Redfield master equation for incoherent excitation of multilevel quantum systems. J. Chem. Phys.*, **142**(10):104107, (2015).

[28] S. Koyu and T. V. Tscherbul. *Long-lived quantum coherences in a V-type system strongly driven by a thermal environment. Phys. Rev. A*, **98**:023811, (2018).

[29] A. Dodin, T. Tscherbul, R. Alicki, A. Vutha, and P. Brumer. *Secular versus nonsecular Redfield dynamics and Fano coherences in incoherent excitation: An experimental proposal. Phys. Rev. A*, **97**:013421, (2018).

[30] S. Koyu, A. Dodin, P. Brumer, and T. V. Tscherbul. *Steady-state Fano coherences in a V-type system driven by polarized incoherent light. Phys. Rev. Res.*, **3**:013295, (2021).

[31] B.-Q. Ou, L.-M. Liang, and C.-Z. Li. *Coherence induced by incoherent pumping field and decay process in three-level* Λ*-type atomic system. Opt. Commun.*, **281**:4940–4945, (2008).

[32] S. Koyu and T. V. Tscherbul. *Long-lived quantum coherent dynamics of a* Λ *system driven by a thermal environment. J. Chem. Phys.*, **157**:124302, (2022).

[33] M. O. Scully, K. R. Chapin, K. E. Dorfman K. E., and A. Svidzinsky. *Quantum heat engine power can be increased by noise-induced coherence. Proc. Natl. Acad. Sci. USA*, **108**:15097–15100, (2011).

[34] A. A. Svidzinsky, K. E. Dorfman, and M. O. Scully. *Enhancing photovoltaic power by Fano-induced coherence. Phys. Rev. A*, **84**:053818, (2011).

[35] H. S. Han, A. Lee, K. Sinha, F. K. Fatemi, and S. L. Rolston. *Observation of Vacuum-Induced Collective Quantum Beats. Phys. Rev. Lett.*, **127**:073604, (2021).

[36] S. Hernández-Gómez, S. Gherardini, A. Belenchia, M. Lostaglio, A. Levy, and N. Fabbri. *Projective measurements can probe nonclassical work extraction and time correlations. Phys. Rev. Research*, **6**(2), (2024).

[37] S. Gherardini and G. De Chiara. *Quasiprobabilities in quantum thermodynamics and many-body systems. PRX Quantum*, **5**:030201, (2024).

[38] S. Hernández-Gómez, Isogawa T., A. Belenchia, A. Levy, N. Fabbri, S. Gherardini, and Cappellaro P. *Interferometry of quantum correlation functions to access quasiprobability distribution of work. Eprint arXiv:2405.21041*, (2024).

[39] R. Loudon. *The Quantum Theory of Light.* Oxford University Press, (2000).

[40] M. O. Scully and M. S. Zubairy. *Quantum Optics.* Third Edition. Cambridge University Press, Cambridge, UK, (1997).

[41] D. A. Steck. *Quantum and Atom Optics.* available online at `http://steck.us/teaching` (revision 0.12.6, 23 April 2019), (2019).

[42] D. F. Walls and G. J. Milburn. *Quantum Optics.* Second Edition. Springer, (2008).

[43] M. A. Nielsen and I. L. Chuang. *Quantum Computation and Quantum Information.* Second Edition. Cambridge University Press, (2000).

[44] H.-B. Breuer and F. Petruccione. *The Theory of Open Quantum Systems.* Oxford University Press, (2002).

[45] D. Manzano. *A short introduction to the Lindblad Master Equation. AIP Advances*, **10**(2):025106, (2020).

[46] R. Dümcke and H. Spohn. *The proper form of the generator in the weak coupling limit. Z. Phys. B Condens. Matter*, **34**:419–422, (1979).

[47] C. Gardiner and P. Zoller. *Quantum Noise.* Springer, New York, USA, (2010).

[48] G. McCauley, B. Cruikshank, D.I. Bondar, and K. Jacobs. *Accurate Lindblad-form master equation for weakly damped quantum systems across all regimes. npj Quantum Inf*, **6**(74), (2020).

[49] D. F. de la Pradilla, E. Moreno, and J. Feist. *Taming the Bloch-Redfield equation: Recovering an accurate Lindblad equation for general open quantum systems. arXiv preprint, arXiv:2402.06354v1*, (2024).

[50] G. Lindblad. *On the generators of quantum dynamical semigroups. Commun. Math. Phys.*, **48**(119), (1976).

[51] A. Dodin, T. V. Tscherbul, and P. Brumer. *Quantum dynamics of incoherently driven V-type systems: Analytic solutions beyond the secular approximation. J. Chem. Phys.*, **144**(24):244108, (2016).

[52] A. Dodin, T. V. Tscherbul, and P. Brumer. *Coherent dynamics of V-type systems driven by time-dependent incoherent radiation. J. Chem. Phys.*, **145**:244313, (2016).

[53] J. Jeske, D. J. Ing, S. F. Huelga M. B. Plenio, and J. H. Cole. *Bloch-Redfield equations for modeling light-harvesting complexes. J. Chem. Phys.*, **142**:064104, (2015).

[54] P. R. Eastham, P. Kirton, H. M. Cammack, B. W. Lovett, and J. Keeling. *Bath-induced coherence and the secular approximation. Phys. Rev. A*, **94**:012110, (2016).

[55] L. Donati, F. S. Cataliotti, and S. Gherardini. *Energetics and quantumness of Fano coherence generation. Sci. Rep.*, **14**:20145, (2024).

[56] C. J. Foot. *Atomic Physics.* Oxford University Press Inc., New York, (2005).

[57] K. Blum. *Density Matrix Theory and Applications.* Springer,Berlin, (2011).

[58] T. F. Havel. *Robust procedures for converting among Lindblad, Kraus and matrix representations of quantum dynamical semigroups. J. Math. Phys.*, **44**:534–557, (2003).

[59] N. J. Higham. *The Scaling and Squaring Method for the Matrix Exponential Revisited. SIAM J. Matrix Anal. Appl.*, **26**(4):1179–1193, (2005).

[60] R. W. Spekkens. *Contextuality for preparations, transformations, and unsharp measurements. Phys. Rev. A*, **71**:052108, (2005).

[61] S. Kochen and E.P. Specker. *The problem of hidden variables in quantum mechanics. Journal of Mathematics and Mechanics*, **17**:59–87, (1967).

[62] E. Wigner. *On the quantum correction for thermodynamic equilibrium. Phys. Rev.*, **40**:749–759, (1932).

[63] E. P. Wigner. *The problem of measurement. Am. J. Phys.*, **31**(1):6–15, (1963).

[64] D.R. M. Arvidsson-Shukur, J. C. Drori, and N. Y. Halpern. *Conditions tighter than noncommutation needed for nonclassicality. J. Phys. A: Math. Theor.*, **54**:284001, (2021).

[65] M. Lostaglio, A. Belenchia, A. Levy, S. Hernández-Gómez, N. Fabbri, and S. Gherardini. *Kirkwood-Dirac quasiprobability approach to the statistics of incompatible observables. Quantum*, **7**:1128, (2023).

[66] J. G. Kirkwood. *Quantum statistics of almost classical assemblies. Phys. Rev.*, **44**:31–37, (1933).

[67] P. A. M. Dirac. *On the analogy between classical and quantum mechanics. Rev. Mod. Phys.*, **17**:195–199, (1945).

[68] M. F. Pusey. *Anomalous Weak Values Are Proofs of Contextuality. Phys. Rev. Lett.*, **113**:200401, (2014).

[69] R. Kunjwal, M. Lostaglio, and M. F. Pusey. *Anomalous weak values and contextuality: Robustness, tightness, and imaginary parts. Phys. Rev. A*, **100**:042116, (2019).

[70] S. Vinjanampathy and J. Anders. *Quantum thermodynamics. Contemporary Physics*, **57**(4):545–579, (2016).

[71] F. Binder, L. A. Correa, C. Gogolin, J. Anders, and G. Adesso. *Thermodynamics in the Quantum Regime: Fundamental Aspects and New Directions.* Fundamental Theories of Physics (Springer), (2018).

[72] M. Campisi, P. Hänggi, and P. Talkner. *Colloquium: Quantum fluctuation relations: Foundations and applications. Rev. Mod. Phys.*, **83**(771):1653, (2011).

[73] R. Alicki. *The quantum open system as a model of the heat engine. J. Phys. A: Math. Gen.*, **12**(5), (1979).

[74] R.F. Werner P. Busch, P. Lahti. *Colloquium: Quantum root-mean-square error and measurement. Rev. Mod. Phys.*, **86**(4):1261–1281, (2014).

[75] P. Talkner, E. Lutz, and P. Hänggi. *Fluctuation theorems: Work is not an observable. Phys. Rev. E*, **75**:050102, (2007).

[76] M. Esposito, U. Harbola, and S. Mukamel. *Nonequilibrium fluctuations, fluctuation theorems, and counting statistics in quantum systems. Rev. Mod. Phys.*, **81**:1665, (2009).

[77] G. H. Aguilar, T. L. Silva, T. E. Guimarães, R. S. Piera, L. C. Céleri, and G. T. Landi. *Two-point measurement of entropy production from the outcomes of a single experiment with correlated photon pairs. Phys. Rev. A*, **106**:L020201, (2022).

[78] P. Talkner and P. Hänggi. *Colloquium: Statistical mechanics and thermodynamics at strong coupling: Quantum and classical. Rev. Mod. Phys.*, **92**:041002, (2020).

[79] K. Luoma K. Beyer, R. Uola and W. T. Strunz. *Joint measurability in nonequilibrium quantum thermodynamics. Phys. Rev. E*, **106**:L022101, (2022).

[80] P. Solinas and S. Gasparinetti. *Full distribution of work done on a quantum system for arbitrary initial states. Phys. Rev. E*, **92**:042150, (2015).

[81] M. Perarnau-Llobet, E. Bäumer, K. V. Hovhannisyan, M. Huber, and A. Acin. *No-Go Theorem for the Characterization of Work Fluctuations in Coherent Quantum Systems. Phys. Rev. Lett.*, **118**:070601, (2017).

[82] A. E. Allahverdyan. *Nonequilibrium quantum fluctuations of work. Phys. Rev. E*, **90**:032137, (2014).

[83] M. Lostaglio. *Quantum Fluctuation Theorems, Contextuality, and Work Quasiprobabilities. Phys. Rev. Lett.*, **120**:040602, (2018).

[84] R. W. Spekkens. *Negativity and Contextuality are Equivalent Notions of Nonclassicality. Phys. Rev. Lett.*, **101**:020401, (2008).

[85] S. De Bièvre. *Complete Incompatibility, Support Uncertainty, and Kirkwood-Dirac Nonclassicality. Phys. Rev. Lett.*, **127**:190404, (2021).

[86] H. Margenau and R. N. Hill. *Correlation between measurements in quantum theory. Prog. Theor. Phys.*, **26**:722, (1961).

[87] J. J. Halliwell. *Leggett-Garg inequalities and no-signaling in time: A quasiprobability approach. Phys. Rev. A*, **93**:022123, (2016).

[88] J. R. González Alonso, N. Yunger Halpern, and J. Dressel. *Out-of-Time-Ordered-Correlator Quasiprobabilities Robustly Witness Scrambling. Phys. Rev. Lett.*, **122**(4):040404, (2019).

[89] F. Campaioli, S. Gherardini, J. Q. Quach, M. Polini, and G. M. Andolina. *Colloquium: Quantum Batteries. Eprint arXiv:2308.02277*, (2023).

[90] A. Levy, L. Diósi, and R. Kosloff. *Quantum flywheel. Phys. Rev. A*, **93**:052119, (2016).

[91] D. A. Steck. *Rubidium 87 D Line Data.* Technical report, available online at `http://steck.us/alkalidata`, (revision 2.3.2, 10 September 2023).

[92] W. Demtröder. *Laser Spectroscopy Vol. 1: Basic Principles.* Springer-Verlag Berlin Heidelberg, (2008).

[93] V. P. Itkin C. B. Alcock and M. K. Horrigan. *Vapor Pressure Equations for the Metallic Elements: 298–2500 K. Canadian Metallurgical Quarterly*, **23**(309), (1984).

[94] W. M. Frix, G. G. Karady, and B. A. Venetz. *Comparison of calibration systems for magnetic measurement equipment. IEEE Transactions on Power Delivery*, **9**:100–106, (1994).

[95] S. Somkun and T. Borirak-Arawin. *Quasi-analytical Design of a Square Helmholtz Coil with Finite Cross-sectional Area as a Magnetic Flux Density Standard.* In *19th Symposium IMEKO TC 4 Symposium and 17th IWADC Workshop Advances in Instrumentation and Sensors Interoperability (Barcelona)*, (2013).

[96] G. Brisebois. *Low Noise Amplifiers for Small and Large Area Photodiodes: Design Note 399.* Technical report, Analog Devices, (2006).

[97] G. Esteves, K. Ramos, C. M. Fancher, and J. L. Jones. *LIPRAS: Line-Profile Analysis Software*, (2017).